



‘Photocatalytic Hydrogen Production with Supported Au and Au-alloy Nanoparticles’

Wilm Jones

**School of Chemistry
Cardiff University**

Thesis for the degree of Doctor of Philosophy

2016

DECLARATION

This work has not been submitted in substance for any other degree or award at this or any other university or place of learning, nor is being submitted concurrently in candidature for any degree or other award.

Signed (candidate) Date
.....

STATEMENT 1

This thesis is being submitted in partial fulfillment of the requirements for the degree of PhD

Signed (candidate) Date
.....

STATEMENT 2

This thesis is the result of my own independent work/investigation, except where otherwise stated, and the thesis has not been edited by a third party beyond what is permitted by Cardiff University's Policy on the Use of Third Party Editors by Research Degree Students. Other sources are acknowledged by explicit references. The views expressed are my own.

Signed (candidate) Date
.....

STATEMENT 3

I hereby give consent for my thesis, if accepted, to be available online in the University's Open Access repository and for inter-library loan, and for the title and summary to be made available to outside organisations.

Signed (candidate) Date
.....

STATEMENT 4: PREVIOUSLY APPROVED BAR ON ACCESS

I hereby give consent for my thesis, if accepted, to be available online in the University's Open Access repository and for inter-library loans **after expiry of a bar on access previously approved by the Academic Standards & Quality Committee.**

Signed (candidate) Date
.....

Summary

Catalysts consisting of noble metal nano-particles (NP) supported on semiconductors were synthesised by mainly colloidal procedures. Photocatalytic reforming reactions of simple alcohols and amines were studied with the synthesised catalysts as a method of hydrogen production. The goal was to develop an alternative environmentally friendly approach to hydrogen generation.

Primarily catalysts were synthesised by the sol immobilisation method, which allows for the formation of noble metal NPs with controlled size (~ 3 nm) on the surface of a support. The sol immobilisation was used to prepare a set of bimetallic structured AgAu NPs supported on TiO_2 (P25). Improvement in activity was found for the AgAu- TiO_2 catalysts (1:1 weight ratio of Ag:Au) over the monometallic Au analogue. However when NPs were prepared to have a structure of Au core and thin layer of Ag on the surface, supported on TiO_2 , no improvement in activity was observed. Preparation of Au NPs supported on TiO_2 with the subsequent deposition of thin layers of Pd onto the surface of the Au by three methods was also undertaken. Here all of the PdAu- TiO_2 catalysts which were made exhibited improved activity over the reference samples tested. This improvement in H_2 was attributed to the NPs having a Au core and PdAu shell on the surface of TiO_2 .

Finally graphitic carbon nitride ($\text{g-C}_3\text{N}_4$) was investigated as a visible light active semiconductor for hydrogen production by photocatalytic reforming reactions. Direct activity comparisons between Pd loaded $\text{g-C}_3\text{N}_4$ (urea derived) and TiO_2 (P25) were undertaken by performing two sets of reactions under identical conditions. The results from these reactions show that under the full arc condition of the solar simulator (150 W Xe arc lamp) TiO_2 was the most active, despite having a larger band gap (3.2 eV) compared to the $\text{g-C}_3\text{N}_4$ (2.8 eV).

Abstract

Photocatalytic reforming reactions of simple alcohols and amines have been studied as a method of hydrogen production. The reactions were carried out with synthesised catalysts consisting of noble metal nano-particles (NP) supported on semiconductor supports. The aim was to develop an alternative environmentally friendly approach to hydrogen production.

Primarily catalysts were synthesised by the sol immobilisation method, which allows for the formation of a colloidal dispersion of noble metals in solution which can then be deposited onto the surface of an appropriate support. By exploring the parameters during the sol immobilisation method a standard synthesis procedure was decided upon and used throughout this thesis. This procedure allowed for the reproducible preparation of Au and Pd NPs in the order of ~ 3 nm as well as bimetallic AgAu and Pd Au NPs on the surface of a TiO_2 support.

The sol immobilisation method was used to prepare two sets of bimetallic AgAu NPs supported on TiO_2 (P25). AgAu- TiO_2 catalysts with a 1:1 weight ratio were prepared and they were found to be more active than the monometallic Au- TiO_2 and Ag- TiO_2 . The most active of the AgAu- TiO_2 catalysts was synthesised by first preparing a Au colloid followed by reduction of the Ag precursor onto the surface of the Au to make a core-shell structure NP. A second set of AgAu- TiO_2 catalysts was prepared starting with Au NPs followed by deposition of a controlled shell thickness of Ag on the surface supported on TiO_2 , by three different methods. Characterisation for these samples was performed by X-ray absorption spectroscopy (XAS) techniques at the Diamond light source. The deposition of thin layers of Ag onto the preformed Au NPs results in the activity being poorer than the reference catalyst of Au- TiO_2 .

Preparation of Au NPs supported on TiO_2 with the subsequent deposition of thin layers of Pd onto the surface of the Au by three methods was also undertaken, and again characterised by XAS. Here all of the PdAu- TiO_2 catalysts which were made exhibited improved activity over the reference samples tested. This improvement in H_2 was attributed to the NPs having a Au core and PdAu shell on the surface of TiO_2 .

Finally graphitic carbon nitride ($\text{g-C}_3\text{N}_4$) was investigated as a visible light active semiconductor for hydrogen production by photocatalytic reforming reactions. In recent years graphitic carbon nitride has gain interest as an alternative semiconductor support for photocatalytic reactions. Direct activity comparisons between Pd loaded $\text{g-C}_3\text{N}_4$ (urea derived) and TiO_2 (P25) were undertaken by performing two sets of reactions under identical

conditions. The results from these reactions show that under the full arc condition of the solar simulator (150 W Xe arc lamp) TiO_2 was the most active, despite having a larger band gap (3.2 eV) compared to the g- C_3N_4 (2.8 eV). Also investigated was the choice of molecule being reformed (or hole scavenger) by Pd- TiO_2 and Pd- C_3N_4 with triethanolamine and methanol compared, as well as a variety of simple amines.

Acknowledgements

Firstly, I would like to express my sincere gratitude to my supervisor, Professor Michael Bowker for giving me the opportunity to study towards a PhD. His guidance and expertise throughout my studies is very much appreciated. Under his supervision I have expanded my knowledge in a range of areas and have been able to publish my own work.

Secondly, I would also like to thank everyone in the Catalysis Hub at Research Complex at Harwell who contributed towards my thesis during my studies. Particularly Dr Peter Wells and Dr Nikolas Dimitratos helped me significantly with their knowledge of X-Ray absorption techniques and colloidal preparation methods.

Also I would like to express my gratitude to everyone who collaborated with in my work including Julia Kennedy who tested samples for me at Cardiff University, Ren Su and Qian Yang who tested samples for me at Aarhus University, Angel Caravaca and Gareth Hartley who assisted with testing of the carbon nitride catalysts.

Special thanks to Scott Rogers for all his help in the lab, and teaching me the basics of catalyst preparation and TEM in my first year. Also thanks to Catherine Brookes for helping me get set up in Oxford when I first arrived and giving me lifts to work, as well as always assisting if I had a problem in the lab. Not forgetting thanks to my fellow PhD students Antonios Vamvakeros, Alex O'Malley, Anna Gould, Donato Decarolis and everybody else for providing me with a friendly environment to learn in.

Finally a special thanks to all of my family who have always been supportive of my studies and without them I would not be in this position.

Contents

Chapter 1: Introduction

1.1	Introduction to photocatalysis	2
1.1.1	Background	2
1.1.2	Hydrogen as a fuel	2
1.1.3	Hydrogen from photocatalytic water splitting	3
1.1.4	Challenges and light energy required for water splitting	3
1.1.5	Requirements for semiconductor photocatalysts	6
1.1.6	Titanium dioxide (TiO ₂)	7
1.1.7	Noble metal loading of TiO ₂	9
1.1.8	Photocatalytic hydrogen production using sacrificial agents	11
1.1.9	Metal loading of co-catalyst	14
1.1.10	Modification of TiO ₂	15
1.1.11	Graphitic carbon nitride	16
1.2	Catalyst preparation by colloidal methods	16
1.2.1	Sol immobilisation	16
1.2.2	NaOH/THPC	18
1.2.3	Other colloidal methods	19
1.3	Chemical preparation of Au NPs on the surface of supports	19
1.3.1	Impregnation to incipient wetness	19
1.3.2	Deposition precipitation	20
1.3.3	Photodeposition	22
1.4	Objectives	22
1.5	References	23

Chapter 2: Experimental

2.1	Introduction	29
2.2	Catalyst preparation: Sol immobilisation	29
2.2.1	Synthesis of 1%Au-TiO ₂	29
2.2.2	Synthesis of Au-TiO ₂ with various weight loadings Au	29
2.2.3	Calcining the sol immobilised catalysts	29
2.2.4	Sol immobilisation of mono metallic silver and palladium	30
2.2.5	Synthesis of bimetallic NPs by sequential reduction of precursors	30
2.2.6	Synthesis of AgAu and PdAu core-shell NPs	32
2.3	Catalyst preparation: Other methods	33
2.3.1	Impregnation to incipient wetness	33
2.3.2	Deposition precipitation urea for Au-TiO ₂ synthesis	34
2.3.3	THPC/NaOH colloidal synthesis	34
2.3.4	Photodeposition	34
2.3.5	Preparation of Cerium doped sol gel TiO ₂	35
2.3.6	Carbon nitride synthesis	35
2.4	Development of the photo reactor	35

2.4.1	Batch set up	35
2.4.2	Reactor	36
2.4.3	Solar simulator lamp	36
2.4.4	Reaction procedure and conditions	37
2.4.5	Set up for flow reactions	37
2.4.6	Reactions with long band pass filters	38
2.4.7	Photoreactor set up at Sydney University	39
2.4.8	Reactor set up in Cardiff University	40
2.4.9	Reactor set up in Aarhus University, Denmark	40
2.5	Gas chromatography (GC)	41
2.5.1	Shimadzu GC	41
2.5.2	Injection and separation of sample	42
2.5.3	Detector - Thermal conductivity detector (TCD)	43
2.5.4	Agilent CG-MS	44
2.5.5	Hydrogen calibration for Shimadzu GC	44
2.5.6	Hydrogen calibration for Agilent GC	46
2.6	Transmission electron microscopy (TEM)	48
2.6.1	Introduction to TEM	48
2.6.2	TEM Sample preparation	50
2.6.3	High Annular Dark-Field TEM analysis	50
2.7	Ultra violet – visible spectroscopy (UV-Vis)	50
2.8	Thermogravimetric analysis (TGA)	51
2.9	X-Ray absorption spectroscopy (XAS)	51
2.9.1	Introduction to XAS	51
2.9.2	Synchrotrons	52
2.9.3	Theory of XAS	52
2.9.4	EXAFS	55
2.9.5	The EXAFS equation	56
2.9.6	XANES	58
2.9.7	XAFS experimental set up and experimental modes	59
2.9.8	Transmission mode	59
2.9.9	Fluorescence mode	60
2.9.10	X-ray generation in the synchrotron	61
2.9.11	XAFS acquisition	62
2.9.12	EXAFS particle size	62
2.10	X-ray diffraction (XRD)	63
2.11	X-ray photoelectron spectroscopy (XPS)	64
2.12	References	66

Chapter 3: Sol immobilisation catalysts for photocatalytic hydrogen production

3.1	Introduction	68
3.2	Synthesis of Au nano-particles	69
3.2.1	Sol immobilisation synthesis of Au-TiO ₂	69
3.2.2	TEM analysis	71
3.2.3	EXAFS particle size vs TEM particle size of 1%Au-TiO ₂	73
3.2.4	Variation of sol immobilisation synthesis parameters	76
3.2.5	Other methods for synthesis of Au-TiO ₂	78
3.2.6	Development of photoreactor	79
3.3	Optimisation of parameters for photocatalytic methanol reforming	80
3.3.1	Varying mass of catalyst	80
3.3.2	Varying amount of methanol	81
3.3.3	Effect of calcination temperature on particle size and photocatalytic performance	82
3.3.4	Effect of metal loading of Au NPs on TiO ₂ for photocatalytic H ₂ evolution	87
3.4	Photocatalytic H₂ production from Pd-TiO₂ with long band-pass filters	94
3.5	Synthesis of Ag-TiO₂ and Pd-TiO₂ by sol immobilisation	96
3.6	Cerium doped TiO₂ loaded with Pd	99
3.7	Conclusions	104
3.8	References	105

Chapter 4: Supported AgAu nanoparticles for photocatalytic hydrogen production

4.1	Introduction	109
4.2	Gold silver bimetallic catalysts 1:1 molar ratio	110
4.2.1	Introduction	110
4.2.2	Catalyst synthesis	111
4.2.3	UV Vis characterisation	111
4.2.4	Bright field TEM analysis	112
4.2.5	STEM-HAADF analysis	116
4.2.6	XPS analysis	119
4.2.7	Catalytic testing	120
4.2.8	Conclusions	123
4.3	Photocatalytic H₂ production from core-shell AgAu-TiO₂ catalysts with controlled shell thickness	123
4.3.1	Introduction	123
4.3.2	Catalyst synthesis	123
4.3.3	UV Analysis	124
4.3.4	TEM analysis	125

4.3.5	XPS analysis	127
4.3.6	XANES analysis	129
4.3.7	d band vacancy calculation	130
4.3.8	EXAFS analysis	132
4.3.9	Photocatalytic performance evaluations	136
4.3.10	Conclusions	138
4.4	References	139

Chapter 5: Supported PdAu nanoparticles for photocatalytic hydrogen production

5.1	Introduction	142
5.2	Photocatalytic H₂ production from core shell PdAu-TiO₂ catalysts with controlled shell thickness	143
5.2.1	Introduction	143
5.2.2	Catalysts synthesis	143
5.2.3	UV analysis	144
5.2.4	Bright field TEM Analysis	145
5.2.5	XPS analysis	147
5.2.6	XANES analysis	150
5.2.7	EXAFS analysis	151
5.2.8	Model of the AuPd NP structure	156
5.2.9	Photocatalytic performance evaluations	156
5.2.10	Conclusion	159
5.3	Restructuring AuPd nano particles by heat treatment for photocatalytic hydrogen production reactions	160
5.3.1	Introduction	160
5.3.2	Catalyst synthesis	160
5.3.3	UV/Vis analysis	161
5.3.4	TEM analysis	162
5.3.5	XANES analysis	164
5.3.6	EXAFS analysis	168
5.3.7	Photocatalytic activity	175
5.3.8	Conclusions	177
5.4	References	177

Chapter 6: Photocatalytic hydrogen production reactions of carbon nitride

6.1	Introduction	181
6.2	g-C₃N₄ properties and background	182
6.2.1	Carbon nitride history	182
6.2.2	Carbon nitride synthesis	183

6.2.3	XRD analysis	183
6.2.4	XPS analysis	184
6.2.5	UV/Vis analysis	185
6.3	Photoalytic activity of g-C₃N₄	187
6.3.1	Comparison of Pd-C ₃ N ₄ catalysts made by incipient wetness and <i>in situ</i> photodeposition	187
6.3.2	Comparison of H ₂ production from photoreforming reactions of g-C ₃ N ₄ loaded with Pd and Pt	189
6.3.3	Variation of TEOA concentration	191
6.3.4	Gas phase photocatalytic reactions of Pd-C ₃ N ₄	192
6.4	Comparison of photocatalytic reforming reactions of methanol and triethanolamine on titania and graphitic carbon nitride	194
6.4.1	Incipient wetness impregnation catalysts comparison of photocatalytic hydrogen production on TiO ₂ and C ₃ N ₄	194
6.4.2	UV-Vis analysis	194
6.4.3	Photo-deposition catalysts comparison of photocatalytic hydrogen production on TiO ₂ and C ₃ N ₄	198
6.4.4	Transmission electron microscopy	199
6.4.5	Effect of pH on rate of hydrogen produced from carbon nitride	202
6.5	Visible light photocatalysis with g-C₃N₄	203
6.6	Photocatalytic reforming reactions of Pd-TiO₂ and Pd-C₃N₄ with various amines and alcohols	204
6.6.1	Amine reforming reactions on Pd-C ₃ N ₄	204
6.6.2	Amine reforming reactions on Pd-TiO ₂	208
6.7	Conclusions	210
6.8	References	211

Chapter 7: Conclusions and future work

7.1.1	Conclusions	214
7.1.2	Future work	217
7.1.3	References	218

Chapter 1: Introduction

Table of contents

1.1	Introduction to photocatalysis.....	2
1.1.1	Background	2
1.1.2	Hydrogen as a fuel	2
1.1.3	Hydrogen from photocatalytic water splitting	3
1.1.4	Challenges and light energy required for water splitting	3
1.1.5	Requirements for semiconductor photocatalysts	6
1.1.6	Titanium dioxide (TiO ₂)	7
1.1.7	Noble metal loading of TiO ₂	9
1.1.8	Photocatalytic hydrogen production using sacrificial agents	11
1.1.9	Metal loading of co-catalyst.....	14
1.1.10	Modification of TiO ₂	15
1.1.11	Graphitic carbon nitride	16
1.2	Catalyst preparation by colloidal methods.....	16
1.2.1	Sol immobilisation.....	16
1.2.2	NaOH/THPC colloidal synthesis.....	18
1.2.3	Other colloidal methods	19
1.3	Chemical preparation of Au NPs on the surface of supports	19
1.3.1	Impregnation to incipient wetness	19
1.3.2	Deposition precipitation	20
1.3.3	Photodeposition.....	22
1.4	Objectives.....	22
1.5	References	23

1.1 Introduction to photocatalysis

1.1.1 Background

Production of a non-polluting and renewable energy source would be highly desirable and is a major challenge for the 21st century. Currently the world reserves of fossil fuels (oil, natural gas and coal) are being burned up at a destructive rate. If population trends and economic growth continues the course of recent decades then by the middle of the century world energy demand is predicted to double, from $5.14 \times 10^{20} \text{J}$ in 2008 to a projected $10 \times 10^{20} \text{J}$ in 2050.¹ Environmental concerns such as the emissions of CO_2 , as well as depletion of reserves and inevitable price increases, will very likely force a shift away from fossil fuels as the primary energy source of the future. Therefore a new energy production strategy is required that does not depend on depleting a finite resource. And ideally would not contribute to polluting the environment, or contribute to climate change.² Several alternative automotive fuels have been used such as biodiesel, ethanol and methanol.³ They have their merits, but also draw backs, biodiesel and ethanol are typically made from crops which displace food production and methanol is still primarily made from fossil fuels. One potential future strategy is the generation of H_2 as an energy carrier from a water splitting reaction with use of solar energy and a catalyst.

1.1.2 Hydrogen as a fuel

Hydrogen has potential for a fuel of the future for the automotive industry and to contribute towards large scale electricity production.⁴ It is a clean burning fuel, with the only by product produced from burning in air being water. It can be burned directly to produce heat or perhaps more promisingly can be used in a hydrogen fuel cell to produce electricity. The latter is very promising as automobiles can carry their own fuel cell to produce electricity for power. The hydrogen economy is a proposed economy where hydrogen replaces traditional fossil fuels for transport fuels and a proportion of electricity generation. In this proposed economy hydrogen would be used for energy storage and transportation, not a primary source. However there is a problem as hydrogen is currently predominately made from fossil fuels, with about 90 % coming from the steam reforming of hydrocarbons. This is an energy intensive process which requires high temperature ($700\text{-}1100 \text{ }^\circ\text{C}$).⁵ Therefore it is clear that using hydrogen from these sources is not a sustainable strategy, especially as CO_2 will also be produced by this process. Discovery of a new sustainable method would be of great significance, and much recent work has been done in this area.⁶ Production of hydrogen in a sustainable manner could be the first step towards a hydrogen economy. There are some

potential drawback with the use of H₂ as a fuel with storage and transportation being practical issues that need to be overcome, however with further research these problems may well be resolved.^{7,8}

1.1.3 Hydrogen from photocatalytic water splitting

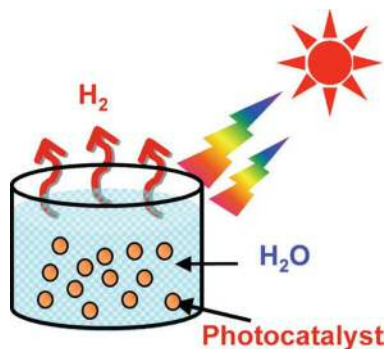


Figure 1. Schematic of idealised photocatalytic H₂ production from water.



Hydrogen production by photocatalytic H₂O splitting into H₂ + O₂ (1) would be an ideal route for future hydrogen production, see Figure 1.⁹ This is because the raw material and energy input for this type of hydrogen generation, water and sunlight, are abundant. If a suitable catalyst can be found it would be of great significance.

Much work has been done on this reaction (1) since the discovery of the Honda-Fujishima effect in 1972.¹⁰ They reported 'electrochemical photolysis of water' a voltage was applied to an electrochemical system, containing a TiO₂ and Pt electrodes in water. When the TiO₂ was irradiated with UV light electrolysis of the water was assisted. Although the paper was brief, lacked detail and did not strictly show photocatalysis, the work is often cited and has stimulated much of the preceding work done on water splitting.

1.1.4 Challenges and light energy required for water splitting

Efficient photocatalytic hydrogen production using sunlight and water has proven to be a difficult task and there are many problems to overcome. Transforming water into gaseous oxygen and hydrogen requires an input of energy to initiate the reaction, as can be seen from Figure 2 and (2).¹¹ In this case it is thermodynamically very difficult to perform this reaction at ambient temperatures. At temperatures above 1800 K the change in free energy becomes zero; therefore high equilibrium yields are possible by thermolysis, however this would be a very inefficient process.¹²

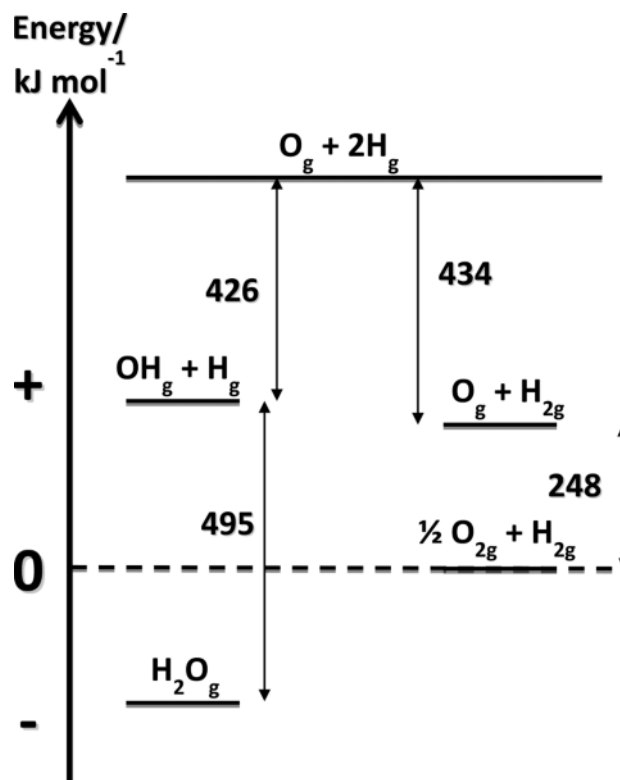


Figure 2. Born-Haber cycle for water dissociation and subsequent formation of hydrogen and oxygen.



$$\Delta G_0 = 229 \text{ kJ mol}^{-1}, \Delta H_0 = 242 \text{ kJ mol}^{-1}, \Delta S = 44 \text{ J K}^{-1} \text{ mol}^{-1}$$

Light energy can be used to provide the thermodynamic energy required for this reaction. Table 1 shows the energy distribution of the terrestrial solar spectrum,¹³ with Figure 3 showing the solar irradiance spectrum.¹¹

Table 1. Summary of the energy of emitted solar light and percentage reaching the earth of each energy region.

Spectral region	Interval boundaries		Solar irradiance	
	Wavelength (nm)	Energy (eV)	W m ⁻²	Percentage of total
Near UV	315–400	3.93–3.09	26	2.9
Blue	400–510	3.09–2.42	140	14.6
Green/ yellow	510–610	2.42–2.03	153	16.0
Red	610–700	2.03–1.77	132	13.8
Near IR	700–920	1.77–1.34	208	23.5
Infrared	920–> 1400	1.34 – <0.88	283	29.4

From (2) it can be seen that a wavelength of around 500 nm ($\sim 240 \text{ kJ}\cdot\text{mol}^{-1}$) is required to make the reaction above free energy neutral. Therefore it is thermodynamically feasible to use light with wavelength of 500 nm to split water. However this does not take into account the activation barrier for this reaction. Breaking the first O-H bond requires around 500 kJ mol^{-1} , which is equivalent to $\sim 250 \text{ nm}$. This is in the UV region of the electromagnetic spectrum and as can be seen in Figure 3 and Table 1 photons of this energy do not reach the earth's surface in significant quantities.¹³ Solar radiation does produce UV light; however it is predominately filtered out in the atmosphere by ozone. Therefore a catalyst is needed to lower the activation barrier, and make this reaction possible with longer wavelengths. However there is an issue with lowering the activation barrier. As the activation barrier for the back reaction is also lowered, meaning recombination of H_2 and O_2 is more likely. Therefore any effective potential catalyst needs to overcome this problem by inhibiting the back reaction. This can be done by adding a sacrificial agent to react with and remove oxygen from the system before recombination with hydrogen can occur (sections 1.1.8). Or choose a catalyst which will not recombine H_2 and O_2 efficiently.¹⁴ Alternatively it is possible to physically separate the H_2 and O_2 to stop recombination.¹⁵ In this thesis primarily methanol and other simple alcohols and amines were used as sacrificial agents to remove the oxygen and hence possibility of recombination.

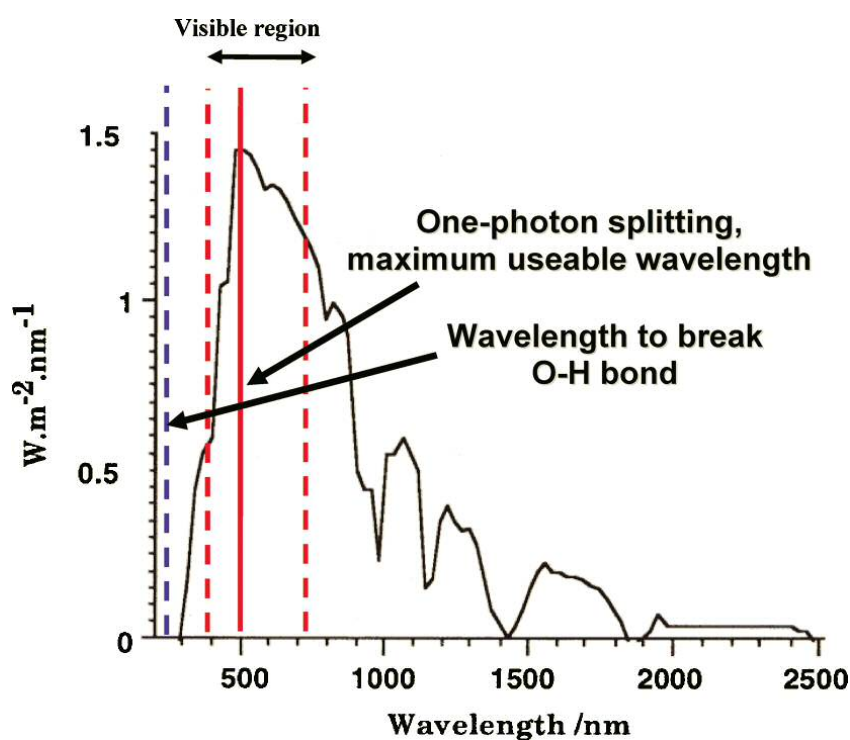


Figure 3. Solar irradiance spectrum at the earth's surface.

1.1.5 Requirements for semiconductor photocatalysts

For a photocatalytic material to be active it must possess the ability to absorb a photon of light and use this absorption to initiate a chemical reaction. Semiconductors and their electronic properties play an essential role in the mechanism of a photocatalyst. In a semiconductor the valence electrons occupy a band called the valence band (VB), which is full. The next band is called the conduction (CB) band which is empty and separated from the VB by a band gap. Between the VB and CB there is a region where electrons are forbidden to exist, see Figure 6 b. Photocatalysts are typically made from semiconductors with a band gap that can absorb a photon and excite an electron from the VB to the CB. This results in an electron (e^-) in the CB and a hole (h^+) in the VB, which is ultimately responsible for initiating the water splitting reactions. The size of the band gap is important for water splitting, with the lowest level of the CB of the semiconductor required to be more negative than the H^+/H_2 (0 V vs NHE) redox potential. And the highest level of the VB required to be more positive than the O_2/H_2O (1.23 eV) redox potential.⁹

As 1.23 eV corresponds to a wavelength of 1008nm, this is theoretically the minimum energy required for the reaction, which is about 70% of all the solar photons (Figure 3). However due to the activation barriers (Figure 2) and energy losses for charge transfer between the water molecules and the photocatalyst more energy than the band gap is required. For water splitting the band gap needs to have a minimum energy of ~ 2.4 eV, which is equivalent to ~ 250 kJ mol⁻¹ or 500 nm which is in the visible region of the spectrum.^{16, 17} Figure 4 shows the band gaps of a variety of semiconductor materials and their relationship with the redox potential for water splitting.¹⁸ Some semiconductors such as Fe_2O_3 and WO_3 as can be seen do not possess the suitable redox potential for water splitting and so will not be active for these reactions. Other potential candidates such as CdS appear to have an ideal band gap (2.5 eV or ~ 500 nm) but are not stable under prolonged use and will undergo a process known as photocorrosion.¹⁹

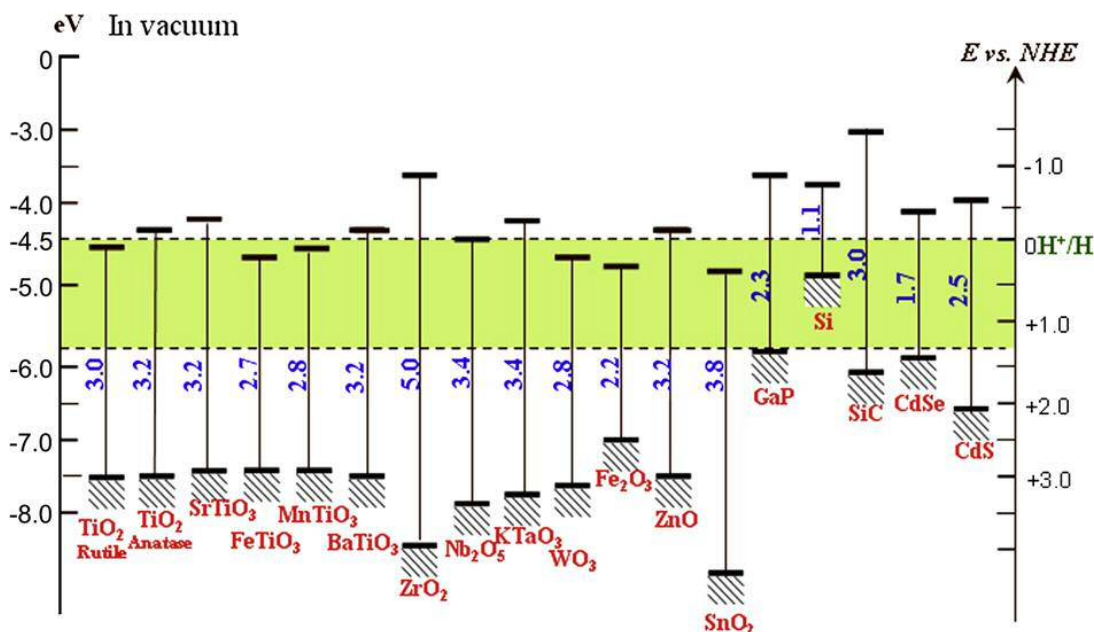


Figure 4. Band gaps of a variety of semiconductor materials and their relationship with the redox potential for water splitting.¹⁸

For a photocatalyst to be efficient at water splitting using the range of available wavelengths from sunlight there are a number of requirements.

1. Band gap of a suitable absorption capacity for solar radiation.
2. Ability to separate photoexcited electrons from the holes. When the e^-/h^+ pairs are made by photoexcitation its lifetime needs to be longer than the limiting step of the reaction.
3. Resistance to photocorrosion in the reaction environment. CdS and CdSe have a suitable band gap, Figure 4. However they are not stable under reaction conditions and will degrade in time by a photocorrosion. An example of photocorrosion is, $\text{CdS} + 2h^+ \rightarrow \text{Cd}^{2+} + \text{S}$, with S⁻ in CdS is oxidised instead of the water.
4. Minimise energy losses during charge transfer and recombination
5. Suitable kinetic properties for the electron transfer from the photocatalyst to the water
6. Ideally for large scale production the material should be cheap and easy to produce

1.1.6 Titanium dioxide (TiO₂)

Titanium dioxide (TiO₂) has received significant attention as an efficient semiconductor for photocatalysis applications and is the most widely studied,²⁰⁻²² which is largely as a consequence of its relative low recombination rate, non-toxicity, stability, and abundance.²³

This is despite the band gap of TiO₂ lying in the UV (~3.2 eV or ~387 nm) and hence limited photoresponse to the solar spectrum. The valence band electrons in TiO₂ are comprised of full O 2p orbitals (on an O²⁻) with the conduction band comprised of empty Ti 3d (on a Ti⁴⁺) states. Upon photoexcitation in TiO₂ the chemical nature of the electron will be that of a Ti³⁺ and the hole as an O⁻.

There are three phases of TiO₂ Rutile (tetragonal), Anatase (tetragonal) and Brookite (orthorhombic), Figure 5 shows the crystal structures of each.²⁴ Rutile is the most stable form of TiO₂, whereas Anatase and Brookite are considered metastable and will undergo a phase change to Rutile when heated to ~700 °C and above.²⁵ Brookite is the most difficult to synthesise as a pure phase and so is the least studied of the TiO₂ forms.²⁶ The band gap of each phase is slightly different with Anatase being 3.2 eV,²⁷ Rutile being 3.0 eV,²⁸ and Brookite ~3.1 eV.²⁶ Anatase and Brookite have been reported as indirect semiconductors with Rutile being a direct semiconductor.²⁹ For photocatalytic applications Anatase is considered to be the most active phase compared to Rutile.³⁰ This is despite the Rutile phase having a smaller band gap (3.0 opposed to 3.2 eV) and is thought to be due to the direct band gap of Rutile being detrimental to the life time of the e⁻/h⁺ pair.

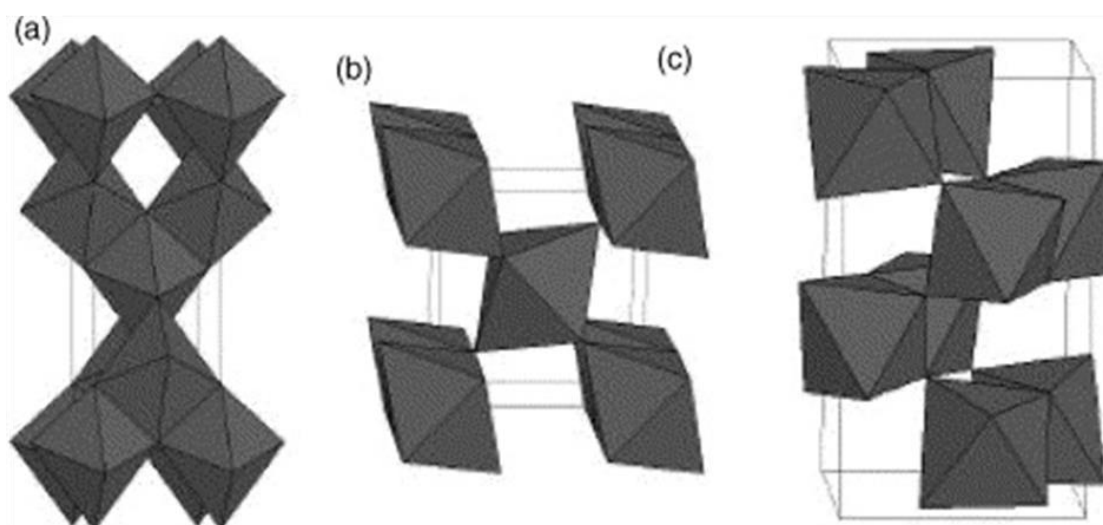


Figure 5. Visual representation of the crystal structure of (a) Rutile, (b) Anatase and (c) Brookite.

In this thesis a commercial TiO₂ called P25 (Degussa/Evonik, surface area 52m²g⁻¹) was primarily used, which is a mixture of Anatase and Rutile with a ratio of around 80:20, made by flame spray pyrolysis. This form of TiO₂ is an industrial standard and is commonly used as a support for a variety of catalytic applications. In fact P25 TiO₂ has been reported to possess

superior photocatalytic activity than single phase polymorphs of TiO₂.³¹ The reason for the enhanced performance of such materials is often reported to be due to the presence of rutile-anatase heterojunctions. Photogenerated electrons can migrate from one phase to another with the h⁺ going the opposite way, prolonging the lifetime of the e⁻/h⁺ pair. There is some debate in the literature as to whether the photogenerated electron migrates from Anatase to Rutile or the other way around, however a recent paper based on density functional theory (DFT) and reviewing previously published work suggested that the photogenerated electron migrates from Rutile to Anatase with the h⁺ going the opposite way.²⁸

1.1.7 Noble metal loading of TiO₂

There are drawbacks associated with pure TiO₂ photocatalysis in that there is a poor response to sunlight, poor catalytic efficiency due to recombination of electron hole pairs and dissociated molecules at the surface can recombine. Addition of noble metal NPs to the surface of TiO₂ can significantly increase the rate of photocatalytic H₂ production.³² The first observation of the enhancement of loading noble metals on to TiO₂ can be traced back to work done by Sato *et al.* in the 1980's where it was discovered the Pt-TiO₂ greatly enhanced the photoconversion of H₂O to H₂.³³ Precious metal such as Pt, Pd, Au, and Ag are perhaps the most commonly used to enhance the H₂ production efficiency.³⁴⁻³⁶ The promotional effect of the metal NPs can be understood in terms of the energy levels of the semiconductor/metal system, where the photo-excited CB electrons on the surface of TiO₂ can be transferred and trapped at the surface of NPs.³⁷ The Fermi level of these noble metals is lower in energy than the CB in TiO₂, so that the photogenerated electrons can become trapped relatively easily. At the semiconductor metal interface two types of contact can be formed, what is known as a Schottky barrier and an Ohmic contact.³⁸ At the interface of TiO₂ with Au, Pd, Ag and Pt a Schottky barrier is formed where the difference between the CB and Fermi level of the metal is increased in the region of contact. The other type of contact is known as an Ohmic contact, where difference between the CB and Fermi level of the metal is decreased by contact. For the case of Au, Ag, Pd and Pt a Schottky barrier will help trap the electrons thus prolonging the lifetime of the trapped electrons thus improving the photoreactivity. Also addition of the noble metal co-catalysts will provide a site for the reaction to occur.^{39, 40}

Figure 6 a, shows an idealised schematic of photocatalytic water splitting using a noble metal loaded semiconductor.⁴¹ In step (i) a photon is absorbed by the semiconductor exciting an electron from the VB to CB creating an e⁻/h⁺ pair. The next step (ii) involves the charges either

recombining or migrating to surface sites where the electron can be trapped by the noble metal co-catalyst, and then finally step (iii) involves surface oxidation and reduction reactions to produce H₂ and O₂. High crystallinity of the photocatalyst is advantageous as defects can act as sites for recombination of the electron hole pair.^{30, 42} The electrons promoted to the CB reduce the water to H₂ (3) while the electron hole h⁺ in the VB oxidises the water to O₂ (4).

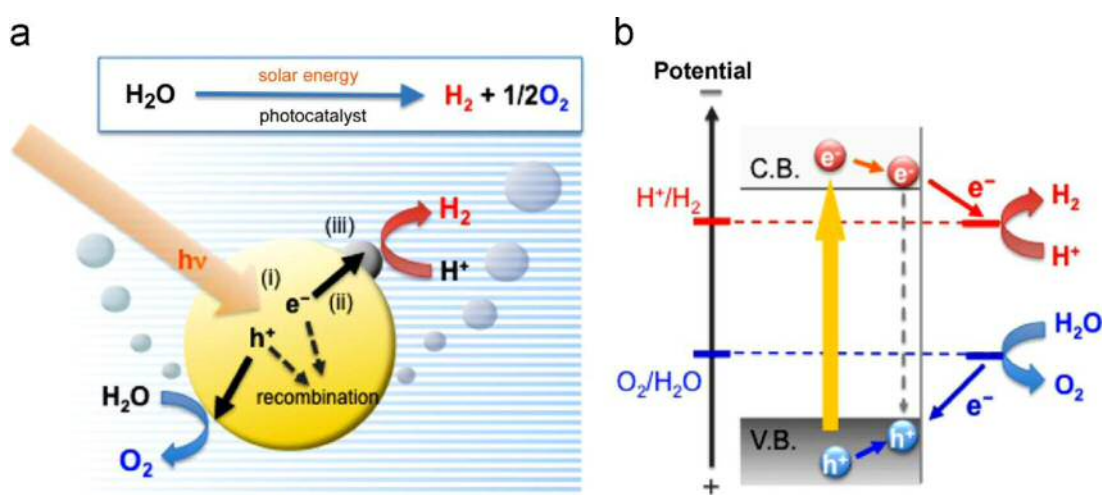


Figure 6. Schematic illustration of water splitting over a noble metal loaded semiconductor photocatalyst.



A variety of transition metals have been studied as the TiO₂ co-catalyst with Pd, Pt, Ir and Au demonstrating good activity, See Figure 7.⁴³ When compared as a weight loading of 1% on TiO₂ Pt and Pd were found to be the most active co-catalysts. This changed somewhat when compared as per mole of metal loaded with Pt being the most active and Au, Pd and Ir having similar H₂ evolution abilities. However, often the particle size of the co-catalyst can vary between metals, recent work by Al-Azri *et al.* considered the particle surface area of Pd, Pt and Au NPs supported on TiO₂ all made by the deposition precipitation method. Testing under identical conditions they found that although Au displayed the lowest overall rate of the three metals when considered as activity of the surface only Au was found to produce more H₂ per unit area as the Au NPs were larger the Pd and Pt.⁴⁴

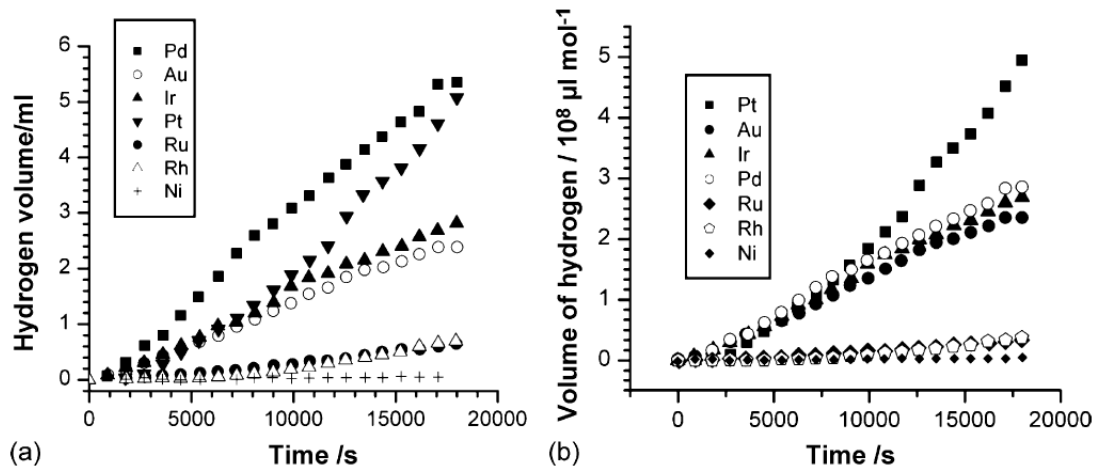
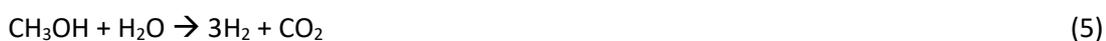


Figure 7. (a) Shows the hydrogen production for the same weight loading (1%) of a variety of group 8–11 elements while (b) shows the production per mole of metal loaded.

1.1.8 Photocatalytic hydrogen production using sacrificial agents

As mentioned previously a drawback of photocatalytic water splitting is the recombination of H₂ and O₂. A common way of overcoming this is to use a sacrificial agent (sometimes called a hole scavenger) which will essentially react with the O₂ removing the possibility of recombination. Much work has been done using methanol as a model sacrificial agent and in this thesis methanol was primarily used.^{21, 43, 45-48} The overall reaction involving methanol is shown below (5). As can be seen one mole of H₂ comes from water and two from methanol, with the production of CO₂. Therefore methanol is an ideal sacrificial agent in that two equivalents of hydrogen are produced from its decomposition. This reaction is equivalent to steam reforming of methanol, with the difference being the energy input of photons opposed to thermal energy.⁴⁹



A proposed mechanism for the photocatalytic production of hydrogen from H₂O by TiO₂ modified with Pd using methanol as a sacrificial agent is shown in Figure 8.⁵⁰ When there is no irradiation on the Pd-TiO₂ photocatalyst methanol (with R=H for this example) will adsorb onto the surface of the Pd releasing 2H₂, CO is then left strongly bound to the Pd surface, blocking any further reaction. Absorption of a photon with sufficient energy to excite an electron across the band gap produces an O⁻ species and Ti³⁺. The active O⁻ can then react with CO on the surface of the Pd releasing CO₂ and opening a vacant site V₀⁻. The vacant site V₀⁻ can accept an electron from the Ti³⁺ leading to regeneration of the Ti⁴⁺ and generation of

a V_0^{2-} . Another methanol molecule can then decompose on the Pd releasing H_2 , while water is reduced at the TiO_2 V_0^{2-} releasing H_2 and completing the cycle.

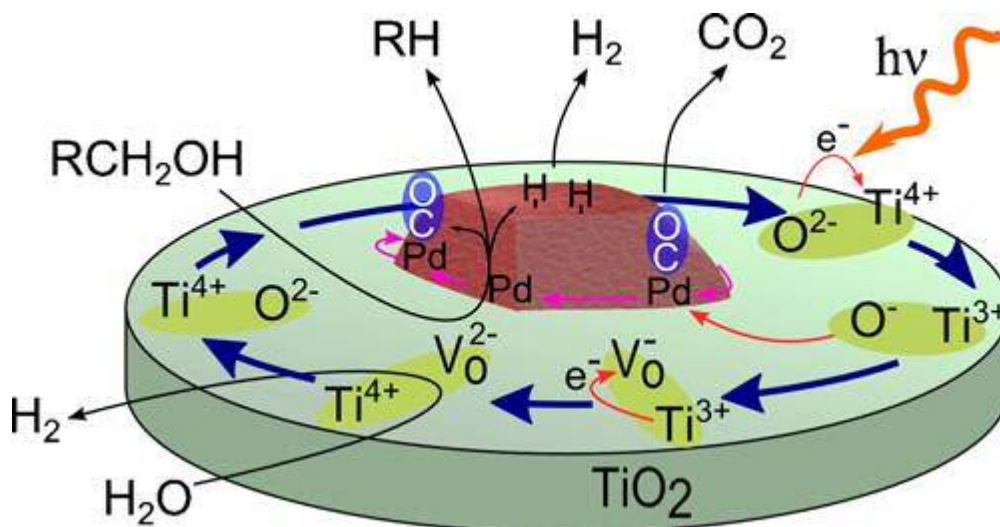


Figure 8. Simplified summary of proposed mechanism for the photo-reforming of a primary alcohol V_0 indicates a vacancy in the lattice.

The schematic in Figure 8 contains the co-catalyst Pd as an example, however it is thought for the case of Pt the same mechanistic model can be applied.⁵⁰ However for the case of Au as the co-catalyst it is thought the methanol instead of decomposing to a tightly bound CO on the surface a methoxy group is formed. For the mechanistic model with Pd as the co-catalyst to be true the reaction should proceed with CO as a replacement for methanol, which has been observed.⁵¹ This is not the case for Au-TiO₂ where no H₂ is evolved photocatalytically when using CO instead of methanol, presumably due to the lower binding energy of CO on Au.

Other alcohols can be used as the sacrificial agent, methanol though as the simplest alcohol minimises the side products.²¹ Ideally alcohols made from biomass would be used for this reaction as they release no net CO₂ into the atmosphere. If a successful reaction could be found using methanol then it's reasonable to assume that a simple alcohol from a biomass derivatives,³⁶ or sugars,^{21,52} would also be active. Table 2, shows the products when a variety of simple alcohols are used as the sacrificial agent while Figure 9 shows H₂ production rates from a variety of different alcohols with 0.5wt%Pd-TiO₂ as the photocatalyst. Taking into account the gas phase products and the structure of the simple alcohol being photoreformed a set of general rules have been suggested to determine the products, which are listed below.⁵⁰

- (i) A hydrogen atom alpha to the alcohol group must be present;
- (ii) Alkyl groups attached to alcohols yield the corresponding alkanes;
- (iii) Methylene groups between alcohols are fully oxidised to CO₂.

As can be seen in Figure 9 acetone and t-butanol yield no H₂ production which as the rules above (i) states is a consequence of having no alpha hydrogen available. Whereas ethanol produces H₂, CO₂ and CH₄ as products as does 1,2-propanediol which again is predicted by the rules above (ii) and (iii).

Table 2. Gas phase products of a variety of simple alcohols from a photocatalytic reaction with a 0.5wt%Pd-TiO₂ catalyst.⁵⁰

Alcohol	Gas phase products
Methanol	H ₂ , CO ₂
Ethanol	H ₂ , CO ₂ , CH ₄
1-Propanol	H ₂ , CO ₂ , C ₂ H ₆
2-Propanol	H ₂ , CO ₂ , CH ₄
1-Butanol	H ₂ , CO ₂ , C ₃ H ₈
2-Butanol	H ₂ , CO ₂ , C ₂ H ₆ , CH ₄
1,2-Propanediol	H ₂ , CO ₂ , CH ₄
1,3-Propanediol	H ₂ , CO ₂
1,3-Butanediol	H ₂ , CO ₂
2,3-Butanediol	H ₂ , CO ₂ , CH ₄
1,2,4-Butanetriol	H ₂ , CO ₂

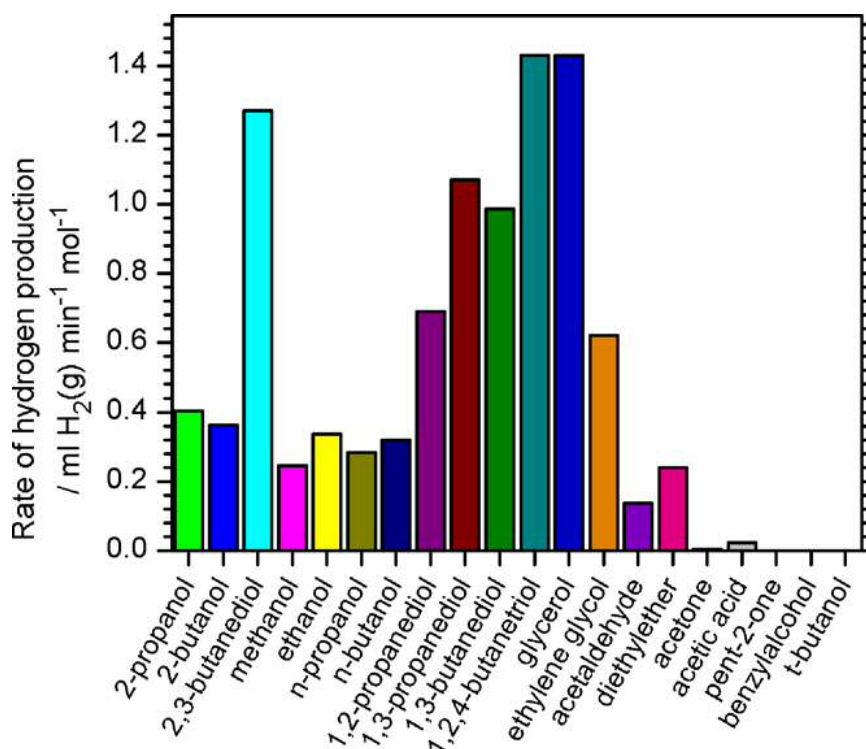


Figure 9. Hydrogen evolution rates from the photocatalytic reforming of a number of different alcohols over Pd-TiO₂ catalysts.

The most common sacrificial agent to find in the literature is a simple alcohol such as methanol or ethanol. However there are reports of photocatalytic amine reforming for H₂ production, although it is clear less research has been performed in this area.⁵³

1.1.9 Metal loading of co-catalyst

The percentage weight of the metal co-catalyst on the TiO₂ surface has a significant effect on the evolution rate of H₂. Figure 10 shows the effect of increasing the loading of Pd and Pt on TiO₂ (P25) on the evolution rate of H₂.⁵⁴ The rate increases substantially with small amounts of metal added, and peaks at low loading, with a maximum at around 0.5 wt% for Pd and Pt. At higher loading the rate drops and eventually the catalyst will become inactive which is likely due to the growth and agglomeration of the NPs. Furthermore, the rate depends on the extent of interface between the Pd and TiO₂ as this is where the reaction occurs, as can be seen in Figure 8. As the metal loading increases so does the TiO₂/Pd interface perimeter, until at a specific loading is reached where the particles touch. When this loading is reached a decrease in TiO₂/Pd interface will follow and hence decrease the rate of H₂ production.⁵⁵ Also the high loading of Pd can be detrimental to activity by preventing TiO₂ to effectively absorb photons.

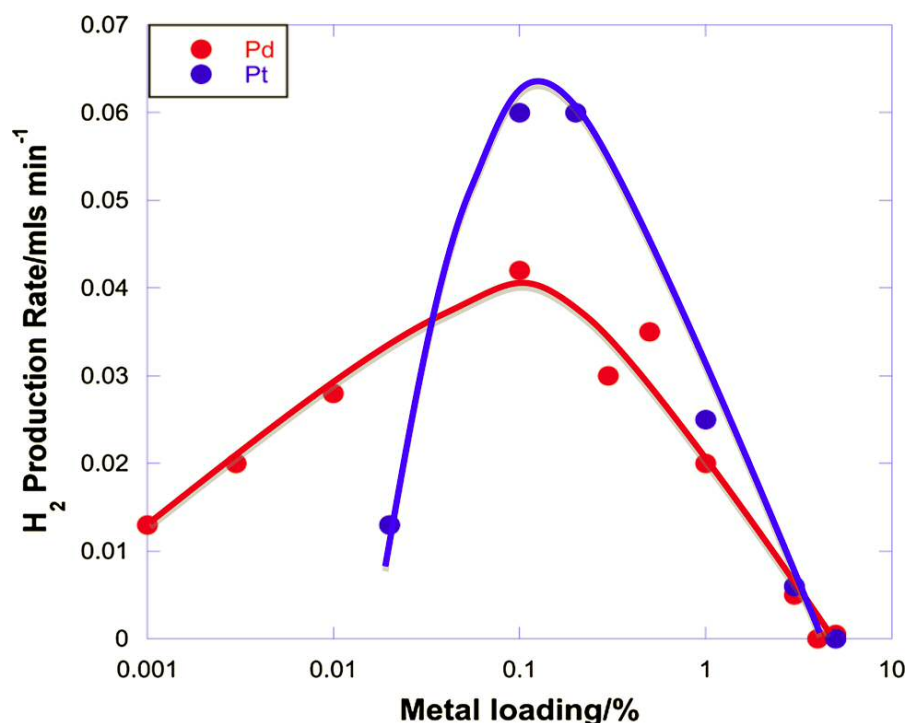


Figure 10. Rates of hydrogen evolution from precious metal catalysts as a function of metal loading. Catalysts prepared by incipient wetness using, 0.2 g catalyst, 100 μ L of methanol on 100 mL of distilled water.

For reactions involving varying the Au weight loadings on TiO₂ there are similarities to Pd and Pt in that at high and low loadings (0.05 and 5%) the rate is low. However unlike Pd and Pt work by Bowker *et al.* shows there to be a double maxima in photocatalytic H₂ production rate, see Figure 11.³⁴ The catalysts in Figure 11 were made by incipient wetness, and the results were reproduced in our own group with Au-TiO₂ with a variety of weight loading made by the sol immobilisation method.⁵⁶ This leads to the conclusion that this double maxima is indeed real, however a full understanding the cause of this phenomenon is still unclear.

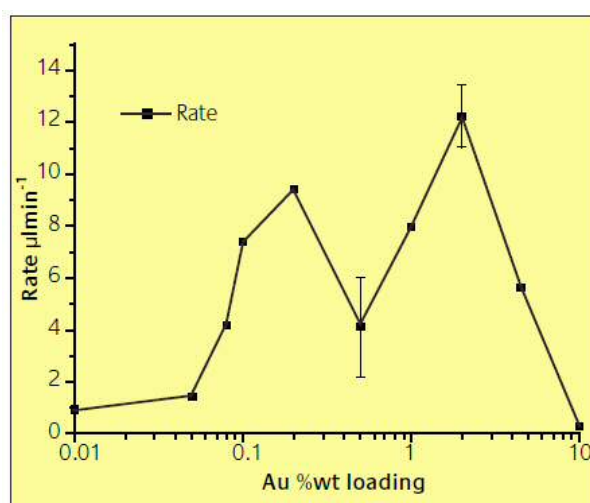


Figure 11. Rate of photocatalytic hydrogen production against gold weight loading on TiO₂ prepared by incipient wetness, using 0.2 g of catalyst, 110 μL methanol and 100 mL deionised water.

1.1.10 Modification of TiO₂

Altering the morphology of TiO₂ is a method by which the activity for photocatalysis can be improved. This can be achieved by affecting certain properties of the TiO₂ such as the surface area, the hydrophilicity and the availability of the charge carriers.⁵⁷ Among these modifications significant work has been done on producing one-dimensional and two-dimensional TiO₂ structures. In the literature several works can be found on the applications of 1-D TiO₂ nanotubes^{57,58}, 1-D TiO₂ nanorods⁵⁹ or 2-D TiO₂ nanosheets⁶⁰ for photocatalytic methanol reforming. The goal of these structures is to enhance the separation and transfer of the photogenerated charges e.g. for TiO₂ nanotubes the charges pass more easily along the longitudinal direction of the nano structure which is favourable to improve separation. Therefore by tuning the morphology of TiO₂ photogenerated e⁻/h⁺ lifetime can be enhanced and thus activity increased.

One alternative method for expanding the photoresponse of TiO₂ is by doping with anions to narrow the band gap and allow excitation by longer wavelength photon. Examples of anion doped TiO₂ are, N-TiO₂⁶¹⁻⁶³, S-TiO₂^{64, 65}, P-TiO₂⁶⁶, B-TiO₂⁶⁷, which have been prepared by different methods. Perhaps the most successful of these dopants has proven to be N, with the improved activity thought to derive from mixing of the O 2p states with the N 2p states at the top of the valance band. This has the effect of narrowing the band gap allowing photoexcitation with wavelengths slightly into the visible ($\lambda > 400$ nm) possible compared to un-doped TiO₂.⁶¹⁻⁶³ However there are also some drawbacks associated with doping of TiO₂, the anions may photocorrode or provide a site for e⁻/h⁺ recombination. This can then lead to doped TiO₂ absorbing a wider range of photons while having an inferior activity compared to un-doped TiO₂.

1.1.11 Graphitic carbon nitride

Carbon nitride (g-C₃N₄) has recently gained interest as an inorganic semiconductor for photocatalytic water splitting. This is predominately due to the band gap of carbon nitride ~2.7-2.9 eV (~420-460 nm) lying partly into the visible region of spectrum, potentially utilising a larger amount of solar radiation compared to TiO₂. Chapter 6 will investigate reaction of g-C₃N₄ as well as a background/introduction section so no further details will be given here.

1.2 Catalyst preparation by colloidal methods

Producing colloidal dispersions of metal NPs in solution which can then be deposited onto a support is an attractive method for catalyst synthesis. By altering the preparation conditions the size and shape of the NPs can be controlled which in turn will affect the activity of the final catalyst. Typically the colloids are formed in solution by chemical reduction of a precursor in the presence of stabilising agent. Once the metal colloid is formed the NPs can be deposited onto the surface of an appropriate support in solution, followed by filtering and drying to produce the final state of the catalyst. The vast majority of the colloidal based catalysts synthesised in this thesis were of Au, so the examples below will primarily be for preparing Au NPs.

1.2.1 Sol immobilisation

The primary method for producing metal NP supported catalysts in this thesis has been sol immobilisation technique, and has been used to prepare primarily Au but also Pd, Ag and bimetallic NPs supported on TiO₂. This methodology has become popular recently largely owing to the ability produce NPs in the range of 2-4 nm, being reproducible as well as being

relatively simple and cheap.⁶⁸⁻⁷⁰ Figure 12 shows a schematic representation of colloidal gold synthesis and immobilisation on the surface of a support.⁷¹ The first step involves preparing a solution of Au precursor (HAuCl_4) and protecting agent with appropriate concentrations in deionised water. The Au precursor is then reduced by addition of a reducing agent (typically NaBH_4) and the protecting agent will cap the newly formed NPs.

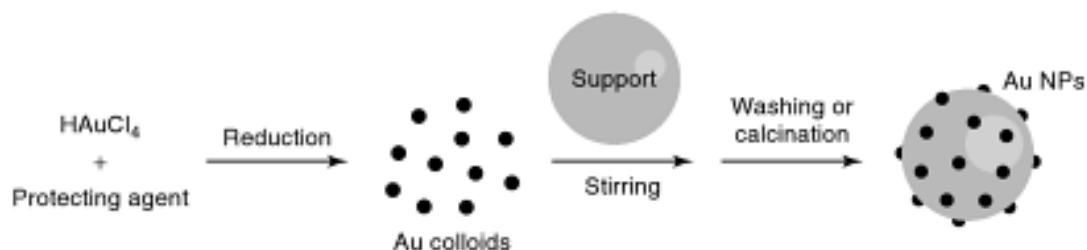


Figure 12. Schematic representation of Au sol generation and immobilisation.

In this thesis the protecting agent solely used was poly vinyl alcohol (PVA) which has an average molecular weight of $9000\text{-}1000\text{ g}\cdot\text{mol}^{-1}$ and is considered a steric stabiliser. The polymer consists of repeating units of $(-\text{CH}_2\text{CHOH}-)_n$, where n will have a value of ~ 215 on average for the PVA used. The PVA will bind to the Au NPs through the OH groups with the polymer forming a physical barrier preventing NP growth. Other polymer stabilising agents are available, but in general to be successful they must contain electron donating moieties such as alcohols and ketones which will bind to the surface. Examples of other stabilising agent are poly vinyl pyrrolidone (PVP)⁷² and poly acrylic acid (PAA).⁷³ The reducing agent used in this thesis with the sol immobilisation method was NaBH_4 as it possesses the required reducing power to transform HAuCl_4 into Au metal, and is the most common for this technique. By tuning parameters such as the PVA/Au ratio, initial concentration of the Au precursor, temperature and NaBH_4/Au ratio the size NP can be controlled, and will be investigated in chapter 3.^{70, 74}

Once the colloid is formed the NPs can be immobilised by adding the support to the solution and adjusting the pH to ~ 1 , Figure 12. Acidifying the solution below the point of zero charge (PZC, which is the pH at which the total electric charge on the surface of the support is zero) of the support will have the effect of charging the surface which will aid deposition. This method is suitable for oxide supports with a PZC value higher than 5. Examples of such supports are TiO_2 , Al_2O_3 and ZnO_2 ,⁷⁵ with an example of unsuitable supports ($\text{PZC} < 5$) being activated carbon and SiO_2 .⁷²

As mentioned previously the advantages of the sol immobilisation method include, narrow particle size distribution (2-4 nm of Au), simplicity, reproducibility and can be used with a

variety of noble metals e.g. Au, Pd, Pt and Ag. Some of the drawbacks include not being suitable for all supports and the protecting ligand can remain on the surface of the NP after deposition onto the support which can be detrimental to activity. However some methods have been developed to remove the protecting ligand from the NPs such as refluxing and calcination.^{76, 77}

1.2.2 NaOH/THPC colloidal synthesis

Another colloidal route to synthesising Au NPs which can then be immobilised onto a support is the tetrakis-(hydroxymethyl)-phosphonium chloride (THPC) method, developed by Baiker *et al.*⁷⁸ In this preparation the THPC molecule acts as both a stabilising agent and a reductant of the precursor in the presence of NaOH. Figure 13 outlines the schematic pathway to noble metals NPs in solution.⁷⁹ In step a) formaldehyde is generated which can act as a reductant for the metal precursor while the HO- groups on the THPC stabilise the NPs. In step b) H₂ is formed which will also act as a reductant.

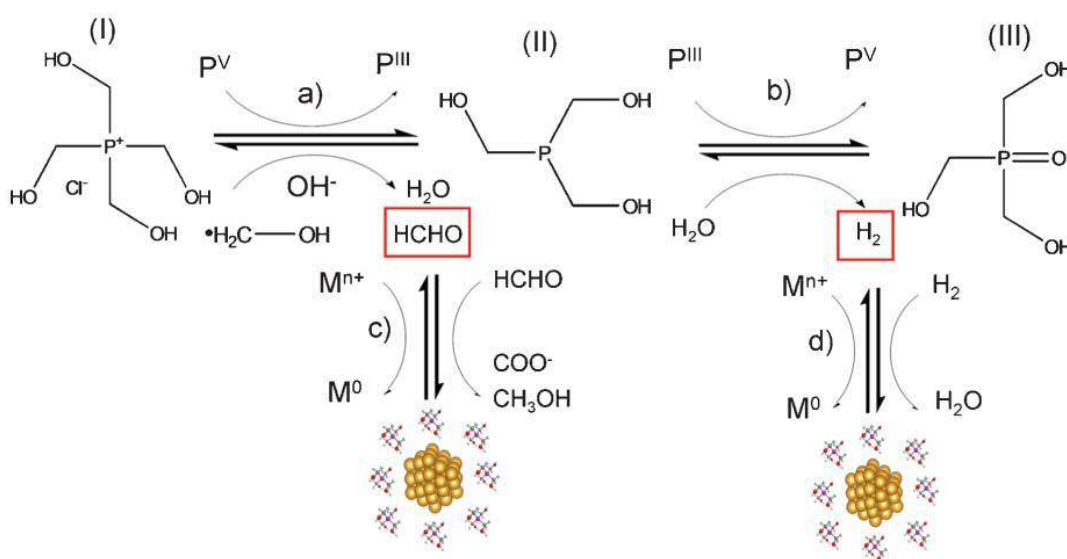


Figure 13. Proposed reaction pathways for the generation of metal nanoparticles, involving the conversion of THPC (Structure I) into THPO (Structure III), and the *in situ* generation of formaldehyde and hydrogen as active reducing agents.

As well as Au this method is suitable for producing NPs of Pd, Pt, Rh and bimetallic NPs of PtAu and PtPd.⁷⁹ As with the sol immobilisation method after sol generation the NPs can be deposited onto the surface of an appropriate support. By this method it has been reported that Au NPs of the order of 1-5 nm can be successfully synthesised.

1.2.3 Other colloidal methods

As mentioned previously the only colloidal noble metal NP synthesis methods used in this thesis are sol immobilisation and the NaOH/THPC method. There are several others however, with some of the most common briefly described below.

Turkevich method – This technique involves preparing a solution of HAuCl_4 with sodium citrate, which is then heated (~ 80 °C). The citrate acts as both a reductant and a capping agent and by this method it is possible to achieve NP in the range of 10-20 nm.^{80, 81}

Brust/Schiffrin method – Here HAuCl_4 is dissolved in organic media (typically toluene) with an organothiols protecting agent (e.g. 1-dodecanethiol). The reductant is NaBH_4 and capping agent binds through the $-\text{SH}$ group and NPs of the order 2-10 nm can be achieved.⁸²

Perrault method – This method uses an aqueous reaction media, hydroquinone as the reductant and citrate as the protecting agent. The size of the NPs produced by this method is a relatively large 50-200 nm.⁸³

Murphy method – this method uses an aqueous reaction media, ascorbic acid as the reductant and Cetyltrimethylammonium bromide (CTAB) as the protecting agent. The possible particle size range from this technique is 5-40 nm.⁸⁴

1.3 Chemical preparation of Au NPs on the surface of supports

1.3.1 Impregnation to incipient wetness

Perhaps the most common and simplest method for producing a noble metal supported TiO_2 catalyst is the impregnation to incipient wetness technique. Typically this method involves impregnating the metal oxide support with an aqueous solution of the metal precursor (e.g. PdCl_2 or HAuCl_4) followed by drying and calcination.^{85, 86} The volume of metal precursor solution required needs to be equal to the pore volume of the support. This is called the incipient wetness amount and the liquid will enter the pores by capillary action. The loading of the required metal will then need to be achieved by the concentration of the precursor solution used. Once the sample is dried to remove the water it can then be calcined at typically ~ 500 °C which for the case of PdCl_2 or HAuCl_4 will remove the Cl and any other volatiles from the surface. For Au the heat treatment can be performed in a reducing atmosphere (e.g. H_2) or in air, in both cases the Au is reduced due to the instability of the Au^{3+} species. When synthesising a Pd catalyst by this method a PdO species will be left on the surface, which can either be reduced or used as is. This method has the advantages of

simplicity, maximising the loading of the metal and reproducibility. There are also some disadvantages with incipient wetness impregnation in that it is difficult to control the particle size and small amounts of Cl can still be present on the surface which can be a poison for many reactions.

1.3.2 Deposition precipitation

The deposition precipitation method (DP) is primarily used to synthesis Au NPs on oxide supports but can be used to produce Pd and Pt catalysts to a lesser extent.⁸⁷ This method was developed by Haruta *et.al.*⁸⁸ for synthesising Au-TiO₂ and involves precipitating a Au precursor (HAuCl₄) onto the surface of a support which is then heat treated to reduce the resulting Au. As only Au-TiO₂ was synthesised in this thesis by this method only this example is given here. To precipitate the Au onto the surface of the support a solution of metal precursor (HAuCl₄) containing the support material (e.g. TiO₂) is prepared. For a solution containing HAuCl₄ the initial pH will be low (~2-3). The pH is then increased by slow addition of NaOH, which will lead to the displacement of a chloride ion with an OH⁻, further pH increase will lead to displacement of further chloride ions, see Figure 14,⁸⁹. At high pH the gold hydroxide species will precipitate on the surface of the TiO₂ which after an appropriate aging time can be filtered and dried. The DP method can be performed at constant pH (~8/9) but it most common to gradually increase the pH of the solution.

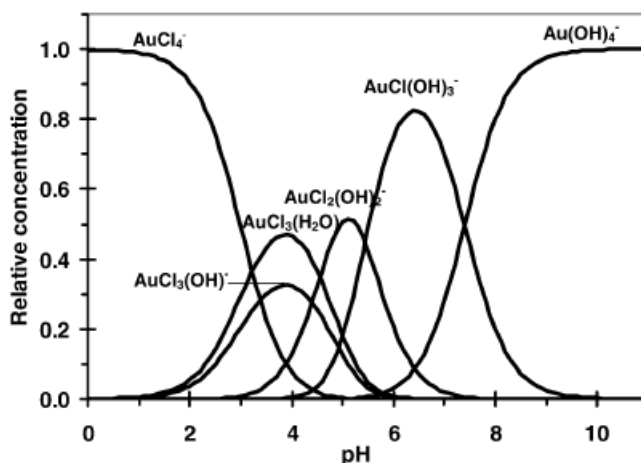


Figure 14. Relative equilibrium concentration of gold complexes ($[Cl^-] = 2.5 \times 10^{-3} M$) as a function of the pH of the solution.

The gold hydroxide ions once produced will then precipitate on to the surface of the support in preference to precipitating in solution. As with sol immobilisation this method is suitable

for oxide supports with PZC greater than 5, e.g. TiO_2 , Al_2O_3 and ZnO ,⁷⁵ and not suitable for activated carbon and SiO_2 which have a lower PZC.⁷²

Slow addition of the precipitating agent is required to avoid local high concentrations of NaOH which could lead to rapid nucleation of the precipitate in solution. This would result in the metal remaining in solution, rather than being deposited on the surface of the support. To avoid this issue a modification of the DP method has been developed called DP urea. Here the initial solution containing the gold precursor also contains urea ($\text{CO}(\text{NH}_2)_2$) which will decompose slowly upon heating ($80\text{ }^\circ\text{C}$) to yield hydroxide ions increasing the pH, see equation 6.⁹⁰

(7)

Once Au-TiO_2 catalysts are prepared either by DP urea or DP NaOH they are typically filtered and washed with distilled water to remove chloride ions. This step is followed by drying to remove water from the catalysts, which is typically done at $100\text{ }^\circ\text{C}$ for 2h or RT for 48h. After the catalysts are dried they are then calcined, this step is required to reduce all the gold on the surface to its metallic form. Gold hydroxide has a negative enthalpy of reduction, as metallic gold is stable thermodynamically. Figure 3 shows a schematic impression of conversion of $\text{Au}(\text{OH})_3$ species supported on TiO_2 into Au-TiO_2 during calcinations,⁹¹. Any gold oxide on the surface will also be reduced with heating as Au_2O_3 is unstable, $\Delta H_f = +19.3\text{ kJmol}^{-1}$.⁹²

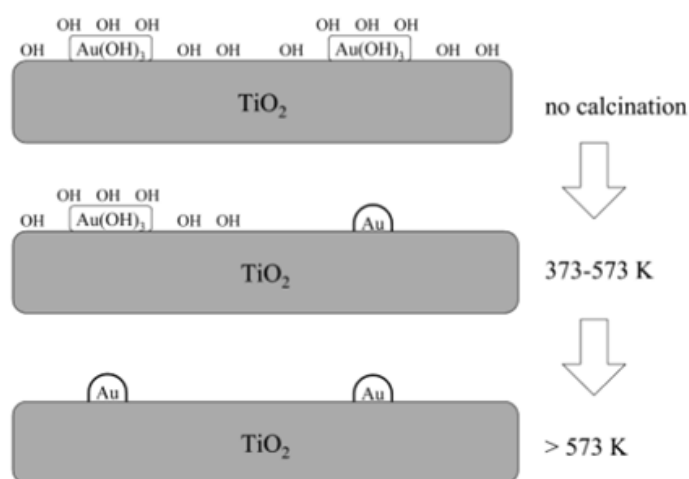


Figure 15. Schematic of conversion of $\text{Au}(\text{OH})_3$ species supported on TiO_2 into Au-TiO_2 during calcination.

There are some drawbacks associated with the DP method in that it can be difficult to achieve mono dispersed NP size, complete deposition of the Au is difficult to achieve, with

the DP urea method improving deposition quantities. Also despite thorough washing and calcination some Cl can still remain on the surface which can increase sintering during heat treatment and is considered a poison for some reactions. However the DP urea method can achieve small Au NPs on the surface of TiO₂ with particles in the order of ~2 nm being reported.⁹³

1.3.3 Photodeposition

Photodeposition is a method of reducing noble metal precursors in solution directly onto the surface of a semiconductor support by use of light energy. As mentioned in section 1.1, when a semiconductor is irradiated with photons of greater energy than the band gap e⁻/h⁺ pairs can be formed. Surface adsorbed precursor ions can then be reduced by the electrons in the conduction band resulting in metal NPs on the surface of the support. For TiO₂ several metals can be deposited onto the surface from solution by UV irradiation e.g. Au, Pd, and Pt.^{94, 95} Often it is possible to achieve small particle size (2-3 nm) dispersed evenly over the surface of the semiconductor support. Once the metal has been photodeposited on the surface of the support the resulting catalyst can be filtered and dried. If required in some photocatalytic reactions involving a sacrificial agent such as methanol, the co-catalyst can be deposited onto the semiconductor and hydrogen production monitored simultaneously. Examples include photocatalytic hydrogen production reactions involving g-C₃N₄ where it is common to reduce the co-catalyst (typically Pt with appropriate hole scavenger) onto the support *in situ* whilst measuring the hydrogen evolution.⁹⁶ Photodeposition is a useful method for producing small NPs on a semiconductor support without the need for chemical reductant or protecting agent. However it is only suitable for semiconductor supports with an appropriate band gap and full deposition of the metals is not always achieved. Therefore it is not widely used for catalyst synthesis.

1.4 Objectives

Main objectives of this thesis were to synthesise mono, bimetallic and structured NPs supported on TiO₂ for improved photocatalytic H₂ production, as well as investigating g-C₃N₄ as a visible light active photocatalyst support material. Chapter 3 focuses on the sol immobilisation method for the synthesis of mono metallic NPs supported on TiO₂ for use as photocatalysts. After a photoreactor was developed, optimisation of reaction conditions was investigated to maximise H₂ production. Building on the work done in chapter 3 the next two chapters (4 and 5) describe the use of the sol immobilisation method to produce bimetallic

NPs and core-shell NPs of both AuAg and AuPd. The structure of the synthesised NPs would be investigated by a variety of characterisation methods including XAFS. Photocatalytic testing of these structured NPs supported to TiO₂ would be performed to ascertain if there are NP structures which are beneficial for activity. The final experimental chapter focuses on g-C₃N₄ as a visible light active semiconductor photocatalyst for the production of H₂. Furthermore comparisons are made between the activity of TiO₂ (P25) and g-C₃N₄ as well as investigation of amine reforming on both semiconductor photocatalysts. Finally, the conclusions chapter summarizes the results obtained from all the experiments with attention on the best synthesis methods and most active catalysts in addition to listing future work.

1.5 References

1. P. Moriarty and D. Honnery, *Renewable & Sustainable Energy Reviews*, 2012, 16, 244-252.
2. M. A. Leonel Caetano, D. F. Marcolino Gherardi and T. Yoneyama, *Ecological Modelling*, 2008, 213, 119-126.
3. G. A. Olah, *Angewandte Chemie-International Edition*, 2005, 44, 2636-2639.
4. M. Ball and M. Wietschel, *International Journal of Hydrogen Energy*, 2009, 34, 615-627.
5. J. M. Ogden, *Annu. Rev. Energ. Environ.*, 1999, 24, 227-279.
6. J. D. Holladay, J. Hu, D. L. King and Y. Wang, *Catalysis Today*, 2009, 139, 244-260.
7. B. Sakintuna, F. Lamari-Darkrim and M. Hirscher, *International Journal of Hydrogen Energy*, 2007, 32, 1121-1140.
8. J. C. F. Wang and E. C. E. Ronnebro, *An overview of hydrogen storage for transportation application*, 2005.
9. A. Kudo and Y. Miseki, *Chemical Society Reviews*, 2009, 38, 253-278.
10. A. Fujishima and K. Honda, *Nature*, 1972, 238, 37-+.
11. M. Bowker, *Green Chem.*, 2011, 13, 2235-2246.
12. A. Kogan, *International Journal of Hydrogen Energy*, 1997, 22, 481-486.
13. R. M. N. Yerga, M. C. A. Galvan, F. del Valle, J. A. V. de la Mano and J. L. G. Fierro, *ChemSusChem*, 2009, 2, 471-485.
14. K. Maeda, A. Xiong, T. Yoshinaga, T. Ikeda, N. Sakamoto, T. Hisatomi, M. Takashima, D. Lu, M. Kanehara, T. Setoyama, T. Teranishi and K. Domen, *Angewandte Chemie International Edition*, 2010, 49, 4096-4099.
15. M. Kitano, K. Tsujimaru and M. Anpo, *Applied Catalysis a-General*, 2006, 314, 179-183.
16. T. Bak, J. Nowotny, M. Rekas and C. C. Sorrell, *International Journal of Hydrogen Energy*, 2002, 27, 991-1022.
17. B. D. Alexander, P. J. Kulesza, L. Rutkowska, R. Solarska and J. Augustynski, *Journal of Materials Chemistry*, 2008, 18, 2298-2303.
18. D. Jing, L. Guo, L. Zhao, X. Zhang, H. Liu, M. Li, S. Shen, G. Liu, X. Hu, X. Zhang, K. Zhang, L. Ma and P. Guo, *International Journal of Hydrogen Energy*, 2010, 35, 7087-7097.
19. M. Kitano and M. Hara, *Journal of Materials Chemistry*, 2010, 20, 627-641.
20. L. Saeed Al-Mazroai, M. Bowker, P. Davies, A. Dickinson, J. Greaves, D. James and L. Millard, *Catalysis Today*, 2007, 122, 46-50.

21. H. Bahruji, M. Bowker, P. R. Davies, L. S. Al-Mazroai, A. Dickinson, J. Greaves, D. James, L. Millard and F. Pedrono, *Journal of Photochemistry and Photobiology a-Chemistry*, 2010, 216, 115-118.
22. A. Fujishima, X. T. Zhang and D. A. Tryk, *Surf. Sci. Rep.*, 2008, 63, 515-582.
23. M. D. Hernandez-Alonso, F. Fresno, S. Suarez and J. M. Coronado, *Energy Environ. Sci.*, 2009, 2, 1231-1257.
24. O. Carp, C. L. Huisman and A. Reller, *Progress in Solid State Chemistry*, 2004, 32, 33-177.
25. D. A. H. Hanaor and C. C. Sorrell, *Journal of Materials Science*, 2011, 46, 855-874.
26. A. Di Paola, M. Bellardita and L. Palmisano, *Catalysts*, 2013, 3, 36-73.
27. K. M. Reddy, S. V. Manorama and A. R. Reddy, *Mater. Chem. Phys.*, 2003, 78, 239-245.
28. D. O. Scanlon, C. W. Dunnill, J. Buckeridge, S. A. Shevlin, A. J. Logsdail, S. M. Woodley, C. R. A. Catlow, M. J. Powell, R. G. Palgrave, I. P. Parkin, G. W. Watson, T. W. Keal, P. Sherwood, A. Walsh and A. A. Sokol, *Nat Mater*, 2013, 12, 798-801.
29. D. Reyes-Coronado, G. Rodríguez-Gattorno, M. E. Espinosa-Pesqueira, C. Cab, R. d. Coss and G. Oskam, *Nanotechnology*, 2008, 19, 145605.
30. G. L. Chiarello, A. Di Paola, L. Palmisano and E. Selli, *Photochemical & Photobiological Sciences*, 2011, 10, 355-360.
31. G. Li and K. A. Gray, *Chemical Physics*, 2007, 339, 173-187.
32. V. Subramanian, E. Wolf and P. V. Kamat, *Journal of Physical Chemistry B*, 2001, 105, 11439-11446.
33. S. Sato and J. M. White, *Chemical Physics Letters*, 1980, 72, 83-86.
34. J. Greaves, L. Al-Mazroai, A. Nuhu, P. Davies and M. Bowker, *Gold Bulletin*, 2006, 39, 216-219.
35. K. Mogyorosi, A. Kmetyko, N. Czirbus, G. Vereb, P. Sipos and A. Dombi, *React. Kinet. Catal. Lett.*, 2009, 98, 215-225.
36. Y. Z. Yang, C. H. Chang and H. Idriss, *Applied Catalysis B-Environmental*, 2006, 67, 217-222.
37. A. Takai and P. V. Kamat, *ACS Nano*, 2011, 5, 7369-7376.
38. F. P. Yan, Y. H. Wang, J. Y. Zhang, Z. Lin, J. S. Zheng and F. Huang, *ChemSusChem*, 2014, 7, 101-104.
39. V. Subramanian, E. E. Wolf and P. V. Kamat, *Journal of the American Chemical Society*, 2004, 126, 4943-4950.
40. R. Su, R. Tiruvalam, A. J. Logsdail, Q. He, C. A. Downing, M. T. Jensen, N. Dimitratos, L. Kesavan, P. P. Wells, R. Bechstein, H. H. Jensen, S. Wendt, C. R. A. Catlow, C. J. Kiely, G. J. Hutchings and F. Besenbacher, *ACS Nano*, 2014, 8, 3490-3497.
41. R. Abe, *Journal of Photochemistry and Photobiology C: Photochemistry Reviews*, 2010, 11, 179-209.
42. J.-H. Huang and M.-S. Wong, *Thin Solid Films*, 2011, 520, 1379-1384.
43. L. S. Al-Mazroai, M. Bowker, P. Davies, A. Dickinson, J. Greaves, D. James and L. Millard, *Catalysis Today*, 2007, 122, 46-50.
44. Z. H. N. Al-Azri, W.-T. Chen, A. Chan, V. Jovic, T. Ina, H. Idriss and G. I. N. Waterhouse, *Journal of Catalysis*, 2015, 329, 355-367.
45. H. Yi, T. Peng, D. Ke, D. Ke, L. Zan and C. Yan, *International Journal of Hydrogen Energy*, 2008, 33, 672-678.
46. T. Kawai and T. Sakata, *Journal of the Chemical Society-Chemical Communications*, 1980, DOI: 10.1039/c39800000694, 694-695.
47. A. Nuhu, J. Soares, M. Gonzalez-Herrera, A. Watts, G. Hussein and M. Bowker, *Top. Catal.*, 2007, 44, 293-297.

48. T. Ishii, H. Kato and A. Kudo, *Journal of Photochemistry and Photobiology a-Chemistry*, 2004, 163, 181-186.
49. G. L. Chiarello, M. H. Aguirre and E. Selli, *Journal of Catalysis*, 2010, 273, 182-190.
50. H. Bahruji, M. Bowker, P. R. Davies and F. Pedrono, *Applied Catalysis B: Environmental*, 2011, 107, 205-209.
51. L. Millard and M. Bowker, *Journal of Photochemistry and Photobiology A: Chemistry*, 2002, 148, 91-95.
52. A. Caravaca, W. Jones, C. Hardacre and M. Bowker, *Proceedings of the Royal Society A: Mathematical, Physical and Engineering Science*, 2016, 472.
53. A. A. Ismail and D. W. Bahnemann, *Solar Energy Materials and Solar Cells*, 2014, 128, 85-101.
54. M. Bowker, H. Bahruji, J. Kennedy, W. Jones, G. Hartley and C. Morton, *Catalysis Letters*, 2015, 145, 214-219.
55. M. Bowker, D. James, P. Stone, R. Bennett, N. Perkins, L. Millard, J. Greaves and A. Dickinson, *Journal of Catalysis*, 2003, 217, 427-433.
56. J. Kennedy, W. Jones, D. J. Morgan, M. Bowker, L. Lu, C. J. Kiely, P. P. Wells and N. Dimitratos, *Catalysis, Structure & Reactivity*, 2014, 1, 35-43.
57. D. D'Elia, C. Beauger, J. F. Hochepped, A. Rigacci, M. H. Berger, N. Keller, V. Keller-Spitzer, Y. Suzuki, J. C. Valmalette, M. Benabdesselam and P. Achard, *International Journal of Hydrogen Energy*, 2011, 36, 14360-14373.
58. A. F. Feil, P. Migowski, F. R. Scheffer, M. D. Pierozan, R. R. Corsetti, M. Rodrigues, R. P. Pezzi, G. Machado, L. Amaral, S. R. Teixeira, D. E. Weibel and J. Dupont, *Journal of the Brazilian Chemical Society*, 2010, 21, 1359-1365.
59. M. Lafjah, A. Mayoufi, E. Schaal, F. Djafri, A. Bengueddach, N. Keller and V. Keller, *Catalysis Today*, 2014, 235, 193-200.
60. Y. Zou, S. Z. Kang, X. Li, L. Qin and J. Mu, *International Journal of Hydrogen Energy*, 2014, 39, 15403-15410.
61. A. Kachina, E. Puzenat, S. Ould-Chikh, C. Geantet, P. Delichere and P. Afanasiev, *Chemistry of Materials*, 2012, 24, 636-642.
62. K. M. Parida, S. Pany and B. Naik, *International Journal of Hydrogen Energy*, 2013, 38, 3545-3553.
63. O. D. Jayakumar, R. Sasikala, C. A. Betty, A. K. Tyagi, S. R. Bharadwaj, U. K. Gautam, P. Srinivasu and A. Vinu, *Journal of Nanoscience and Nanotechnology*, 2009, 9, 4663-4667.
64. G. Yang, Z. Yan and T. Xiao, *Applied Surface Science*, 2012, 258, 4016-4022.
65. W. Zhang, S. Wang, J. Li and X. Yang, *Catalysis Communications*, 2015, 59, 189-194.
66. L. Lin, W. Lin, J. L. Xie, Y. X. Zhu, B. Y. Zhao and Y. C. Xie, *Applied Catalysis B: Environmental*, 2007, 75, 52-58.
67. F. Wang, Y. Jiang, A. Gautam, Y. Li and R. Amal, *ACS Catalysis*, 2014, 4, 1451-1457.
68. F. Porta, L. Prati, M. Rossi, S. Coluccia and G. Martra, *Catalysis Today*, 2000, 61, 165-172.
69. N. Dimitratos, J. A. Lopez-Sanchez, D. Morgan, A. Carley, L. Prati and G. J. Hutchings, *Catalysis Today*, 2007, 122, 317-324.
70. N. Dimitratos, A. Villa, L. Prati, C. Hammond, C. E. Chan-Thaw, J. Cookson and P. T. Bishop, *Applied Catalysis A: General*, 2016, 514, 267-275.
71. T. Takei, T. Ishida and M. Haruta, in *Novel Concepts in Catalysis and Chemical Reactors*, Wiley-VCH Verlag GmbH & Co. KGaA, 2010, DOI: 10.1002/9783527630882.ch3, pp. 51-71.
72. L. Prati and G. Martra, *Gold Bulletin*, 1999, 32, 96-101.
73. J. Hilde, J. Karolien, L. Liesbet, B. Gustaaf, M. Guido and H. Qun, *Nanotechnology*, 2010, 21, 455702.

74. F. Porta and L. Prati, in *Metal Nanoclusters in Catalysis and Materials Science*, eds. G. Schmid and N. Toshima, Elsevier, Amsterdam, 2008, pp. 355-360.
75. A. Wolf and F. Schüth, *Applied Catalysis A: General*, 2002, 226, 1-13.
76. J. A. Lopez-Sanchez, N. Dimitratos, C. Hammond, G. L. Brett, L. Kesavan, S. White, P. Miedziak, R. Tiruvalam, R. L. Jenkins, A. F. Carley, D. Knight, C. J. Kiely and G. J. Hutchings, *Nat Chem*, 2011, 3, 551-556.
77. M. Bowker, C. Morton, J. Kennedy, H. Bahruji, J. Greves, W. Jones, P. R. Davies, C. Brookes, P. P. Wells and N. Dimitratos, *Journal of Catalysis*, 2014, 310, 10-15.
78. D. G. Duff, A. Baiker and P. P. Edwards, *Langmuir*, 1993, 9, 2301-2309.
79. J. L. Hueso, V. Sebastian, A. Mayoral, L. Uson, M. Arruebo and J. Santamaria, *RSC Advances*, 2013, 3, 10427-10433.
80. J. Turkevich, P. C. Stevenson and J. Hillier, *Discussions of the Faraday Society*, 1951, 11, 55-75.
81. J. Turkevich and G. Kim, *Science*, 1970, 169, 873.
82. M. Brust, J. Fink, D. Bethell, D. J. Schiffrin and C. Kiely, *Journal of the Chemical Society, Chemical Communications*, 1995, DOI: 10.1039/c39950001655, 1655-1656.
83. S. D. Perrault and W. C. W. Chan, *Journal of the American Chemical Society*, 2009, 131, 17042-17043.
84. N. R. Jana, L. Gearheart and C. J. Murphy, *Langmuir*, 2001, 17, 6782-6786.
85. M. Bowker, A. Nuhu and J. Soares, *Catalysis Today*, 2007, 122, 245-247.
86. H. Bahruji, M. Bowker, P. R. Davies, D. J. Morgan, C. A. Morton, T. A. Egerton, J. Kennedy and W. Jones, *Top. Catal.*, 2015, 58, 70-76.
87. S. Song, Z. Sheng, Y. Liu, H. Wang and Z. Wu, *Journal of Environmental Sciences*, 2012, 24, 1519-1524.
88. S. Tsubota, D. A. H. Cunningham, Y. Bando and M. Haruta, in *Studies in Surface Science and Catalysis*, eds. J. M. B. D. P. A. J. G. Poncelet and P. Grange, Elsevier, 1995, vol. Volume 91, pp. 227-235.
89. F. Moreau, G. C. Bond and A. O. Taylor, *Journal of Catalysis*, 2005, 231, 105-114.
90. R. Zanella, L. Delannoy and C. Louis, *Applied Catalysis A: General*, 2005, 291, 62-72.
91. A. Zwijnenburg, A. Goossens, W. G. Sloof, M. W. J. Craje, A. M. van der Kraan, L. J. de Jongh, M. Makkee and J. A. Moulijn, *Journal of Physical Chemistry B*, 2002, 106, 9853-9862.
92. G. C. Bond, *Catalysis Today*, 2002, 72, 5-9.
93. R. Zanella, S. Giorgio, C.-H. Shin, C. R. Henry and C. Louis, *Journal of Catalysis*, 2004, 222, 357-367.
94. F. X. Zhang, J. X. Chen, X. Zhang, W. L. Gao, R. C. Jin and N. J. Guan, *Catalysis Today*, 2004, 93-5, 645-650.
95. M. Maicu, M. C. Hidalgo, G. Colón and J. A. Navío, *Journal of Photochemistry and Photobiology A: Chemistry*, 2011, 217, 275-283.
96. D. J. Martin, K. Qiu, S. A. Shevlin, A. D. Handoko, X. Chen, Z. Guo and J. Tang, *Angewandte Chemie International Edition*, 2014, 53, 9240-9245.

Chapter 2: Experimental

Table of contents

2.1	Introduction	29
2.2	Catalyst preparation: Sol immobilisation.....	29
2.2.1	Synthesis of 1%Au-TiO ₂	29
2.2.2	Synthesis of Au-TiO ₂ with various weight loadings Au	29
2.2.3	Calcining the sol immobilised catalysts.....	29
2.2.4	Sol immobilisation of mono metallic silver and palladium	30
2.2.5	Synthesis of bimetallic NPs by sequential reduction of precursors.....	30
2.2.6	Synthesis of AgAu and PdAu core-shell NPs	32
2.3	Catalyst preparation: Other methods.....	33
2.3.1	Impregnation to incipient wetness.....	33
2.3.2	Deposition precipitation urea for Au-TiO ₂ synthesis	34
2.3.3	THPC/NaOH colloidal synthesis.....	34
2.3.4	Photodeposition.....	34
2.3.5	Preparation of Cerium doped sol gel TiO ₂	35
2.3.6	Carbon nitride synthesis	35
2.4	Development of the photo reactor.....	35
2.4.1	Batch set up	35
2.4.2	Reactor	36
2.4.3	Solar simulator lamp	36
2.4.4	Reaction procedure and conditions.....	37
2.4.5	Set up for flow reactions.....	37
2.4.6	Reactions with long band pass filters	38
2.4.7	Photoreactor set up at Sydney University	39
2.4.8	Reactor set up in Cardiff University	40
2.4.9	Reactor set up in Aarhus University, Denmark.....	40
2.5	Gas chromatography.....	41
2.5.1	Shimadzu GC	41
2.5.2	Injection and separation of sample	42

2.5.3	Detector - Thermal conductivity detector (TCD)	43
2.5.4	Agilent CG-MS	43
2.5.5	Hydrogen calibration for Shimadzu GC	44
2.5.6	Hydrogen calibration for Agilent GC	46
2.6	Transmission electron microscopy (TEM)	48
2.6.1	Introduction to TEM	48
2.6.2	TEM Sample preparation	50
2.6.3	High Annular Dark-Field TEM analysis	50
2.7	Ultra violet – visible spectroscopy (UV-Vis)	50
2.8	Thermogravimetric analysis (TGA)	51
2.9	X-Ray absorption spectroscopy (XAS)	51
2.9.1	Introduction to XAS	51
2.9.2	Synchrotrons	52
2.9.3	Theory of XAS	52
2.9.4	EXAFS	54
2.9.5	The EXAFS equation	55
2.9.6	XANES	58
2.9.7	XAFS experimental set up and experimental modes	59
2.9.8	Transmission mode	59
2.9.9	Fluorescence mode	60
2.9.10	X-ray generation in the synchrotron	61
2.9.11	XAFS acquisition	62
2.9.12	EXAFS particle size	62
2.10	X-ray diffraction (XRD)	63
2.11	X-ray photoelectron spectroscopy (XPS)	64
2.12	References	66

2.1 Introduction

The first experimental section details all of the catalyst preparation methods used for sample synthesis. With emphasis on the sol immobilisation technique and variations as this was the primary method undertaken for catalysts synthesis. A second section on catalytic testing outlines the details of the photoreactors used for catalyst performance evaluations. Finally a section will focus the on characterisation techniques used.

2.2 Catalyst preparation: Sol immobilisation

2.2.1 Synthesis of 1%Au-TiO₂

For a typical procedure an aqueous solution of the H₂AuCl₄·3H₂O (Sigma Aldrich) of the desired concentration (typically 1.27×10^{-4} M) was prepared. To this solution, polyvinyl alcohol (PVA) (1 wt% solution, Aldrich, average molecular weight = 9000–10,000 g mol⁻¹, 80% hydrolysed) was added (PVA/Au (wt/wt) = 0.65). Subsequently, a 0.1 M freshly prepared solution of NaBH₄ (>96%, Aldrich, NaBH₄/Au (mol/mol) = 5) was then added to form a dark red/brown solution. After 30 min of sol generation, the colloid was immobilised by adding TiO₂ (P-25 Evonik) acidified to pH 1 by sulphuric acid, under vigorous stirring conditions. The amount of support material required was calculated so as to have a total final metal loading of 1 wt%. After 2 hours immobilisation time the slurry was filtered, the solid washed thoroughly with distilled water (2 L MilliQ water) to remove all the dissolvable species, such as Na⁺, Cl⁻ and dried at 120 °C for 8 hours, The resulting catalyst was then dried at 120 °C for 8 hours.

2.2.2 Synthesis of Au-TiO₂ with various weight loadings Au

Changing the desired weight loading of Au on the catalyst was achieved by adding the corresponding amount of titania to the colloidal dispersion, e.g. if the sol contained 10 mg of Au colloids then 990 mg of TiO₂ would be added to form 1 g of 1%Au-TiO₂. The concentration of the initial Au precursor was always kept constant, unless otherwise stated. Weight loading of 0.1-5% Au on TiO₂ were synthesised for these studies.

2.2.3 Calcining the sol immobilised catalysts

Once the dried catalysts were prepared calcinations were performed to remove the protecting ligands and any volatile species. Typically calcinations were carried out in a muffle furnace at 200, 300 and 400 °C with a dwell time at the maximum temperature of 3 hours

and a ramp rate of 5 / °C. To ensure that the correct temperature was achieved during the calcination step a thermocouple was placed in the middle of the bottom of the muffle furnace. This was done to verify the temperature in the immediate vicinity of the sample, it was noticed that temperature measurements of the muffle were recorded by a thermocouple placed at the top of the oven. Figure 1 represents the temperature as measured by the muffle furnace (from the top of the oven) and by the placed thermocouple (at the bottom) during calcination at 200, 300 and 400 °C with a ramp rate of 5 / °C. As can be seen there is a lag in the reading of the muffle and the temperature at the sample. The target temperature was reached after 100 min for 200 °C, 120 min for 300 °C and 115 min for 400 °C. Once the desired temperature was reached the dwell time was begun, which was followed by samples being allowed to cool to room temperature.

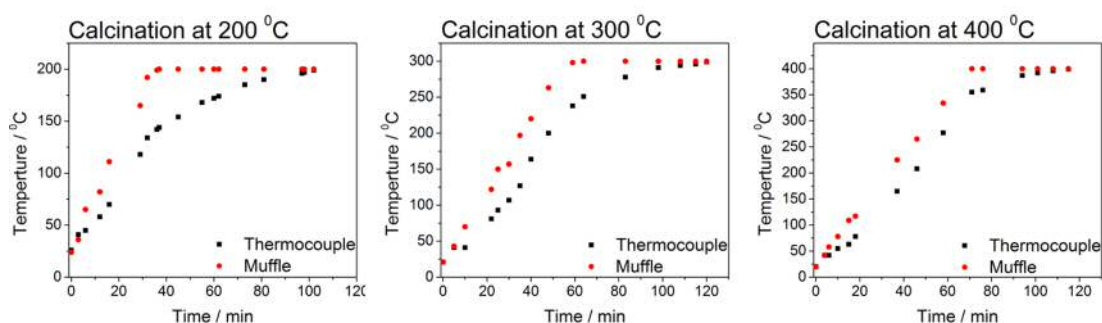


Figure 1. Graphs of temperature as a function of time inside the muffle furnace. As measured by the muffle (recorded from the top of the oven) and a thermocouple (recorded at the bottom of the oven) during calcination at 200, 300 and 400 °C with a ramp rate of 5°C min⁻¹.

2.2.4 Sol immobilisation of mono metallic silver and palladium

As well as Au-TiO₂ catalysts Pd-TiO₂ and Ag-TiO₂ were also prepared by the sol immobilisation method. These were prepared with the same procedure as the Au sol immobilisation catalysts with the exception being the metal precursor of AgNO₃ and K₂PdCl₄. Parameters kept identical included, concentration of the metal precursor (1.27x10⁻⁴ M,) PVA to metal ratio (0.65 by wt/wt) and metal to reducing agent NaBH₄ (5 by mole/mole) ratio.

2.2.5 Synthesis of bimetallic NPs by sequential reduction of precursors

Synthesis of Ag[Au] and Pd[Au] sols

To an aqueous HAuCl_4 solution of the desired concentration the required amount of a PVA solution (1 wt%) was added ($\text{PVA}/(\text{Au}+(\text{Ag or Pd})) (\text{wt}/\text{wt})=1.2$, corresponding to the total final amount of metal present); a freshly prepared solution of NaBH_4 (0.1M, NaBH_4/Au (mol/mol)=5) was then added to form a sol. The solution was stirred for 30 min. Then, the required amount of the stock aqueous AgNO_3 or K_2PdCl_4 solution was added, followed by the desired amount of NaBH_4 ($\text{NaBH}_4/(\text{Ag or Pd}))$ (mol/mol)=5), obtaining a sol. The solution was stirred for a further 30 min.

Synthesis of Au[Ag] or Au[Pd] sols

To an aqueous AgNO_3 or K_2PdCl_4 solution of the desired concentration and the required amount of a PVA solution (1wt%) was added ($\text{PVA}/(\text{Au}+(\text{Ag or Pd})) (\text{wt}/\text{wt})=1.2$, corresponding to the total final amount of metal present); a 0.1M freshly prepared solution of NaBH_4 ($\text{NaBH}_4/(\text{Ag or Pd}))$ (mol/mol)=5) was then added to form a sol. The solution was stirred for 30 min. Then, the desired amount of the stock HAuCl_4 aqueous solution was added, followed by the desired amount of NaBH_4 (NaBH_4/Au (mol/mol)=5), obtaining a sol. The solution was stirred for further 30 min.

Synthesis of AuAg or AuPd sols

To an aqueous HAuCl_4 solution with AgNO_3 or K_2PdCl_4 of the desired concentrations the required amount of a PVA solution (1 wt%) was added ($\text{PVA}/(\text{Au}+(\text{Ag or Pd})) (\text{wt}/\text{wt})=1.2$, corresponding to the total final amount of metal present); a freshly prepared solution of NaBH_4 (0.1M, $\text{NaBH}_4/(\text{Au}+(\text{Ag or Pd}))$ (mol/mol)=5) was then added to form a sol. The solution was stirred for 30 min.

Supported catalysts

After 30 min of sol generation, the bimetallic colloid was immobilized by adding TiO_2 (acidified at pH 1 by sulfuric acid) under vigorous stirring conditions. The amount of TiO_2 support material required was calculated so as to have a total final metal loading of 1 wt%. The metal ratio for the 1 wt% $(\text{Au}+(\text{Ag or Pd}))/\text{TiO}_2$ catalyst was 1:1 molar. After 2 hours the slurry was filtered, the catalyst was washed thoroughly with distilled water to remove all the

dissolvable species, (such as Na^+ , K^+ or Cl^-) and the powder was collected and dried at 120°C overnight.

2.2.6 Synthesis of AgAu and PdAu core-shell NPs

For the synthesis of core-shell structured metal NPs supported with 1 and 2 monolayers (ML's) Ag and Pd on Au-TiO₂, we first prepared the 1 wt% of Au supported on TiO₂ (Au/TiO₂) by standard sol immobilisation.¹ TEM analysis was performed to estimate the dispersion and calculate amount of Ag or Pd for 1 and 2 ML's. Then the thin layers of Ag and Pd were deposited on Au either by photodeposition or sequential reduction methods, as demonstrated in below:

Photodeposition method (PD): The as-prepared Au/TiO₂ photocatalyst was placed in a Pyrex round bottom flask with 250 mL of Milli Q water and sonicated for 1 hour to obtain a homogeneous dispersion of the catalyst. To which a solution of AgNO₃ or K₂PdCl₄ corresponding to a thickness of either one or two ML of Ag or Pd was added. Reduction of the precursors was performed by photo irradiation using a Lot-Oriel solar simulator (LSO104) containing a 150 W Xe arc lamp under continuous stirring. After two hours the mixture was filtered and dried at 120°C for 8 hours to produce the final photocatalysts. The samples were labelled as 1ML (PD) and 2ML (PD), respectively.

Double reduction method (DR): The as-prepared Au/TiO₂ photocatalyst was added into 800 mL of Milli Q water and sonicated for 1 hour to disperse the catalyst. To which a solution of AgNO₃ or K₂PdCl₄ corresponding to a thickness of either one or two ML of Ag or Pd was added. Reduction of the precursors was performed by addition of excess NaBH₄. After 30 minutes of reduction, the mixture was filtered and dried at 120°C for 8 hours to produce the final photocatalysts. The samples were labelled as 1ML (DR) and 2ML (DR), respectively.

Sequential reduction method (SR): An Au colloid was formed as in the standard sol immobilisation method. To which a solution of AgNO₃ or K₂PdCl₄ corresponding to a thickness of either one or two ML of Ag or Pd was added and further reduced by NaBH₄. After 30 minutes of reduction TiO₂ was added and the solution was acidified with H₂SO₄ (pH ~ 2) to immobilise the newly formed colloid. The mixture was filtered and dried at 120°C for 8 hours to produce the final photocatalysts. The samples were labelled as 1ML (SR) and 2ML (SR), respectively.

2.3.2 Deposition precipitation urea for Au-TiO₂ synthesis

Example for making 2 g 1%Au-TiO₂, a solution of HAuCl₄ (1.26x10⁻⁴ M 400 mL) was prepared in a 500 mL conical flask. To this TiO₂ 1.98 g and urea (CO(NH₂)₂) 10.08 g was added to give a concentration of 0.42 M. The initial pH was in the region of 3.4 and the solution was then heated and kept at 65 °C. At this temperature, the urea decomposes as in

Equation 5 to produce OH⁻

ions increasing the pH to 11 after 2 hours. After this time the hydroxide ions will displace all the chlorine ions in HAuCl₄ resulting in Au(OH)₃ and Au(OH)₄⁻. The solution was then cooled in an ice bath and filtered under suction washing with 1L of milliQ water. A white powder was then recovered which turned purple/blue after drying in a muffle furnace for 8 hours at 120 °C.³

Equation 5

2.3.3 THPC/NaOH colloidal synthesis

Procedure for making 1 g of 1wt%Au-TiO₂, prepare a Tetrakis(hydroxymethyl)phosphonium chloride (THPC) water solution by using 0.120 mL of 80wt% THPC in 10 mL water in a volumetric flask (0.0675 M). Also prepare a 0.2 M NaOH solution in a volumetric flask, 0.2 g of NaOH in 25 mL of water. Fill a beaker with 46.5 mL of MilliQ water, add 1.5 mL of the NaOH solution to the water followed by 1 mL of the THPC solution. Add the Au precursor containing 10 mg of Au and stir for 30 min. After this time a red Au colloid is formed, then add the TiO₂ (0.99 g). Allow to stir for 2 minutes then acidify with H₂SO₄ to pH 1 and stir for one hour. Filter under vacuum and dry at 120 °C for 8 hours. More details can be found in the references.^{4,5}

2.3.4 Photodeposition

3%Pd-C₃N₄ and 3%Pd-TiO₂ catalysts were prepared using *in-situ* photodeposition. Pd was deposited on the surface of the support during an induction period, whilst also simultaneously measuring the hydrogen production. Firstly, a solution of the Pd precursor, K₂PdCl₄ containing the desired mass of metal (0.6 mg) was added to the reaction mixture of water (200 mL), hole scavenger (TEOA or MeOH 0.025 moles) and support (20 mg). Secondly, this mixture was then exposed to full arc irradiation from the 150 W Xe lamp under reaction conditions for 3 hours, with full immobilisation of the Pd assumed once the hydrogen production rate becomes stable.

2.3.5 Preparation of Cerium doped sol gel TiO₂

Sol gel TiO₂ Procedure; A solution of titanium isopropoxide (5 mL) and isopropyl alcohol (95 mL) was prepared. A second solution of acidified water (900 mL) with nitric acid until pH 1.5 was also prepared. The titanium isopropoxide solution was added dropwise over 10 minutes to the acidified water. The mixture was allowed to stir for 24 hours followed heating at 80 °C until all liquids were evaporated leaving a white powder. The newly made TiO₂ was then dried at 120 °C for 8 hours then calcined at 200 °C for 3 hours.⁶ In the cases of cerium doping of sol gel TiO₂ the required amount of Ce(NO₃)₃ was added to the acidified water before addition of titanium isopropoxide solution. After the sol gel TiO₂ and cerium doped TiO₂ was prepared 0.5%wt loading of Pd was added to the surface by incipient wetness impregnation, section 2.3.1.

2.3.6 Carbon nitride synthesis

Graphitic carbon nitride (g-C₃N₄) was prepared by thermal decomposition of urea as reported in reference.⁷ The precursor urea was placed in a lidded high quality alumina crucible, then placed inside a muffle furnace and calcined in air. A ramp rate of 5 °C.min⁻¹ with a final temperature of 600 °C held for 4 hours was used. The resulting powder was then washed with water, HCl, NaOH and once again with water to remove all unreacted and potentially detrimental surface species. Synthesis of the carbon nitride for all reactions performed at RCaH was done by David Martin a collaborator from UCL.

2.4 Development of the photo reactor

2.4.1 Batch set up

Figure 2 shows a schematic set up of the batch photo reactor system which was set up in research complex at Harwell (RCaH). Reactions were typically performed in the liquid phase by irradiating the reaction mixture containing the catalyst by a Xenon arc lamp. An inert atmosphere was provided by purging the reactor with argon (nitrogen was used before argon was available) and the course of the reaction was followed by injecting a sample of gas from the reactor into a GC machine. The experimental set up and procedures are similar to those reported by A. Dickinson *et al.*⁸

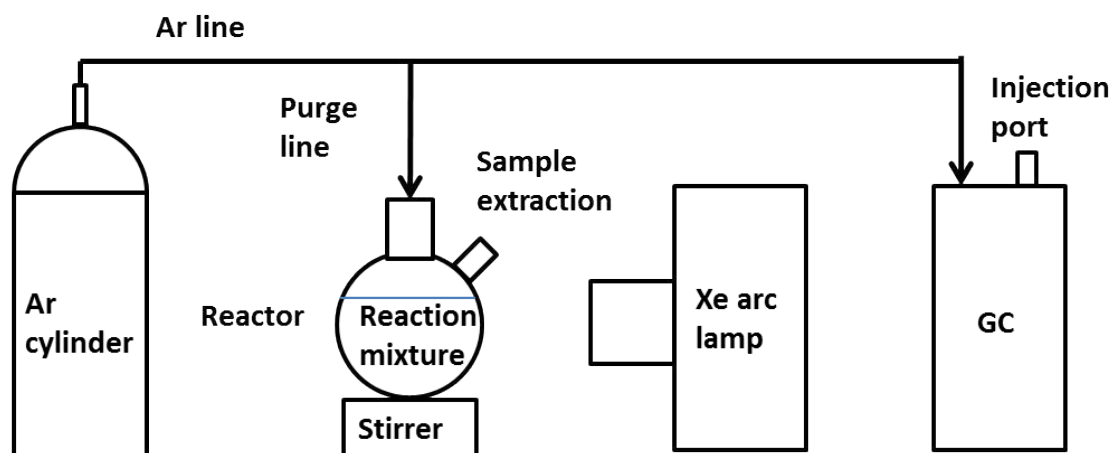


Figure 2. Schematic set up of batch photo reactor system.

2.4.2 Reactor

The reactor used for all liquid phase reactions was a 250 mL Pyrex two necked round bottom flask. The top of the flask was fitted with a stopcock to allow a plastic Swagelok pipe to be inserted and argon flowed into the system for purging of oxygen. After purging the system was complete the pipe could be removed and the tap closed to maintain the inert environment. The second neck could be fitted with an air tight rubber septum through which samples could be extracted during reactions for analysis with a gas tight syringe (1 mL Hamilton).

2.4.3 Solar simulator lamp

The light source used for photo catalytic reactions was a Lot-Oriel full spectrum solar simulator Xenon 150 W arc lamp (LSB521U) ozone free. The lamp was placed inside a housing box (Lot-Oriel LSO104) which was fitted with lens optics a rear reflector for focusing the beam and connected to a power supply. This lamp was chosen as it emitted broadly with the lack of any major peaks across the spectrum 200-1000 nm, see Figure 3 Therefore this lamp was suitable for photo reactions requiring UV and/or visible light. The arc lamp consists of a quartz tube filled with Xenon with an anode and cathode protruding inwards from each end separated by about 1 cm. As a voltage is applied an electric spark or arc is generated bridging between the two electrodes. The initial current is high to ignite the arc and ionise the gas, once the arc is sustained a steady current is applied. The emitted light originates from the ionised Xenon which emits photons when relaxing back to the ground state.

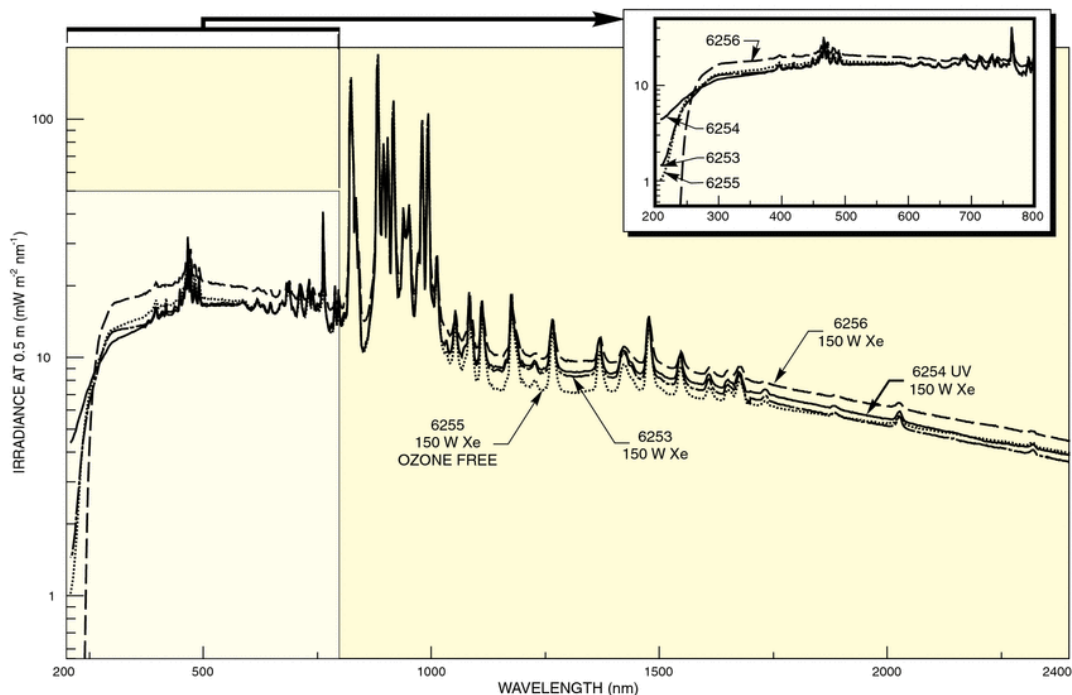


Figure 3. Emission spectra of 150 W Xenon arc lamp (Ozone free) used for photocatalytic reactions in RCaH.⁹

2.4.4 Reaction procedure and conditions

A typical reaction procedure follows, 150 mg of catalyst would be weight out and placed inside the two necked round bottom reactor with 200 mL of MilliQ water. The mixture would then be sonicated for 30 min to ensure the catalyst powder was dispersed. Methanol and a magnetic stirrer bar would then be added and the reactor would be purged by bubbling argon through the liquid for 30 min. After purging the two necks of the reactor would be sealed by a switching valve and a rubber septum. The reaction mixture was then ready for the Xenon arc lamp to be turned on and the reaction progress followed by sampling with a gas tight syringe through the rubber septum. The exact amount of catalyst and reforming agent used varied depending on the study; however some parameter remained constant including 200 mL volume of liquid, 30 min purge time and 30 min sonication time.

2.4.5 Set up for flow reactions

As well as the batch set up the system was also modified for continuous flow measurements with a schematic in Figure 4. In this set up the argon carrier line was connected directly to the reactor with a Swagelok to glass fitting, with a rotameter flow meter also connected. A second Swagelok to glass fitting was connected to the second neck of the reactor which was then connected directly to the GC for analysis. For a typical reaction with this system a flow

of 20 mL min^{-1} argon was allowed through the reactor and GC, the flow was also checked with a bubble flow meter after passing through the GC. Once purging was complete a reaction was began by turning on the Xenon arc lamp which started the generating of hydrogen. A GC batch method would then be set up to sample the gas steam exiting the reactor every 10 minutes by injecting a $50 \mu\text{L}$ sample for analysis.

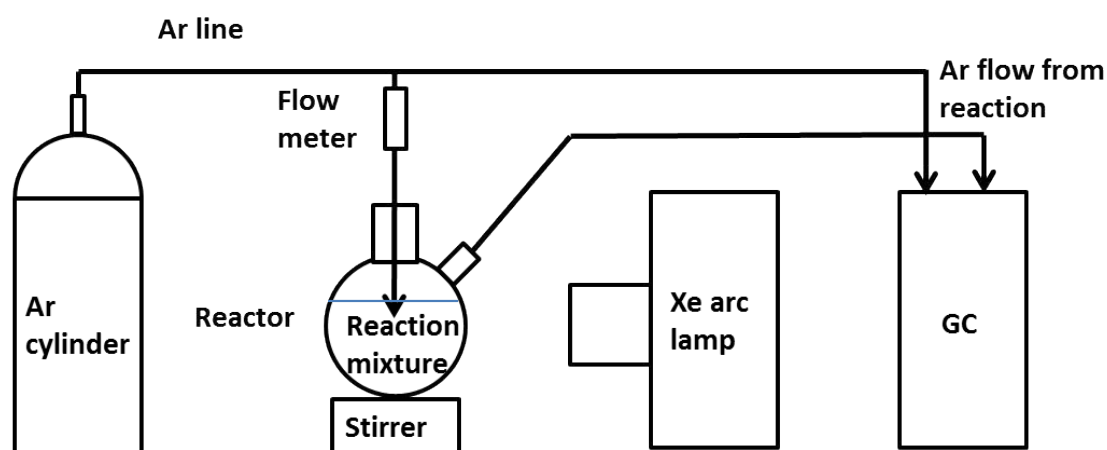


Figure 4. Schematic set up of batch photo reactor system set up for continuous flow measurements.

2.4.6 Reactions with long band pass filters

A set of long band pass filters was employed for investigations of the wavelength dependence during photocatalytic reactions. Four filters were purchased (350, 375, 400 and 420 nm Lot-Oriel) and the UV-Vis spectra of each are shown in Figure 5. The Xenon arc lamp was fitted with a holder at the front to accommodate the filters when required. Figure 5 show the UV/vis absorption properties of the four filters.

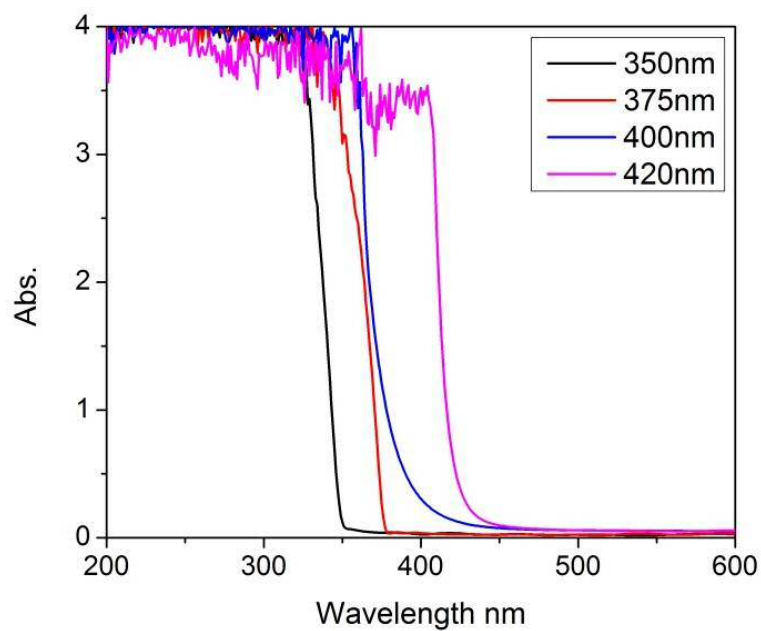


Figure 5. UV/Vis absorbance spectra of long wave band pass filters (Lot-Oriel)

2.4.7 Photoreactor set up at Sydney University



Figure 6. Image of the reactor set up used at Sydney University

Figure 6 shows the reactor set up used when performing photocatalytic reactions at Sydney University. The set up consisted of a quartz reactor cell with water jacket to maintain a constant temperature of 15 °C. Helium was flown through the reactor at 30 mL min⁻¹ bubbling through the reaction mixture before passing through a GC with switching valves for gas analysis. The flow was set with a flow meter before passing through the reactor and checked with a bubble flow meter after leaving the GC. The GC used was a Shimadzu 2014

fitted with a discharge ionisation detector. The lamp used was a 400 W Xenon Hg arc lamp with a holder in place for fitting long band pass filters.

2.4.8 Reactor set up in Cardiff University

Samples were sent to Cardiff University as part of collaboration with Julia Kennedy, before there was a reactor system set up in Harwell. The reactor set up Harwell was based on the system in Cardiff University therefore the two configurations are very similar. Figure 7 shows a schematic diagram of the set up in Cardiff.

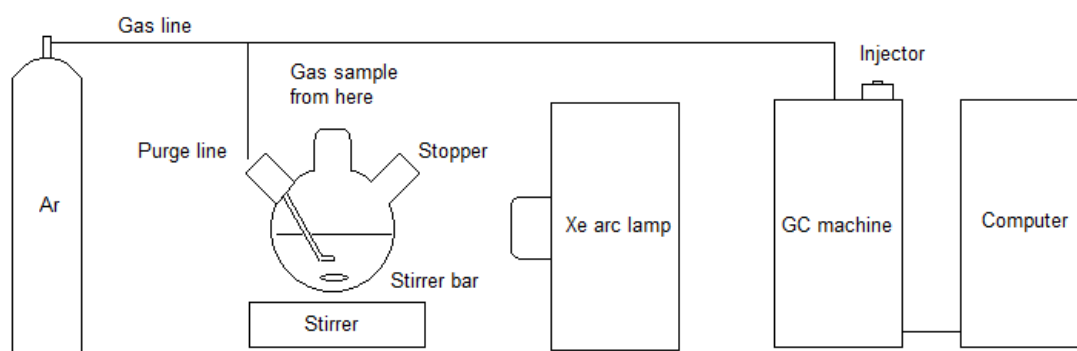


Figure 7. Schematic set up of batch photo reactor system in Cardiff University

Reactions were performed in three necked Pyrex round bottom flask with one neck fitted with a stopper, one with a purging line for bubbling argon and the other neck fitted with rubber septum for sample extraction. A 450 W xenon arc lamp (Oriol model 66921) was used as an illumination source and sample analysis was performed by a varian 3300 gas chromatograph (GC), fitted with an MD13X molecular sieve column and a Thermal conductivity detector (TCD).

2.4.9 Reactor set up in Aarhus University, Denmark

Samples were sent to Aarhus University in Denmark as part of collaboration with Ren Su and Qian Yan. Details of the experimental set up can be found in the supplementary information from reference,¹⁰ and is summarised briefly here. The reaction chamber consists of a cylindrical glass vessel (total volume 215 mL) with a quartz window at the top for illumination of the reaction mixture by a LED (WL: 365 nm, FWHM: 10 nm, Tritant 365, Spectroline). The chamber is connected to a rotary pump and gas tight inlets for providing the required inert reaction environment. The gas phase was monitored by a mass spectrometer (HPR-20, Hiden) attached by a leak tight valve. The evolution of hydrogen during a photocatalytic reaction was monitored by measuring the partial pressure of the gasses inside the reaction

chamber during illumination. The system was calibrated for H₂ quantification by measuring the relative sensitivity factor of H₂ with a standard. The produced H₂ [n(H₂)_{gas}] and can therefore derived using the following equations:

$$n(\text{H}_2)_{\text{gas}} = p(\text{H}_2)_{\text{rea}} \times V_{\text{rea}} / RT \quad \text{Equation 6}$$

$$p(\text{H}_2)_{\text{rea}} = \text{RSF}(\text{H}_2) \times p(\text{H}_2)_{\text{det}} \times p(\text{Air})_{\text{rea}} / p(\text{Air})_{\text{det}} \quad \text{Equation 7}$$

Reaction parameters for the samples sent were 25 mg of catalyst in 25 mL of 25% ethanol water mixture illuminated with UV light for 2.5 hours.

2.5 Gas chromatography

Gas chromatography (GC) is a useful type of chromatography for separating and analysing compounds and can be either quantitative or qualitative. Samples can to be either a gas or a liquid able to be vaporised without decomposition before analysis by GC. Primarily in this project GC analysis was performed for detection quantification of hydrogen produced during photocatalytic reactions. Typically, a sample is injected into a column with a constant flow of carrier gas where the compounds are separated based on the affinity of the constituents to the stationary phase. The column is placed inside an oven for control of the temperature which could be either isothermal or a temperature program. After separation and elution from the column the constituents of the sample are passed through a detector. The signal from the detector is proportional to the concentration of the individual constituents of the sample allowing for quantification. During this project two GC were used for hydrogen detection a Shimadzu and Agilent.

2.5.1 Shimadzu GC

Figure 8 shows a schematic of the setup of the column inside Shimadzu GC used (Shimadzu 2014 Gas Chromatograph) for the majority of the reactions in this this project.

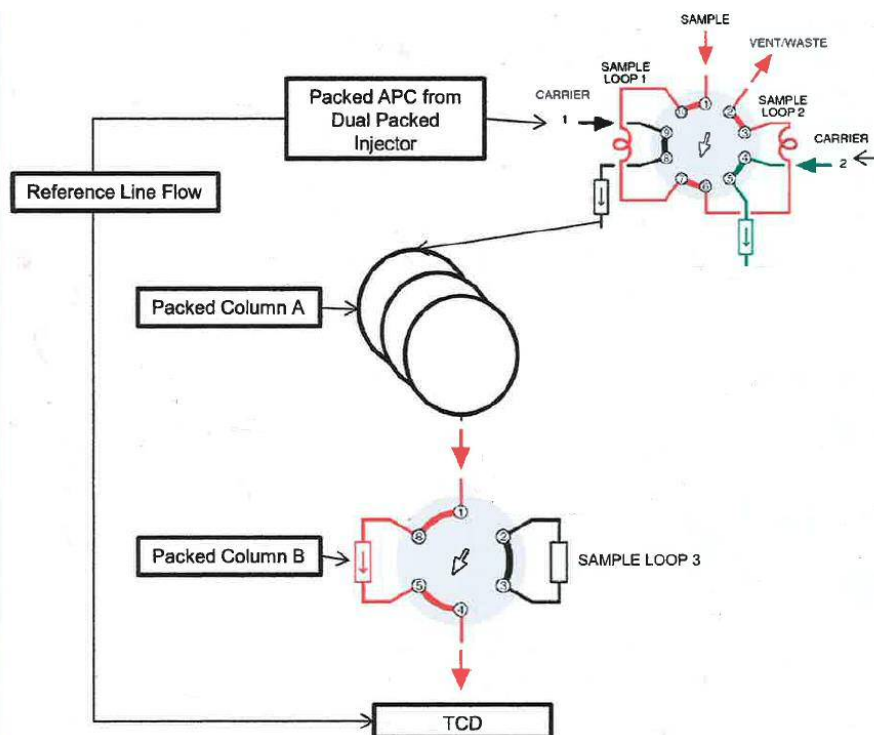


Figure 8. Schematic set up of switching valves and columns of the Shimadzu GC.

2.5.2 Injection and separation of sample

To begin a measurement the gas sample is injected typically with a gas tight syringe into the sample loops (loop 1), a minimum of 1 mL of gas is need to fill the dead space. Each loop has a fixed volume, 1 = 50 μL and 2 = 250 μL , once the valves are switched this volume is injected into the columns. Sample loop 2 injected into two capillary columns which was not used in this project. Loop 1 however injected the volume towards two packed columns in parallel. Packed column A was a Haysep N (Shimadzu 80-100 mesh)) which would separate only the heavier gasses (e.g. CH_4 , C_2H_6 or higher hydrocarbons) allowing lighter gasses to pass through unaffected. Packet column B contained a molecular sieve (Shimadzu 80-100 mesh) which would allow for the separation of the lighter gasses not separated by the Haysep N (e.g. N_2 , H_2 and O_2). Sample loop 3 was effectively a switchable bypass column which was important as heavier gasses should not be allowed to pass through the molecular sieve as there was the possibility of some gasses taking an impractically long time to elute or even getting stuck in the column at low temperatures. When setting up a method it is then important to set the switching column so as the lighter gasses pass through the molecular sieve then switches to prevent heavier gasses passing through.

2.5.3 Detector - Thermal conductivity detector (TCD)

A thermal conductivity detector (TCD) was used to analyse hydrogen after being separated by the column. This detector operates by measuring the thermal conductivity of the column effluent and compares it to a reference flow of carrier gas, in this case Argon. Thermal conductivity is measured by a fine filament in a detector cell kept at constant temperature (in this case 240°C). Under normal conditions there is a steady flow of the Argon carrier gas over the filament. When the analyte passes out of the column, and over the filament, the thermal conductivity of the gas surrounding the filament will change. This will result in a temperature change, and hence a change in current across the filament which is measured. A signal is generated by comparison with the reference cell containing a flow of pure carrier gas. To detect a gas effectively by a TCD detector the difference in thermal conductivity between the carrier gas and the analyte gas need to be taken into consideration. If the difference is too small, then the signal will be weak which will result in detection limit of the GC being low. However if the difference in the thermal conductivity is large then smaller concentrations can be measured with better signal to noise ratio. Table 1 shows the thermal conductivity of several common gases. For measurement of hydrogen, Argon was used as there is a suitable difference in thermal conductivities.

Table 1. List of several common gas with their corresponding thermal conductivities, units in milli Watts per metre Kelvin.

Gas	Thermal conductivity (mWm⁻¹K⁻¹)
Hydrogen	186.9
Argon	17.9
Helium	156.7
Oxygen	26.3
Nitrogen	26.0

Conditions used with Shimadzu GC: Flow rate 34 mL min⁻¹, carrier Argon, oven temperature 40 °C, injection volume 50 µL, inlet temperature 120 °C and TCD temperature 240 °C.

2.5.4 Agilent CG-MS

An Agilent gas chromatography-mass spectrometer (GC-MS 5975C) was also used for measurement of hydrogen during the photocatalytic reactions. This was used for initial

hydrogen measurements before use of the Shimadzu GC was available. Also all GC-MS analysis of gas phase products analysis was carried out the Agilent GC. The setup of the Agilent GC was similar to the Shimadzu however a little more basic. A manual injector was in place which had no fixed volume and there was only one column (HP molsieve Agilent) which the whole sample passed through. For detecting hydrogen a TCD detector was used with Argon carrier gas.

As well as the TCD detector the Agilent GC was also fitted with a mass spectrometer (MS) detector which could be connected to the molsieve column. The primary advantage of an MS detector fitted to a GC is identification of unknown compounds. As the constituents of the sample are separated by the column they reach the MS at different times. The detector can then take a mass spectrum of each compound leaving the column separately. Comparison of these spectra which are characteristic to each compound with a database can then be used for identification of the unknowns. The MS detector in the Agilent GC works by using a filament to generate electrons and bombardment of the sample producing ions and ionic fragments of the initial compound. These ions are then accelerated via an electric field towards the detector. Before reaching the detector the ions pass through a quadrupole which is a device for separating ions with a particular mass to charge ratio (m/e). The quadrupole system consists of four cylindrical stainless steel electrodes arranged symmetrically and set parallel to each other, with the detector at one end and the ions entering from the other. Each opposing rode is connected together electrically and a radio frequency (RF) voltage is applied to each pair with a direct current voltage applied over the top of each pair. Ions traveling down the quadrupole will be deflected by the electric field, with the exception of certain ions with specific m/e ratio. It is then possible to separate the ions based on their m/e and a mass spectrum can be generated. Conditions used with Agilent GC: Injection volume 0.1 mL, carrier gas Argon flow rate 30 mL min⁻¹, Oven temperature 35 °C, inlet temperature 120 °C, TCD temperature 240 °C.

2.5.5 Hydrogen calibration for Shimadzu GC

Quantities of hydrogen produced during a typical photocatalytic reaction were measured by Shimadzu and Agilent GC. For the case of the Shimadzu GC a hydrogen calibration was performed using high purity hydrogen (99.9995%) from a hydrogen generator (Peak PH series). The hydrogen was extracted and diluted with air in a 5 mL gas tight syringe. Table 2 shows the concentrations of hydrogen made up along with the mL of hydrogen injected considering the GC has a fixed 50 μ L injection loop. Each concentration was made 3 times and injected to record the peak area with the average taken for the calibration curve. The

range of hydrogen concentration was chosen so that the expected quantiles of hydrogen produced will fit in the middle of the calibration curve.

Table 2. Concentrations of hydrogen used for calibration and respective peak area's

H₂ ppm	mL H₂ injected	area 1	area 2	area 3	Average
100000	0.005	12884	12148	12260	12431
20000	0.001	2509	2562	2631	2567
10000	0.0005	1501	1517	1399	1461
5000	0.00025	705	693	784	740
1000	0.00005	190	175	188	184
500	0.000025	81	88	92	87
100	0.000005	22	22	20	21

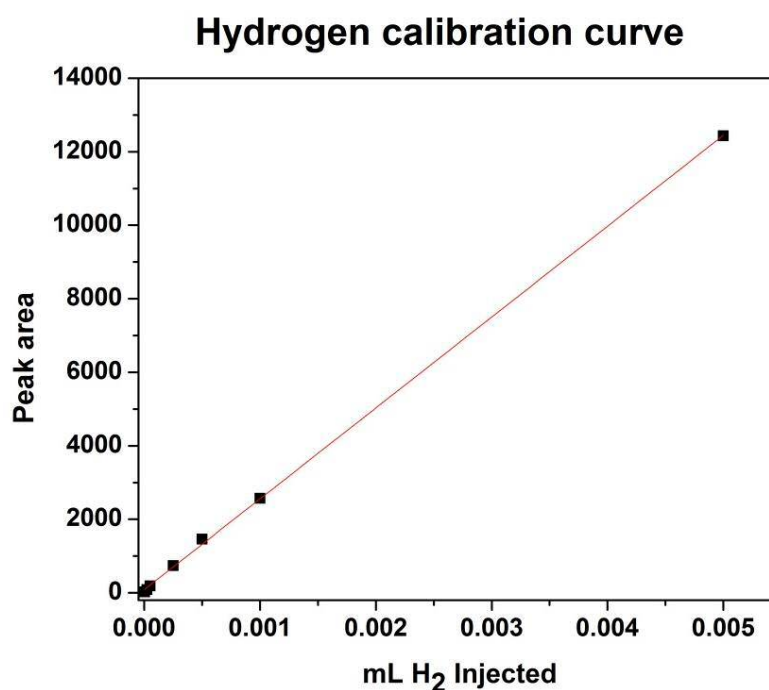


Figure 9. Hydrogen calibration plot for Shimadzu GC, $R^2 = 0.9997$.

Figure 9 shows the plot of hydrogen against peak area for the volumes of inject hydrogen from Table 2. A line of best fit was added which had an R^2 value of 0.9997 demonstrating a consistent linear relationship. The slope of the line was calculated to be 2494597 (peak area per mL H₂) which was then used in calculating the total amount of hydrogen produced during a photocatalytic reaction. The hydrogen calibration was tested against a standard gas containing 4120 ppm of hydrogen (BOC on 06/06/14). After three measurements of the

standard gas (4083, 4096 and 4091 ppm) the average concentration was calculated to be 4090 ppm indicating a good fit with the calibration curve. The calibration was also retested on the 15/04/15 with a second standard gas of 192653 ppm hydrogen (BOC) with the average measurement after two runs (207400 and 206300 ppm) being 206850 indicating that the calibration had not drifted significantly in the duration of using the Shimadzu GC. Calculation of hydrogen produced was done using Equations 8 and 9.

_____ Equation 8

By knowing the volume of the GC sample loop (50 μ L) and the head space volume of the reaction vessel it is possible to calculate the volume of hydrogen produced, Equation 9, all units in mL's.

_____ Equation 9

For liquid phase experiments a 250 mL Pyrex two necked round bottom flask with a 115 mL head space volume when filled with 200 mL of liquid was used.

2.5.6 Hydrogen calibration for Agilent GC

As with Shimadzu GC the Agilent was fitted with a molecular sieve column with a TCD detector. There were no switching valves present and the GC was fitted with a manual injection port so the volume of hydrogen could be directly injected without dilution.

Hydrogen calibration curve

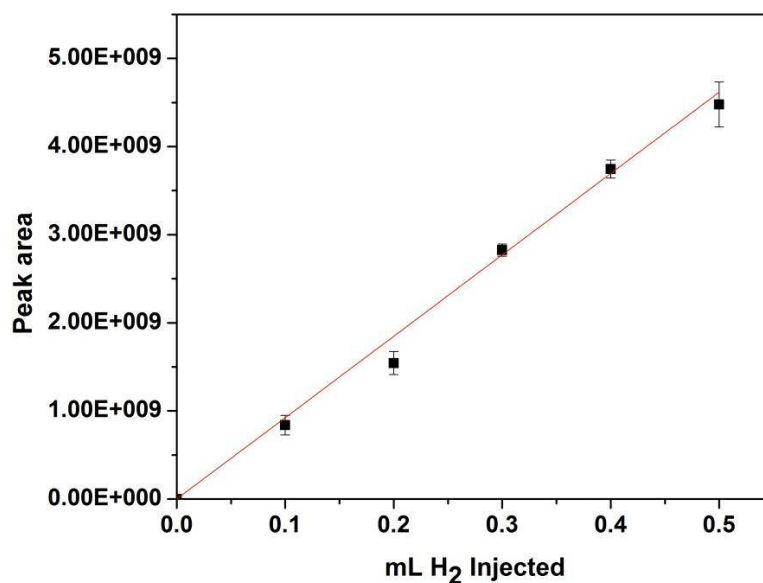


Figure 10. Hydrogen calibration plot for Agilent GC

Figure 10 shows the plot of hydrogen against peak area for the volumes of inject hydrogen six injections were done with the standard deviation displayed on the graph as error bars. A line of best fit was added which had an R^2 value of 0.997 demonstrating a consistent linear relationship. The slope of the line was calculated to be 8953368831 which were then used in calculating the total amount of hydrogen produced with the Agilent GC during a photocatalytic reaction. The total hydrogen produced during a reaction was then calculated by equations 10 and 11.

$$\text{Peak area} = \text{slope} \times \text{mL H}_2 \text{ Injected} \quad \text{Equation 10}$$

10

By knowing the volume injected into the GC machine and the total volume of gas in the reaction vessel it is therefore possible to calculate the volume of hydrogen produced by the equation, all units in mL.

$$\text{Volume of H}_2 = \frac{\text{Peak area}}{\text{slope}} \quad \text{Equation 11}$$

For liquid phase experiments a 250 mL Pyrex two necked round bottom flask with a 115 mL head space volume when filled with 200 mL of liquid was used.

2.6 Transmission electron microscopy (TEM)

2.6.1 Introduction to TEM

Transmission electron microscopy is a useful electron microscopy technique in heterogeneous catalysis for imaging samples on the nanometre scale. Unlike optical microscopy this method does not use photons instead a beam of high energy electrons are utilised. The beam of electrons is accelerated to typically 200 keV and focused using magnetic lenses. These electrons are then transmitted through an ultra-thin specimen and an image is created as the electrons interact with the sample. When studying a supported catalyst TEM analysis operating in bright field mode allows for the measurement of metal NP shape, size, lattice fringes as well as calculation of particle size histograms. The majority of samples in this study were analysed using bright field imaging. The TEM used for catalyst analysis at RCaH is a JEOL: JEM-2100 operating at 200 keV with a LaB6 filament.

Typically a TEM system consists of a column under a vacuum in the region of 1×10^{-5} mbar to allow the electron beam to travel unhindered by air molecules. The filament (or electron gun) is situated at the top and emits an electron beam which is accelerated down the column with energy of typically 200 keV. This beam is then focussed by an electromagnetic lens system consisting of two condenser lenses, see Figure 11. The focused beam passes through a specimen with a required thickness of less than 100 nm or less for high resolution imaging. As the beam passes through the sample some electrons will interact resulting in some being absorbed or scattered. This will happen more in areas that contain heavier atoms or the sample is thicker. After the beam has exits the sample a set of projection lenses spreads the beam on to florescent viewing screen. This allows the user to see a rough image through a lead glass viewing window of electrons hitting the screen and emitting fluorescent photons in the visible range. This image is useful as it is used as an aid during beam focussing, which is done manually. Below the fluorescent screen is a charge couple device (CCD) camera which a device used to convert the electron intensity at a given coordinate into a digital image.

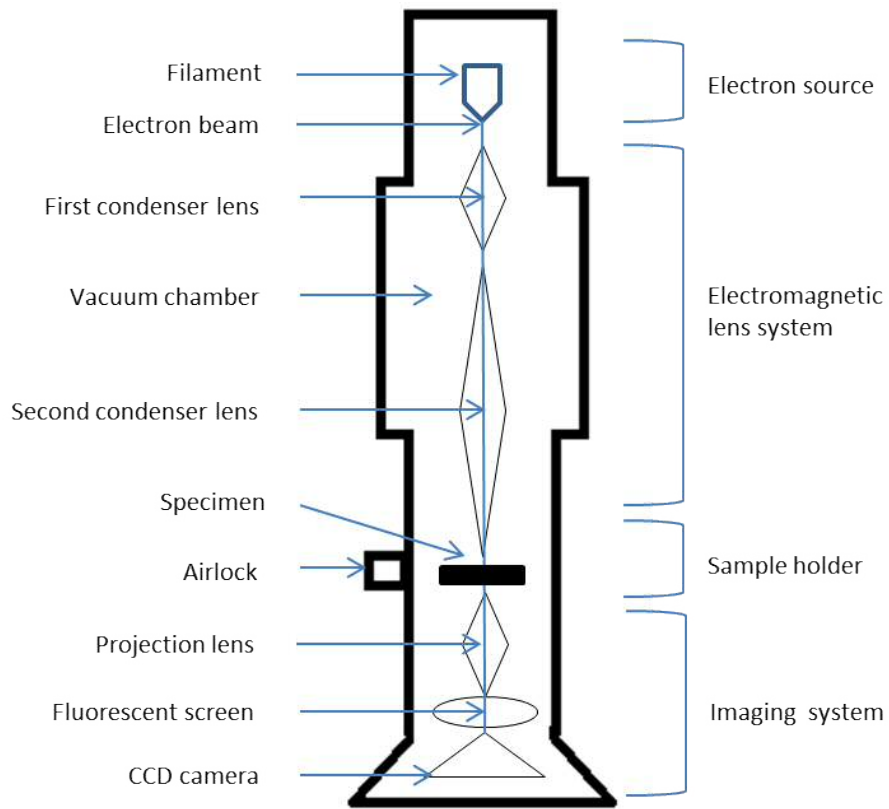


Figure 11. Schematic set up of TEM column operating in bright field mode.

The resolution of light microscopes is limited to roughly half the wavelength of the illumination source used to image the sample. As the visible region of the spectrum spans a photon wavelength of approximately 400-700 nm, therefore it is only possible to resolve objects of 200 nm with light microscopy. However in heterogenous catalysis metal NP can typically be in the range of sub 10 nm. Therefore electron microscopy is used as the wavelength of electrons accelerated to high energies can be far smaller than photons. The De Broglie equation describes how every particle including electrons can propagate like a wave, and can be calculated as follows.

— Equation 12

Where λ is the wavelength of the particle, h is planks constant (6.626×10^{-34} Js) and p is the momentum of the particle (mass x velocity). This equation can be modified for determining the wavelength of an electron by taking into account the velocity of the electron as the accelerating voltage, which yields the following expression.

==== Equation 13

Where m is the mass of an electron (9.1×10^{-31} kg), e is 1.6×10^{-19} J and V is the accelerating voltage. However as the velocities of electrons accelerated to 200 keV reaches in the region 70% the speed of light then relativist effect on the electrons needs to be taken into account, resulting in the equation being modified as follows.

$$\lambda = \frac{h}{m \cdot c \cdot \sqrt{1 - \frac{v^2}{c^2}}}$$

Equation 14

Where c is the speed of light (3×10^8 ms⁻¹). The standard accelerating voltage of a transmission electron microscope is 200 keV. Therefore using this expression yields a wavelength of 2.52 pm for an electron accelerated to 200 keV. However due to limitations of the magnetic lenses resolution of 0.1 nm is attainable.

2.6.2 TEM Sample preparation

Samples for examination by TEM were prepared by dispersing the dry catalyst powder in high purity ethanol, followed by sonication. A drop of this suspension was then evaporated onto a holey carbon film supported by a 300 mesh copper TEM grid.

2.6.3 High Annular Dark-Field TEM analysis

Some samples were sent to Christopher Kiely at Lehigh University for analysis by High Annular Dark-Field (HAADF) analysis. This is a form of scanning dark field imaging when only electrons scattered at high angles and not Bragg scattered electrons are measured. This method is highly sensitive to the atomic number of the scattering atoms (Z number) with heavier elements scattering more electrons. Therefore heavier elements appear as bright regions in an image in contrast to bright field imaging where they are characterised by dark regions.

2.7 Ultra violet – visible spectroscopy (UV-Vis)

Ultra violet – visible spectroscopy is a form of absorption or reflectance spectroscopy typically in the region of 200 – 800 nm. This lies mainly in the visible range of the electromagnetic spectrum therefore the perceived colour of the sample is interrogated. For liquids, photons in this energy range are able to instigate transitions from ground state of electrons to excited states in molecules. Molecules containing π electrons or non-bonding electrons are able to absorb a photon in the UV-Vis region and promote an electron into a

higher anti-bonding orbital. The higher the energy gap between the HOMO (highest occupied molecular orbital) and the LUMO (lowest unoccupied molecular orbital) the lower the photon wavelength need for excitation.

Primarily UV-Vis was used during these studies for investigating the band gap of the semiconductor materials used before and after deposition of metal NPs. UV-Vis was also used during a sol immobilisation preparation to observe the disappearance of the precursor peak (e.g. HAuCl_4) after treatment with NaBH_4 to ensure full reduction. At this stage it was also possible to observe the surface plasmon resonance of Au NPs, which confirms the formation of an Au colloid. The size and shape of the Au plasmon (~520 nm) can also provide information of the average particle size and dispersion of a prepared colloid.

2.8 Thermogravimetric analysis (TGA)

This is a method where the mass loss of a sample as a function temperature can be measured. This can be performed either by increasing the temperature with chosen ramp rate or by holding the sample at a specific temperature and measuring the mass of sample. This technique can be used to observe the decomposition, vaporization, sublimation, adsorption, desorption and dehydration of a sample. A sample is weighed on a platinum pan to a typical accuracy of down to seven decimal places of a gram. This pan is then placed inside an oven hanging by a thin platinum rod whilst still being weighed. The space inside the oven can be air with an atmosphere of choice commonly air or an inert gas. Depending on the temperature program required the oven is heated to the desired temperature typically to maximum of 1000 °C. TGA was used in this project to measure the removal of the organic stabiliser from the surface of a colloidal Au-TiO₂ catalyst which was present as a consequence of the preparation.

2.9 X-Ray absorption spectroscopy (XAS)

2.9.1 Introduction to XAS

XAS is capable for providing detailed information on chemical composition and local structure of materials without any long rang order. In this study XAS has primarily been used to characterise metal NPs in order to gain information on the structure, oxidation state, coordination number and bond length. There are two main regions of XAS spectra, the X-ray Absorption Near Edge Structure (XANES) and the Extended X-ray Absorption Fine Structure (EXAFS). These provide different information and will be discussed in detail.

2.9.2 Synchrotrons

X-Rays are high photons with energy ranging from 500 eV to 500 keV (2.5 nm to 0.0025nm). To perform XAS studies high intensity X-Ray beams are required which are only available at synchrotrons. A synchrotron light sources accelerates electrons in a cyclic ring typically around 500 m in length to relativistic velocities in the order of <90% the speed of light. The energy of these electrons is in the GeV energy ranges, which are used to produce what is known as 'synchrotron radiation'. Photons of required energy can be generated from the accelerated electrons by bending magnets, undulators and/or wigglers. Photons produced in this way typically have a characteristic polarity, and frequencies generated can range over the electromagnetic spectrum, microwaves to X-ray. However most commonly at synchrotrons, the wavelength range of interest is between infrared and X-rays, especially in catalysis.

2.9.3 Theory of XAS

This technique relies on attenuation in the intensity of X-rays as they pass through a material. The loss in the energy of the X-rays as they pass through a material is described by the beer lambert law (Equation 15).¹¹

Equation 15

Where I is the intensity of the X-ray beam after it passes through the sample, I_0 is the initial intensity of the X-rays, μ is the linear absorption coefficient (which is a function X-ray energy E) and x is the path length. This law states that as the energy of X-ray photons increases their absorption by a material will decrease. This is true until the energy of core electrons in the absorbing materials atoms is reached. At this point the core electrons can either be excited to either a higher unfilled energy level in the absorbing atom or ejected altogether as photoelectrons. Photoelectrons which are ejected poses kinetic energy as described below (Equation 16), and this overall process is known as the photoelectric effect.

Equation 16

Where E_k is the kinetic energy of a photo emitted electron, $h\nu$ is the energy of the X-rays and E_b is the binding energy of the electron. Therefore there is a sharp absorption in the spectrum corresponding to the binding energy of all core electron levels in the absorbing atom. The

names of the edges depend on which electron is being excited and originate from the principal quantum number n . Table 3 shows the relationship between the principal quantum number, the corresponding edge/orbital and the spin state j .

Table 3. List of edges with corresponding orbital and spin state j

n	Edge	orbital	j
1	K	1s	
2	L1	2s	
2	L2	2p	1/2
2	L3	2p	3/2
3	M1	3s	
3	M2	3p	1/2
3	M3	3p	3/2
4	M4	3d	3/2
4	M5	3d	5/2

The intensity of the absorption edge is dictated by the X-ray absorption coefficient μ , and is proportional to the probability of absorption of a photon. Fermi's Golden Rule (equation 17) states the probability of an electron being transferred from the initial state to the final state.¹¹

Equation 17

Where ψ_i and ψ_f describe the initial and final state, p is the momentum operator, $A(r)$ is the vector potential of the incident electromagnetic field and ω angular frequency.

The absorption of X-rays as a function of photon energy for a free atom ($\mu(E)$) corresponding to the energy of the core orbital being scanned will result in a sharp edge jump followed by a declining plateau. An example can be seen in Figure 12 which shows the K edge jump for a free Pd atom, also known as the background. This absorption line is smooth and contains no fine structure as the electron is effectively ejected into the continuum. Whereas for an atom bound in a lattice the X-rays absorption is affected by the local coordination to other atoms. Back scattered electrons gives rise to fine structure after the main absorption edge. This is called the EXAFS region and originates from the ψ_i and ψ_f terms in Equation 17. These

oscillations contain valuable information on the local environment of the scattering atom; an example can be seen in Figure 12 of the fine structure following the main jump of a Pd foil K edge.

The region of 50 eV above the main absorption edge is known as the XANES region and can yield information of the oxidation state and bonding geometry. Above 50 eV (up to 1000 eV) is known as the EXAFS region and deals with the interference of back scattered electrons which gives rise to the oscillations after the main absorption edge, see Figure 12. Information which can be obtained from the EXAFS region includes atomic distances, types of neighbouring atoms, coordination number and the presence of long range order.

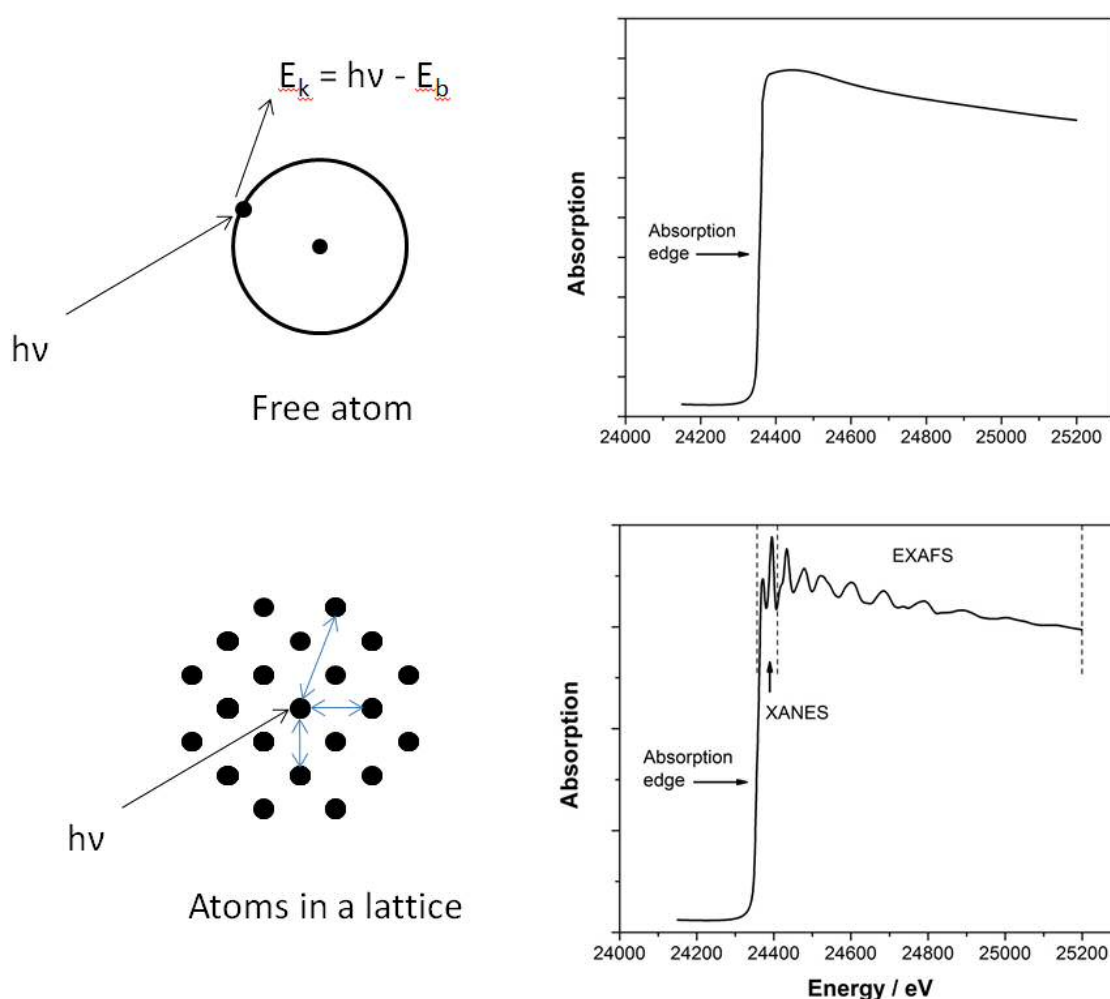


Figure 12. Absorption of X-rays as a function of photon energy $E = h\nu$ for a free atom (top) and an atom in a lattice (bottom). Example shown is of the Pd K edge.

2.9.4 EXAFS

The EXAFS phenomenon has been known about since the 1920's but only gained significant attention in catalysis in the 1970's.¹² This is due to the development of high energy tuneable

X-ray beams at synchrotrons. The oscillations in the EXAFS region are due to the wave like properties of the emitted photoelectrons. Interference from back scattered electrons can be added to yield either constructive or deconstructive interference, see Figure 13. This happens when a wave maxima for the outgoing electron wave interacts with a maxima of a back scattered wave for constructive interference, or a maxima and a minima for destructive interference. This will lead to the absorption cross section being modulated by the interference between the photoelectron waves, resulting in enhancement at energies where constructive interference is occurring. It is therefore this modulation of the absorption cross section which is responsible for the fine structure observed in the EXAFS region. Depending on the wavelength of the photoelectron, the scattering atom and the atomic distance between two scatters, the size and shape of the oscillations will be affected. Typically the intensity of the oscillations is a consequence of the coordination number, with higher coordination giving rise to more intense oscillations. Interatomic distances are inversely proportional to the number of oscillation and the edge step height is proportional to the concentration of the sample.

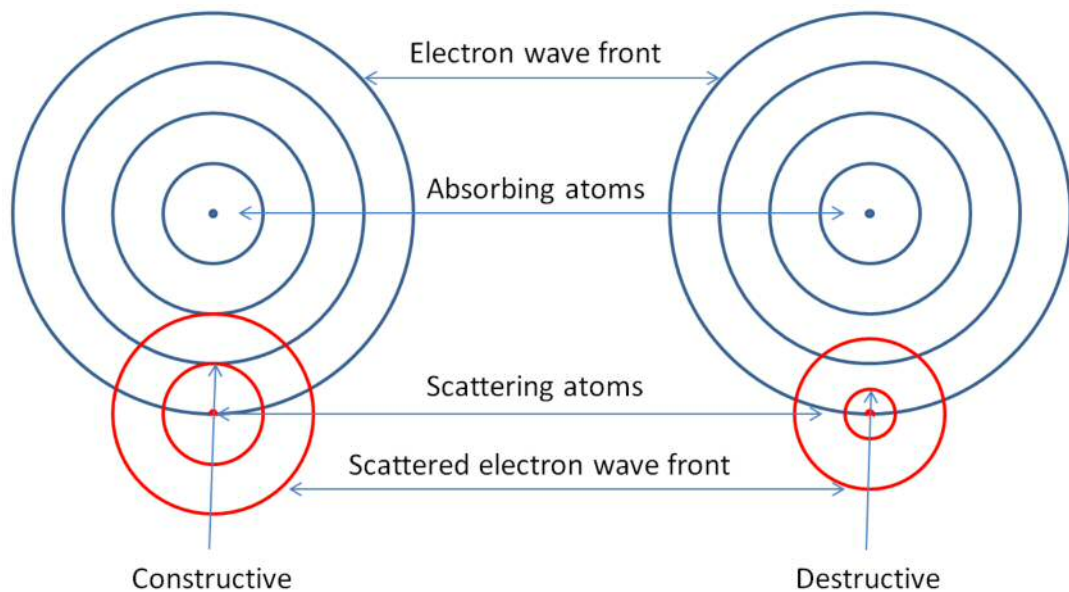


Figure 13. Schematic representation of the interference pattern between outgoing and back scattered electrons.

2.9.5 The EXAFS equation

The emitted photoelectrons have both wave and particle like properties, with the wave function of the outgoing electron propagating spherically described by the wave vector k .

$$\frac{\chi(k)}{k^3} = \sum_j \frac{N_j}{k^3} \frac{f_j(k)}{r_j^2} \sin(kr_j + \phi_j(k))$$

Equation 18

Where m_e is the mass of an electron (9.1×10^{-31} kg), h is planks constant (6.6×10^{-34} m² kg s⁻¹) and E_0 is the energy at the absorption edge. Typically E_0 is taken to be the maxima of the first differential of the absorption edge which is the point of inflection. The EXAFS parameter is called χ and is a function of the wave vector k . In a monoatomic solid $\chi(k)$ is given by Equation 19 and is the sum of all the scattering contribution of neighbouring atoms.

Equation 19

Where $\chi(k)$ is the EXAFS function, j is the label of the coordination shell around the emitting atom, $A_j(k)$ is the amplitude of the scattering intensity due to the j^{th} coordination shell, r_j is the inter atomic distance between the emitting atom and the atoms in the j^{th} shell and $\phi(k)$ is the phase shift. Therefore a sine function multiplied by amplitude contributes to each coordination shell. The argument of each coordination shell depends on several factors k , r , and the phase shift ϕ . The $A_j(k)$ term can be described by Equation 20 and contains valuable information on the coordination environment of the emitting centre. This equation is known as the EXAFS equation and is used to extract several parameters from the spectra.¹¹

$$A_j(k) = \frac{N_j}{k^3} \frac{f_j(k)}{r_j^2} \exp(-2\sigma_j^2 k^2) \exp(-\tau_j)$$

Equation 20

Where N_j is the number of atom of type j at a distance r_j from the emitting atom, S_0 is the aptitude reduction factor, F_j is the backscattering amplitude of the j^{th} atom, σ_j^2 is the Debye Waller factor and arises from the thermal disorder of the emitting atom, τ_j is the relative mean squared disorder and τ_j accounts for the lifetime of the excited states. Of these parameters the coordination number and amplitude are typically the most valuable. For a fcc metal such as Pd we would expect a coordination number of 12 in the first shell and 6 in the second. However if the metal is in the form of NPs the number of nearest neighbours decrease compared to the bulk metal. In these cases the coordination number is often not an integer as the calculated value is an average of all environments of the element of interest in the sample. The first shell contributes to the majority of the scattering with contributions of successive shells become weaker, as can be seen by the $1/r^2$ term. The amplitude reduction factor accounts for process which contributes to the absorption of X-rays which

do not contribute to the EXAFS. This factor typically originates from multiple excitations and can be fixed using a reference for a specific element.

The EXAFS function $\chi(k)$ is extracted from the raw data by a series of processes described below. Analysis was performed using IFEFFIT,¹³ software with the Horae package (Athena and Artemis).¹⁴ An example of raw data obtained from a Pd foil is shown in Figure 14 A. The energy range of each specific edge is set to record at roughly 50 eV before the edge step and 800 eV after. The first step is to remove the approximate parabolic background. This is done by fitting a pre edge and post edge line to the spectrum, these are then used to normalise the intensity of the edge jump to a value of 1 as well as flattening the pre and post edge lines, see Figure 14 B. The energy at the point of inflection of the edge jump or the maximum of the first differential is defined as the E_0 value. At this stage the background or absorption of a free atom is subtracted from the spectra, resulting in the χ plot seen in Figure 14 C. A Fourier transform of the χ plot will result in the radial distribution function, seen in Figure 14 D. Once the data has been processed and normalised in Athena it can be transferred to Artemis and a fit generated for determination of coordination number, R distance, Debye Waller factor and R factor (measure of how close the fit is) for a given sample. The first step in Artemis is to calculate the amplitude reduction factor for a given element by fitting the foil for the appropriate element with a cif file and used as a fixed input parameter. Once this is done the cif file/files containing the scattering path/paths to be fitted needs to be imported. With all the parameters set up the software can generate a fit with the calculated values for coordination number, R distance, Debye Waller factor and R factor. To improve the quality of the fit it is sometimes necessary feed the calculated values back in to the software and refit in an iteration process.

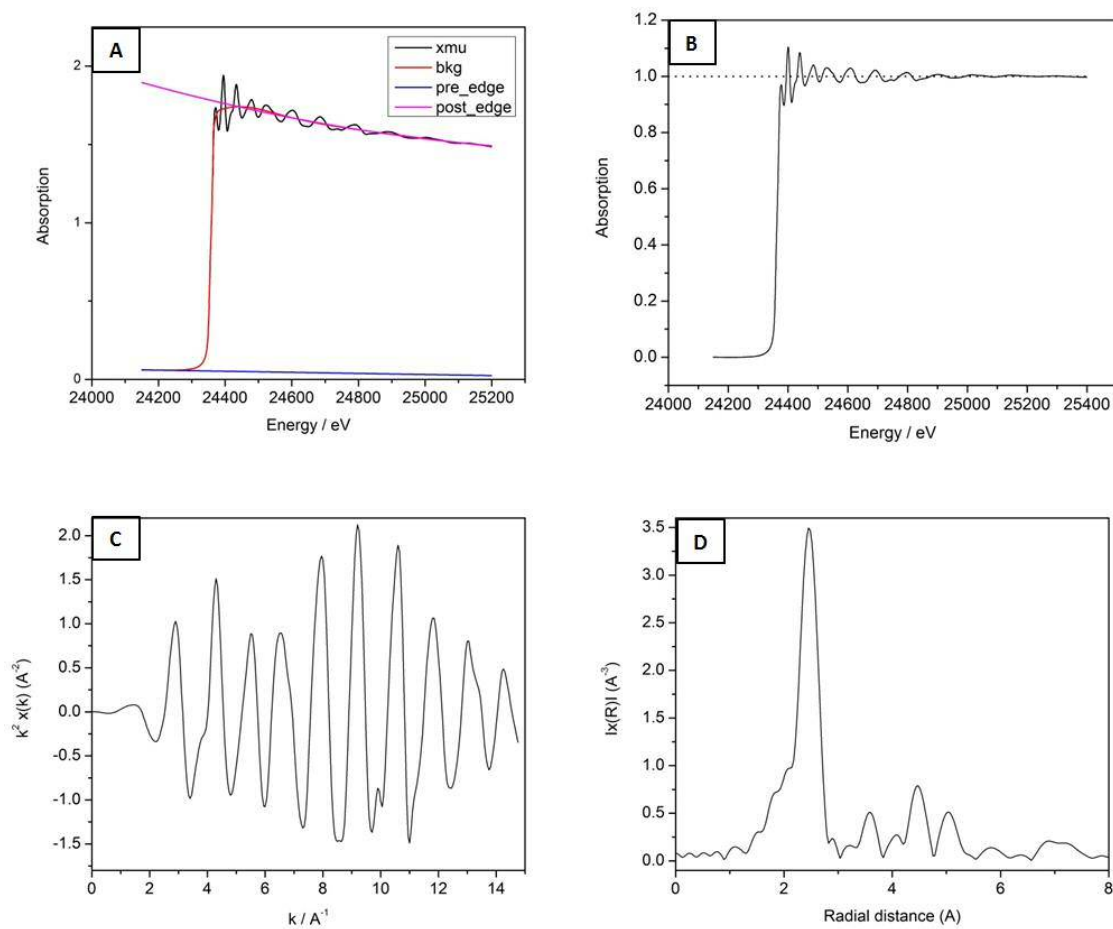


Figure 14 A, raw data of Pd K edge including absorption (xmu), background (bkg), post and pre edge lines, B normalised absorption, C, removal of background (χ) and D, radial distance produced by a Fourier Transform of χ

2.9.6 XANES

As mentioned XANES deals with the region of the XAFS spectra to about 50 eV past the main absorption jump of the edge of interest. This is a powerful technique for measuring the oxidation state, local environment and geometry of the element being studied. Unlike surface techniques such as XPS, XANES provides a per atom average, therefore probing all environments – both surface and bulk – equally and providing an average signal.

The XANES region largely originates from electronic transitions from the core levels of the element being studied to higher levels either unfilled or partially filled. The dipole selection rules for transitions determination is: $\Delta l = \pm 1$, $\Delta j = \pm 1$, $\Delta s = 0$ with examples being $s \rightarrow p$ and $p \rightarrow d$ ($K \rightarrow L$ and $L \rightarrow M$). The interpretation of XANES data can be quite complex due to effects such as multiple-scattering resonances of the photoelectrons ejected at low kinetic energy and distortions of the excited state adding to the overall absorption. In certain XANES spectra there is an intense initial peak after the absorption edge. This peak historically called a 'white

line' as it was first detected in early experiments on photographic plates which showed up as a white line due to the strong absorption. Primarily XANES was used for determination of oxidation state by comparison with standards. XANES analysis was also performed to quantify difference in the Au L₂ and L₃ white lines to calculate fractional d band vacancies of Au alloys (AuAg). A more detailed description of the method used will be discussed in chapter 4.

2.9.7 XAFS experimental set up and experimental modes

There are two common modes to measure XAFS spectra, transmission and fluorescence, a schematic of the experimental set up is shown in Figure 15. Both modes will yield absorption spectra, but a choice of which is most appropriate depends on the sample being studied.

2.9.8 Transmission mode

This is the most common and straightforward mode which involves measuring the X-ray flux before and after the beam passes through the sample, see Figure 15. The ion chambers measure I_0 (initial intensity), I_t (intensity after passing through the sample) and I_f (intensity after passing through the foil). Each ion chamber is filled with a mixture of inert gasses; depending on the X-ray flux the gas composition will be set accordingly. Inside the chambers there are two metal plates with a potential applied between them. A current is then generated when X-rays ionise the gas molecules which are then attracted to the plates. Therefore the size of the current is proportional to the number of X-ray photons entering the ion chamber. The absorption of the X-rays by the sample can be given by the equation.

—

Equation 21

Measuring I_t and I_f allows for the calculation of the absorption spectra over the reference foil. This is useful as it can act as an internal calibration as it is measured at the same time as the sample. Data recorded months apart or on different beamlines could have a small shift in the energy values. Therefore this internal calibration can be used to align spectra where small shifts in energy are important.

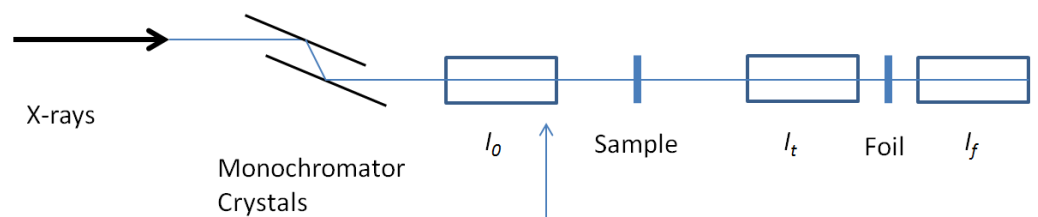
To conduct experiments in transmission mode the concentration of the element of interest and the total absorption at the working energy of the whole sample needs to be considered. If the concentration of the target element is too dilute not enough X-rays will be absorbed and there will be a poor signal to noise ratio. On the other hand if the sample is too concentrated then it is possible that there will be too much X-ray absorption for clean data,

Equation 22 can be used to calculate the required mass of sample to use during sample preparation to achieve a suitable absorption.

Equation 22

Where, μ_x is the absorption edge, a is the area of the pellet and μ/ρ is the mass absorption coefficient. The values of the mass absorption coefficient are calculated at the energy of the absorption edge being studied. When calculating the suitability of a sample's concentration ideally a value of $0.1 \rightarrow 1$ would be achieved for the absorption edge of the target element. The total absorption of the sample at the energy of interest must also be considered and the combined absorption should not exceed 2.5. Transmission mode is considered the best way of acquiring XAFS data, if the sample permits. This is primarily due to relatively high quality of data (signal to noise ratio) as well as the speeds at which the spectra can be recorded.

Transmission set up



Fluorescence set up

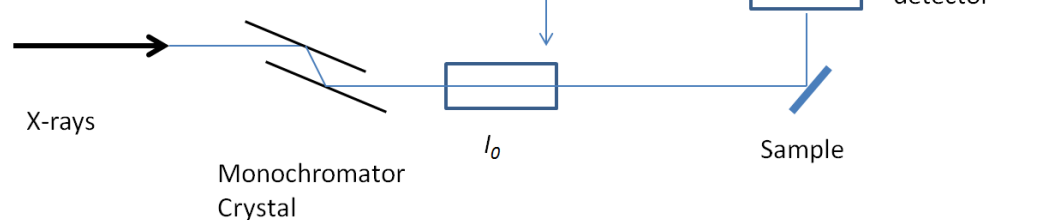


Figure 15. Schematic of XAFS experimental modes transmission and fluorescence, where I_0 , I_t and I_f are the initial intensity, intensity after passing through the sample and intensity after passing through the foil respectively.

2.9.9 Fluorescence mode

If the sample is not able to be run in transmission due to an unsuitable concentration or a high absorption matrix then fluorescence mode can be used. During a fluorescence measurement, the sample is placed at 90° to the solid states fluorescence detector, see

Figure 15. As the sample is irradiated with X-rays a fluorescence signal is produced by the removal of a core electron followed by an electron from a higher orbital filling the hole and emitting a photon, e.g. $K\alpha$ radiation. As the fluorescence signal is produced at the same time as the absorption cross section is being modulated by constructive and destructive interference of the outgoing photoelectron waves. Therefore it is possible to record the XAFS spectrum from the intensity of the fluorescence signal. The fluorescence EXAFS signal is proportional to the total absorption by Equation 23, and consists of only a small fraction of the total Absorption.

Equation 23

Advantages of measuring in fluorescence mode are that it is suitable for most samples, can be run for a sample with low concentration of the target element and as a specific fluorescence energy is measured it is possible to measure a XAFS spectrum of a sample with a large absorption matrix. However there are several draw-backs to fluorescence including poor data quality (signal to noise ratio) especially at high k values and often measurements can be time consuming which can be a problem when synchrotron time is limited.

2.9.10 X-ray generation in the synchrotron

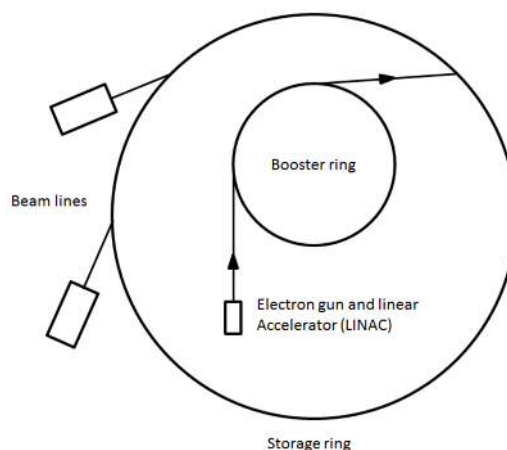


Figure 16. Schematic of electron beam generation, storage and generation of X-rays at Diamond light source

The electrons are generated by a high voltage cathode heated under vacuum resulting in the electrons having sufficient energy to escape from the surface (thermionic emission). These electrons are then accelerated towards an anode producing a stream of high energy electrons. A linear accelerator (linac) is then used to accelerate the electrons before injection

into the booster ring. Once in the booster ring the electrons are further accelerated and injected into the storage ring. At this stage the electrons have been given enough energy to reach relativistic speeds. Diamond light source produces an electron beam with 3 GeV of energy. Sampling stations situated around the ring can then generate the synchrotron radiation by two methods an insertion device or a bending magnet.

2.9.11 XAFS acquisition

Ag K-edge, Pd K-edge and Au L₃-edge XAFS spectra were measured using a QEXAFS setup on the B18 beamline at the Diamond Light Source. For spectra recorded in transmission mode using ion chambers a typical run consisted of an acquisition time of 5 min with $k_{\text{max}}=14$. For spectra ran in florescence mode a 9 element solid-state Ge detector was used, with typical run consisted of an acquisition time of 40 min with $k_{\text{max}}=14$. The normalized X-ray absorption near edge structure (XANES) spectra and X-ray Absorption Fine Structure (EXAFS) analysis were carried out using IFEFFIT,¹³ with the Horae package (Athena and Artemis).¹⁴ The amplitude reduction factor () stem from EXAFS data analysis of required foil, and was used as a fixed input parameter. The EXAFS data was fitted over the $1 < R < 3.5 \text{ \AA}$ range.

2.9.12 EXAFS particle size

Conversion of EXAFS coordination numbers into a particle size can be achieved by the approach of Beale *et al.*¹⁵ the work focused on simulating the average first shell CN versus the number of atoms for the first shell for the possible packing types available in the NPs.¹⁶ Assumptions need to be made that the particles are spherical face centred cubic and are below $\sim 3 \text{ nm}$. Figure 17 shows a plot of coordination number versus particle radius, and will be discussed in more detail in section 3.2.3.^{15, 17}

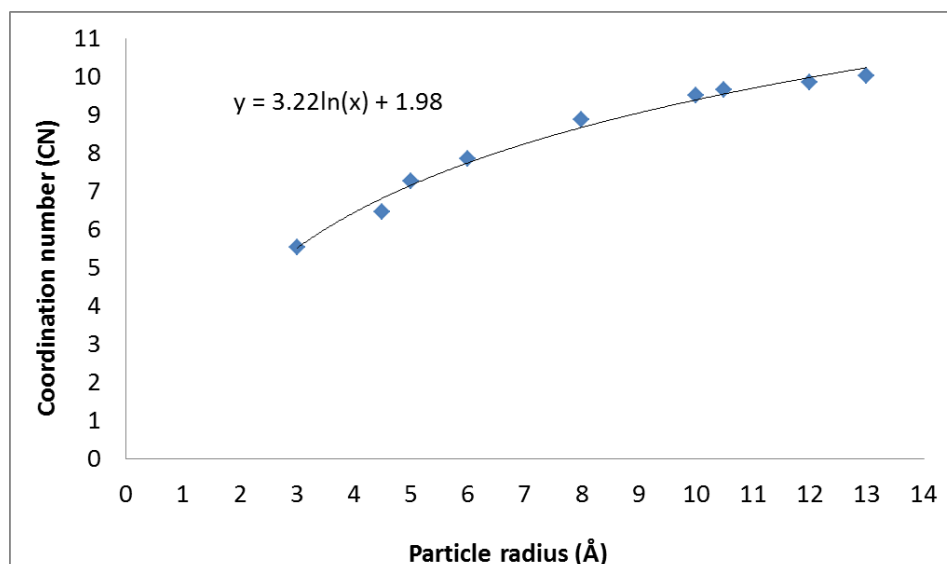


Figure 17. Plot of coordination number versus particle radius (Å).

2.10 X-ray diffraction (XRD)

X-ray Powder Diffraction (XRD) is an extremely useful technique for structural analysis of crystalline solids. Information which can be gained from this technique includes phase identification, composition of phases, unit cell information, crystallite size and morphology. During XRD analysis an X-ray beam is focused at the sample, the electron density surrounding the atomic nuclei in the sample will scatter the X-rays. Stacked crystal planes in the solid sample will reflect the X-rays similar to a mirror. When the incident angle of the X-rays gives rise to a path length difference between successive planes which is equal to an integer number of wavelengths, then constructive interference will result in maxima. This condition can be expressed mathematically as Bragg's law:

$$n\lambda = 2d_{hkl} \sin(\theta) \quad \text{Equation 24}$$

Where n is an integer, λ is the wavelength of the incident X-rays, d_{hkl} is the inter-planar distance (hkl) and θ is the angle of the X-rays. A schematic of Bragg scattering can be seen in Figure 18.¹¹

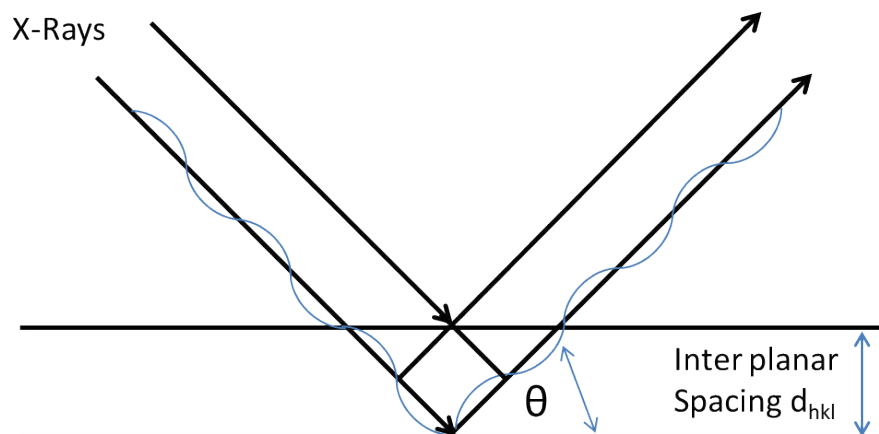


Figure 18. Schematic representation of diffracted beams in crystal lattice

For powder XRD the sample is placed on a flat holder with the X-ray source and detector designed to be movable. The range of 2θ angles desired (typical $10-80^\circ$) can be scanned across and intensity of the scattered X-rays can then be measured. As the powder consists of small particles randomly orientated, all diffraction angles will be represented. The X-ray beam striking the powder sample will be diffracted at all the Bragg angles giving rise to cones of diffracted X-rays. A 2D slice of the cone will give rise to the typical diffraction pattern of intensity versus 2θ . For diffraction experiments a monochromatic source of X-rays should be used, with wavelength similar to the inter-planar spacing. Typically $K\alpha$ radiation is used, which is emitted by an atom as a result of an electron transition from $L \rightarrow K$ after generation of a core hole by electron bombardment. A common X-ray source to use is $Cu\ K\alpha_1$ ($2P_{3/2} \rightarrow 1S$ transition) radiation, which in conjunction with appropriate filters produces monochromatic radiation at wavelength of $1.5405\ \text{\AA}$. Therefore by measuring the 2θ angle and by choosing the wavelength, the lattice spacing d can be calculated by the Bragg equation. Each crystalline solid will exhibit its own unique diffraction pattern which is similar to a fingerprint for that material. Around 80000 crystalline compounds have been databased, so with clean data a diffraction pattern can be checked for phase identification.

2.11 X-ray photoelectron spectroscopy (XPS)

XPS is a commonly used technique in heterogeneous catalysis for the study of the chemical composition of surfaces. The main principle of this method is based on the photoelectric effect and allows for the measurement of binding energies of specific atomic orbitals of interest. It is therefore possible to determine the oxidation state and local electronic environment of the target element by comparison with standards. By irradiating a sample with photons of a chosen wavelength higher in energy of that of the binding energy of

electrons in the atomic orbital being studied photoelectrons can be emitted, a schematic is shown in Figure 19. The kinetic energy of the emitted photons is given by Equation 25, and is characteristic of elements present and electronic state of the elements.¹⁸

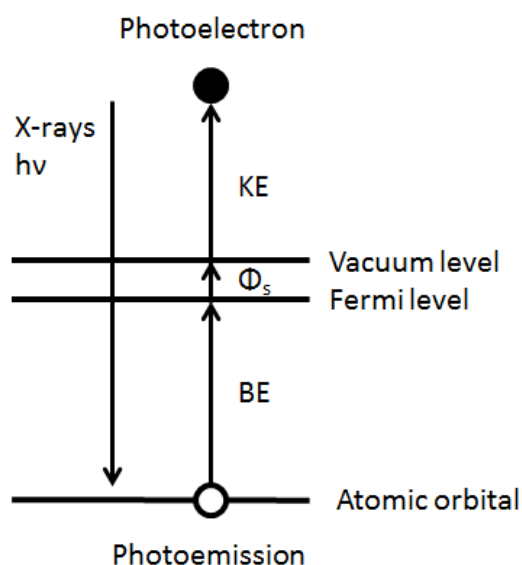


Figure 19. Schematic of photoemission by absorption of a photon

Equation 25

Where KE is the kinetic energy of the emitted photoelectron, $h\nu$ is the energy of the incident photon, BE is the binding energy of the atomic orbital from which the photoelectron is ejected and Φ_s is the spectrometer work function and can be calibrated for each instrument. The X-rays sources commonly used for XPS analysis are Mg Ka (1253.6 eV, 0.989 nm) and Al Ka (1486.3 eV, 0.834 nm). A typical XPS spectrum is of the measured intensity of the photoelectrons as a function binding energy, as calculated by Equation 25. Peaks appearing in the XPS spectra correspond to the binding energy of shell from which the electron was ejected (1s, 2s, 2p, etc.). A shift in the peak position provides information on the electronic environment. Shifts in binding energies can arise from shielding effects of the nucleus from the electrons. If a metal is in a positive oxidation state (e.g. Pd^{2+}) then the nucleus will have a greater attraction to the electrons compared to the zero-valent metal (e.g. Pd^0). This will result in a higher binding energy and the potential to distinguish between two oxidation states of a metal of interest. In some cases the difference in binding energy is too small for accurate discrimination between oxidation states; however it is possible in most cases. Often the peaks overlap when it happens a Gaussian can be fitted for each contribution and calculation of composition is possible.

XPS is classed as a surface technique; the X-rays typically penetrate in the order of 1 μm below the surface of the sample. The photoelectrons generated have a very small inelastic mean free pathway which results in only those produced in the near surface region able to escape and be detected. The sample needs to be scanned in a high vacuum chamber with the emitted electrons being detected by an electron spectrometer.

The XPS machine used was a Kratos Ultra-DLD system at Cardiff University, with monochromatic Al K α source, analysed by casa software.

2.12 References

1. N. Dimitratos, A. Villa, C. L. Bianchi, L. Prati and M. Makkee, *Appl. Catal. A-Gen.*, 2006, 311, 185-192.
2. W. C. Ketchie, M. Murayama and R. J. Davis, *J. Catal.*, 2007, 250, 264-273.
3. R. Zanella, L. Delannoy and C. Louis, *Applied Catalysis A: General*, 2005, 291, 62-72.
4. J. L. Hueso, V. Sebastian, A. Mayoral, L. Uson, M. Arruebo and J. Santamaria, *RSC Advances*, 2013, 3, 10427-10433.
5. J.-D. Grunwaldt, C. Kiener, C. Wögerbauer and A. Baiker, *Journal of Catalysis*, 1999, 181, 223-232.
6. G. Ramakrishna, A. K. Singh, D. K. Palit and H. N. Ghosh, *The Journal of Physical Chemistry B*, 2004, 108, 4775-4783.
7. D. J. Martin, K. P. Qiu, S. A. Shevlin, A. D. Handoko, X. W. Chen, Z. X. Guo and J. W. Tang, *Angew. Chem.-Int. Edit.*, 2014, 53, 9240-9245.
8. A. Dickinson, D. James, N. Perkins, T. Cassidy and M. Bowker, *J. Mol. Catal. A-Chem.*, 1999, 146, 211-221.
9. lot-oriel.com.
10. R. Su, R. Tiruvalam, A. J. Logsdail, Q. He, C. A. Downing, M. T. Jensen, N. Dimitratos, L. Kesavan, P. P. Wells, R. Bechstein, H. H. Jensen, S. Wendt, C. R. A. Catlow, C. J. Kiely, G. J. Hutchings and F. Besenbacher, *ACS Nano*, 2014, 8, 3490-3497.
11. J. W. Niemantsverdriet, in *Spectroscopy in Catalysis*, Wiley-VCH Verlag GmbH & Co. KGaA, 2007, DOI: 10.1002/9783527611348.ch6, pp. 147-177.
12. F. W. Lytle, *J. Synchrot. Radiat.*, 1999, 6, 123-134.
13. M. Newville, *J. Synchrot. Radiat.*, 2001, 8, 322-324.
14. B. Ravel and M. Newville, *J. Synchrot. Radiat.*, 2005, 12, 537-541.
15. A. M. Beale and B. M. Weckhuysen, *Physical Chemistry Chemical Physics*, 2010, 12, 5562-5574.
16. W. Szczerba, H. Riesemeier and A. F. Thünemann, *Analytical and Bioanalytical Chemistry*, 2010, 398, 1967-1972.
17. S. M. Rogers, C. R. A. Catlow, C. E. Chan-Thaw, D. Gianolio, E. K. Gibson, A. L. Gould, N. Jian, A. J. Logsdail, R. E. Palmer, L. Prati, N. Dimitratos, A. Villa and P. P. Wells, *ACS Catal.*, 2015, 5, 4377-4384.
18. J. W. Niemantsverdriet, in *Spectroscopy in Catalysis*, Wiley-VCH Verlag GmbH & Co. KGaA, 2007, DOI: 10.1002/9783527611348.ch3, pp. 39-83.

Chapter 3: Sol immobilisation catalysts for photocatalytic hydrogen production

Table of contents

3.1	Introduction	68
3.2	Synthesis of Au nano-particles.....	69
3.2.1	Sol immobilisation synthesis of Au-TiO ₂	69
3.2.2	TEM analysis.....	71
3.2.3	EXAFS particle size vs TEM particle size of 1%Au-TiO ₂	73
3.2.4	Variation of sol immobilisation synthesis parameters.....	76
3.2.5	Other methods for synthesis of Au-TiO ₂	78
3.2.6	Development of photoreactor	79
3.3	Optimisation of parameters for photocatalytic methanol reforming	80
3.3.1	Varying mass of catalyst.....	80
3.3.2	Varying amount of methanol.....	81
3.3.3	Effect of calcination temperature on particle size and photocatalytic performance	82
3.3.4	Effect of metal loading of Au NPs on TiO ₂ for photocatalytic H ₂ evolution... ..	87
3.4	Photocatalytic H ₂ production from Pd-TiO ₂ with long band-pass filters	94
3.5	Synthesis of Ag-TiO ₂ and Pd-TiO ₂ by sol immobilisation.....	95
3.6	Cerium doped TiO ₂ loaded with Pd.....	98
3.7	Conclusions	104
3.8	References	105

3.1 Introduction

The process of photocatalysis converts light energy, whether it is solar radiation or photons from an artificial source into chemical energy. This process requires a material that allows for the absorption of a photon to generate a transient state that will decay to make a new chemical species. Typical photocatalysts consist of light absorbing semiconductors comprising of metal oxides. One of the properties a semiconductor must possess to be considered as a viable photocatalyst is stability and durability under irradiation.¹ The most commonly used semiconductor for photocatalysis being TiO₂ for this very reason, with other potential candidates such as sulphide and chalcogenides failing in this regard owing to photocorrosion. Despite TiO₂ being a robust semiconductor under irradiation, it has some drawbacks as a photocatalyst in that its band gap (3.2 eV or ~380 nm) which is the energy difference between the conduction band and the valence band lies in the UV region. As ~4% of solar radiation reaching the earth's surface is in the UV this leads to TiO₂ being a poor photocatalyst with regards to sunlight but excellent photocatalyst in the UV region. In this chapter P25 TiO₂ was used primarily as it is an industrial standard and experiments are performed with a xenon arc lamp which produces the required UV radiation and simulates the spectral output of the sun. For a TiO₂ photocatalyst it is typical to add a co-catalyst in the form of nanoparticles (NPs) deposited on the surface to improve reaction rates. Precious metals such as Pt, Pd, Au, and Ag are often used, as they can trap the photogenerated electron increasing the lifetime of the e⁻/h⁺ pair as well as providing a site for the reaction to occur.²⁻⁵ Perhaps the most commonly used precious metal co-catalysts for photocatalytic reactions is Pt and Pd as they produce amongst the most active catalysts.⁶

The type of H₂ production performed in this chapter is primarily photocatalytic methanol reforming, in which the overall reaction can be written as, CH₃OH + H₂O → 3H₂ + CO₂. By this method one mole of H₂ is from water splitting and two moles come from the decomposition of methanol to CO₂.⁷ Other simple alcohols such as ethanol and glycerol will also produce H₂ by photocatalytic reforming reactions; however methanol was primarily used in this chapter as a model chemical.⁷ However despite Au being a less active co-catalyst than Pt and Pd at a constant weight loading, when considered on per atom basis activities are comparable.⁸ In this chapter the co-catalyst primarily used was Au NPs deposited on the surface of TiO₂ by the sol immobilisation method. The effect of varying parameters during synthesis and calcination was investigated to observe changes in Au NP size. Optimising the conditions for improved photocatalytic H₂ yield were also investigated by varying calcination temperature, Au loading on TiO₂, volume of methanol used and mass of catalyst used. As well as using the

sol immobilisation method for synthesising Pd and Ag supported catalysts. Also investigated was wavelength dependent photocatalytic reactions and cerium doping of TiO₂. Later chapters will expand on the ground work in this chapter and use the sol immobilisation method and modifications of this technique to produce NP supported catalysts with NPs other than Au, bimetallic NPs and core-shell NPs.

3.2 Synthesis of Au nano-particles

3.2.1 Sol immobilisation synthesis of Au-TiO₂

Sol immobilisation is a relatively new method for synthesising and depositing Au NP onto a support.⁹⁻¹¹ Details of the synthesis method can be found in section 2.2.1. Figure 1 shows some images from a typical preparation of a 1wt%Au-TiO₂ catalyst by the sol immobilisation method, while Figure 2 shows UV/Vis analysis of the solution at various stages. Figure 1 A, presents an image of a solution containing PVA and HAuCl₄ which is colourless to the eye. However Figure 2 shows the presence a precursor peaks at ~ 210 and 290 nm which can be attributed to ligand to metal charge transfer in the AuCl₄⁻ species.¹² Reduction of the HAuCl₄ in PVA solution with NaBH₄ results in the formation of the red colloid seen in Figure 1 B, which comprises of Au NPs in the order of ~ 3 nm which can be seen in Figure 1 C, which is a TEM image of the colloid (dropped onto a TEM grid for imaging) where Au NPs can be seen as dark spheres. It is widely reported the role of the PVA in the reduction step is to prevent the Au NPs growing large and agglomerating by binding on the surface producing a protecting layer.^{13, 14} The red colour of the Au colloid is cause by the surface plasmon resonance of Au NPs of this size and can be seen in Figure 2 as the absorption centred on ~ 510 nm.¹⁵ Once the Au colloid has been synthesised TiO₂ can be added and the solution acidified to around pH 1 (bellow the isoelectric point of TiO₂ ~ pH 6.5), this will have the effect of immobilising the Au NPs on the surface of the support. This can be seen in Figure 1 A and B, which is an image of the Au-TiO₂ in solution and a TEM image of the catalyst. Finally Figure 1 F, is of the filtered and dried (120 °C) catalyst with a blue/purple colour. The red colour of the colloid is lost when the colloid is immobilised (blue/purple colour) due to interaction with the TiO₂ support.

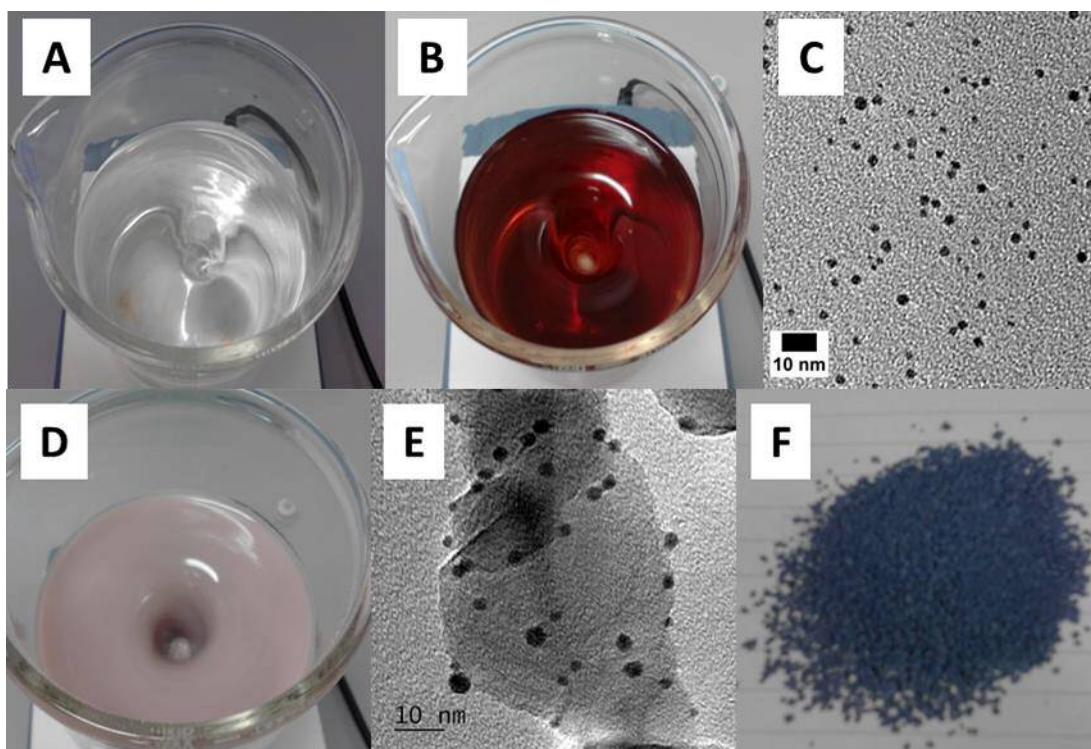


Figure 1. A, HAuCl_4 and PVA solution, B, PVA protected Au colloid after NaBH_4 reduction, C, TEM image of the colloid, D, solution containing newly formed Au-TiO₂, E, TEM image showing Au NPs immobilised on TiO₂ and F, the dried state of the 1%Au-TiO₂ catalyst

During the preparation procedure, the UV/Vis analysis can be a useful check for full reduction of the HAuCl_4 , the formation of the Au plasmon peak and the absence of either the precursor or Au plasmon peaks in the filtrate. Therefore, by carefully checking the UV/Vis analysis it can be assumed that the entire amount of Au precursor is reduced and full immobilisation is obtained resulting in the required weight loading of Au being achieved, which can be seen in Figure 2. The position and broadness of the Au SPR can also be used as a rough guide to the size of the NPs in solution. When the peak is centred at ~ 520 nm and relatively sharp it is often reported that the Au NPs are below 10 nm in size. Whereas if the peak is broadened and red shifted up to 600 nm this is consistent with larger particles potentially 100 nm in diameter.¹⁶ Although the Au SPR in Figure 2 does not have a sharp feature this is thought to be due to the concentration of the Au and the effect of the media.

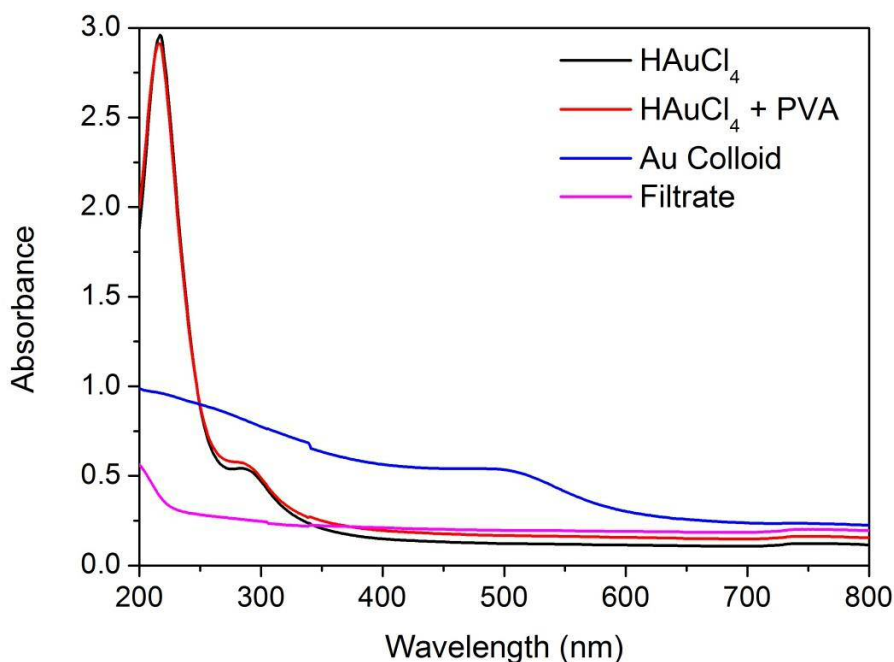


Figure 2. UV/Vis analysis of various stages of the solution during sol immobilisation preparation of 1%Au-TiO₂, including HAuCl₄, HAuCl₄ and PVA, Au colloid after reduction and filtrate.

3.2.2 TEM analysis

One of the attractive properties of the sol immobilisation method is the generation of Au NPs of the size of ~3 nm which can be easily deposited onto a support. A useful method for characterising the synthesised NPs is bright field TEM analysis. As bright field TEM analysis works by Z number dependent image contrasting the Au NPs (Z=79) are seen as distinct dark particles in images compare to the support, in this case TiO₂ (Ti, Z=22 and O, Z=8). This can be seen in Figure 3 which presents high and low resolution TEM images of 1%Au-TiO₂ catalyst dried and calcined made by the sol immobilisation technique. The images in Figure 3 A and C, show the Moire fringes of TiO₂ which is equivalent to the lattice spacing in the crystal.¹⁷ The high resolution images show of mainly spherical but with some faceted Au NPs for the dried catalyst, it is evident that after heating the Au NPs change shape to hemispherical and form an extended flat surface to the TiO₂. This will result in an increased number of particle/support sites and perhaps the development of a strong metal support interaction.¹⁴ Moreover from the image in Figure 3 C, it can be seen that the lattice lines in TiO₂ and the Au NP appear to line up, this may be coincidence or could represent a beneficial alignment of the Au NP on the surface. Also there is some evidence of encapsulation of the Au NP by the support when comparing the dried and calcined high resolution images.

As well as observing the shape of the NP, location on the support and any lattice fringes present, TEM analysis will also allow for the measurement of the diameter of the NP. This can be very useful for characterisation of a catalyst where the particle size is a key factor.¹⁸ During this project the particle size for various catalysts was determined by TEM analysis. In all case this was achieved with the use of 'imageJ' software, which allowed the NPs to be measured and counted.¹⁹ Once the NP's diameter is determined a particle size histogram can be created which displays the number and size of particles of each size, as well as allow for the generation of an average particle size and standard deviation. Figure 4 shows particle size histograms for a 1%Au-TiO₂ catalyst synthesised by the sol immobilisation method.

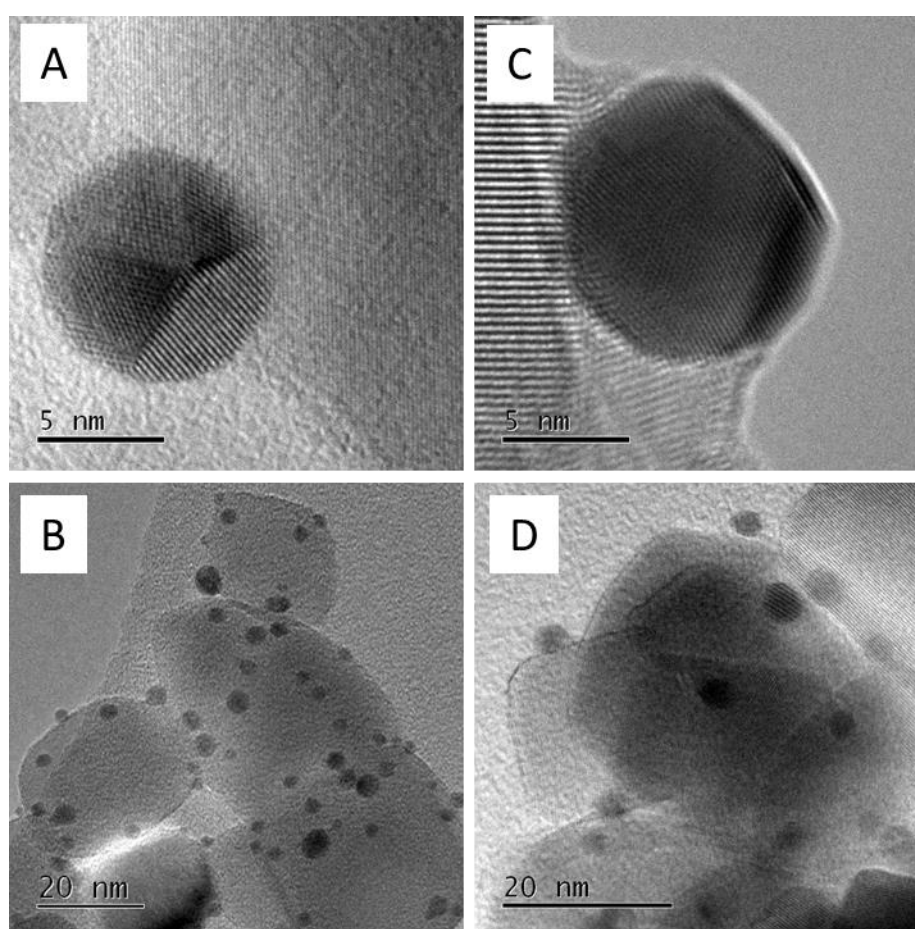


Figure 3. TEM images of A and B, high and low resolution 1%Au-TiO₂ dried at 120 °C, B and D high and low resolution 1%Au-TiO₂ dried at 400 °C.

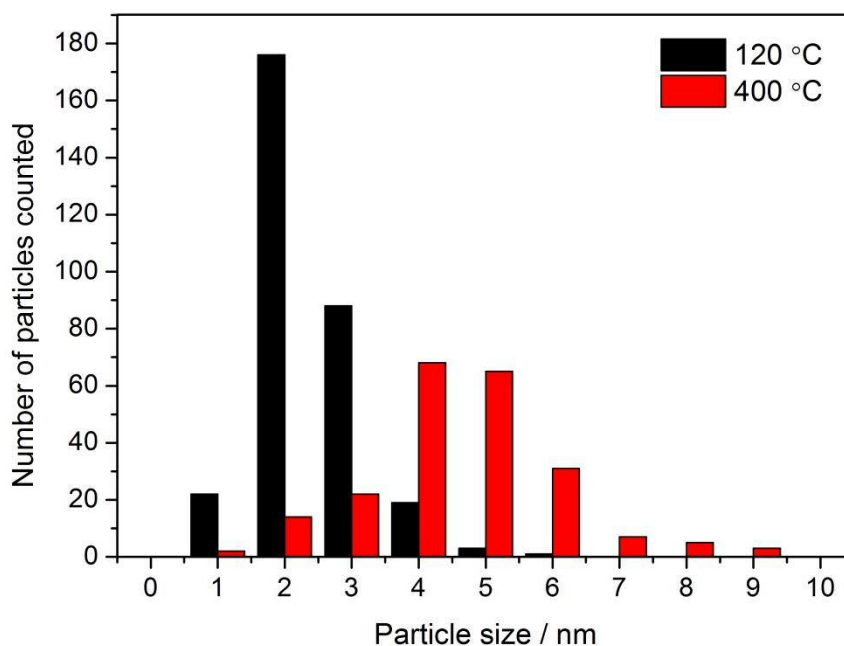


Figure 4. Particle size histogram of 1%Au-TiO₂ dried 120 °C and calcined at 400 °C.

Table 1. Summary of the average particle size and standard deviation of a 1%Au-TiO₂ catalyst dried at 120 °C and calcined at 400 °C. The Au NPs were measured and counted using ImageJ software.

1%Au-TiO ₂ catalyst heat treatment	Average particle size / nm	Standard deviation	Number of particles counted
120 °C	2.9	0.7	309
400 °C	5.1	2.1	215

3.2.3 EXAFS particle size vs TEM particle size of 1%Au-TiO₂

A relatively new alternative method for determining particle size other than TEM analysis is from calculations based on EXAFS coordination numbers (CN). Conversion of CN's of NPs to particle size can be achieved by applying the approach of Beale *et al.*²⁰ The work focused on simulating the average first shell CN versus the number of atoms for the first shell for the possible packing types available in the NPs.²¹ Detailed theory of EXAFS and how data was collected and manipulated into CN's can be found in section 2.9. For bulk gold the average CN for first shell of a gold atom will be 12, for Nano sized Au the average CN will be lower due to the high surface to volume ratio.²² A decrease in Au-Au CN from the bulk value of 12 will have the effect of dampening the EXAFS oscillations. This is due to the ejected photoelectron from the absorbing atom having less scattering neighbouring atoms, with EXAFS probing all environments in the sample and giving an average signal. Taking this into

account it is possible to calculate the average CN with use of Athena and Artemis software packages,²³ for the sol immobilisation synthesised 1%Au-TiO₂. Figure 5 presents the Au L₃ edge EXAFS of the k² weighted experimental data and Fourier transform for the Au foil and 1%Au-TiO₂ catalyst. Performing a Fourier transform on the k² weighted experimental data will result in the radial distance plot seen in Figure 5. From this plot it is possible to gain information on the distance of the neighbouring scattering atoms and calculate the CN. The dampening of EXAFS the oscillations of the 1%Au-TiO₂ samples are evident compared to the Au foil as with the decrease in the intensity of the Fourier transform peak. Figure 3 shows images of the Au NPs of the 1%Au-TiO₂ (dried) which are determined to have a particle size of ~2.9 nm, therefore it would be expected not to act as bulk Au and the dampening of the signal confirms this. Table 2 summarises the first shell EXAFS fitting parameters derived from the k² weighted Fourier transform for the Au L₃ edge of Au-TiO₂, with the values for the Au foil taken from the cif file where appropriate. The calculated CN for the 1%Au-TiO₂ catalyst has a value of 10 (± 1) which as expected is a decrease on the value of 12 for the Au foil. Also calculated is the distance between the first shell Au atoms (R) where a contraction of the bond length is overserved from the bulk Au value of 0.04 Å, in agreement with reports in the literature.²¹

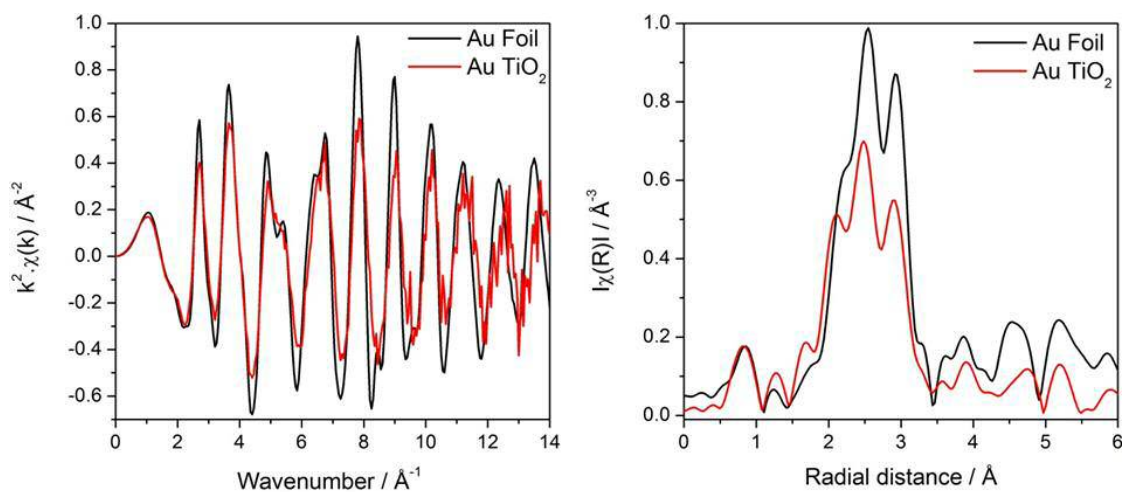


Figure 5. Au L₃ edge EXAFS for Au foil and 1%Au-TiO₂, left, k² weighted experimental data and right, the k² weighted Fourier transform.

Table 2. 1st shell EXAFS fitting parameters derived from the k^2 weighted Fourier transform for the Au L_3 edge of Au-TiO₂. * Values for the Au foil taken from the cif file.

Sample	Edge	Abs Sc	N	R / Å	$2\sigma^2 / \text{Å}^2$	E_f / eV	R _{factor}
Au Foil*	Au L_3	-	12	2.88	-	-	-
1%Au-TiO ₂	Au L_3	Au – Au	10 (1)	2.84 (2)	0.009 (1)	4(1)	0.02

The EXAFS Au particle size was determined by the equations of Beale *et al.* where the number of particles in an Au NP was modelled to generate a particle size, with the assumption that the NPs are spherical, face centred cubic and are below ~ 3 nm.^{20, 24} A plot of CN number versus NP radius can then be generated (section 2.9.12) and a logarithmic line of best fit used to generate,

Equation 1. Table 3 presents the Au particle size as determined by TEM and by EXAFS analysis for a 1%Au-TiO₂ sol immobilisation catalyst. The errors for the EXAFS particle size was calculated by using the limits of CN from Table 2 (CN = 9 and 11) with the errors for the TEM particle size from the standard deviation. Both methods for calculating the particle size give a comparable result with the EXAFS having the smaller average size. As EXAFS will probe all Au environments in the sample and give an average result this method also takes into account small clusters of Au which may be difficult to see in TEM images. Therefore this may be a factor as to why the average particle size is small by the EXAFS method, which was also seen by Rogers *et al.*²⁴ However the two particle sizes here are within the calculated error of each other here. Despite being a potentially new accurate method for determining Au particle size the EXAFS method is unlikely to become the preferred technique. This is mainly due to the synchrotron access and the increased amount for time to generate a particle size. Whereas a particle size can be generated in an afternoon with access to a TEM, an EXAFS particle size will only be available when there is access to the beam line.

Table 3. Determined Au particle size by TEM and EXAFS of a standard 1%Au-TiO₂ sol immobilisation catalyst dried at 120 °C.

Catalyst	TEM particle size / nm	EXAFS particle size / nm
1%Au-TiO ₂	2.9 ± 0.7	2.4 ± 0.8

Equation 1.

3.2.4 Variation of sol immobilisation synthesis parameters

During the synthesis of the 1%Au-TiO₂ by sol immobilisation there are several parameters in the method which may affect the size of the NPs synthesised. To investigate whether varying these parameters has a significant outcome on the particle size several preparations was conducted. The typical procedure for the sol immobilisation is outlined in section 2.2.1 and was in this thesis unless otherwise stated. The main parameters used for the standard synthesis is HAuCl₄ concentration of 1.26×10^{-4} mol, PVA/metal weight ratio of 0.65, NaBH₄/Au molar ratio of 5 and temperature of the solution of 25 °C. These are established values and have been reported in various publications.^{9, 25, 26}

The temperature of the solution of Au precursor and PVA before and during reduction to form the NPs may affect the particle size by altering reduction rate, nucleation of the NP and the effectiveness of PVA as a stabilising agent. Table 4 summarises the TEM particle sizes obtained when performing the sol immobilisation synthesis at elevated temperatures. Synthesis performed at 25 °C (room temperature) and 60 °C did not show a significant change in Au particle size 2.9 and 3.2 nm, with the average size of each being well within the standard deviation of the other. Although when this method was performed at 80 °C the average particle size was increased markedly to 5.8 nm with a larger value of standard deviation. This trend of increasing particle size with synthesis temperature has been reported previously by Rogers *et. al.* and is likely due to increased rate of nucleation as well the temperature hindering the ability of PVA as an affective stabilising agent.²⁴ It is clear then temperature is not a significant factor effecting particle size for this procedure as all preparations were performed at room temperature in this thesis.

Table 4. Summary of TEM Au particle size for 1%Au-TiO₂ catalysts made by the sol immobilisation method at 25, 60 and 80 °C.

Temperature of solution during synthesis	Average particle size / nm	Standard deviation	Number of particles counted
25 °C	2.9	0.7	309
60 °C	3.2	1.2	346
80 °C	5.8	2.4	362

Increasing the HAuCl₄ concentration of the initial solution before reduction with NaBH₄ was also investigated as a parameter which could affect particle size. For the typical sol immobilisation procedure the concentration of Au precursor used was 1.26×10^{-4} mol.L⁻¹

which was kept constant, therefore changing in the weight loading of the Au on a fixed mass of TiO₂ required different volumes of solution. Table 5 presents the average particle size of Au NPs on TiO₂ by the sol immobilisation method with X2 and X4 the concentration of HAuCl₄ from the standard 1.26 x 10⁻⁴ mol.L⁻¹. It was expected that an increase in the concentration of the Au precursor would lead to larger particles, however this was not observed here, at least in this concentration range. Instead there was perhaps a small decrease in particle size for the x2 and x4 Au concentration syntheses, although again this was still within the standard deviation of each other. This leads to the conclusion that the initial concentration of the Au before reduction does not have a significant effect on the Au particle size and will produce ~3 nm NPs comfortably within the concentrations investigated.

Table 5. Summary of TEM Au particle size for 1%Au-TiO₂ catalysts made by the sol immobilisation method with various initial concentrations of HAuCl₄.

Concentration of HAuCl₄ during synthesis	Average particle size / nm	Standard deviation	Number of particles counted
1.26 x 10⁻⁴ mol.L⁻¹	2.9	0.7	309
2.52 x 10⁻⁴ mol.L⁻¹	2.3	0.6	345
5.04 x 10⁻⁴ mol.L⁻¹	2.3	0.7	333

A further parameter investigated was the PVA/Au ratio which is thought to be critical for stabilising the Au NPs and has a commonly used value of 0.65.^{9, 25, 26} Here only one further synthesis was undertaken with a lower ratio of 0.2, as residue PVA left on the catalyst can be a problem (see section 3.3.3) higher ratios were not investigated. Table 6 presents the average particle size of Au NPs on TiO₂ with a PVA/Au ratio of 0.65 and 0.2. Despite lowering the PVA/HAuCl₄ ratio by roughly a factor of 3 the Au particle size remained identical.

Table 6. Summary of TEM Au particle size for 1%Au-TiO₂ catalysts, made by the sol immobilisation method with different initial PVA/ HAuCl₄ ratios.

Ratio of PVA/Au	Average particle size / nm	Standard deviation	Number of particles counted
0.65	2.9	0.7	309
0.2	2.7	0.9	281

Taking into account the Au average particle size when varying the synthesis temperature, PVA/Au weight ratio and concentration of HAuCl₄, it is clear that the sol immobilisation method will produce Au NPs in the region of ~ 3 nm over a range of parameters. This indicates that this method is a reproducible and robust way of synthesising Au NPs in the region of ~

3 nm. The molar ratio of NaBH_4/Au was not investigated here and was kept at a constant value of 5. However as this value is already five times the molar excess to Au and full reduction was achieved after 30 min with this value, it may be expected that the particle size may not be affected significantly if it was increased. A recently published paper by Dimitratos *et al.* explored the effect of varying these parameters (initial Au concentration and PVA/Au weight ratio) thoroughly and broadly agree with the results presented here, in that there is a range of values which will produce ~ 3 nm Au NPs.¹³

3.2.5 Other methods for synthesis of Au-TiO₂

The primary synthesis method to produce supported metal NPs (Au, Ag, Pd or bimetallic NPs) in this thesis has been the sol immobilisation method. Other methods to produce Au-TiO₂ were also investigated, such as deposition precipitation urea (DP urea),²⁷ tetrakis-(hydroxymethyl)phosphonium chloride in an alkaline solution (THPC/NaOH),^{11, 28, 29} and photodeposition (PD).³⁰ Details of the synthesis methods can be found in section 2.3.

Table 7 summarises the Au particle size of a 1%Au-TiO₂ catalyst made by these other methods for dried and calcined samples. As can be seen of the method employed here sol immobilisation achieved on average the smallest Au particle size ~ 3 nm for the dried sample. More traditional methods such as DP urea and THPC/NaOH produced Au NP in the order of $\sim 5/6$ nm whereas the PD method resulted in Au NPs of ~ 27 nm for the dried samples. In all cases calcination at 400 °C lead to an increase of the average particle size through sintering. As the sol immobilisation method produced the smallest sized NPs and could achieve near full deposition of the metal sol onto the support, which isn't the case for some methods (PD and DP), it was decided that this would be the primary method for catalyst synthesis in this thesis.

Table 7. Summary of the TEM average particle size for 1%Au-TiO₂ made by Sol immobilisation, DP urea, THPC/NaOH and PD both dried and calcined. Standard deviation given as the error.

Synthesis method for 1%Au-TiO ₂	Average particle size / nm dried	Average particle size / nm calcined	Particles counted dried and calcined
Sol immobilisation	2.9 ± 0.7	5.6 ± 1.4	309 and 234
DP urea	5.3 ± 0.9	6.3 ± 1.5	253 and 182
THPC/NaOH	6.6 ± 2.1	6.9 ± 2.3	217 and 221
PD	19 ± 12	27 ± 15	49 and 51

3.2.6 Development of photoreactor

From the outset there was no photoreactor in place in Research Complex at Harwell (RCaH) due to the building being recently completed. Therefore a reactor system was set up based on the reactor in place at Cardiff University which was similar to what has been reported by A. Dickinson *et al.*³¹ Section 2.4 details the set up developed in RCaH with Figure 6 showing an image of the completed photoreactor. Two GC's were used to measure the evolved H₂ in Harwell made by Shimatzu and Aglient, details can be found in section 2.5. The Agilent CG was used to measure H₂ for reaction in sections 3.3.1 and 3.3.2 with other experiments using the Shimatzu unless otherwise stated.

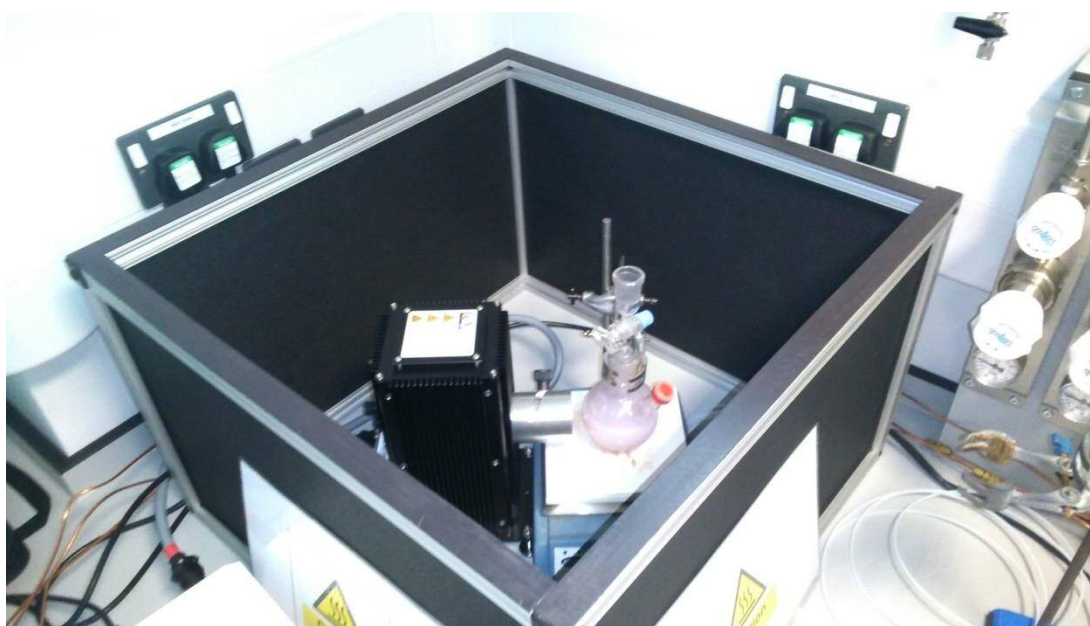


Figure 6. Image of the Photoreactor set up in Harwell including the xenon arc lamp, round bottom flask reactor and black out box.

Primarily reactions were run in a batch method, where head space gas samples were taken periodically for analysis by GC to determine H₂ concentration. However the reactor was also set up for a continuous flow operation. In this set up a fix flow of inter gas was purged into the reactor during irradiation, with the out let flowing to the GC for analysis. This method had advantages of quick sampling times of 5 mins per analysis. However due to some difficulties in reproducibility this set up was used sparingly and the batch procedure preferred.

3.3 Optimisation of parameters for photocatalytic methanol reforming

3.3.1 Varying mass of catalyst

To investigate the effect of the mass used of the 1%Au-TiO₂ catalyst for H₂ evolution from photocatalytic methanol reforming a set of reaction was performed with different masses. All other parameters were kept constant e.g. volume of methanol used (100 μL), volume of water (100 mL), same batch of catalyst and identical reaction set up, section 2.4. Figure 7, left, shows the H₂ evolution plots for photocatalytic methanol reforming for various masses of 1%Au-TiO₂, and right, rate of H₂ evolution as a function of mass of catalyst. All H₂ evolution plots in Figure 7 show a near linear dependence of concentration with time. The lack of an induction period likely originates from the Au being in its metallic form and not needing to be reduced during the initial stage of the reaction.³² Between the masses used of 1 to 50 mg of 1%Au-TiO₂ there is a general trend observed of increasing rate with additional catalyst added. Above 50 mg addition of further amount of catalyst has no observable effect on the quantity of H₂ evolved from the reaction. The lack of further increase in the rate of the reaction is thought to be a consequence of the energy input for the reaction, light, being used to a maximum. At the level of 50 mg catalyst for 200 mL of water and above it is assumed increasing the concentration of the catalyst in solution will not lead to absorption of more light and hence the rate does not improve.

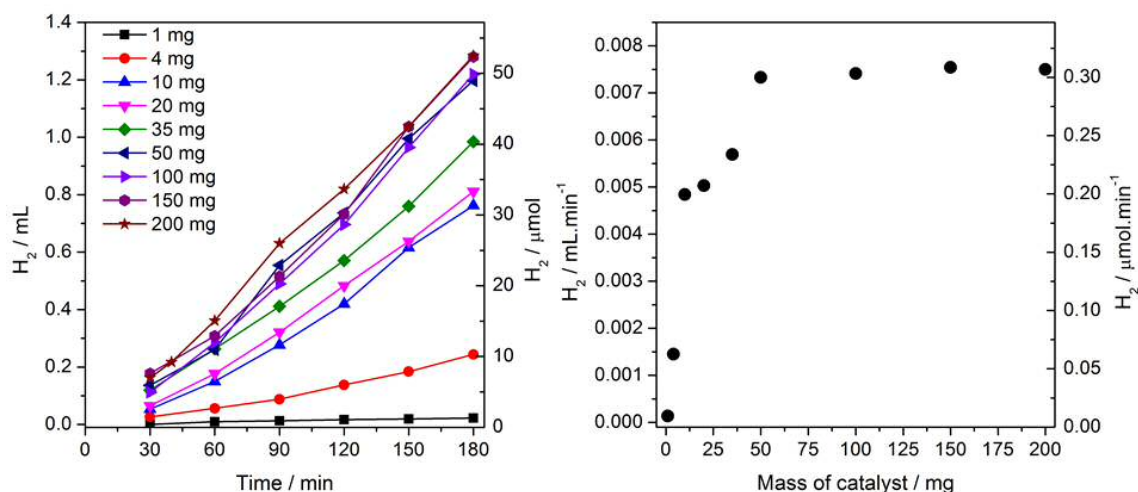


Figure 7. Left, time dependent H₂ evolution plots for photocatalytic methanol reforming (constant volume of 100 μL) for various masses of 1%Au-TiO₂, and right, rate of H₂ evolution as a function of mass of catalyst.

3.3.2 Varying amount of methanol

To investigate the effect of volume of methanol used on photocatalytic H₂ evolution set reactions were performed with various amount of methanol. All other parameters were kept constant e.g. mass of catalyst (100 mg), volume of water (200 mL), same batch of catalyst and identical reaction set up, section 2.4. Figure 8, left shows the H₂ evolution plots for photocatalytic H₂ production for various volumes of methanol, and right rate of H₂ evolution as a function of methanol concentration. Under low methanol conditions 10-100 μL the rate of H₂ evolution is strongly dependent on the concentration of methanol, indicating a first order dependence. Upon increasing the methanol content further 100 μL to 10 mL a second region of linear increase of rate with methanol concentration is observed. When considering a 0.5%Pd-TiO₂ catalyst it has been reported that the effect of methanol concentration follows a similar trend with a linear dependence to rate at low methanol content.^{6, 31} However for higher levels of methanol for the 0.5%Pd-TiO₂ catalyst the rate resembles zero order, in that addition of further methanol (100 μL in 200 mL water) does not increase the H₂ production rate significantly. For the Au-TiO₂ catalysts here the second region of linear dependence (100 μL to 10 mL) of methanol volume to rate does not follow a zero order reaction, but is of lower order.

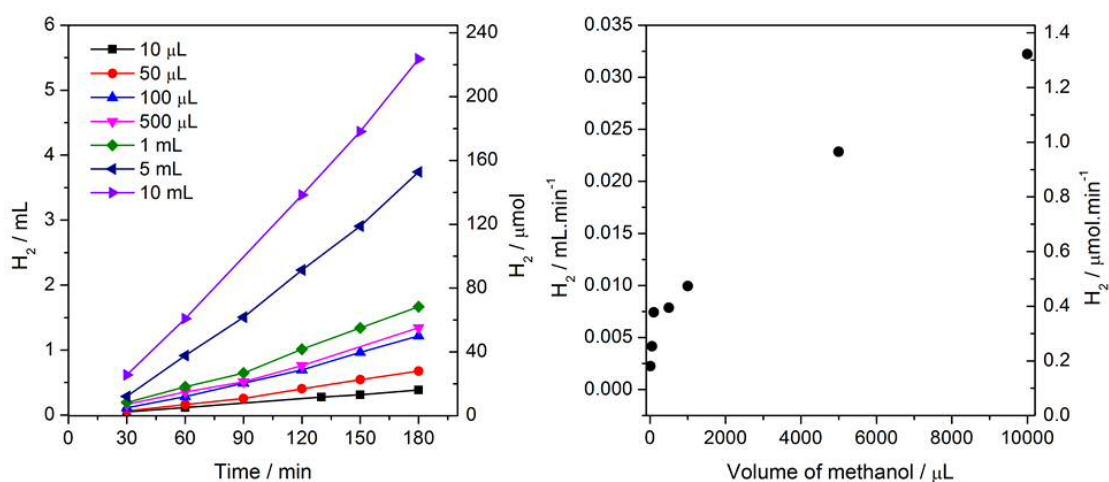


Figure 8. Left, time dependent H₂ evolution plots from various volumes of methanol with a 1%Au-TiO₂ catalyst (constant mass of 100 mg), and right, rate of H₂ evolution as a function of volume of methanol.

Considering the tests for varying the mass of catalyst and the volume of methanol it was decided that a standard activity test for synthesised catalysts would be to use 150 mg of catalyst and 100 μL of methanol. This was to ensure that the maximum amount of light is being used as well as to prevent too much H₂ being produced which may lead to the rubber septum of the photo reactor being forced out.

3.3.3 Effect of calcination temperature on particle size and photocatalytic performance

The effect of calcination in air on a 1%Au-TiO₂ sol immobilisation catalyst was investigated by heat treated a sample of the catalyst at 120 °C, 200 °C, 300 °C and 400 °C, with the procedure in section 2.2.3. After calcination the Au particle size were characterised by TEM and XPS analysis with the photocatalytic performance also investigated.

Figure 9 shows the XPS wide survey scans of all samples, with high resolution spectra of Au 4f (7/2), Ti 2p (5/2) and O 1s. The survey scans suggest all samples are mainly TiO₂ with surface adventitious carbon and minor amounts Au. As expected the oxidation state of Au was unaffected by the heat treatment remaining in its metallic form with a value of ~ 83.4 eV for Au NP's, which is in agreement with reports in the literature.²⁶ It is worth noting the binding energy of Au 4f(7/2) is shifted slightly to lower energy compared to bulk Au (84.0 eV), this can be attributed to TiO₂ negatively charging the small (~3 nm) Au NPs.^{33, 34} Also the

positions of the Ti 2p and O 1s peaks, and hence the oxidation states of Ti and O are unaffected by the heat treatment.

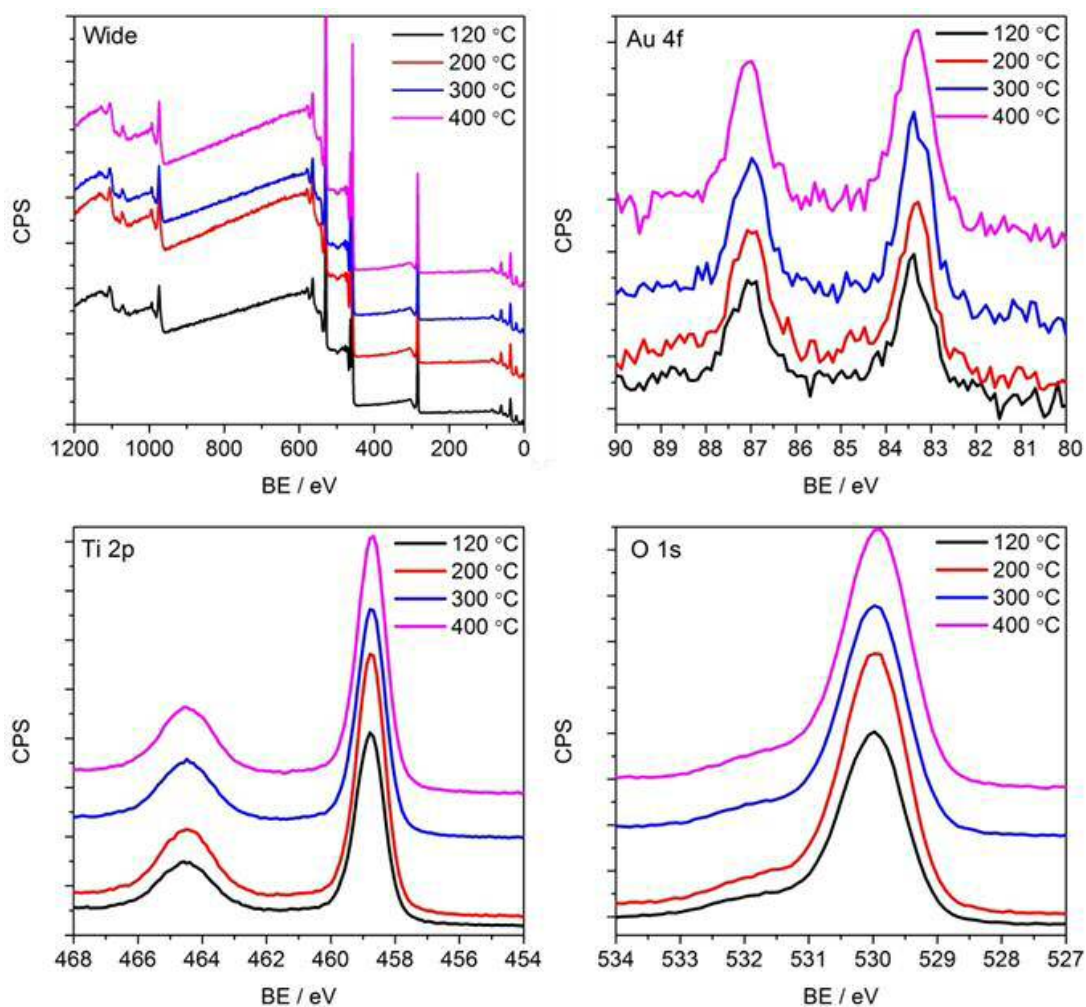


Figure 9. XPS analysis of the 1%Au-TiO₂ sol immobilisation catalyst heat treated at 120 °C, 200 °C, 300 °C and 400 °C. Including wide survey scans of all samples, with high resolution spectra of Au 4f, Ti 2p and O 1s.

During preparation by the sol immobilisation method PVA can remain on the surface of the catalyst. This residual organic layer can have the effect of hindering the possibility of adsorption of a methanol molecule on the surface of the Au NPs. By calcination of the samples the organic layer can be removed cleaning the surface and resulting in a more active catalyst.³⁵ To understand the temperature promoted removal of the protecting ligand better thermo gravimetric analysis (TGA) was performed of the PVA and the 1%Au-TiO₂. Figure 10 shows the percentage mass loss as a function of temperature for of PVA and 1%Au-TiO₂ with starting mass for both of 50 mg in static air conditions. Up to 120 °C there is a drop in mass for both the red line (PVA) and the green line (1%Au-TiO₂), this is likely due to the removal of physisorbed water from the samples. In the region of 150-400 °C there is a decrease in

mass from the 1%Au-TiO₂ which then plateaus to 600 °C, this is likely due to the removal of PVA.³⁵ Whereas the PVA decomposes in the region of 250-450 °C, the difference of the two regions could be due to the PVA being spread over the surface of the 1%Au-TiO₂. From this result it is evident that calcination over 400 °C is not required to remove PVA and could lead to further sintering. Calcination over 700 °C would not be desirable as anatase in the P25 will undergo a phase change to rutile.³⁶

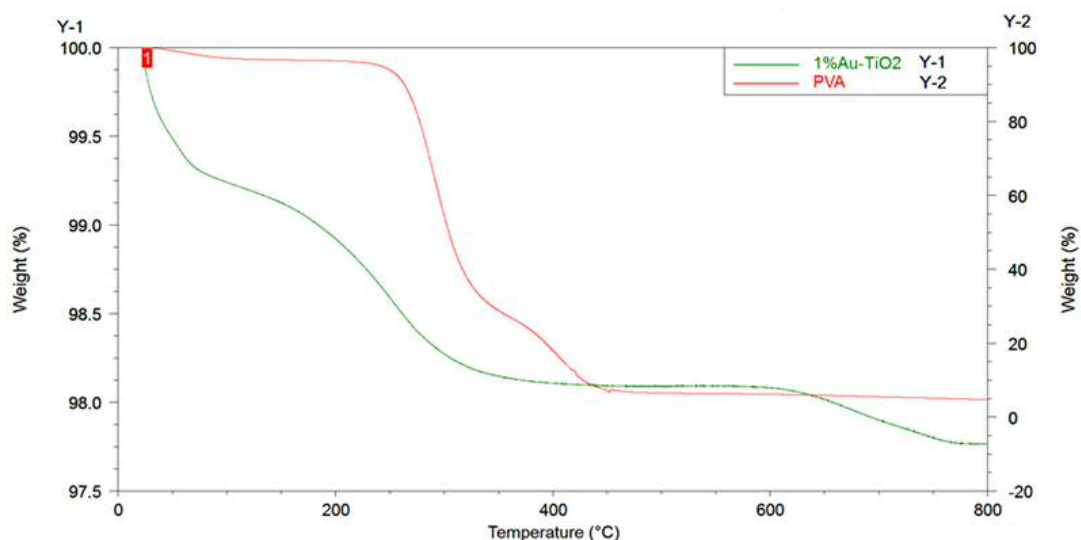


Figure 10. Thermo gravimetric analysis (TGA) analysis of PVA and 1%Au-TiO₂ (starting mass for both of 50mg) in air with a heating rate of 2 °C.min⁻¹ and final temperature of 800 °C

TEM analysis of the four heat treated samples of the 1%Au-TiO₂ catalyst was performed to observe any sintering of the Au NPs during the calcination. Figure 11 shows representative TEM images of the four samples while Table 8 summarises the particle sizes and Figure 12 containing the generated histograms for the Au NPs in each sample. It was clear that in all samples imaged the Au NPs were deposited evenly over the surface with the lack of any significant agglomeration. By this analysis it is clear to see that the Au NPs have sintered and grown in size with increasing calcination temperature, with the exception of the 200 and 300 °C samples which showed comparable particle size. However the particle size has not increased drastically between the dried and calcined (400 °C) ~ 3 nm to 5 nm average.

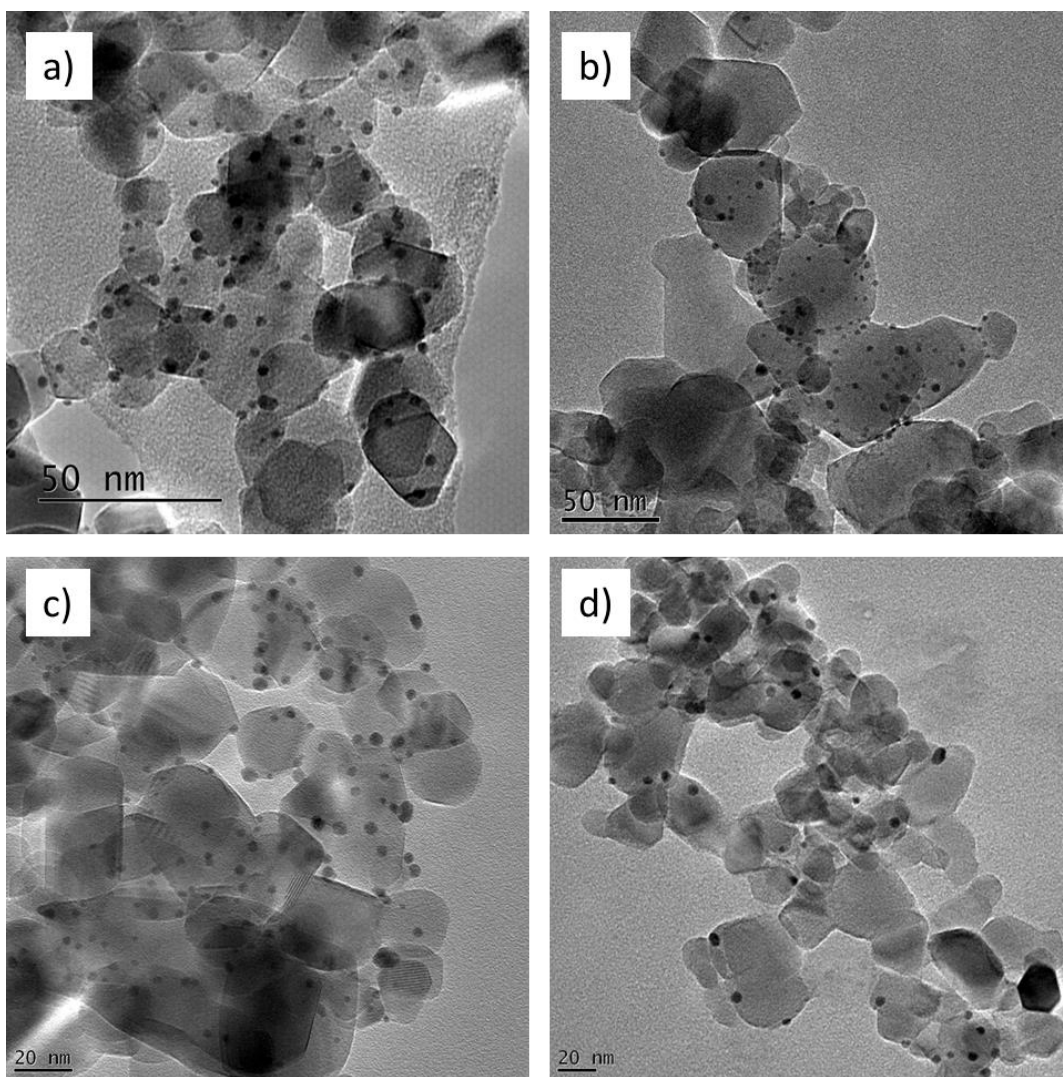


Figure 11. Representative TEM images of the 1%Au-TiO₂ dried at 120 °C (a) or heat treated at 200 (b), 300 (c) or 400 °C (d).

Table 8. Summary of the average particle size and standard deviation of the 1%Au-TiO₂ catalyst, dried at 120 °C or heat treated at 200, 300 or 400 °C.

1%Au-TiO₂ catalyst heat treatment	Average particle size / nm	Standard deviation	Number of particles counted
120 °C	2.9	0.7	309
200 °C	4.1	1.2	200
300 °C	4.1	1.3	232
400 °C	5.1	2.1	215

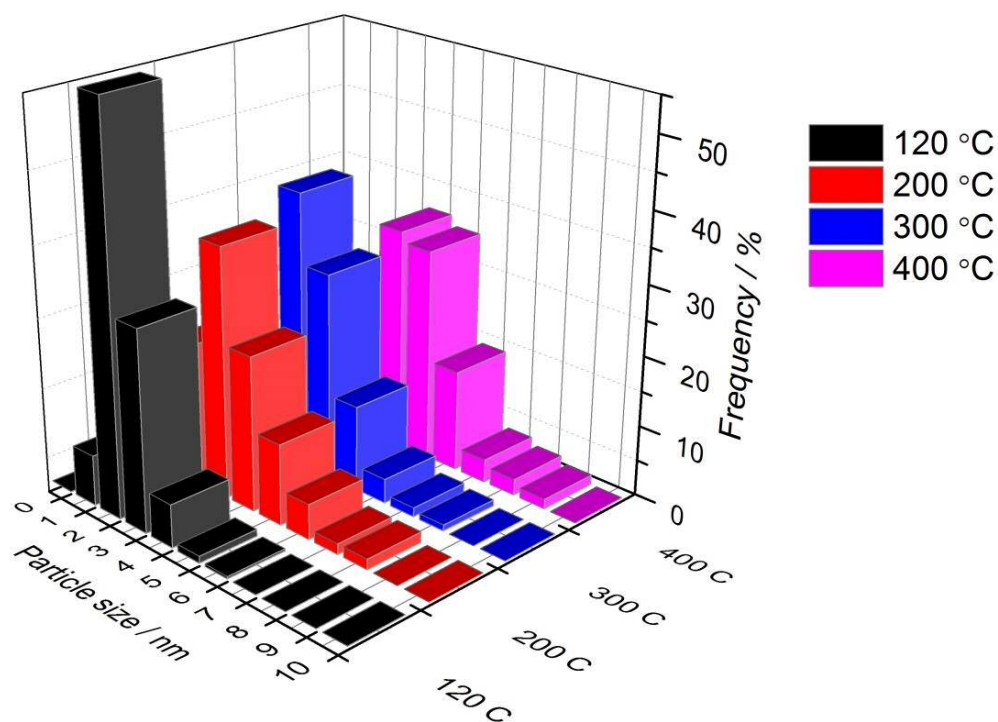


Figure 12. Particle size histograms for the 1%Au-TiO₂ catalysts made by sol immobilisation, after drying at 120 °C or calcination at 200, 300 or 400 °C.

Photocatalytic performance was evaluated for the four heat treated samples by photocatalytic methanol reforming for hydrogen production. Samples were sent to Cardiff University for activity testing which was undertaken by Julia Kennedy; see section 2.4.8 for details of the set up. Figure 13 shows the H₂ evolution as a function of time for the four heat treated samples as well as the rate of H₂ evolution for each sample. There is a clear trend of improvement in photocatalytic H₂ evolution with increasing calcination temperature, with the 400 °C sample producing roughly 5 times the amount of H₂ after 3 hours compared to the dried at 120 °C sample. The likely explanation for this is the removal of the protecting ligand PVA during the heat treatment. As the PVA binds to the surface of the Au NPs during the synthesis, preventing the NPs from growing large and agglomerating, it is likely that any residual PVA on the Au will block sites for the reaction to occur. Calcination removes the remaining PVA freeing up the surface of the Au; also it is likely that the contact between the Au NPs and the TiO₂ surface (metal support interaction) will be improved by the heat treatment. So the rate is higher, even though, as Table 8 shows, the particle size has increased.

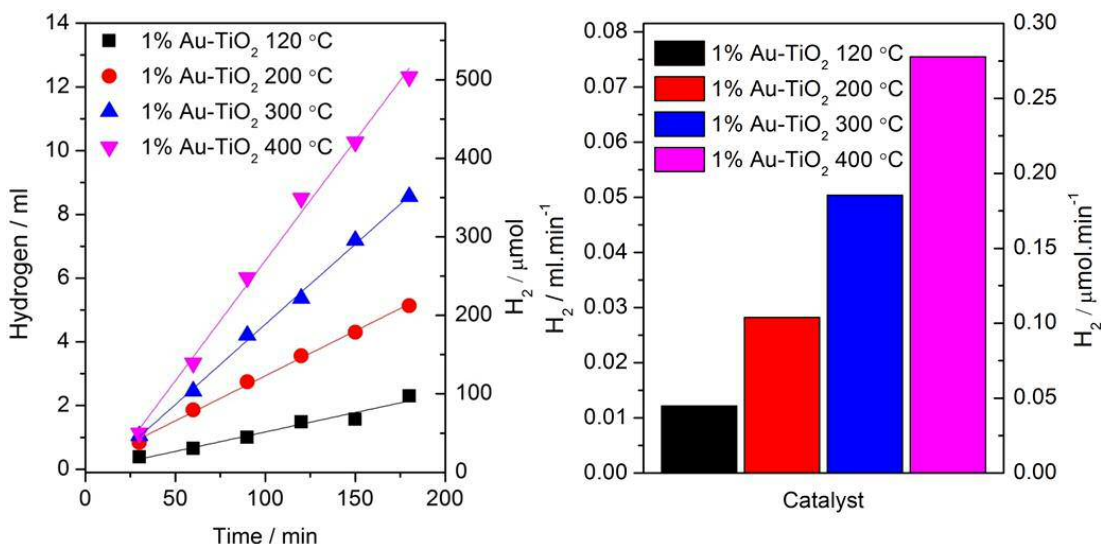


Figure 13. Time resolved hydrogen production plots, left) and average rate of hydrogen production, right). For a 1%Au-TiO₂ catalyst made by sol immobilisation either dried at 120 °C or heat treated at 200, 300 or 400 °C.

3.3.4 Effect of metal loading of Au NPs on TiO₂ for photocatalytic H₂ evolution

To investigate the effect of Au loading on TiO₂ on the photocatalytic performance for methanol reforming a series of catalysts was made by the sol immobilisation method to have total Au weight loading of 0.1, 0.25, 0.4, 0.5, 0.7, 1.0, 2.0 and 5%. These catalysts were dried at 120 °C and then a sample of each was further heat treated at 400 °C.

The sol immobilisation method is known to produce small reproducible sized Au NPs with a narrow size distribution. Therefore by keeping the Au particle size of each catalyst as similar as possible this parameter can be eliminated as a factor which could affect the activity of the catalyst, and the effect of metal loading could be more clearly determined. Figure 14 shows representative bright field TEM images of the series of dried Au-TiO₂ catalysts with varying Au loading, while Figure 15 shows the corresponding TEM images for the calcined (400 °C) catalysts. Results for the calculated average particle size are summarised in Table 9 with corresponding particle size histograms are displayed in Figure 16 and Figure 17. Across range of dried catalysts the mean average particle sizes were found to be in the range 2.9 to 4.4 nm respectively and the majority of the particles were smaller than 10 nm. For the calcined Au-TiO₂ samples, the mean particle size increased from 4 to 6-7 nm, demonstrating that the Au particles on TiO₂ exhibited a low degree of sintering. This has previously been reported to be due to the strong-metal support interaction.³⁷

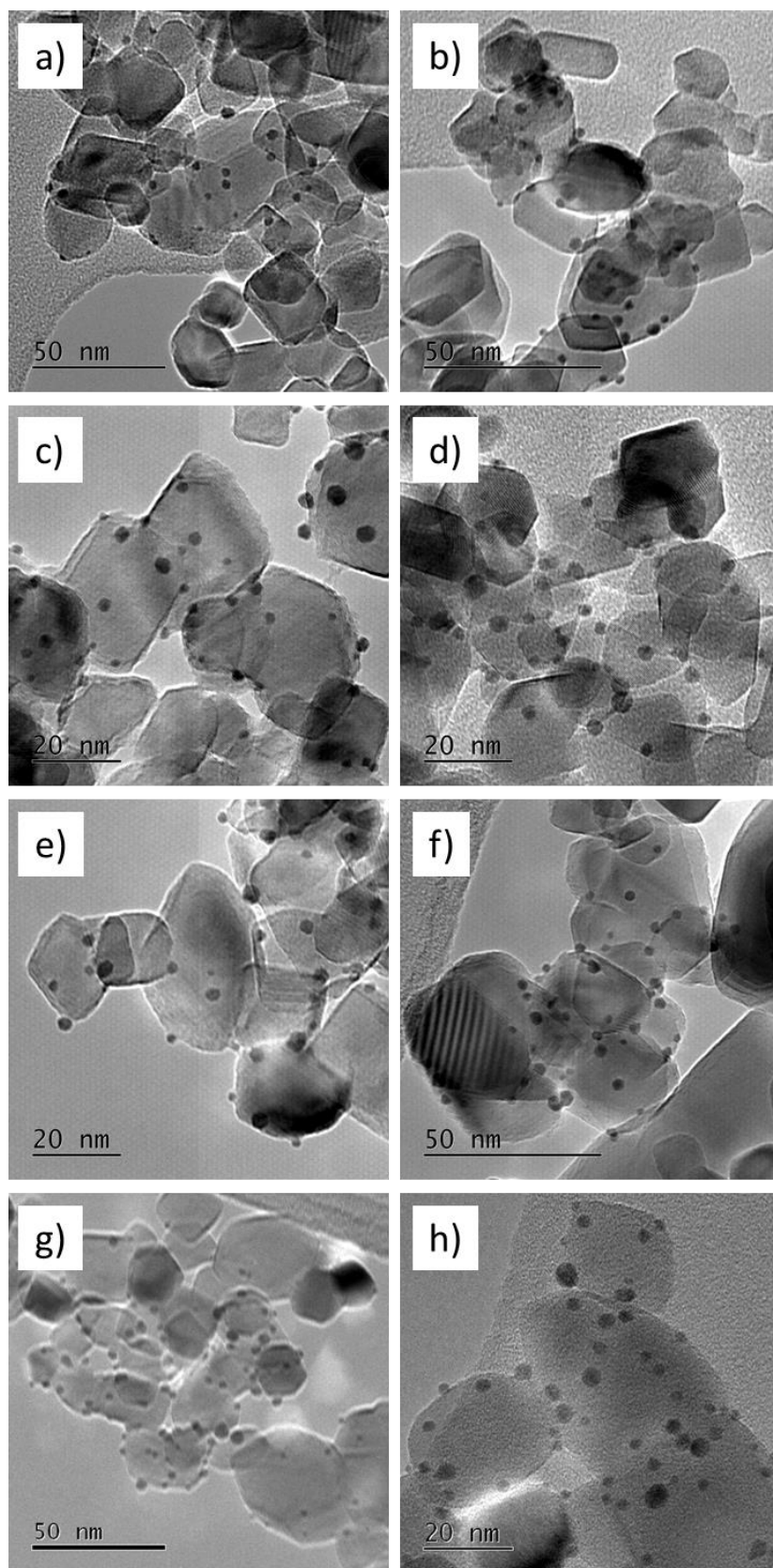


Figure 14. Representative TEM images of Au NPs supported on TiO₂, dried at 120 °C with Au weight loadings of a) 0.1%, b) 0.25%, c) 0.4%, d) 0.5%, e) 0.7%, f) 1.0%, g) 2.0% and h) 5.0%

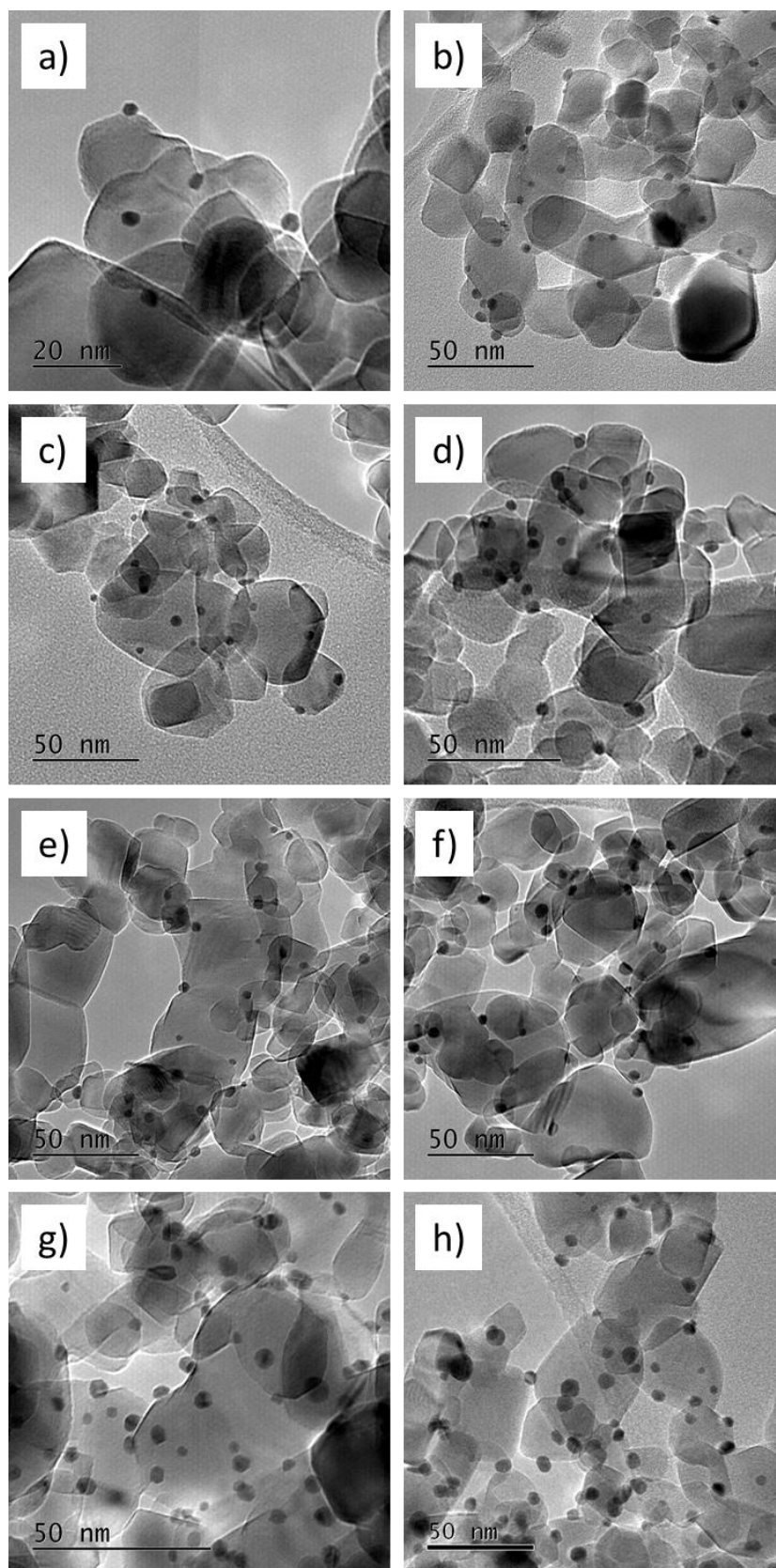


Figure 15. . Representative TEM images of Au NPs supported on TiO₂, calcined at 400 °C with Au weight loadings of a) 0.1%, b) 0.25%, c) 0.4%, d) 0.5%, e) 0.7%, f) 1.0%, g) 2.0% and h) 5.0%.

Table 9. Summary of average particle size (by TEM), standard deviation and number of particles counted for a series of different weight loadings of Au NP supported TiO₂ dried and calcined.

Dried 120 °C				Calcined 400 °C			
Weight Loading	Average Size / nm	Standard Deviation	particles counted	Weight Loading	Average Size / nm	Standard Deviation	particles counted
0.1	3.2	0.9	274	0.1	3.5	1.1	205
0.25	3.0	0.9	278	0.25	4.3	1.0	284
0.4	2.9	0.8	294	0.4	4.2	1.0	251
0.5	3.3	1.0	279	0.5	4.8	1.3	303
0.7	3.0	0.9	285	0.7	4.5	1.2	321
1.0	2.9	0.7	309	1.0	5.5	1.4	254
2.0	3.5	1.1	340	2.0	4.6	1.4	310
5.0	4.4	1.6	248	5.0	6.6	1.6	244

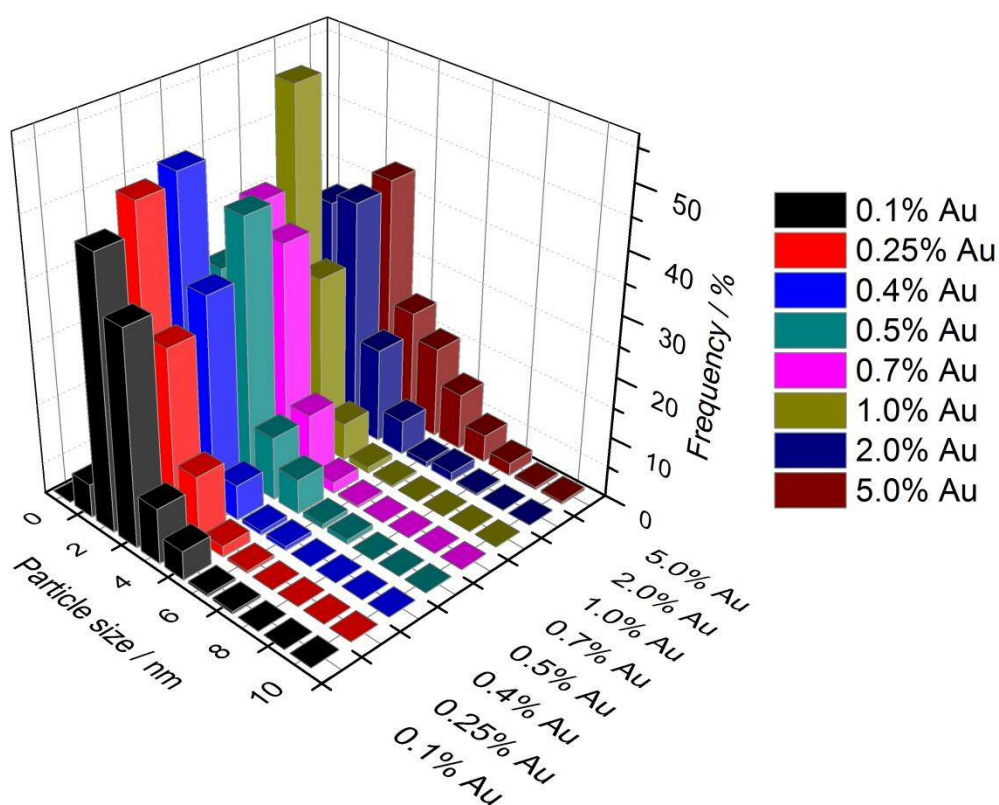


Figure 16. Particle size histograms for a series of different weight loadings of Au NP supported TiO₂ dried at 120 °C.

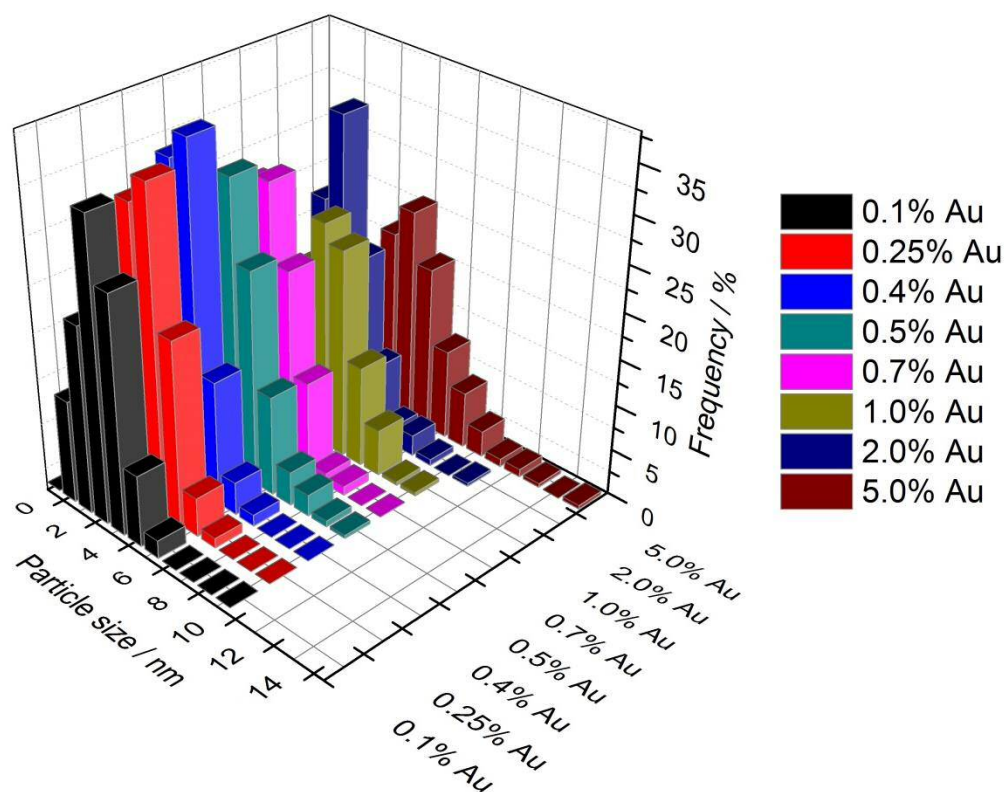


Figure 17. Particle size histograms for a series of different weight loadings of Au NP supported TiO₂ calcined at 400 °C.

The series of Au-TiO₂ catalysts with various weight loadings both dried (120 °C) and calcined (400 °C) were sent to Cardiff University to be tested for photocatalytic methanol reforming for H₂ production. All tests were performed by Julia Kennedy at Cardiff University with details of the experimental set up in section 2.4.8. Figure 18 shows the H₂ evolution as a function of time for the dried (120 °C) and calcined (400 °C) Au-TiO₂ catalysts respectively. The majority of the dried and calcined Au-TiO₂ catalysts showed almost linear H₂ concentration dependence as a function of reaction time.

Figure 19 presents H₂ evolution rates from methanol over Au-TiO₂ catalysts (dried and calcined at 400 °C) as a function of Au loading. It is evident that the catalytic performance of the calcined catalysts was improved by a factor of 2-3 with respect to the dried only catalysts. Considering that there is also an increase of the mean particle size between the dried and calcined Au-TiO₂ catalysts (i.e. from ~3 to ~5 nm), the main reason for the enhancement of the catalytic activity of the latter may be related to the removal of the PVA ligands around the metal particle and as well as from the TiO₂ surface. It is known from TGA studies the effective removal of PVA from the Au-TiO₂ catalyst requires heating above ~ 300 °C.¹⁴

It was observed that the rate for hydrogen production was poor for low (0.1 wt% Au) and high (5 wt. % Au) metal loading, whereas with intermediate loading levels between 0.2 to 2 wt% Au highest H₂ production rates were observed. In fact two maxima in rates was observed at loadings of 0.4 and 1 wt. % Au for the dried catalysts, whereas for the calcined Au supported catalysts the maximum rates were found for loadings of 0.5 and 2wt. %. This was not entirely expected, as for a similar system where Pd has been loaded on to the surface of TiO₂ for photocatalytic methanol reforming there was one maximum in rate when varying the metal loading.^{31, 38} However this observed double maximum in rate for H₂ is in agreement with previous published results for Au-TiO₂ catalysts made by the incipient wetness technique, although the maximum was at slightly different weight loadings of 0.2 and 2 % Au.³⁹ The decrease of H₂ evolution rate above 2 wt. % can be attributed to a reduction of the available metal-support sites since both metal and support sites are essential for the reaction. An important question to consider is the cause of the dual peak for the hydrogen production rate. Previous studies have shown that different morphologies and structures of gold can exist, depending on the gold loading and calcination temperature,^{37, 40-42} and therefore could affect catalytic activity. It has been shown that in the case of Au-TiO₂ catalysts synthesised by sol-immobilisation method a mixture of cuboctahedral, singly twinned and multiply twinned morphologies (icosahedral and decahedral particles) are present.¹⁴ Moreover, a heat treatment has a substantial effect on the morphology of the Au particles supported onto TiO₂ where an increase of heat treatment temperature from 120 to 400 °C leads to an increase in the formation of gold particles with cuboctahedral morphology and the Au particles form an extended flat interface structure with the crystalline TiO₂ substrate. This could be reflected in the position of the maxima changing after calcination from 0.5 and 1 % for the dried and 0.7 and 2 % for the calcined. Therefore, the combination of these parameters can explain partly the observation of two peaks in H₂ production rate in the case of Au/TiO₂ catalysts as a function of Au loading. However work by Murdoch et al. on varying the weight loading of Au on pure Anatase and Rutile for photocatalytic ethanol reforming observed only one maximum in rate.⁴³ Therefore it is possible that this phenomenon is limited to P25 TiO₂ only, however a full understanding of this double maximum is still unclear.

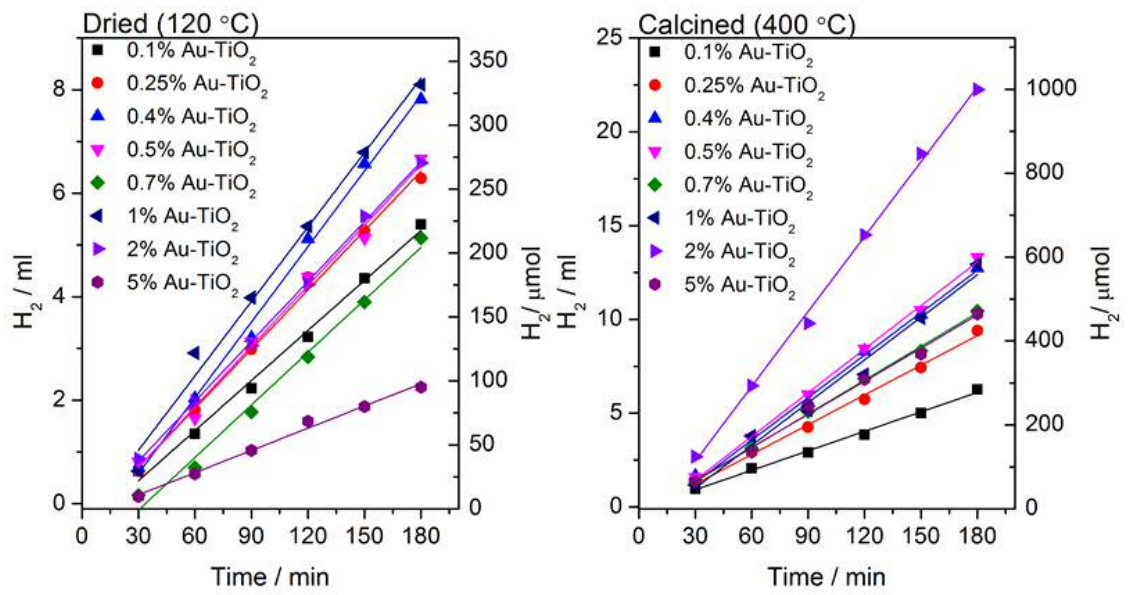


Figure 18. Hydrogen production from Au-TiO₂ catalysts with various weight loadings of Au dried at 120 °C and calcined at 400 °C.

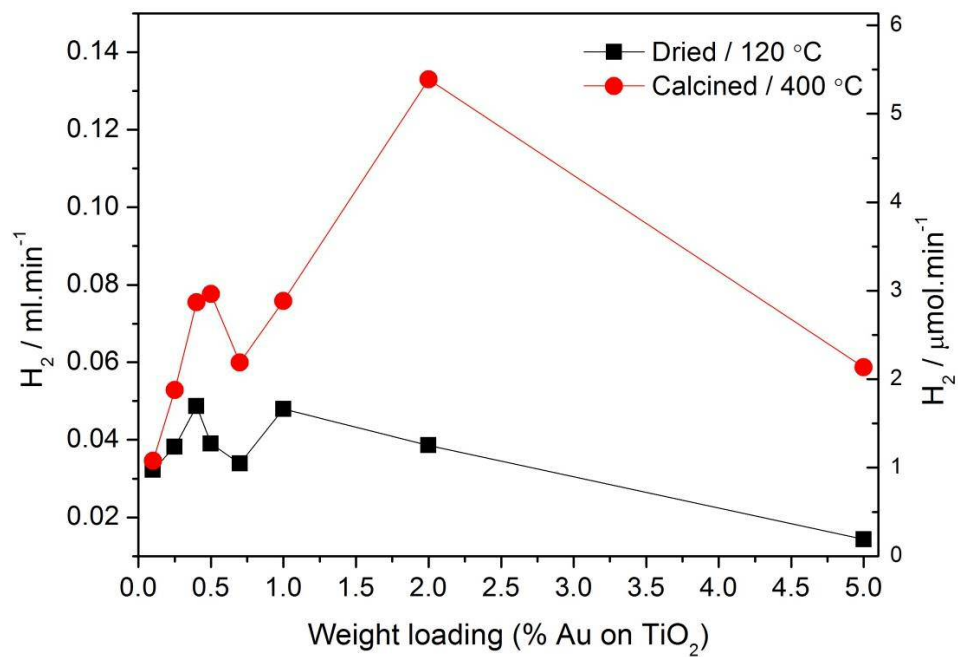


Figure 19. Rate of photocatalytic H₂ production versus Au loading for both dried (120 °C) and calcined (400 °C) catalysts.

3.4 Photocatalytic H₂ production from Pd-TiO₂ with long band-pass filters

To investigate the visible light response of a standard 0.5%Pd-TiO₂ catalyst UV/Vis analysis and a reaction with a set of long band pass filters was performed. TiO₂ is perhaps the most commonly studied and used photocatalyst, this is despite it having a band gap which lies in the UV region. The absorption properties of pristine TiO₂ (P25), 0.5%Pd-TiO₂ (incipient wetness) and a 0.5%Pd-TiO₂ used catalyst were analysed by diffuse reflectance UV-Vis spectroscopy and the results are displayed in Figure 20. The main absorption edge in the region of 380-400 nm corresponds to the band gap of Titania which has a commonly reported value of 3.2 eV.^{8,44} Both palladium loaded TiO₂ catalysts display an increased absorption in the visible region (400-800 nm) especially the used sample compared to the bare TiO₂. However extra absorption observed here is due to the presence of the Pd, specifically d-d transitions, and will not affect activity.⁴⁵

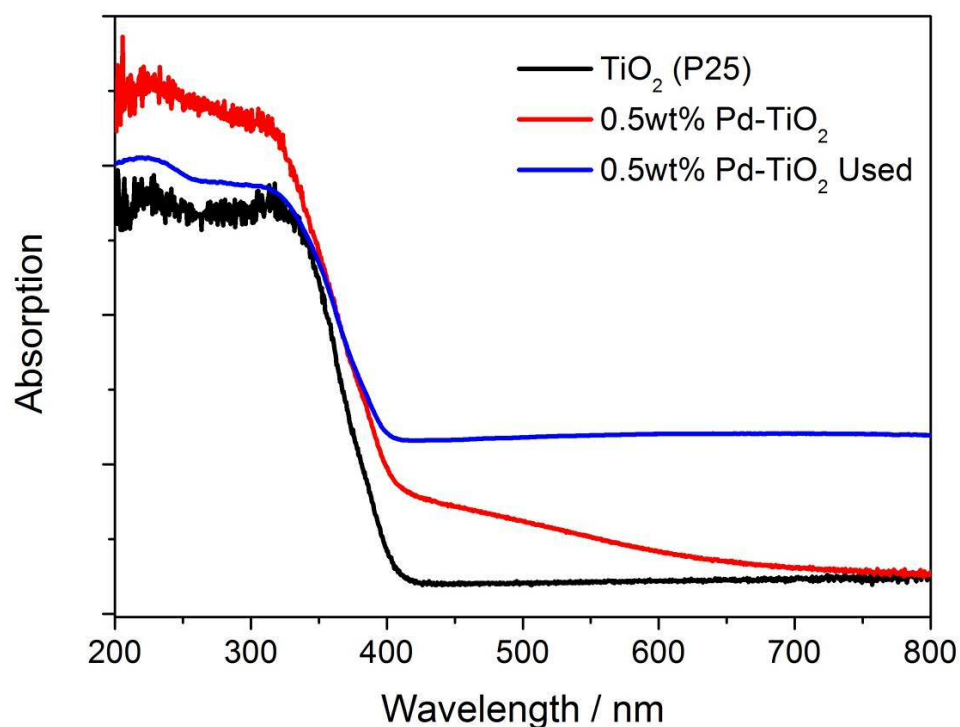


Figure 20. UV/Vis analysis of TiO₂ (P25), 0.5%Pd-TiO₂ (incipient wetness) and 0.5%Pd-TiO₂ used.

The wavelength dependent photocatalytic H₂ evolution of 0.5%Pd-TiO₂ (incipient wetness) was measured using a continuous flow set up; details can be found in section 2.4.5 along with UV/Vis spectra of the filters used. Briefly a round bottom flask with the catalyst, water

and methanol was connected with an inlet flow delivering N_2 at $30 \text{ mL}\cdot\text{min}^{-1}$. During irradiation an outlet pipe was connected to a GC fitted with gas sampling valves which would take a sample of the stream at 10 minute intervals for analysis. A graph of reaction rate verses time where the long band pass filters were added and remove is shown in Figure 21. The round bottom flask used in this experiment was made of Pyrex and when analysed by UV/Vis analysis was found to have little to no absorption in the UV between 400-300 nm. However a sharp absorption was observed at wavelengths below 300 nm. As expected the rate of H_2 production drops with each successive increase filter until no H_2 is produced with the 400 nm filter in place. This is consistent with the UV/Vis analysis from Figure 20.

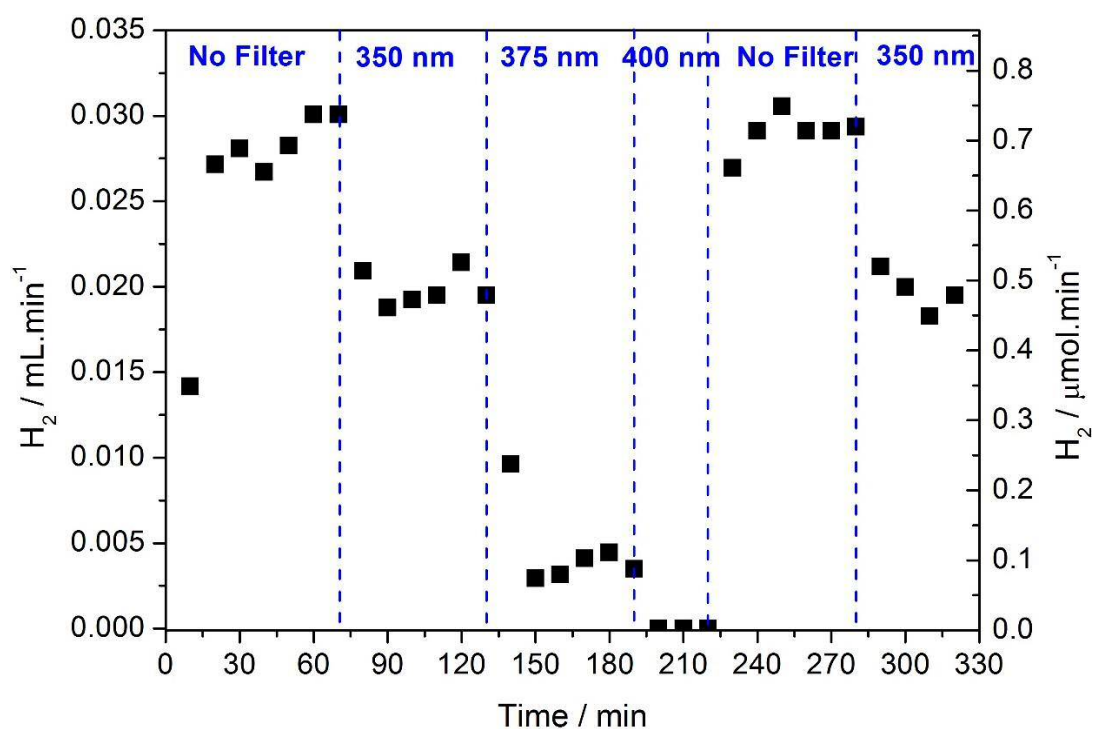


Figure 21. Rate of photocatalytic H_2 evolution from a 0.5% Pd-TiO₂ catalyst made by incipient wetness with a series of long band pass filters. Reactions was performed under continuous flow operation, $30 \text{ mL}\cdot\text{min}^{-1}$ N_2 flow, 150 mg catalyst, 1 mL of methanol and 200 mL water.

3.5 Synthesis of Ag-TiO₂ and Pd-TiO₂ by sol immobilisation

As well as being used to produce and Au colloids the sol immobilisation method can also be used to synthesise other noble metal NPs, e.g. Pd and Ag.^{46, 47} The same principles apply as with Au, in that a metal precursor (e.g. HAuCl₄, Ag(NO₃) and PdCl₂) is reduced with NaBH₄ in the presence of the protecting agent PVA to produce the NPs, details can be found in section

2.2.5. Figure 22 displays representative TEM images of the dried at 120 °C 1%Au-TiO₂, 1%Ag-TiO₂ and 1%Pd-TiO₂ catalysts with the associated histogram in Figure 23 and summary of the results in Table 10. As can be seen in all cases the NPs are visible on the surface of the TiO₂ evenly dispersed without significant agglomeration. Also included in Figure 22 (D) is a high resolution image of an Ag NP on the surface of TiO₂ where the lattice structure of the Ag NP is clearly observable.

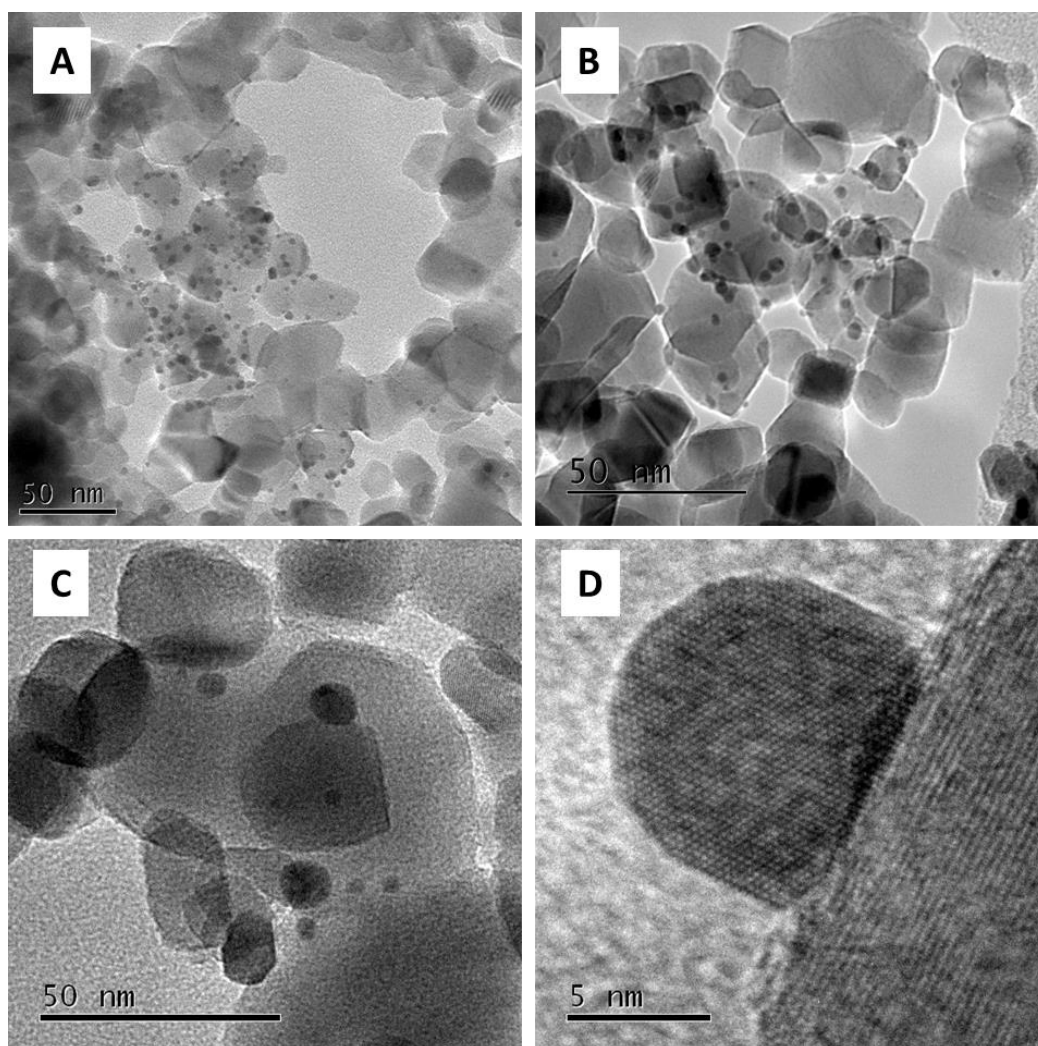


Figure 22. TEM images 1wt% noble metals on TiO₂ made by the sol immobilisation method, A) Au-TiO₂ B) Pd-TiO₂ C) Ag-TiO₂ and D) high resolution image of Ag-TiO₂, all catalysts dried at 120 °C.

For the case of the Ag NPs the particle size was significantly larger than that of the Au and Pd which is reflected by there being fewer particles on average in the Ag-TiO₂ TEM image. The Au and Pd NPs show comparable particle size however this is not the case for the Ag NPs and may arise from the ability of the PVA to stabilise the Ag colloid. Changing the synthesis

parameters such as increasing the PVA to metal ratio may be a route to producing small Ag NPs by the sol immobilisation method, however more work needs to be done. Therefore the sol immobilisation method can be used to relatively easily produce NPs of the order of ~ 3 nm of Au and Pd, with reports of the same true for Pt in the literature.⁴⁸

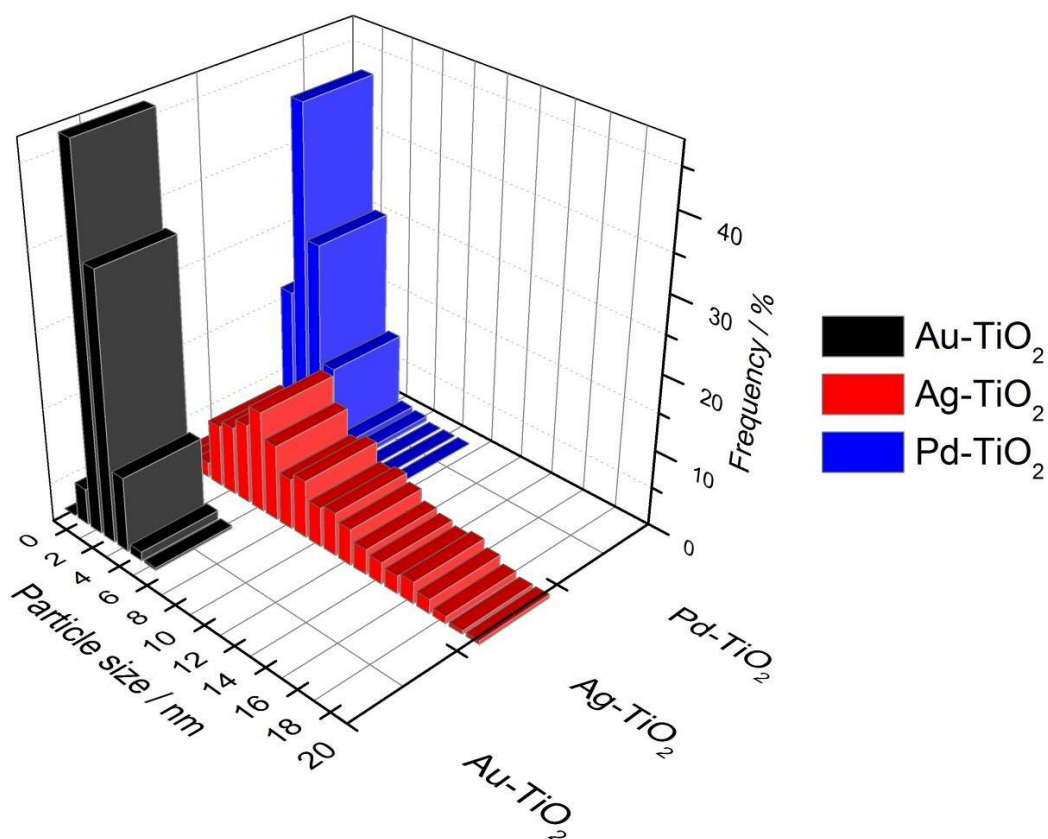


Figure 23. Particle size distributions determined by TEM of 1%Au-TiO₂, 1%Ag-TiO₂ and 1%Pd-TiO₂ catalysts made by the sol immobilisation technique.

Table 10. TEM particle size summary of 1%Au-TiO₂, 1%Ag-TiO₂ and 1%Pd-TiO₂ catalysts made by the sol immobilisation technique, with standard deviation and number of particles counted.

Catalyst	Average Particle size (nm)	Standard deviation (nm)	Number of particles counted
Au-TiO ₂	3.0	1.2	335
Ag-TiO ₂	8.7	4.1	208
Pd-TiO ₂	2.8	1.0	318

Comparative H₂ evolution reactions of Au and Ag-TiO₂ are discussed in more detail in chapter 4, with reactions involving Au and Pd elaborated on more in chapter 5, so will be kept brief here. However as can be seen in Figure 24 the activity of the three catalysts is as follows

1%Pd-TiO₂ > 1%Au-TiO₂ > 1%Ag-TiO₂ which is in agreement with reports in the literature.^{8, 46} One factor which may explain the relatively low rate of H₂ evolution from the Ag based catalyst may be the particle size of ~ 8.7 nm. As the volume of the NP is dependent on the radius cubed, the larger Ag NPs of ~ 8.7 nm as opposed to ~ 3 nm for the Au and Pd, will have more atoms in the bulk and less at the surface. Also there will be fewer NPs of Ag and these factors may then be main cause of the lower activity.

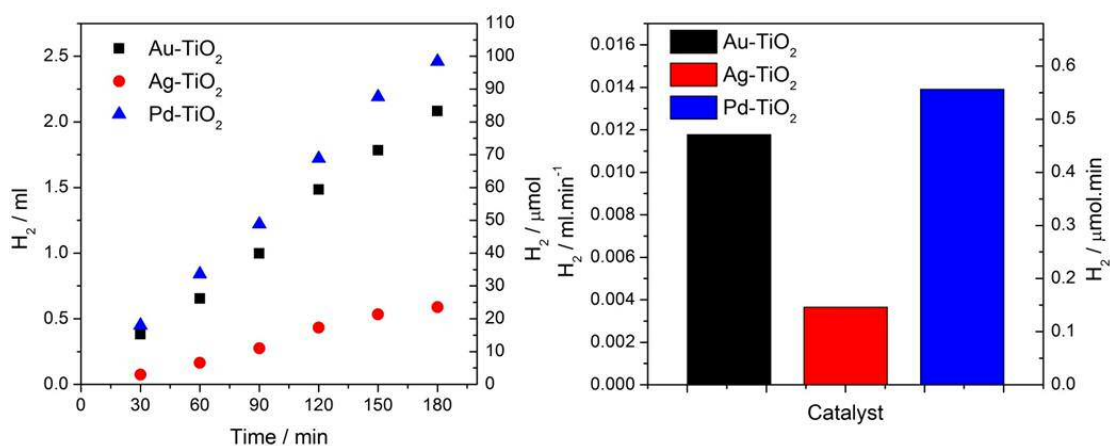


Figure 24. Time dependent H₂ evolution from photocatalytic methanol reforming and associated reaction rate plots for 1 weight percent Au, Ag and Pd on TiO₂ catalysts made by the sol immobilisation method (dried at 120 °C).

3.6 Cerium doped TiO₂ loaded with Pd

The photocatalytic activity of TiO₂ is amongst the highest of all semiconductors, however this is only true when irradiated with photons of energy greater than band gap of ~3.2 eV (~380 nm) as was demonstrated in section 3.4 and has been widely established.⁴⁴ There is much interest in expanding the photoresponse of TiO₂ to longer wavelengths thereby making use of a wider range of solar light. One method for achieving this is by tuning the band gap by doping the TiO₂ with non-metallic elements such as N, C and S etc. as well as metallic elements.^{15, 30, 49-51} Among these metallic dopants Ce has shown some promise,⁵² also Ce is relatively stable and non-toxic as is TiO₂. Here sol gel TiO₂ was synthesised with various amounts of Ce added to produce doped sol gel TiO₂ to investigate whether an increase in activity photocatalytic can be achieved. Cerium oxide has useful properties as a catalyst owing to the ability to store oxygen and have reversible oxidation state, arising from the facile cycling between Ce³⁺ (Ce₂O₃ electronic configuration 4f¹5d⁰) and Ce⁴⁺ (Ce₂O₄ electronic configuration 4f⁰5d⁰).⁵³

Cerium doped TiO₂ was synthesised by addition of cerium nitrate during a standard sol gel preparation of TiO₂ from titanium isopropoxide, details of the procedure can be found in section 2.2.13. A series of doped sol gel TiO₂ was synthesised with weight loadings of Ce by mass of 0.1%, 1%, 3.9% and 39%. Addition of the co-catalyst Pd (0.5wt %) was achieved by incipient wetness impregnation for all catalyst tested. Note the 3.9 and 39% weight Ce samples were made by error, however as they had interesting UV/Vis absorption properties (see below) it was decided to test them regardless. The radii of Ti⁴⁺ has a value of 0.68 Å while that of Ce⁴⁺/ Ce³⁺ has a value of 0.90 Å, as a result of these differences CeO₂ and TiO₂ phases have been reported to coexist in Ce doped TiO₂ made by the sol gel process.⁵⁴ Despite this the interface between these two phases can be regarded as another phase Ce_{1-x}Ti_xO_{2-y} which is formed due to Ti⁴⁺ entering the CeO_{2-y} phase.

Figure 25 shows the UV/Vis spectra of 0.5%Pd loaded sol gel TiO₂ doped with Ce, also with references of 0.5%Pd-TiO₂ (P25), CeO₂ and TiO₂ (P25). The spectrum of TiO₂ (P25) shows the characteristic absorption at 400 nm and below corresponding to the band gap of the semiconductor with negligible absorption in the visible region. Addition of Ce to the sol gel TiO₂ has the effect of shifting the onset of the absorption band further into the visible with the higher amounts of Ce shifting it furthest. Both the references of bare TiO₂ (P25) and CeO₂ demonstrates negligible absorption in the visible, therefore this shift in the absorption is unlikely to be due to the presence of a combination of TiO₂ and CeO₂, as can be seen visually from the pictures included in Figure 25.

It has been reported that an impurity band of interfacial Ce_{1-x}Ti_xO_{2-y} with n-type identity has been established for these Ce doped TiO₂ systems.⁵⁴ Therefore this observed red shift in the Ce doped sol gel TiO₂ can be attributed to charge transfer between this impurity band and the conduction band of the TiO₂.⁵¹ However some of the absorption observed here in the range 400-800 nm is due to the presence of the Pd on the surface of the support, specifically d-d transitions, and will not affect activity.⁴⁵ Catalytic testing is required to determine whether the increased absorption in the visible (400-500 nm) of the Ce doped sol gel TiO₂ can actually be utilised for photocatalytic reactions, with results to follow.

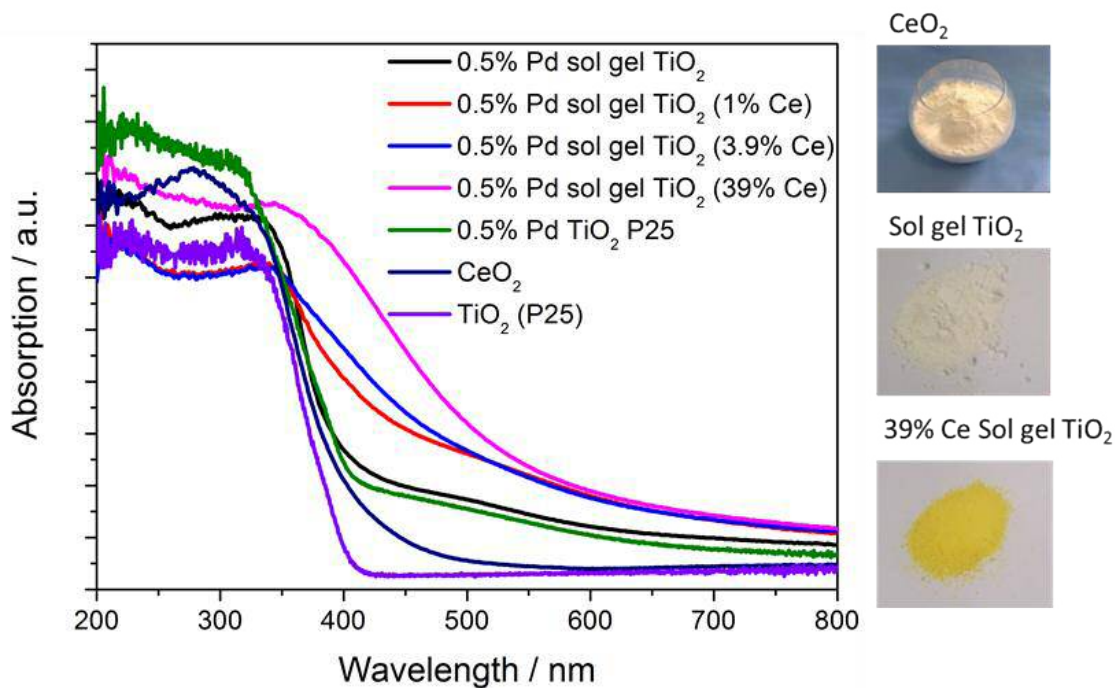


Figure 25. UV/Vis spectra of 0.5%Pd loaded sol gel TiO₂ doped with Ce, and references of CeO₂ and TiO₂ (P25). Also included on the right are picture taken of CeO₂, sol gel TiO₂ and 39% Ce sol gel TiO₂ as a visual aid.

TEM analysis was performed on the synthesised sol gel TiO₂ and Ce doped sol gel TiO₂ to gain an understanding of the size and shape of the TiO₂ crystallites. Representative images are displayed in Figure 26 where it can be seen that the average size of the TiO₂ is roughly ~ 10 nm with some agglomeration of the particles. In all cases lattice fringes were observed indicating that not only amorphous phases are present, with the XRD analysis below providing more information on this. However it is clear from the images taken that a nano sized powder was synthesised, as no large particles (greater than ~ 100 nm) were observed.

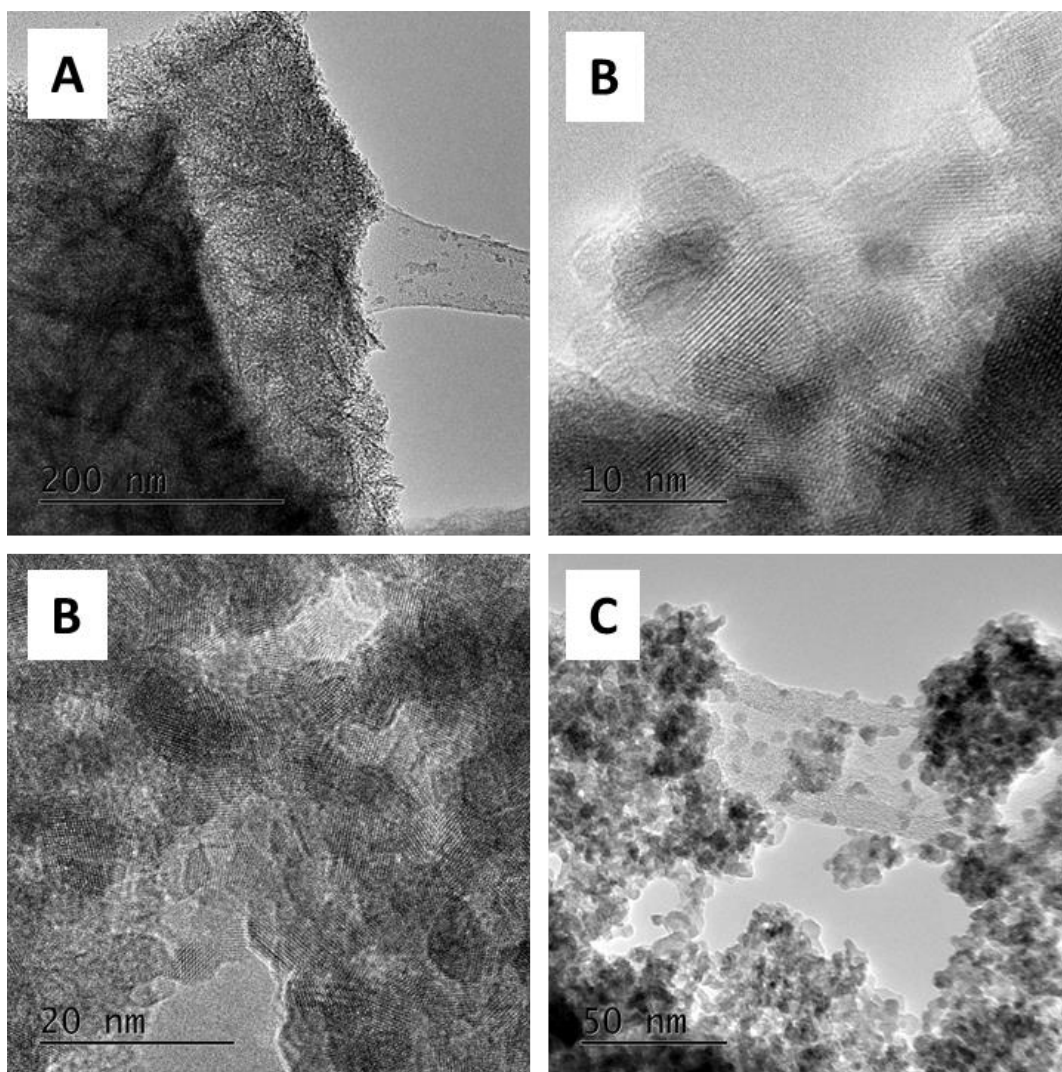


Figure 26. TEM images of A) sol gel TiO₂, B) sol gel TiO₂ 1% Ce C) sol gel TiO₂ 3.9% Ce and D) sol gel TiO₂ 39% Ce

Figure 27 presents XRD analysis of the Ce doped sol gel TiO₂ catalyst before the addition of Pd which was performed to gain an understanding of the phases present in the synthesised samples. The XRD data suggests that the sol gel TiO₂ is in the anatase phase which has three large peaks at 2 θ values of 25.3, 38.1 and 47.9.⁵⁵ No rutile phase is observed in any sample, as there are no clear peaks at 2 θ values of 27.5, 36.1 and 54.4.⁵⁶ Titania modified with 1 and 3.9% Ce matches with anatase with the appearance of a small peak at 2 θ value of 33. This peak can be attributed to the presence of a small amount of CeO₂, which has large 2 θ values at 28.6, 33.1 and 47.5.⁵⁷ Peaks of titania modified with 39% Ce can be associated to a mixture of anatase and CeO₂. However there may be another phase present in the doped TiO₂ which is too low in concentration to be measured here. Perhaps the interfacial Ce_{1-x}Ti_xO_{2-y} phase, although more work would be needed to establish this.

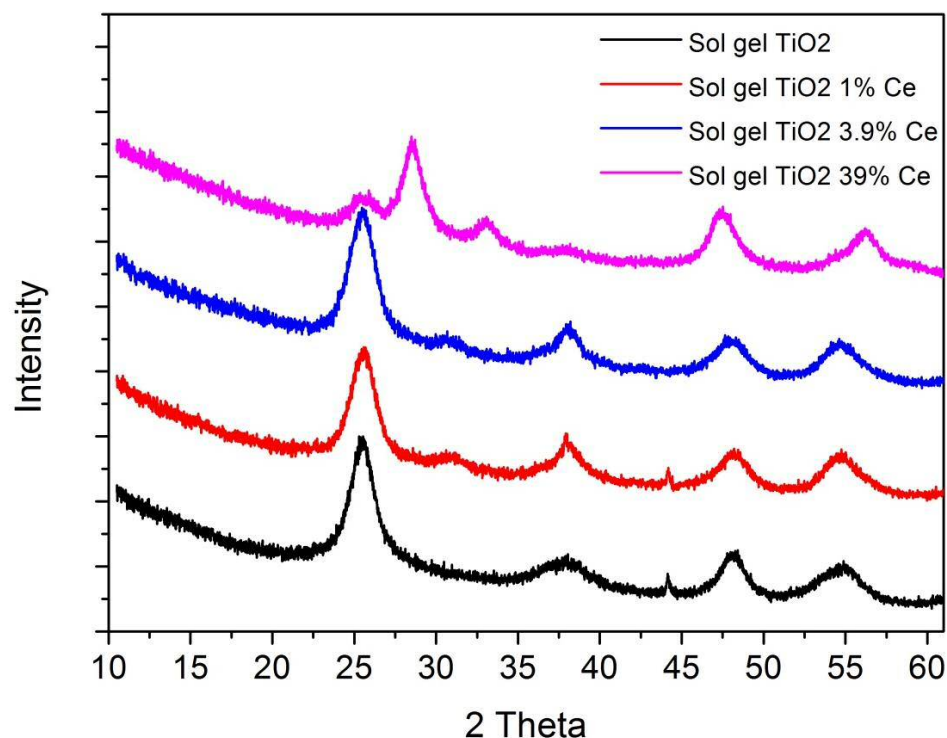


Figure 27. XRD spectra of sol gel modified with 1, 3.9 and 39% Ce. Also including images of sol gel TiO₂, 39% sol gel TiO₂ and CeO₂ samples.

Figure 28 depicts the rate of H₂ evolved from photocatalytic ethylene glycol reforming for the Ce doped catalysts as well as un-doped Pd loaded sol-gel TiO₂ and TiO₂ (P25) references. The choice of ethylene glycol over methanol as a standard alcohol sacrificial agent was made as the reactor set up in Sydney University was for continuous flow operation with 30 mL.min⁻¹ N₂ passing through the reactor. Therefore as the reaction was run for 3 hours it was thought a possibility that methanol would be lost as vapour during the run. Ethylene glycol has a higher boiling point and vapour pressure compared to methanol (197 °C and 0.08 mbar at 20 °C opposed to 65 °C and 130 mbar at 20 °C) and was assumed to be a better choice for continuous flow reactions here. Disappointingly the addition of Ce to the sol gel TiO₂ did not result in the overall improvement of H₂ evolution rates, as can be seen in Figure 28. In fact the catalyst with the highest activity was the standard 0.5%Pd-TiO₂ (P25). Also in all cases the more Ce added to the sol gel TiO₂ the worse the rate of H₂ evolution with the catalyst with 39% Ce showing no activity. This is despite the UV/Vis analysis in Figure 25 showing that the Ce doped TiO₂ have superior visible light absorption properties over the un-doped TiO₂ tested here. The reason for this may be that although more light is absorbed by the Ce doped catalysts the energy produced cannot be used for catalysis. Often it reported that dopant

can act as recombination centres for the photo generated electron-hole pairs, reducing their life time and thereby decreasing activity, which is likely what happens here.⁵⁸

Interestingly the 0.5%Pd-TiO₂ (sol gel) 0.1% Ce catalyst exhibited initial activity higher than that of un-doped 0.5%Pd-TiO₂ (sol gel). After about 40 minutes however the rate of H₂ evolution drops below the un-doped catalyst where it remains.

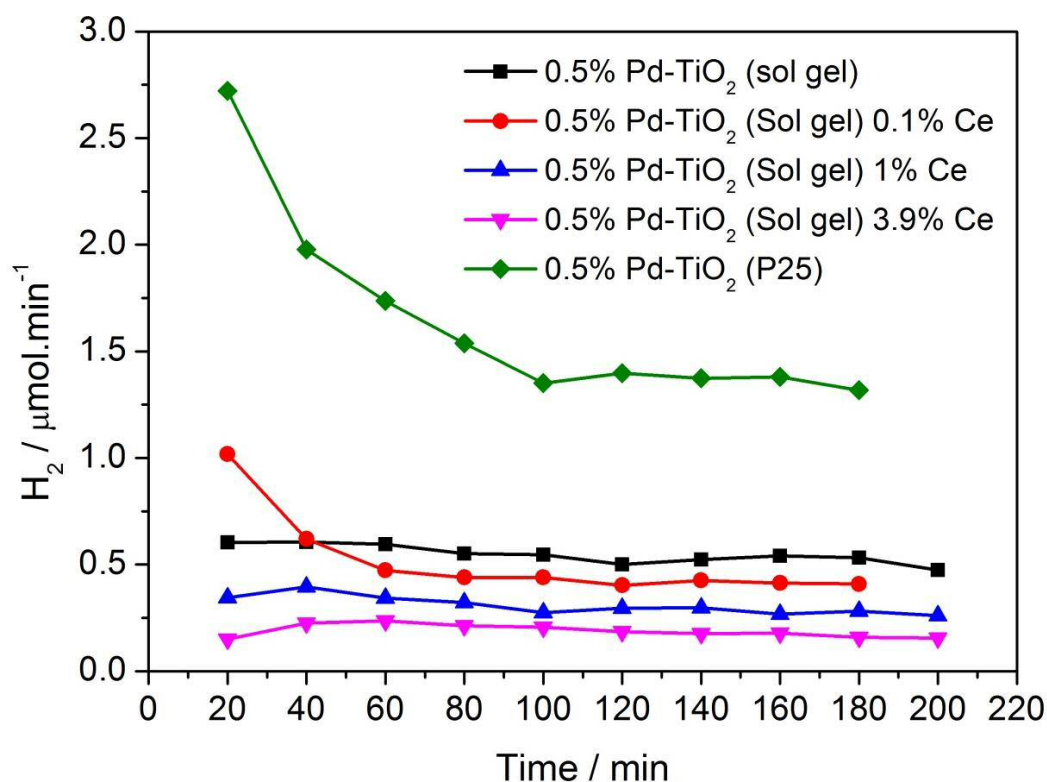


Figure 28. Rate of photocatalytic H₂ evolution from a series of Ce doped catalysts and references. Reactions was performed under continuous flow operation, 30 mL.min⁻¹ N₂ flow, 20 mg catalyst, 20 mL of 10% ethylene glycol solution and a constant temperature of 15 °C.

The exact reason for the poor activity for the Ce doped sol gel TiO₂ catalysts here is somewhat unclear, but may well relate to the introduction of e⁻/h⁺ recombination centres. As these samples were tested under full arc conditions it cannot be ascertained if the extra absorption in the visible overserved in the UV/Vis analysis of the Ce doped sol gel TiO₂ catalysts could be used to produce H₂ with the UV region blocked out. However if this was the case the activity would likely be extremely low and not promising, therefore these catalysts were not pursued further here.

3.7 Conclusions

In this chapter the sol immobilisation method has been used to produce metal NP supported on TiO₂ primarily for photocatalytic H₂ production reaction. The effect of varying parameter during synthesis of the Au colloid was investigated and it was found the small Au NPs (~3 nm) could be produced and immobilised onto TiO₂ under a range of conditions. This suggests that the sol immobilisation method is a useful technique for producing Au NPs which is relatively simple and reproducible. Other preparation methods were also investigated to produce Au-TiO₂ were employed such as DP urea, PD and NaOH/THPC, however of these tried none were able to produce ~ 3 nm Au NP here. The effect of calcination on a 1%Au-TiO₂ catalyst was investigated where it was found that particle size increased to ~ 5 nm for samples heat treated a 400 °C. The photocatalytic activity for H₂ production also increased with higher calcination temperature which was attributed to the removal the stabilising ligand PVA. Optimisation of the mass of 1%Au-TiO₂ catalyst and volume of methanol used during a photocatalytic reaction was investigated. It was found that for the reactor system in Harwell more than 50 mg of catalyst did not produce significant improvement in rates likely due to the light entering the solution being used to a maximum. Upon increasing the amount of methanol content in the 200 mL of water used for a photocatalytic reaction with constant mass of catalyst it was found that there were two regions where rate increases was linearly dependent on volume of methanol added. For low methanol volumes between 1 µL and 100 µL and a second region from 100 µL to 10 mL where the rate increases with additional methanol was significantly less. The weight loading of Au on TiO₂ was also varied to investigate the effect on H₂ and it observed that there was a double maximum at 0.5 and 1 % for the dried catalyst and at 0.7 and 2 % for the calcined catalyst. Wavelength dependent photocatalytic H₂ production from a 1%Au-TiO₂ catalyst was examined with activity found to follow what was expected from the UV/Vis analysis. As well as monometallic Au NPs the sol immobilisation method was also employed to synthesise monometallic Ag and Pd, with their photocatalytic activity determined. Cerium doping of sol gel TiO₂ was performed in a hope to increase activity by expanding the photoresponse of the synthesised TiO₂ into the visible. However this disappointingly this was not achieved and activity was instead lessened. Overall in this chapter has looked at variations of the sol immobilisation technique to make supported metal NPs as well as initial testing of these catalysts, with these methods and testing expanded upon in later chapters.

3.8 References

1. M. D. Hernandez-Alonso, F. Fresno, S. Suarez and J. M. Coronado, *Energy Environ. Sci.*, 2009, 2, 1231-1257.
2. J. Greaves, L. Al-Mazroai, A. Nuhu, P. Davies and M. Bowker, *Gold Bulletin*, 2006, 39, 216-219.
3. K. Mogyorosi, A. Kmetyko, N. Czirbus, G. Vereb, P. Sipos and A. Dombi, *React. Kinet. Catal. Lett.*, 2009, 98, 215-225.
4. Y. Z. Yang, C. H. Chang and H. Idriss, *Applied Catalysis B-Environmental*, 2006, 67, 217-222.
5. M. S. Park and M. Kang, *Mater. Lett.*, 2008, 62, 183-187.
6. L. Saeed Al-Mazroai, M. Bowker, P. Davies, A. Dickinson, J. Greaves, D. James and L. Millard, *Catalysis Today*, 2007, 122, 46-50.
7. H. Bahruji, M. Bowker, P. R. Davies and F. Pedrono, *Applied Catalysis B: Environmental*, 2011, 107, 205-209.
8. Z. H. N. Al-Azri, W.-T. Chen, A. Chan, V. Jovic, T. Ina, H. Idriss and G. I. N. Waterhouse, *Journal of Catalysis*, 2015, 329, 355-367.
9. C. Bianchi, F. Porta, L. Prati and M. Rossi, *Top. Catal.*, 2000, 13, 231-236.
10. F. Porta, L. Prati, M. Rossi, S. Coluccia and G. Martra, *Catalysis Today*, 2000, 61, 165-172.
11. J.-D. Grunwaldt, C. Kiener, C. Wögerbauer and A. Baiker, *Journal of Catalysis*, 1999, 181, 223-232.
12. C.-j. Liu, *Nanoscale Research Letters*, 2010, 5, 124-129.
13. N. Dimitratos, A. Villa, L. Prati, C. Hammond, C. E. Chan-Thaw, J. Cookson and P. T. Bishop, *Applied Catalysis A: General*, 2016, 514, 267-275.
14. J. A. Lopez-Sanchez, N. Dimitratos, C. Hammond, G. L. Brett, L. Kesavan, S. White, P. Miedziak, R. Tiruvalam, R. L. Jenkins, A. F. Carley, D. Knight, C. J. Kiely and G. J. Hutchings, *Nat Chem*, 2011, 3, 551-556.
15. K. L. Kelly, E. Coronado, L. L. Zhao and G. C. Schatz, *The Journal of Physical Chemistry B*, 2003, 107, 668-677.
16. X. Huang and M. A. El-Sayed, *Journal of Advanced Research*, 2010, 1, 13-28.
17. P. Soundarrajan, K. Sankarasubramanian, K. Sethuraman and K. Ramamurthi, *Crystengcomm*, 2014, 16, 8756-8768.
18. W. D. Pyrz and D. J. Buttrey, *Langmuir*, 2008, 24, 11350-11360.
19. C. A. Schneider, W. S. Rasband and K. W. Eliceiri, *Nat Meth*, 2012, 9, 671-675.
20. A. M. Beale and B. M. Weckhuysen, *Physical Chemistry Chemical Physics*, 2010, 12, 5562-5574.
21. W. Szczerba, H. Riesemeier and A. F. Thünemann, *Analytical and Bioanalytical Chemistry*, 2010, 398, 1967-1972.
22. T. V. W. Janssens, B. S. Clausen, B. Hvolbæk, H. Falsig, C. H. Christensen, T. Bligaard and J. K. Nørskov, *Top. Catal.*, 2007, 44, 15-26.
23. B. Ravel and M. Newville, *J. Synchrot. Radiat.*, 2005, 12, 537-541.
24. S. M. Rogers, C. R. A. Catlow, C. E. Chan-Thaw, D. Gianolio, E. K. Gibson, A. L. Gould, N. Jian, A. J. Logsdail, R. E. Palmer, L. Prati, N. Dimitratos, A. Villa and P. P. Wells, *ACS Catal.*, 2015, 5, 4377-4384.
25. N. Dimitratos, J. A. Lopez-Sanchez, D. Morgan, A. Carley, L. Prati and G. J. Hutchings, *Catalysis Today*, 2007, 122, 317-324.
26. M. Mrowetz, A. Villa, L. Prati and E. Selli, *Gold Bulletin*, 2007, 40, 154-160.
27. R. Zanella, L. Delannoy and C. Louis, *Applied Catalysis A: General*, 2005, 291, 62-72.
28. S. Oros-Ruiz, R. Zanella, R. López, A. Hernández-Gordillo and R. Gómez, *Journal of Hazardous Materials*, 2013, 263, Part 1, 2-10.

29. J. L. Hueso, V. Sebastian, A. Mayoral, L. Uson, M. Arruebo and J. Santamaria, *RSC Advances*, 2013, 3, 10427-10433.
30. Y.-F. Yang, P. Sangeetha and Y.-W. Chen, *International Journal of Hydrogen Energy*, 2009, 34, 8912-8920.
31. A. Dickinson, D. James, N. Perkins, T. Cassidy and M. Bowker, *J. Mol. Catal. A-Chem.*, 1999, 146, 211-221.
32. H. Bahruji, M. Bowker, P. R. Davies, J. Kennedy and D. J. Morgan, *International Journal of Hydrogen Energy*, 2015, 40, 1465-1471.
33. Z. Jiang, W. Zhang, L. Jin, X. Yang, F. Xu, J. Zhu and W. Huang, *The Journal of Physical Chemistry C*, 2007, 111, 12434-12439.
34. P. Fu and P. Zhang, *Applied Catalysis B: Environmental*, 2010, 96, 176-184.
35. J. W. Gilman, D. L. Vanderhart and T. Kashiwagi, in *Fire and Polymers II: Materials and Tests for Hazard Prevention*, ed. G. L. Nelson, 1995, vol. 599, pp. 161-185.
36. D. A. H. Hanaor and C. C. Sorrell, *Journal of Materials Science*, 2011, 46, 855-874.
37. N. Dimitratos, J. A. Lopez-Sanchez, D. Morgan, A. F. Carley, R. Tiruvalam, C. J. Kiely, D. Bethell and G. J. Hutchings, *Physical Chemistry Chemical Physics*, 2009, 11, 5142-5153.
38. L. S. Al-Mazroai, M. Bowker, P. Davies, A. Dickinson, J. Greaves, D. James and L. Millard, *Catalysis Today*, 2007, 122, 46-50.
39. M. Bowker, L. Millard, J. Greaves, D. James and J. Soares, *Gold Bulletin*, 2004, DOI: 10.1007/bf03215209.
40. P. Claus, A. Brückner, C. Mohr and H. Hofmeister, *Journal of the American Chemical Society*, 2000, 122, 11430-11439.
41. M. S. Chen and D. W. Goodman, *Science*, 2004.
42. A. A. Herzing, C. J. Kiely, A. F. Carley, P. Landon and G. J. Hutchings, *Science*, 2008, 321, 1331-1335.
43. MurdochM, G. I. N. Waterhouse, M. A. Nadeem, J. B. Metson, M. A. Keane, R. F. Howe, LlorcaJ and IdrissH, *Nat Chem*, 2011, 3, 489-492.
44. K. M. Reddy, S. V. Manorama and A. R. Reddy, *Mater. Chem. Phys.*, 2003, 78, 239-245.
45. Z. Zhang, G. Mestl, H. Knozinger and W. M. H. Sachtler, *Appl. Catal. A-Gen.*, 1992, 89, 155-168.
46. J. Kennedy, W. Jones, D. J. Morgan, M. Bowker, L. Lu, C. J. Kiely, P. P. Wells and N. Dimitratos, *Catalysis, Structure & Reactivity*, 2014, 1, 35-43.
47. W. Jones, R. Su, P. P. Wells, Y. Shen, N. Dimitratos, M. Bowker, D. Morgan, B. B. Iversen, A. Chutia, F. Besenbacher and G. Hutchings, *Physical Chemistry Chemical Physics*, 2014, 16, 26638-26644.
48. I. Gandarias, E. Nowicka, B. J. May, S. Alghareed, R. D. Armstrong, P. J. Miedziak and S. H. Taylor, *Catalysis Science & Technology*, 2016, 6, 4201-4209.
49. J. W. Niemantsverdriet, in *Spectroscopy in Catalysis*, Wiley-VCH Verlag GmbH & Co. KGaA, 2007, DOI: 10.1002/9783527611348.ch6, pp. 147-177.
50. J. W. Niemantsverdriet, in *Spectroscopy in Catalysis*, Wiley-VCH Verlag GmbH & Co. KGaA, 2007, DOI: 10.1002/9783527611348.ch3, pp. 39-83.
51. A.-W. Xu, Y. Gao and H.-Q. Liu, *Journal of Catalysis*, 2002, 207, 151-157.
52. T. Tong, J. Zhang, B. Tian, F. Chen, D. He and M. Anpo, *Journal of Colloid and Interface Science*, 2007, 315, 382-388.
53. J. Kašpar, P. Fornasiero and M. Graziani, *Catalysis Today*, 1999, 50, 285-298.
54. Z. Liu, B. Guo, L. Hong and H. Jiang, *Journal of Physics and Chemistry of Solids*, 2005, 66, 161-167.
55. ICSD154602.
56. ICSD167954.

57. ICSD 156250.
58. A. Di Paola, E. García-López, S. Ikeda, G. Marci, B. Ohtani and L. Palmisano, *Catalysis Today*, 2002, 75, 87-93.

Chapter 4: Supported AgAu nanoparticles for photocatalytic hydrogen production

Table of contents

4.1	Introduction	109
4.2	Gold silver bimetallic catalysts 1:1 molar ratio.....	110
4.2.1	Introduction	110
4.2.2	Catalyst synthesis.....	111
4.2.3	UV Vis characterisation	111
4.2.4	Bright field TEM analysis.....	112
4.2.5	STEM-HAADF analysis	116
4.2.6	XPS analysis	119
4.2.7	Catalytic testing.....	120
4.2.8	Conclusions	123
4.3	Photocatalytic H ₂ production from core-shell AgAu-TiO ₂ catalysts with controlled shell thickness	123
4.3.1	Introduction	123
4.3.2	Catalyst synthesis.....	123
4.3.3	UV Analysis.....	124
4.3.4	TEM analysis.....	125
4.3.5	XPS analysis	127
4.3.6	XANES analysis	129
4.3.7	d band vacancy calculation	130
4.3.8	EXAFS analysis.....	132
4.3.9	Photocatalytic performance evaluations.....	136
4.3.10	Conclusions	138
4.4	References	139

4.1 Introduction

In recent years interest in producing hydrogen by means of photocatalysis has gained significant attention. This is predominately due to the potential of hydrogen as a green fuel for the future, especially for the use in fuel cells. Current world reserves of fossil fuel are being depleted as well as releasing harmful amounts of CO₂ into the atmosphere. Therefore efficiently converting the abundant amounts of solar energy into stored chemical energy is an attractive strategy. Studies have identified that noble metal nanoparticles (NPs) supported on TiO₂ are efficient at photocatalytically reforming alcohols (i.e., methanol, ethanol and glycerol) for hydrogen production. See chapter 1 for more details on photocatalytic reforming reactions of TiO₂ supported NPs. Bimetallic NPs supported on TiO₂ have been used to tune the efficiency of the charge separation e.g. AuPt, AgPt, AuAg and AuPd.¹⁻⁴ Recent studies have found that the core-shell structured Au-Pd and Au-Pt NPs exhibited significantly enhanced performance for photocatalytic H₂ production and selective oxidation of benzene.⁵ Theoretical calculations and kinetic analysis suggest that the increased photocatalytic activity from core-shell NPs on a semiconductor support can result from improved charge trapping and release rates, and it is thought this originates from optimising the density and position of unoccupied d states of the metal NP.⁶

A potential drawback for photocatalytic reforming reactions of noble metals NPs supported on TiO₂ could be the high price and rarity of the metals (e.g. Au, Pt and Pd). Although in many cases the precious metals used for the synthesis of catalysts can be recovered and recycled, using less expensive metals from the outset would be a more promising strategy. Silver is one of the cheaper noble metals and would be an attractive candidate metal to perform photocatalytic reforming reactions. Depending on the crystal facet of Ag the work function can be in the range of 4.3-4.7 eV while for Au this value is 5.1-5.4 eV. This suggests a higher Fermi level of a trapped electron in Ag compared to Au. Work by Taki *et al.*⁷ on electron transfer from photoexcited TiO₂ and subsequent storage in Au, Pt and Ag by a titration method demonstrated that 440 electrons can be stored in 1 μM of Ag NPs, while Au NPs has a capacity of 280 electrons in 1 μM and Pt 190 electrons in 1 μM. These results would indicate that Ag NPs are efficient at trapping electrons and on those grounds it is a promising candidate for a photocatalytic reduction co-catalyst for H₂ production. However despite these findings Ag is a relatively poor co-catalyst for H₂ production compared to Au, Pt and Pd.^{8,9} Work by Tsukamoto *et al.* suggested that the relatively poor performance of the Ag NPs as a co-catalyst for H₂O₂ production from O₂ reduction could stem from the relatively small Schottky barrier at the interface of the TiO₂ and Ag NPs (~0.2 eV) resulting in

recombination of e^- and h^+ pairs.¹⁰ In comparison the Schottky barrier height between Au NPs and TiO_2 was reported to be 1.3 eV (due to the higher work function of Au 5.1 eV) suppressing recombination of the e^- and h^+ pairs. The work function of a AuAg NP alloy has been reported to lie intermediately between Au and Ag.¹¹ Therefore an AuAg alloy NP/ TiO_2 junction creates a barrier which is larger than Ag/ TiO_2 but smaller than Au/ TiO_2 which may allow for efficient e^- and h^+ pair separation. At the same time allowing smooth e^- transfer from the TiO_2 , whilst taking advantage of the electron trapping ability of Ag NPs.

Therefore taking this into account AuAg based catalysts for photocatalytic hydrogen production shows promise as a strategy of potentially improving activity and reducing cost of a metal/ TiO_2 system. In this section we have investigated Au, Ag and AuAg NPs supported on TiO_2 (P25) for photocatalytic reforming of simple alcohols (methanol and ethanol). Different preparation methods (based on the sol immobilisation technique, section 3.2.1) were employed to synthesise monometallic Au and Ag catalysts as well as an AuAg alloy, all supported on TiO_2 . In addition core-shell NPs supported on TiO_2 were also synthesised, characterised and tested for photocatalytic H_2 production.

4.2 Gold silver bimetallic catalysts 1:1 molar ratio

4.2.1 Introduction

The majority of the results concerning AuAg photocatalysts in this first section formed the basis for the published paper 'Photocatalytic hydrogen production by reforming of methanol using Au/ TiO_2 , Ag/ TiO_2 and Au-Ag/ TiO_2 catalysts' by Kennedy *et al.*¹² The catalyst synthesis and characterisation (with the exception of the STEM-HAADF images which was performed by Christopher Kiely at Lehigh University) was performed by Wilm Jones, while the catalytic testing was performed by Julia Kennedy at Cardiff University.

We have investigated AuAg NPs supported on TiO_2 (P25) for the anaerobic, ambient temperature photocatalytic reforming of methanol with water for the production of hydrogen. The NPs were synthesised by the sol immobilisation technique by sequential reduction of precursors with the aim to make a core-shell structure (or enrichment of either Au or Ag at the surface of the NPs). Also prepared were standards of co-reduced AgAu and mono-metallic Au and Ag NPs references all supported on TiO_2 . The relationship between the structure of the NPs synthesised by sequential reduction of the precursors and the photocatalytic activity was investigated. Work by Gomes *et al.* identified that AuAg NPs with

the structure Au_{core}Ag_{shell} (Ag[Au]) have the most stable structure compared to other possible compositions.¹³

4.2.2 Catalyst synthesis

Details of the preparation methods of the core shell AuAg NPs catalysts supported on TiO₂ can be found in section 2.2.5. As described, a set of catalysts was prepared with two monometallic standards of Au and Ag, a random alloy of AuAg (with both precursors reduced simultaneously), and with the two core shell NPs, Ag[Au] and Au[Ag] all immobilised on TiO₂. The core-shell samples were prepared by successive reductions of the precursors with the aim of the metal reduced first providing a seed for the reduction of the second. Monometallic references were prepared as in section 2.2.1 a list of the samples prepared is in Table 1. All catalysts here were dried at 120 °C for 8 hours and not calcined to maintain the structure of the NPs.

Table 1 list of samples prepared with weight and atomic ratios of Au and Ag along with metal PVA ratio, all samples dried at 120 °C for 8 hours.

Catalyst	Au/Ag weight ratio	Au/Ag atomic ratio	Metal/PVA ratio
Au-TiO₂	-	-	0.65
Ag-TiO₂	-	-	0.65
Au+Ag-TiO₂	1	0.54	1.2
Ag[Au]-TiO₂	1	0.54	1.2
Au[Ag]-TiO₂	1	0.54	1.2

4.2.3 UV Vis characterisation

Analysis of the Au, Ag and Au-Ag colloidal sols was performed by UV/Vis analysis before immobilisation on TiO₂ during catalyst synthesis. This would allow for surface information of the composition of the NPs by observing the plasmon resonances of Au and Ag and their associated effect on alloying. For the monometallic catalysts the UV analysis showed the appearance of the plasmon resonance peaks centred at ~520 nm for colloidal Au and ~400 nm for colloidal Ag (Figure 1 a). These resonance peak positions are characteristic of Au and Ag NPs below a particle size of 10 nm.^{14, 15} For the case of the Au[Ag] colloid the peak associated with the Ag plasmon disappeared, whilst there was a blue shift (shift to lower wavelength) of the Au peak to 497 nm. This is indicative of either an AuAg alloy or of a core-shell structure consisting of a thick Au shell, with the lack of any monometallic Ag NPs, since only the metal on the surface of the NPs gives a plasmon signal.^{16, 17} For the Ag[Au] colloid

two peaks at 500 and 373 nm were observed with comparable intensity. This could suggest that there is a thin layer of Ag over Au (as the plasmon peak of the core metal is still present,¹⁶) along with the presence of an AuAg alloy. The presence of significant quantities of monometallic Ag NPs is unlikely as the peak is shifted to lower wavelengths. Finally for the case of the AuAg colloid there were two peaks at 484 and 372 nm present suggesting the presence of an AuAg alloy.¹⁸ Work by Murphy *et al.* demonstrated that alloyed AuAg NPs can be formed by co-reduction of the precursors when using citrate as a capping agent.¹⁹ Diffuse reflectance UV/Vis spectra (transformed to absorption) were measured of the catalyst after the immobilisation of the NPs on to TiO₂ and are shown in Figure 1 b. All samples as expected show the absorption associated with the band gap of TiO₂ (P-25) starting in the region of 400 nm and increasing with higher energy photons. The plasmon peak of the Ag NPs on TiO₂ is significantly red shifted compared to the colloidal solution (from ~400 to 500 nm) which has been observed in previous studies of Ag.²⁰ The double peak features for Au and Ag have been lost after the deposition of the bimetallic NPs after immobilisation. Instead only one peak is observed with positions intermediate between the monometallic NPs, this may be due to interactions of the NPs with TiO₂.

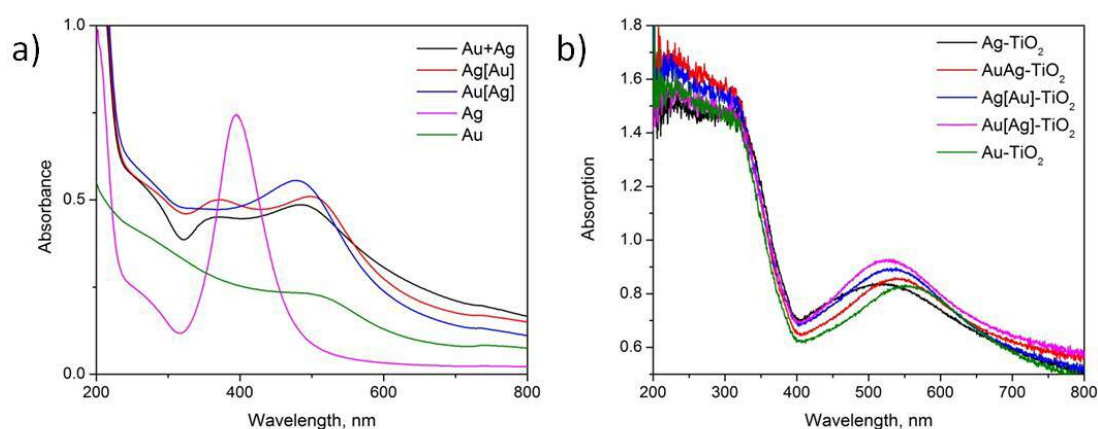


Figure 1. a) UV-vis absorbance spectra obtained from Au, Ag, AuAg, Ag[Au] and Au[Ag] colloidal solutions, (intensity of the Ag colloid spectrum was divided by 4). b) Diffuse reflectance spectra (converted to absorption) of the Ag, Au, AuAg, Ag[Au] and Au[Ag] NPs supported on TiO₂.

4.2.4 Bright field TEM analysis

TEM analysis was performed on the series of monometallic Au and Ag NPs along with the AuAg bimetallic NPs all supported on TiO₂. This was done to gain an insight into the size and morphology of the synthesised NPs. Representative bright field TEM images of each catalyst

are shown in Figure 2 and Figure 3. Particle size distribution histograms for the series of catalysts were constructed (Figure 4) from the TEM images taken, results are summarised in Table 2 along with standard deviations. The 1% Au-TiO₂ mono metallic reference sample as expected showed that the NPs are evenly dispersed over the surface of the support with an average size of 2.9 nm and standard deviation of 0.7. When 1% Ag-TiO₂ was synthesised by the colloidal method with identical parameters as that of the 1% Au-TiO₂ the average particle size was significantly higher at 8.7 nm, as in section 3.5. Also the standard deviation was a far larger value of 4.1 nm compared to the monometallic Au catalyst. This is represented in the range of Ag NPs size from 1-20 nm, while the range for the Au-TiO₂ is a significantly narrower at 1-6 nm. This is likely to be a result of PVA not being able to stabilise Ag NPs as efficiently as Au NPs.

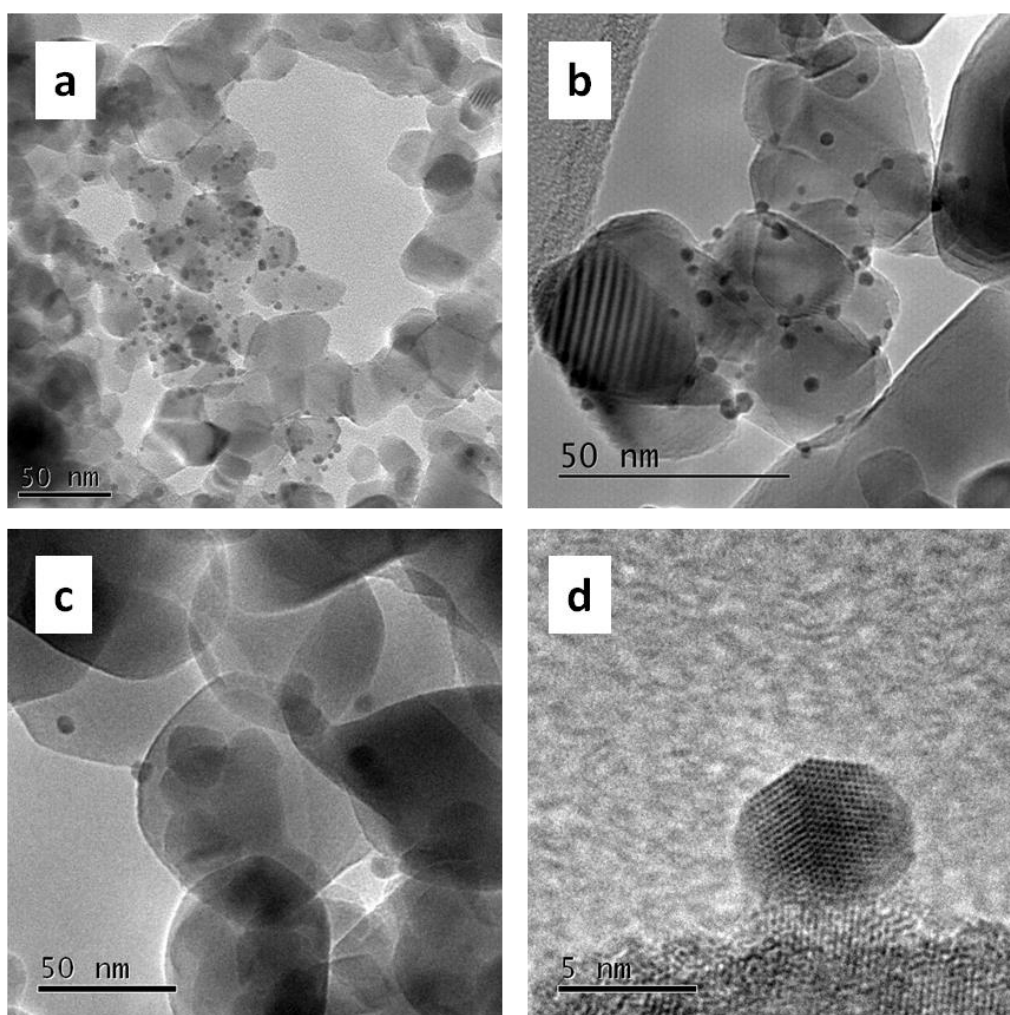


Figure 2. a and b TEM images of 1wt% Au-TiO₂, c and d TEM images of 1wt% Ag-TiO₂.

For the AuAg catalysts made by the co-reduction and sequential reduction methods the particle size was found to be in the region of 4 nm for all cases, with a standard deviation

ranging from 1.3 to 1.6 nm. Representative low and high magnification TEM images are shown in Figure 3 while particle size summary is in Table 2. It is interesting to note that the particle size of the bimetallic AuAg NPs was significantly reduced compared to the monometallic Ag NPs. For the case of the Au[Ag] NPs where Ag was reduced first there was no bimodal distribution in particle size which may be expected from the differing average particle sizes of the monometallic Au and Ag catalysts. This can be attributed to two factors i) the effect of Ag alloying with Au stabilising the NPs, thus reducing the particle size and ii) the increased metal/PVA ratio. For the case of the high resolution TEM images of the AuAg NPs (Figure 3 b, d and f) the nanoparticle lattice structure is clearly observable. The bimetallic AuAg NPs have a faceted structure which was also evident in the monometallic Au and Ag samples. Direct observation of any enrichment of either Au or Ag was not possible from these bright field images. However there may be enrichment at the surface for which bright field imaging has insufficient sensitivity to image it. STEM-HAADF imaging is a more powerful technique for TEM Z contrast imaging and will be discussed in the following section.

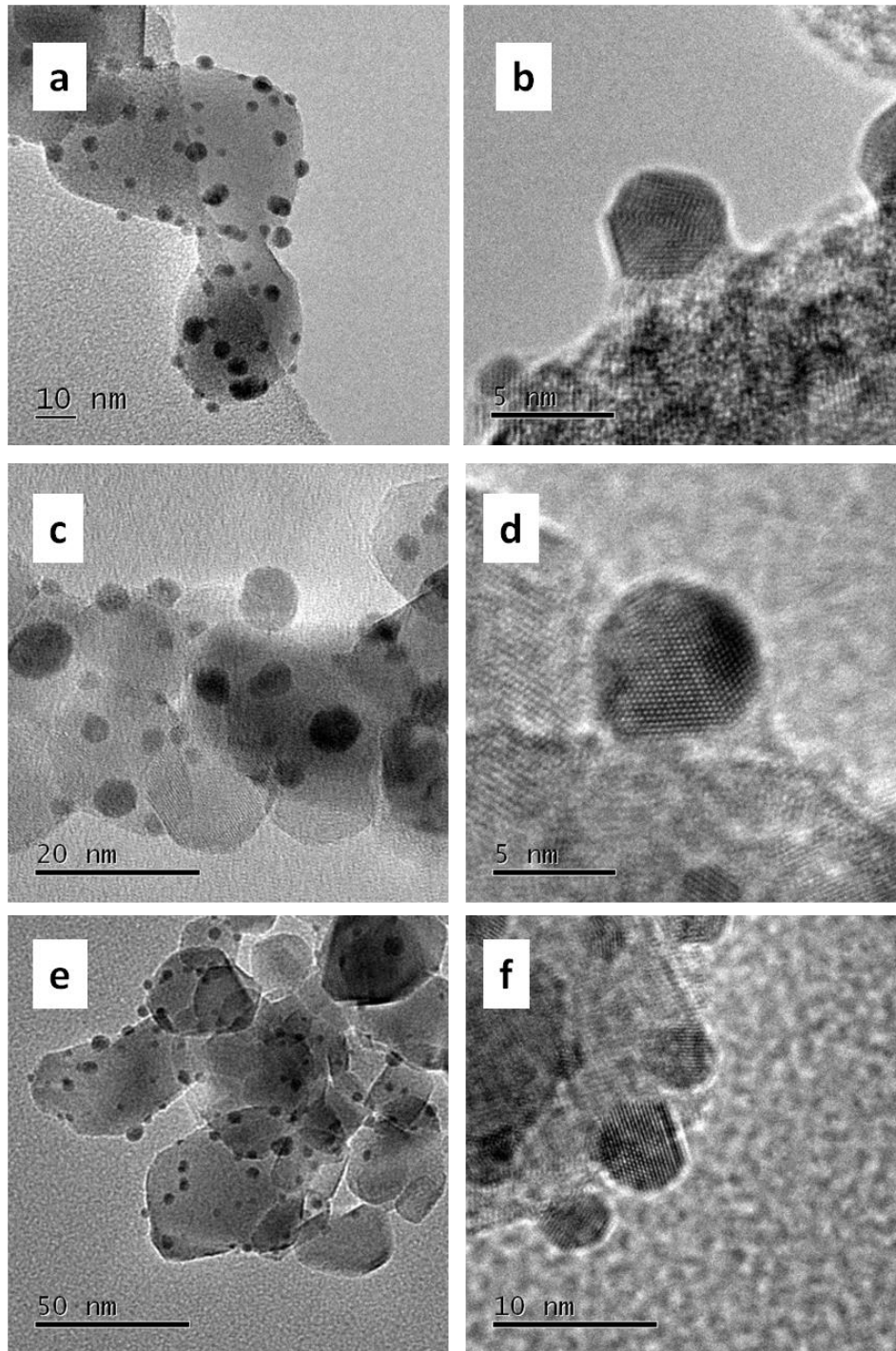


Figure 3. A, B high and low resolution TEM image of 1wt% AuAg-TiO₂, C, D high and low resolution TEM image of 1wt% Au[Ag]-TiO₂ and E, F high and low resolution TEM image of 1wt% Ag[Au]-TiO₂.

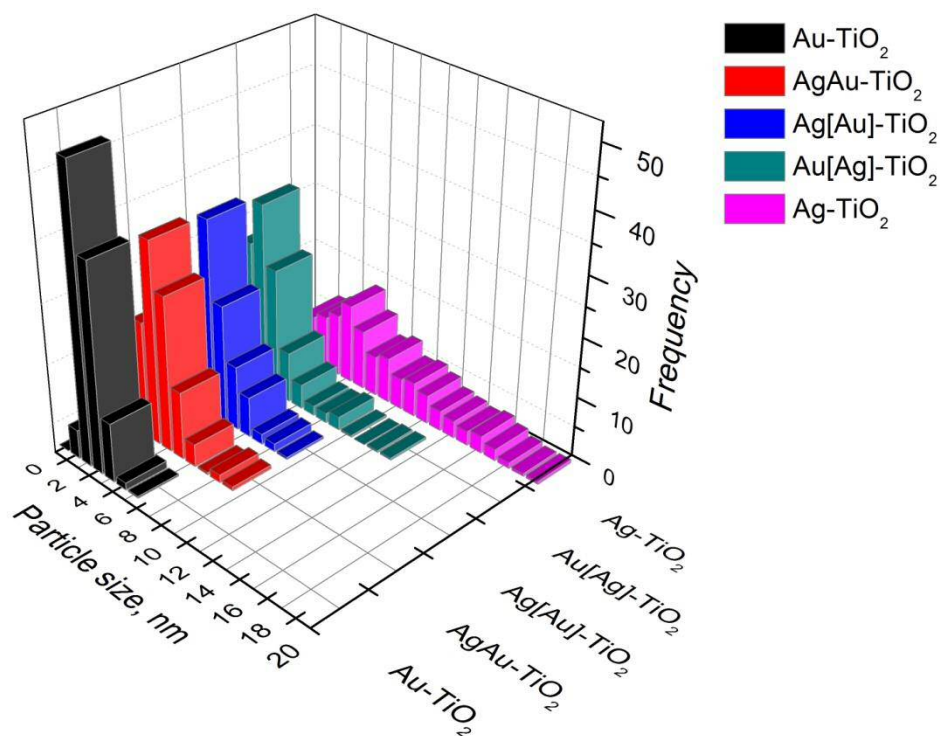


Figure 4. Histograms for the series of Au-TiO₂, Ag-TiO₂, AuAg-TiO₂, Ag[Au]-TiO₂ and Au[Ag]-TiO₂ catalysts.

Table 2. Mean particle sizes as determined from TEM measurements of the various immobilized supported Au, Ag and Au-Ag catalysts investigated in the photocatalytic experiments.

Catalyst	Average Particle size (nm)	Standard deviation (nm)	Particles counted
Au-TiO ₂	3.0	0.7	335
AuAg-TiO ₂	3.9	1.3	319
Ag-TiO ₂	8.7	4.1	208
Ag[Au]	3.9	1.5	296
Au[Ag]	4.0	1.6	320

4.2.5 STEM-HAADF analysis

The AuAg catalysts were sent to Christopher Kiely at Leigh University for further characterisation by aberration corrected scanning transmission electron microscopy (STEM). This was done in conjunction with high-angle annular dark-field imaging (HAADF) to gain information on the structure and elemental composition of individual AuAg NPs. The HAADF imaging technique collects electrons incoherently scattered at high angles (compared to the forward angle of the electron beam) as the TEM electron beam is scanned across the area of

interest on the sample. Therefore elements with a higher Z number will scatter more electrons and are seen as brighter areas on the sample. It is possible to directly image a core shell structure of a NP by this technique if the two elements have sufficiently differing Z numbers. Haruta and co-workers have previously used HAADF-STEM analysis to show the formation of Ag[Au] NPs immobilised on a metal organic framework, since Au (Z=79) and Ag (Z=47) have considerable difference in atomic number.²¹ Figure 5 shows representative high and low magnification STEM-HAADF images of the synthesised AuAg co-reduction and two sequential reduction samples. In the AuAg-TiO₂ sample prepared by simultaneous reduction (Figure 5 a-c) there was a very slight HAADF contrast decrease at the edge of the particles compared to what would be expected for a core shell structure, this leads to the conclusion that the majority of the particles are homogeneous random alloys. For the case of the Ag[Au]-TiO₂ (Figure 5 g-i) example images show a more distinct contrast change in the HAADF intensity at the edge of the NPs, this indicates that an Au rich core and a Ag rich shell is present in the NPs imaged. Finally for the case of the Au[Ag]-TiO₂ (Figure 5 d-f) no contrast changes at the edges of the NPs was observed. However UV analysis of the Au[Ag] colloid suggested an Au rich shell on the NPs as the Ag Plasmon disappeared after reduction of the Au precursor. Taking this into account no difference in contrast at the periphery of the NPs imaged would be expected due to the higher Z number of Au, instead the centre of the NPs should be lighter by comparison to the edges. This was not clearly observed here, which could be due the NPs not having a discreet Au Shell Ag core structure, instead enrichment of the metals at the shell and core.

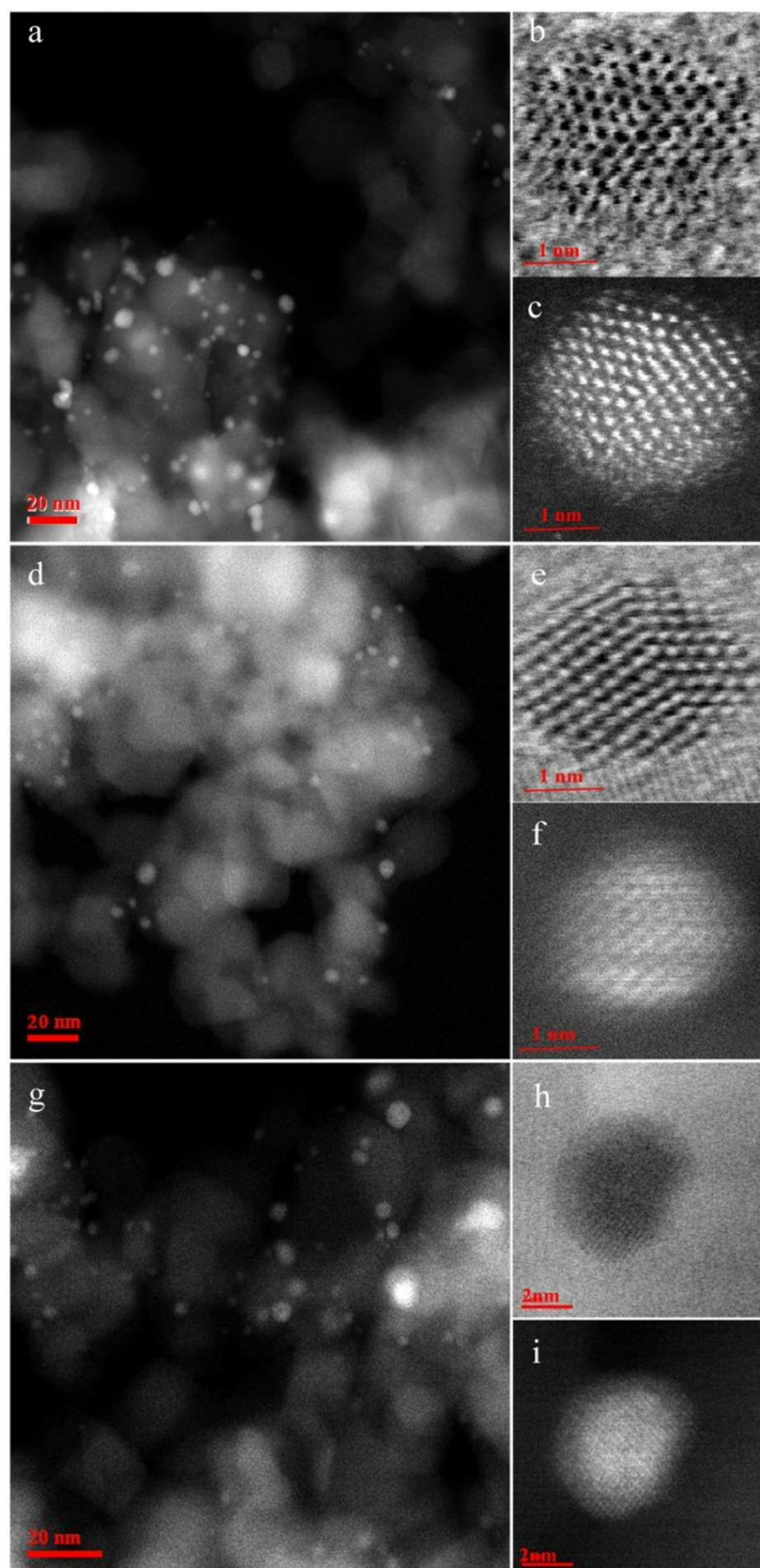


Figure 5. Representative low magnification HAADF images and high magnification BF and HAADF-STEM images of a,b,c 1wt% AuAg-TiO₂; d,e,f 1 wt-%Au[Ag]/TiO₂; g,h,i 1wt% Ag[Au]-TiO₂ catalysts

4.2.6 XPS analysis

XPS analysis of the series of AuAg catalysts with the mono metallic Au and Ag references was performed to gain an insight into the oxidation state of the elements present, as well as the atomic surface ratios of Au and Ag. Figure 6 shows the survey, Ti 2P, Au 4f and Ag 3d scans of the series of catalysts. Binding energies of the Au 4f (7/2) and Ag 3d (5/2) orbitals along with the atomic surface ratios are summarised in Table 3. The survey scans suggest all samples are mainly TiO₂ with surface adventitious carbon and minor amount of Au and Ag, as expected. Analysis of the Ti 2p (3/2) spectra clearly show that the deposition of the NPs does not alter the oxidation states of Ti, which remained to be Ti⁴⁺ in all cases. Meanwhile the Au 4f (7/2) spectra indicate the presence of metallic Au, at binding energies of 83.3-83.6 eV. It is worth noting that the binding energy of Au 4f (7/2) is shifted slightly to lower energy compared to bulk Au (84.0 eV), this can be attributed to TiO₂ negatively charging the small (~3 nm) Au NPs.^{22, 23} Caution must be taken in assigning an oxidation state of either (0) or (+1) to Ag from the Ag 3d (5/2) peak as the two peaks are separated by a small difference (~0.1 eV) which lies within experimental error. Therefore the component of metallic Ag in the samples is difficult to quantify with XPS alone. The atomic surface ratios Au/Ag (Table 3) suggest that the AuAg catalyst is enriched with Au with a value of 2 and to a lesser extent the Au[Ag] sample also shows an Au rich surface with a value of 1.24. As expected the sample which shows the least Au enrichment at the surface is the Ag[Au]-TiO₂ catalyst with a value of 1.14. This implies the sample with the highest enrichment of Ag at the surface is the Ag[Au] which is in agreement with the HAADF images showing a thin layer of Ag on the surface. The binding energy shift from the Ag-TiO₂ sample to the AgAu-TiO₂ samples may be a consequence of charge transfer from the Au to the Ag, therefore decreasing the binding energy, section 4.3.7 will explore this concept further.

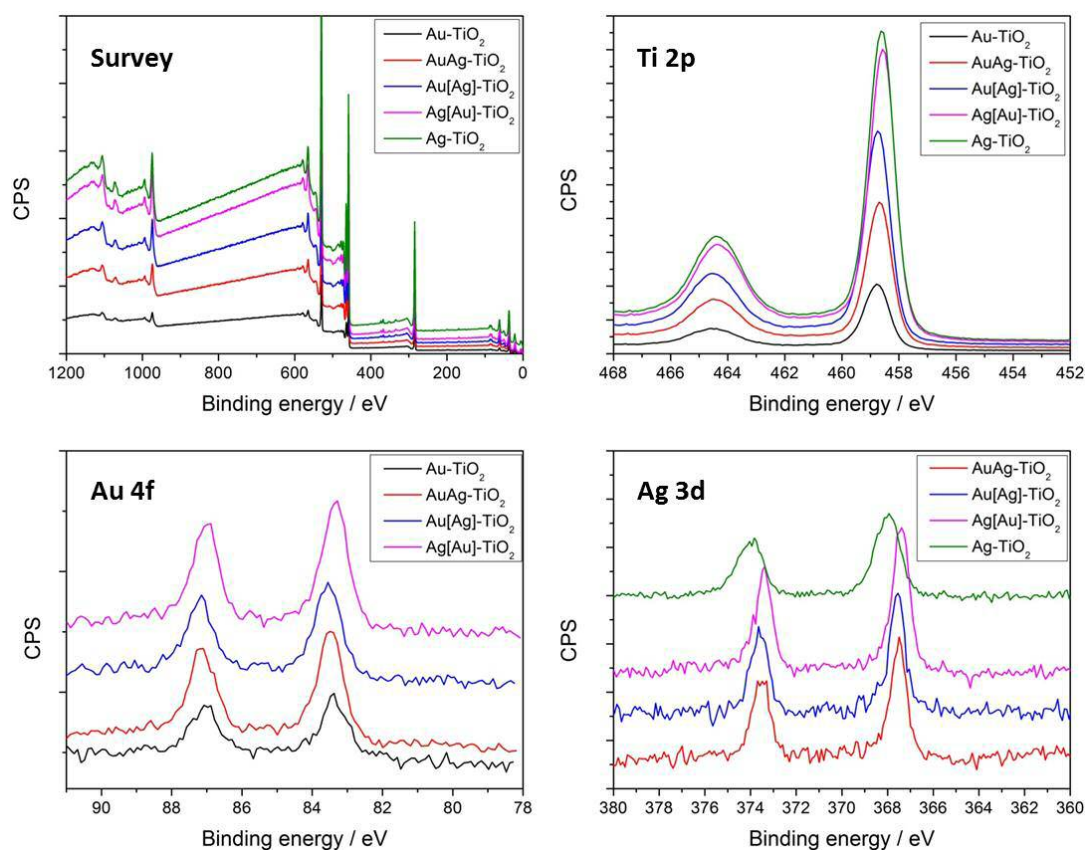


Figure 6. XPS analysis of the series of catalysts showing the Survey, Ti 2P, Au 4f and Ag 3d scans.

Table 3. Binding energies and Au/Ag atomic ratios of the supported Au, Ag, Au-Ag (1/1 atomic ratio) catalysts determined by XPS investigated in the photocatalytic experiments

Catalyst	BE (eV) Au 4f (7/2)	BE (eV) Ag 3d (5/2)	Au/Ag atomic ratio
Au/TiO ₂	83.4	-	-
Ag-TiO ₂	-	368.1	-
AuAg-TiO ₂	83.4	367.5	2.00
Ag[Au]-TiO ₂	83.3	367.3	1.14
Au[Ag]-TiO ₂	83.6	367.6	1.24

4.2.7 Catalytic testing

Photocatalytic activity of series of catalysts was evaluated by photocatalytic methanol reforming. The catalysts were made by me, as in section 2.2.5, but testing in this case was performed at Cardiff University by Julia Kennedy, with experimental set up detailed in section 2.3.8. Briefly the parameters of the reaction used were 150 mg of catalyst, 100 μ L of

methanol, 200 mL deionised water with a reaction time of 3 hours and samples taken at intervals of 30 minutes.

The H₂ production as a function of time for the series of catalysts is displayed in Figure 7, while the average rates of H₂ production is shown in Figure 8 (averaged over 3 hours). All the catalysts show a near linear H₂ production rate with time. The order of activity for the synthesised catalysts was Ag-TiO₂ < Au-TiO₂ ~ Au[Ag]-TiO₂ ~ AuAg-TiO₂ < Ag[Au]-TiO₂. It is clear from these results that the least active catalyst is the mono metallic Ag-TiO₂ which is in agreement with other published work comparing Au, Ag and AuAg NPs supported on TiO₂ for photocatalytic H₂ production.²⁴ This could be a reflection of a particle size effect as Ag NPs made by the sol immobilisation method were larger than the other NPs in the study (8.7 compared to 3-4 nm). However this is unlikely to be the main reason as to why the Ag was less active than the Au, as no reports in the literature could be found where Ag was as active as Au. The results demonstrate that the most active catalyst of the series of samples was the Ag[Au]-TiO₂ producing more H₂ than the other bimetallic AuAg catalyst and the Au-TiO₂ reference. These results show that the most effective synthesis method for the production of an active AuAg catalyst is sequential reduction of Ag onto a preformed Au sol, suggesting that the order of reduction of the metals has a significant effect on the performance of the catalyst. As the metal loading and particle size (~4 nm) is the same for the AuAg catalysts the difference in activity can in part be attributed to a variation in particle structure. Especially as analysis by UV, TEM and XPS suggest a different structure between the bimetallic samples. Taking into account the Au 4f B.E. from the XPS it was observed that there was no shift in B.E. of the AuAg NPs in comparison to the Au 4f B.E. of the monometallic Au (83.4 eV) which indicates the lack of significant charge transfer between the two metals. A slight shift in to lower B.E. was observed for Ag[Au] NPs (83.3 eV) while there was a slight increase in B.E. for the Au[Ag] NPs (83.6 eV). These results suggest that there was minimal charge transfer from the Ag to the Au for the Ag[Au] NPs and from the Au to the Ag for the Au[Ag], whilst the AuAg catalyst was largely unaffected. Therefore it is possible this slight charge transfer combined with the NPs structural differences may be the cause of the differing activity between the three bimetallic samples. One role of the NP co-catalyst is to trap electrons and prolong the lifetime of the e⁻ and h⁺ pairs thus improving the activity. As the Ag[Au]-TiO₂ catalyst demonstrated the highest activity it is reasonable to assume that this enhancement of electron transfer from Ag to Au atoms could make them a reservoir for the capture of photo-excited electrons. For the AuAg and Au[Ag] catalysts the Au 4f B.E. was higher therefore a

lower degree of electron transfer from Ag to Au is expected diminishing their ability to act as an electron reservoir.

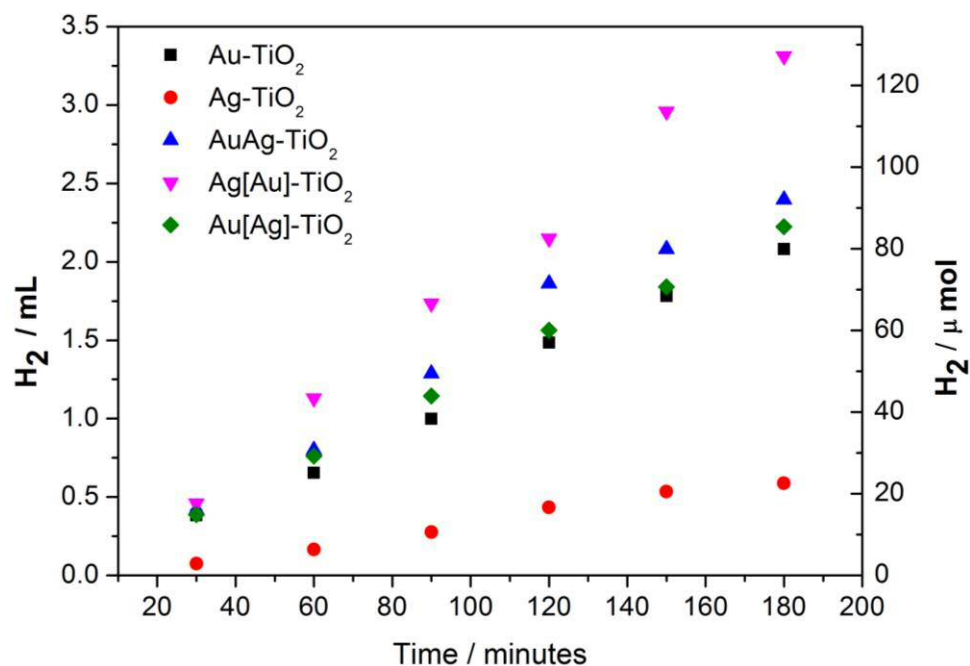


Figure 7. H₂ production as a function of time for the series of Au-TiO₂, Ag-TiO₂, AuAg-TiO₂, Ag[Au]-TiO₂ and Au[Ag]-TiO₂ catalysts from a water methanol mixture.

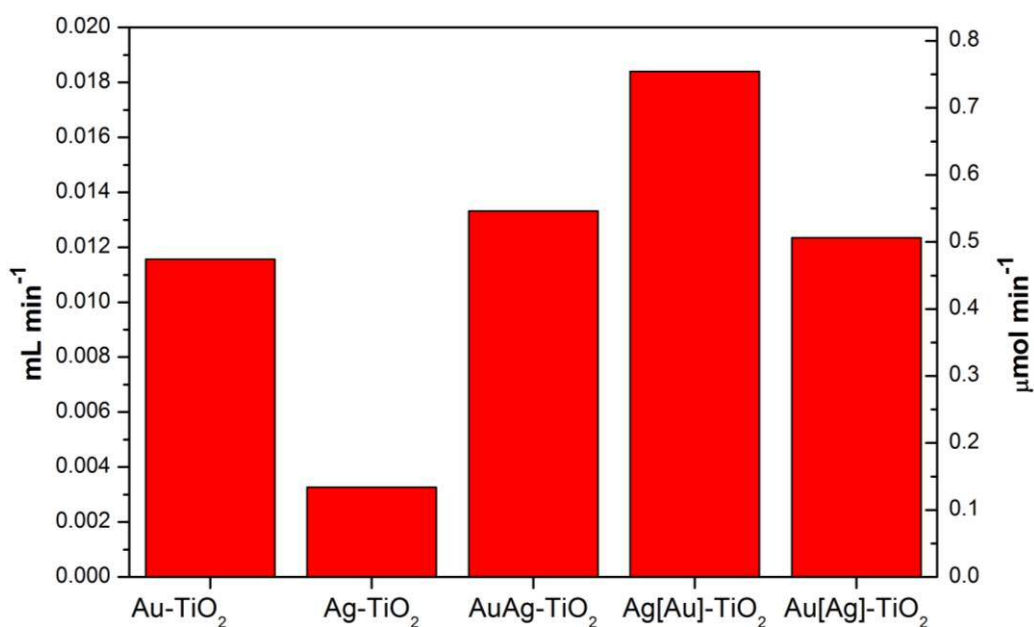


Figure 8. Rate of H₂ production averaged over 3 hours of the series of Au-TiO₂, Ag-TiO₂, AuAg-TiO₂, Ag[Au]-TiO₂ and Au[Ag]-TiO₂ catalysts in mL min⁻¹ and μmol min⁻¹.

4.2.8 Conclusions

Photocatalytic hydrogen production was studied over Au-TiO₂, Ag-TiO₂, AuAg-TiO₂, Ag[Au]-TiO₂ and Au[Ag]-TiO₂ catalysts made by the sol immobilisation technique. The bimetallic NPs were synthesised by co-reduction of the precursors to produce an AuAg alloy NPs and core-shell NPs were prepared by sequential reduction of the precursors. Enhancement in photocatalytic activity was discovered for the AuAg based catalysts over the monometallic Au and Ag references. The catalyst observed with the greatest enhancement in activity was the Ag[Au]-TiO₂ which produced in the order of 1.6 and 7 times more hydrogen than the Au-TiO₂ and Ag-TiO₂ references respectively. These results show that the order of the metal addition and reduction is significant for the preparation of active AuAg-TiO₂ photocatalysts and improving the activity of Ag-based catalysts.

4.3 Photocatalytic H₂ production from core-shell AgAu-TiO₂ catalysts with controlled shell thickness

4.3.1 Introduction

After encouraging photocatalytic results from the Ag[Au]-TiO₂ catalyst (section 4.2) which indicated that NPs with a structure of Au rich core and Ag rich shell demonstrated improved activity over other possible structures, further investigations into this system were pursued. It was decided that further Au core Ag shell catalysts (supported on TiO₂) would be synthesised with the aim being to produce Au NPs with 1 and 2 monolayers (ML) of Ag on the surface. This structure was chosen for two main reasons i) it was hoped that a thin layer of Ag on an Au NP would maximise any effect of Au on the Ag and ii) a thin layer of Ag would allow for surface information from XAFS analysis, whereas a thick layer would not. The majority of work in the section formed the basis for a published paper.²⁵ All catalysts were synthesised by Wilm Jones. Characterisation by TEM, UV, XRD and XAFS was also performed by Wilm Jones with Peter Wells helping with EXAFS analysis and XPS analysis done at Cardiff University. Catalytic testing was performed by Qian Yang at Aarhus University.

4.3.2 Catalyst synthesis

Three methods for synthesising the Au NPs with 1 and 2 ML of Ag on the surface based on modifications to the sol immobilisation technique were employed. Detailed experimental procedures for the syntheses are in section 2.2.6. The ML catalysts were given the names PD (photodeposition), SR (sequential reduction) and DR (double reduction) with either 1ML or

2ML denoting the number of monolayers of Ag theoretically deposited. A list of catalysts made is in Table 4 with theoretical weight loadings based on the amount of metal used. Samples were dried at 120 °C for 8 hours and not calcined to preserve the structure of the NPs.

Table 4. List of samples made with theoretical Au and Ag weight loadings based on amounts used in the preparation.

Catalyst	Au weight loading %	Ag weight loading %
Au-TiO₂	1	-
Ag-TiO₂	-	1
AuAg-TiO₂	0.65	0.35
1ML PD	1	0.18
2ML PD	1	0.36
1ML SR	1	0.18
2ML SR	1	0.36
1ML DR	1	0.18
2ML DR	1	0.36

4.3.3 UV Analysis

Diffuse reflectance (transformed to absorption) UV Vis analysis was performed on the series of ML samples and the two references, the results are shown in Figure 9. All samples showed the characteristic absorption of the band gap of TiO₂ (3.2 eV for anatase,²⁶) in the region of 400 nm increasing to lower wavelength. No significant shift in the position of the TiO₂ band gap was observed between the samples. The Au-TiO₂ sample exhibits the characteristic surface plasmon resonance for Au NPs in the region of 550 nm.^{27, 28} The monometallic Ag catalyst has no peak at 550 nm, while there is a peak centred at 480 nm which is due to the plasmon resonance of Ag NPs on the surface of TiO₂.²⁹ All bimetallic samples had no observable peak associated with monometallic Ag. The suggestion is that the Ag was deposited onto the Au NPs changing the absorption properties, and suggesting there are no significant quantities of segregated Ag NPs on the surface of TiO₂.

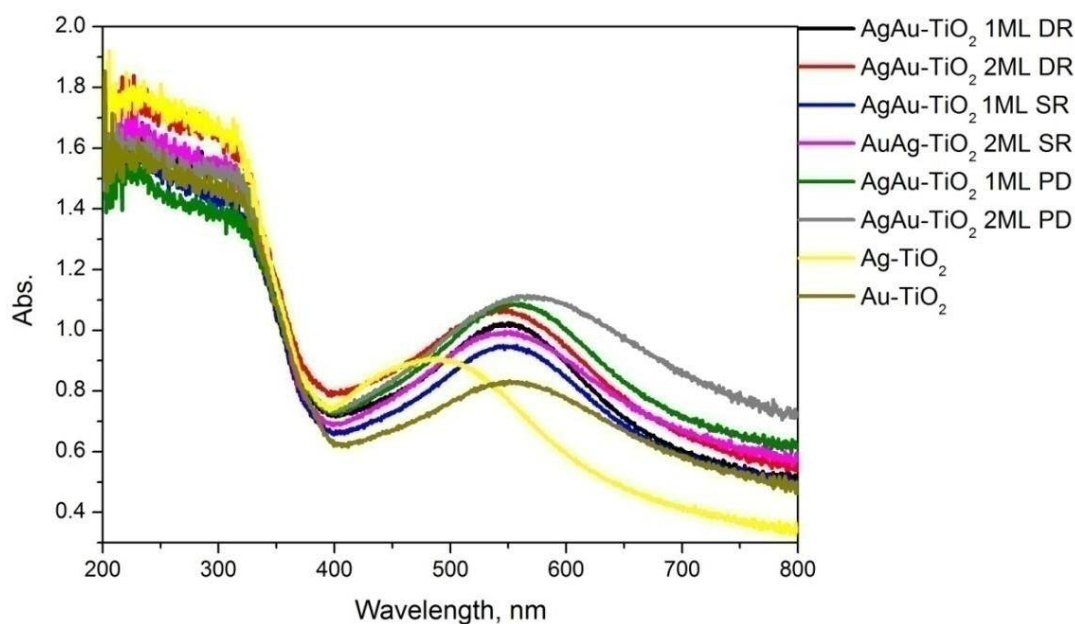


Figure 9. Diffuse reflectance UV Vis analysis (transformed to absorption) for the series of catalysts.

4.3.4 TEM analysis

Bright field TEM characterisation was performed on all samples to determine the metal NPs average size as well as the particle size distribution. Representative TEM images and the derived histograms are shown in Figure 10, and Figure 11, and the calculated average particle sizes along with standard deviations are summarised in Table 5. The TEM images demonstrate that metal NPs were deposited on the surface of the TiO₂ homogeneously with the lack of aggregation regardless of the chemical composition of the NPs and preparation method. All the core-shell NPs synthesised by the three different methods were shown to have a very similar average particle size in the region of ~ 3 nm, with a standard deviation of around 1 nm. Whilst monometallic Au NPs showed a narrow size distribution with averaged particle size of ~ 3 nm, the monometallic Ag NPs were characterised by very broad size distribution ranging from 2-20 nm with a standard deviation of 4.1 nm. It might be expected that deposition of the silver onto the surface of the Au NPs would increase the average particle size observed. However in these measurements the standard deviation is roughly a third of the value of the average particle size for the bimetallic catalysts. This results in any average particle size increase by Ag modification of Au NPs by TEM analysis difficult to observe accurately. As the particle size has remained roughly constant, it is thought possible to rule out two potential scenarios, (i) Ag was deposited in small particles away from the Au only and (ii) Ag was deposited in large particles either separate or in combination with the

Au. In both cases the average particle size would be shifted to either smaller or larger values. This can be seen more clearly from TEM images and the particle size distribution histograms (Figure 11). It is thought that since charge transfer from TiO_2 to Au is accessible resulting in negatively charged Au NPs,^{7, 23} the deposition of Ag can be achieved by a seed growth mechanism on the Au core.

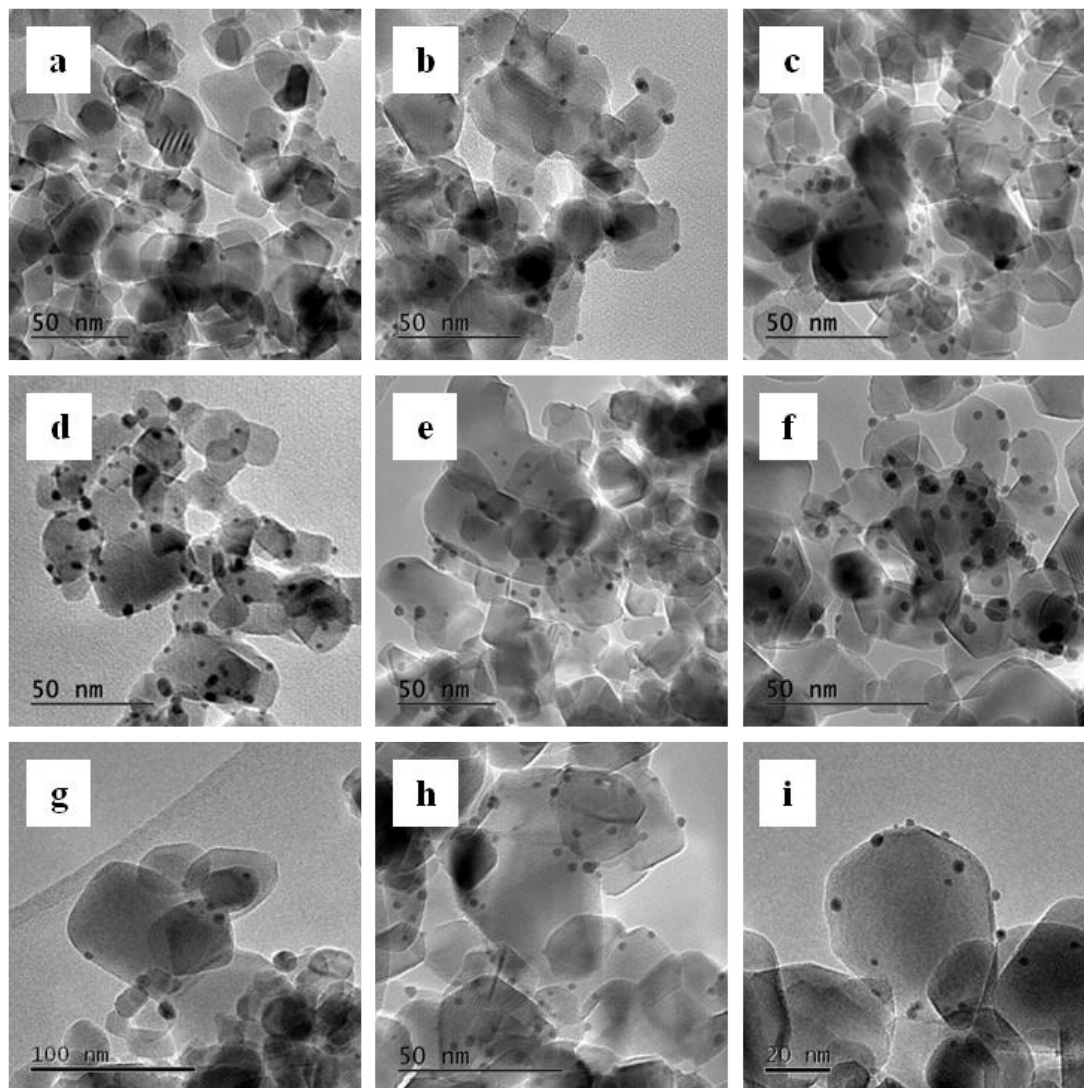


Figure 10. Representative bright field images TEM of a) 1ML PD, b) 2ML PD, c) 1ML SR, d) 2ML SR, e) 1ML DR, f) 2ML DR, g) Ag- TiO_2 , h) Au- TiO_2 and AuAg- TiO_2 .

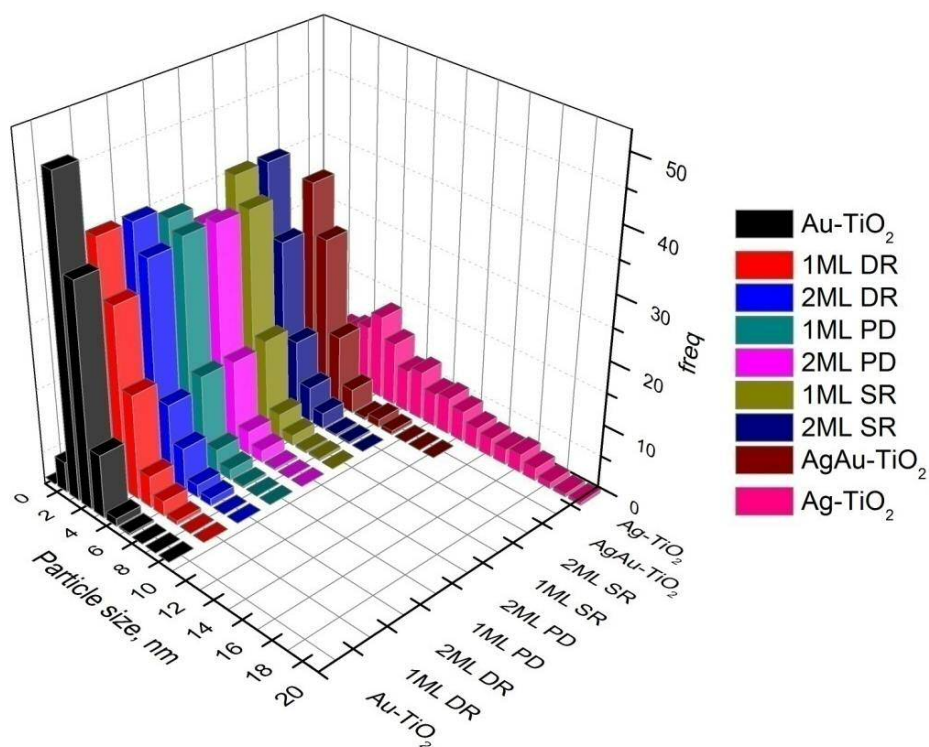


Figure 11. Particle size distributions of as-prepared metal NPs supported on TiO₂.

Table 5. Average particle size and standard deviation of metal NPs supported on TiO₂

Catalyst	Average Particle size (nm)	Standard deviation (nm)	Particles counted
Au/TiO ₂	3.1	1.2	335
AuAg/TiO ₂	3.9	1.3	319
Ag/TiO ₂	8.7	4.1	208
1ML SR	3.2	1.1	378
2ML SR	3.1	1.1	327
1ML PD	3.2	1.1	320
2ML PD	3.2	1.1	316
1ML DR	3.3	1.1	330
2ML DR	3.4	1.1	324

4.3.5 XPS analysis

XPS analysis was performed for all samples and representative scans are shown in Figure 12 along with a summary of binding energies in Table 6. The survey scans show that the samples are predominantly TiO₂ with minor amounts of surface metals (Au and Ag) as well as adventitious carbon. The Ti 2P spectra clearly show Ti in the +4 oxidation state in all cases suggesting that the deposition of the metal NPs had no effect on the oxidation Ti state. As expected the position of the Au 4f (7/2) peak for the Au-TiO₂ sample suggests the presence

of metallic Au NPs on TiO₂ (83.4 eV).²³ After the deposition of Ag by all methods onto the Au NPs the B.E. of the Au 4f (7/2) peak shifts to a slightly higher value of ~83.7 eV. The shift could be due to some charge transfer from the Au to the Ag.

The position of the Ag (3d) peaks for Ag(0) and Ag(I) are separated by only ~0.1 eV therefore it is not possible to accurately distinguish between them in XPS analysis (the XANES and EXAFS in later sections will be more useful for this). There is a shift in the Ag 3d B.E. of all the ML samples to a lower value (~0.3 eV) compared to an Ag-TiO₂ reference. These two shifts in the Ag 3d and Au 4f complement each other and the suggestion is that they originate from charge transfer from the Au to the Ag (with the d band vacancy from the XANES analysis providing more information on this). All three core-shell 1ML samples presented very similar Ag/Au ratios (0.43 – 0.46) as was the case for the three 2ML samples (0.69 – 0.74). This confirms that the synthesis of metal/TiO₂ catalysts was successful and a larger amount of Ag has been deposited for the 2ML samples.

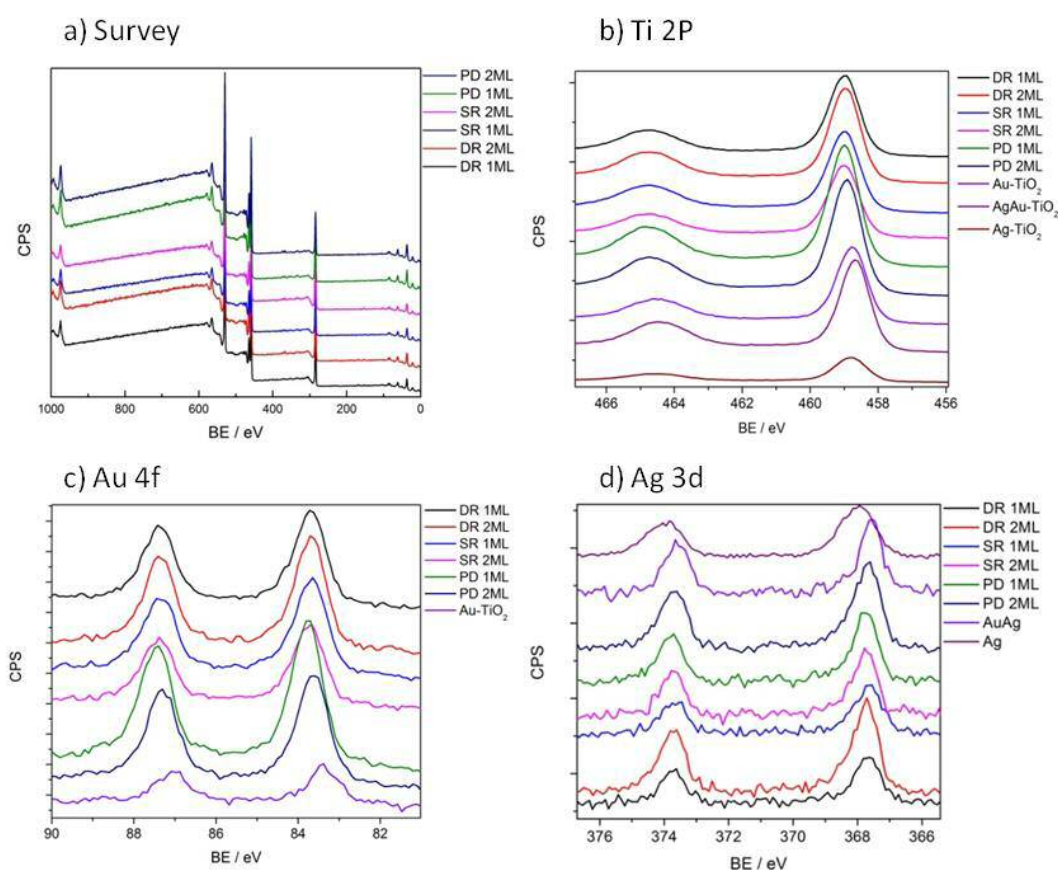


Figure 12. XPS survey spectra of all samples a) high resolution XPS spectra of Ti 2p b), Au 4f c), and Ag 3d d).

Table 6. Summary of metal loading, BE, and Ag/Au ratios derived from XPS analysis.

Catalyst	Peak name	BE(eV)	Ag/Au ratio
Au-TiO₂	Au 4f	83.4	-
Ag-TiO₂	Ag 3d	368.0	-
1ML PD	Au 4f	83.7	0.45
	Ag 3d	367.8	
1ML SR	Au 4f	83.7	0.43
	Ag 3d	367.6	
1ML DR	Au 4f	83.7	0.46
	Ag 3d	367.6	
2ML PD	Au 4f	83.6	0.69
	Ag 3d	367.6	
2ML SR	Au 4f	83.7	0.69
	Ag 3d	367.8	
2ML DR	Au 4f	83.7	0.74
	Ag 3d	367.7	

4.3.6 XANES analysis

Analysis of the whole series of catalysts was performed by XAFS at station B18 at the Diamond light source synchrotron to gain an insight into Au and Ag oxidation state, coordination number and bond length. Data were collected in fluorescence mode; several scans were taken and merged together to reduce noise. Details are in the experimental section (2.9.9). The goal of this combined analysis was to provide information on the average structure of the NPs and to support whether a core-shell structure was indeed formed.

Figure 13 shows the XANES spectra and first derivative of the XANES spectra for the series of catalysts. Typically the position of the main absorption edge can be affected by the oxidation state of the element of interest. However for Ag the initial edge jump of the references of Ag foil and Ag₂O are similar in energy with differences only occurring after this. Distinguishing between Ag(0) and Ag(I) quantitatively by the XANES alone with a degree of certainty is then difficult. A linear combination fit would in theory be able to quantify the oxide content, however an accurate reference sample of core-shell NPs would be necessary, and this was unavailable. The derivative plot is alternative way of looking at the data to see changes in the position of the absorption edge, Figure 13. From this plot all of the core-shell samples have a similar absorption in the XANES region. The shape of the XANES spectra for the core-shell samples beyond the main absorption edge is affected by alloying and the reduction in particle size; therefore it would not be expected for the samples to match either reference exactly. It can be inferred, however, from the shape of the absorption edge that the oxidation

state of the Ag in the core shell samples is not exclusively metallic, and a mixture of Ag(0) and Ag(I) is likely to be present, with the EXAFS providing more information on this.

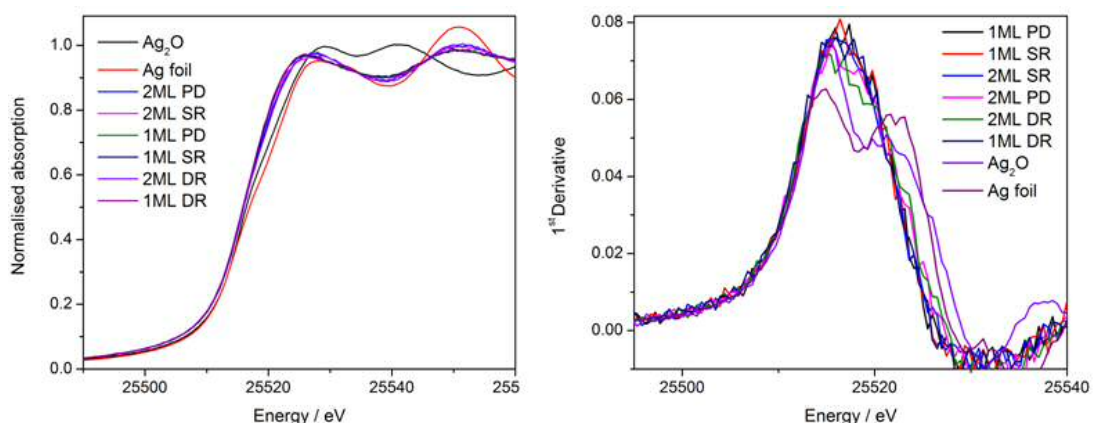


Figure 13. Ag K edge XANES spectra (left) and first derivative (right) of Ag foil, Ag₂O, 1ML PD, 2ML PD, c) 1ML SR, d) 2ML SR, e) 1ML DR and f) 2ML DR.

4.3.7 d band vacancy calculation

Estimation of the d band orbital electron density of Au was carried out using the method developed by Mansour.³⁰ Due to time constraints (at Diamond light source) only catalysts made by the PD method were analysed by this process. The white line feature of the Au L₃ edge is caused by the $2p_{1/2} \rightarrow 5d_{3/2}$ dipole allowed transition, while for the L₂ edge white line is due to the $2p_{3/2} \rightarrow 5d_{3/2}$ and $5d_{5/2}$ dipole allowed transition, this results from the spin-orbit interaction of the Au d-states.³¹ These transition are governed by the selection rules $\Delta L = \pm 1$ and $\Delta J = 0, \pm 1$ where L is the orbital angular momentum quantum number and J total orbital angular momentum number. Taking into account the selection rules, the white line can be solely attributed to $p \rightarrow d$ transitions. To calculate the d-band vacancies in all the samples the L₂ and L₃ XANES spectra were normalised to an edge jump value of one (Figure 14 b). Both the XANES spectra were then adjusted so that the $E_0 = 0$ eV, taking E_0 as the maxima of the peak of the first differential of the edge jump (Figure 14 c). This resulted in the oscillations in the EXAFS region of the spectra symmetrically overlapping one another at more than 40 eV above the X-ray absorption edge. The region between -10 and 13 eV relative the absorption edge ($E_0 = 0$ eV) was used for calculating the hole density. Figure 14 d shows the Au L₂ and L₃ edges (for the 1wt% Au-TiO₂ sample) normalised and on the same scale, with the difference in the white line intensity between the L₃ and L₂ evident. This procedure is used as theoretically the EXAFS oscillations for both the L₃ and L₂ should be the same, with the differences in the XANES due to the transition selection rules. Changes in the vacancies of the $d_{3/2}$ and $d_{5/2}$ states were calculated by the following equations.³²

Equation 1

Equation 2

Where $\Delta A_j = \Delta A_{j,\text{Bulk}} - \Delta A_{j,\text{Sample}}$ is the difference in area values of the L_j -edge XANES spectrum in $\text{eV}\cdot\text{cm}^{-1}$. Finally, all areas calculated were multiplied by the x-ray absorption cross-section area at the absorbing edge and the density of the absorbing material. Values of 57.3 and $107.7\text{cm}^2\text{g}^{-1}$ were used for the L_2 and L_3 edges respectively. The density of Au used was 19.3g cm^{-3} .³³

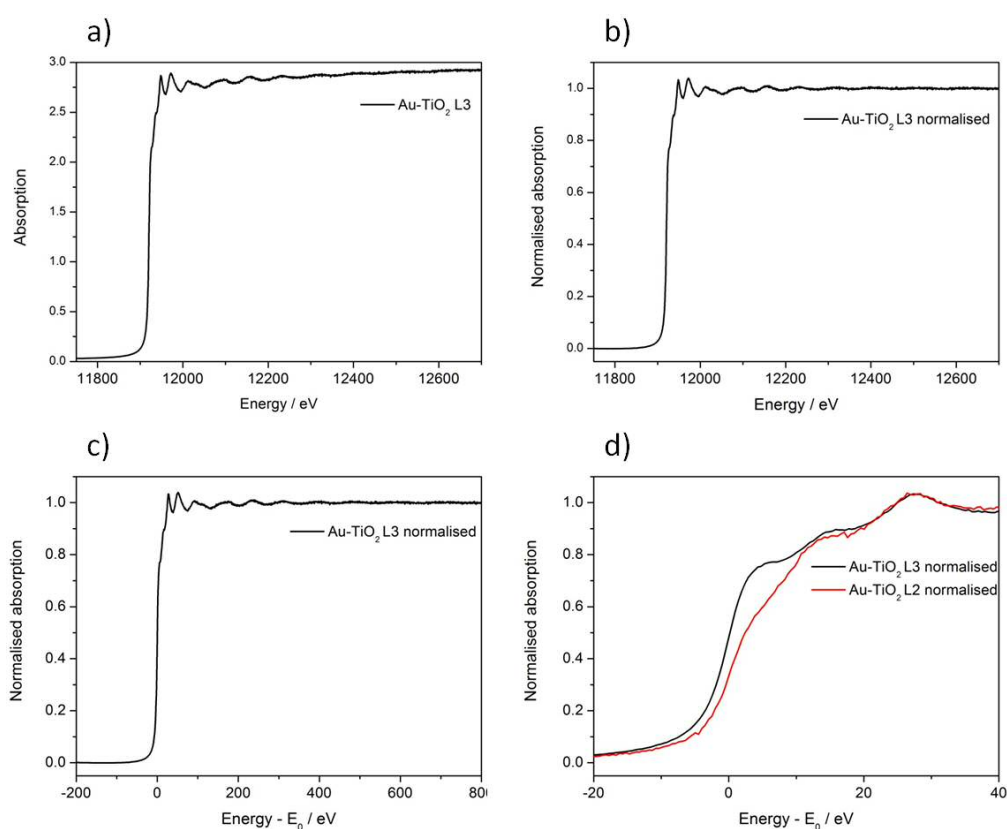


Figure 14. shows a) raw data of Au L₃ absorption b) Au L₃ absorption normalised to an edge jump of 1 c) Alignment of energy scale to maxima in the first derivative of the absorption edge and d) XANES region (-20 to 40 eV relative to E₀).

Table 7 summarises results from Equations 1 and 2 for the Au foil, Au-TiO₂ and the two AgAu-TiO₂ catalysts, with Figure 15 differences of the d-orbital vacancies from bulk Au. As can be seen addition of 1ML of Ag increases the d-orbital vacancy from the Au-TiO₂ sample with the 2ML sample increasing this even further.

Table 7. Derived parameters for the unoccupied d states (values for Au foil were taken from reference,³⁴), units of h in atom^{-1} .

Sample	ΔA_2 ($\text{eV}\cdot\text{cm}^{-1}$)	ΔA_3 ($\text{eV}\cdot\text{cm}^{-1}$)	$\Delta h_{3/2}$	$h_{3/2}$	$\Delta h_{5/2}$	$h_{5/2}$	$\Delta h_{3/2} + \Delta h_{5/2}$
Au Foil, ³⁴	0	0	0	0.118	0.000	0.283	0.000
Au-TiO₂	610	540	0.024	0.142	0.012	0.295	0.036
1ML PD	1667	1018	0.067	0.185	0.019	0.302	0.086
2ML PD	1114	1912	0.044	0.162	0.050	0.333	0.094

Obviously the d band properties of the Au NPs were different from those of the Au foil. The influence of additional Ag on Au was to further increase the vacancy density of d orbitals, indicating improved charge storage on Core-shell NPs. The results presented here agree with work published by Nishimura *et al.*³² Therefore the BE shift observed from XPS on all core-shell co-catalysts most likely originated from charge transfer from Au to Ag.

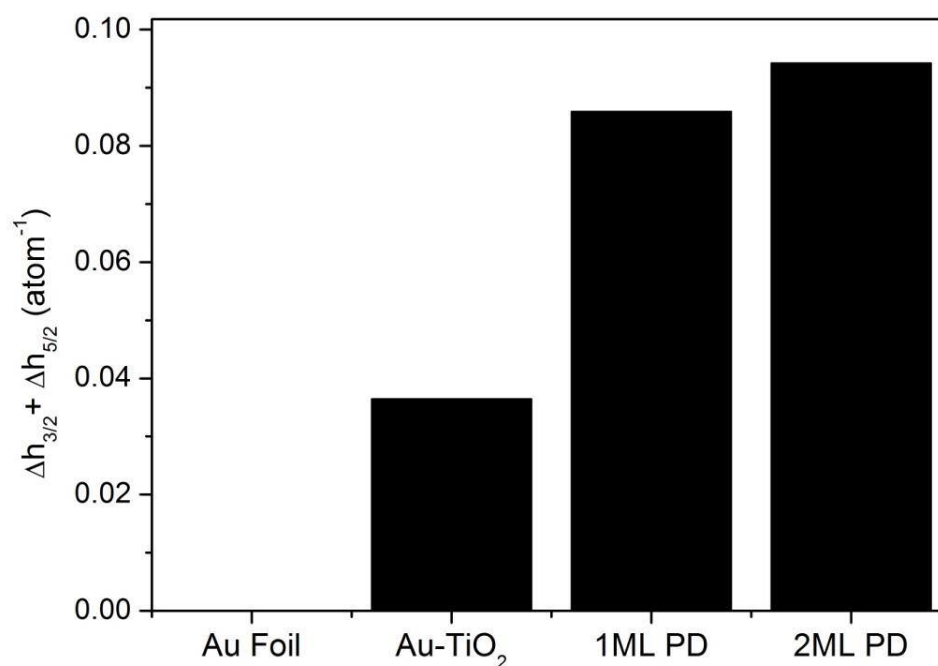


Figure 15. Differences of the d-orbital vacancies from bulk Au.

4.3.8 EXAFS analysis

The determined 1st shell EXAFS fitting parameters derived from the k^2 weighted Fourier transform for both Au L₃ and Ag K data are shown in Table 8, as well as the k^2 weighted magnitude of Fourier transformed data and the corresponding 1st shell fit, which is shown in Figure 17 (Au L₃) and Figure 16 (Ag K).

The EXAFS data show that for all ML catalysts prepared that the Ag environment has a consistent coordination to O of roughly 1. It would be expected that the oxidic Ag present in the samples would be in the form of Ag₂O which has a primary coordination to O of 2. Therefore as all the core-shell samples have an Ag-O coordination of 1 it can be estimated that roughly 50% of the Ag present in the samples is in the Ag₂O form (or Ag⁺).

As EXAFS probes all environments equally and gives an average signal it would be expected the Ag-M coordination number will be much reduced due to the large oxide content. This indeed was the case as the Ag-Au and Ag-Ag coordination number never exceeded a value of ~3.5 for all ML samples. For the case of Ag-Ag the first shell coordination in the Ag₂O reference will be 0. An increase in the Ag-Au and Ag-Ag coordination numbers between the 1 and 2 ML samples was observed as would be expected from an increase in the Ag content. However the oxide content remained roughly constant at ~1 whether 1 or 2 ML equivalent of Ag was deposited.

The Au L₃ edge EXAFS analysis indicates that the Au environment appears largely unchanged by the addition of Ag for the 1 and 2 ML samples (see Table 8). As the coordination number for the Au-TiO₂ sample on to which the Ag was deposited has a value of 10(1) with this value not changing significantly after deposition. Coordination of Au-Au in a monometallic NP is equivalent to a particle size of 2.4 ± 0.8 nm, see section 3.2.3. This, combined with the Ag-Au coordination numbers, suggests that the Ag has not penetrated into the Au NPs and has remained on the surface.

The Ag K edge k² weighted experimental data for all ML samples becomes noisy at around a K (Å⁻¹) value of 6 (Figure 16), whereas the Au L₃ k² weighted experimental data becomes noisy around K (Å⁻¹) values of around 10 (Figure 17). This is indicative of the lack of long range order for Ag, suggesting that there are no segregated large particles of Ag on the surface, which is supported by the UV analysis. As the EXAFS data shows, near equal contributions from the Au and Ag neighbours this is what would be expected from an overlayer of Ag on the surface of the Au NPs. It is therefore proposed by combining the XAFS characterisation that Ag is present on the surface of the Au NPs as a mixture of AgAu alloy Ag₂O.

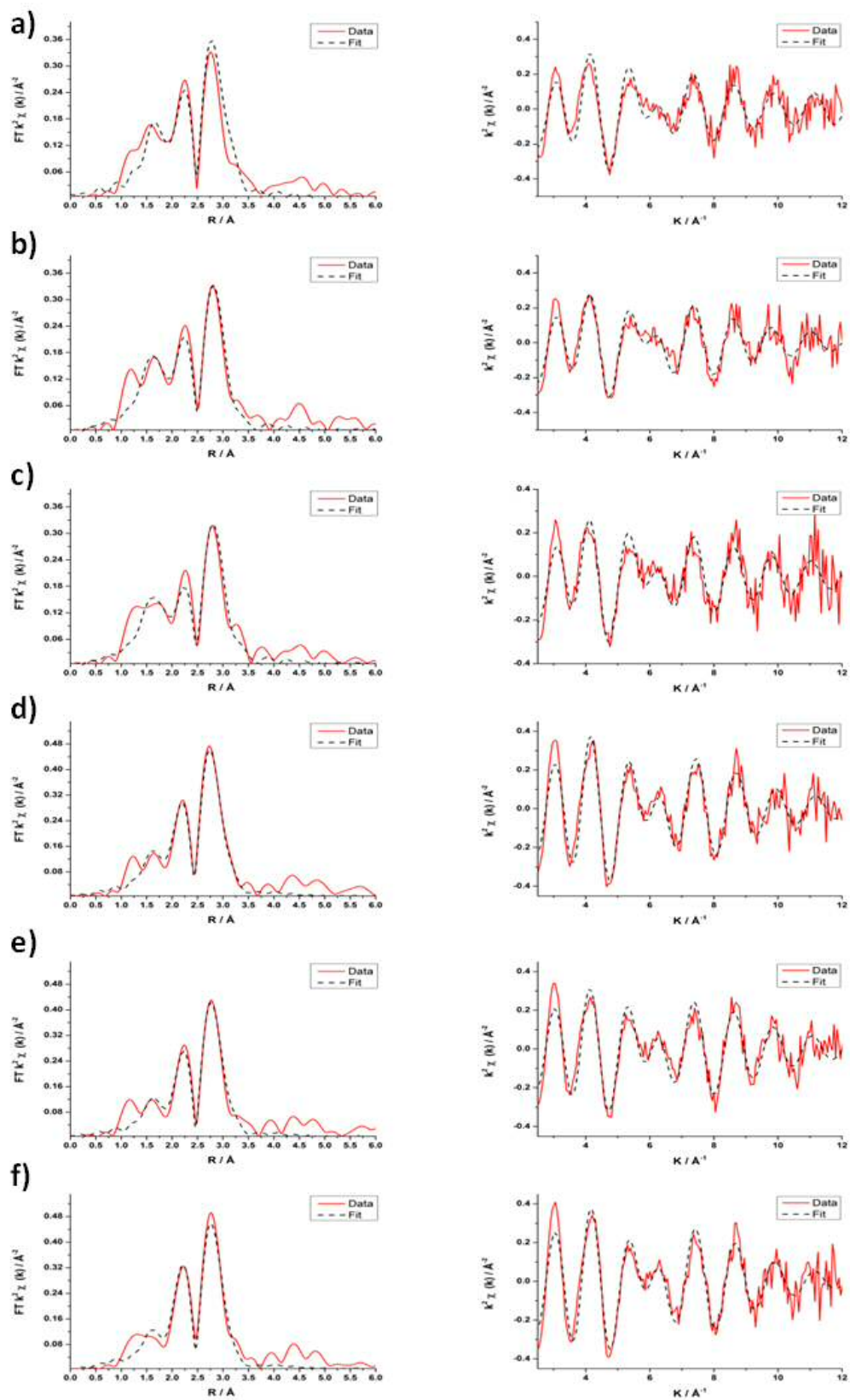


Figure 16 Right Ag K edge k^2 weighted experimental data and 1st shell fit, left corresponding furrier transform for a) 1ML PD b) 1ML SR c) 1ML DR d) 2ML PD e) 2ML SR and f) 2ML DR.

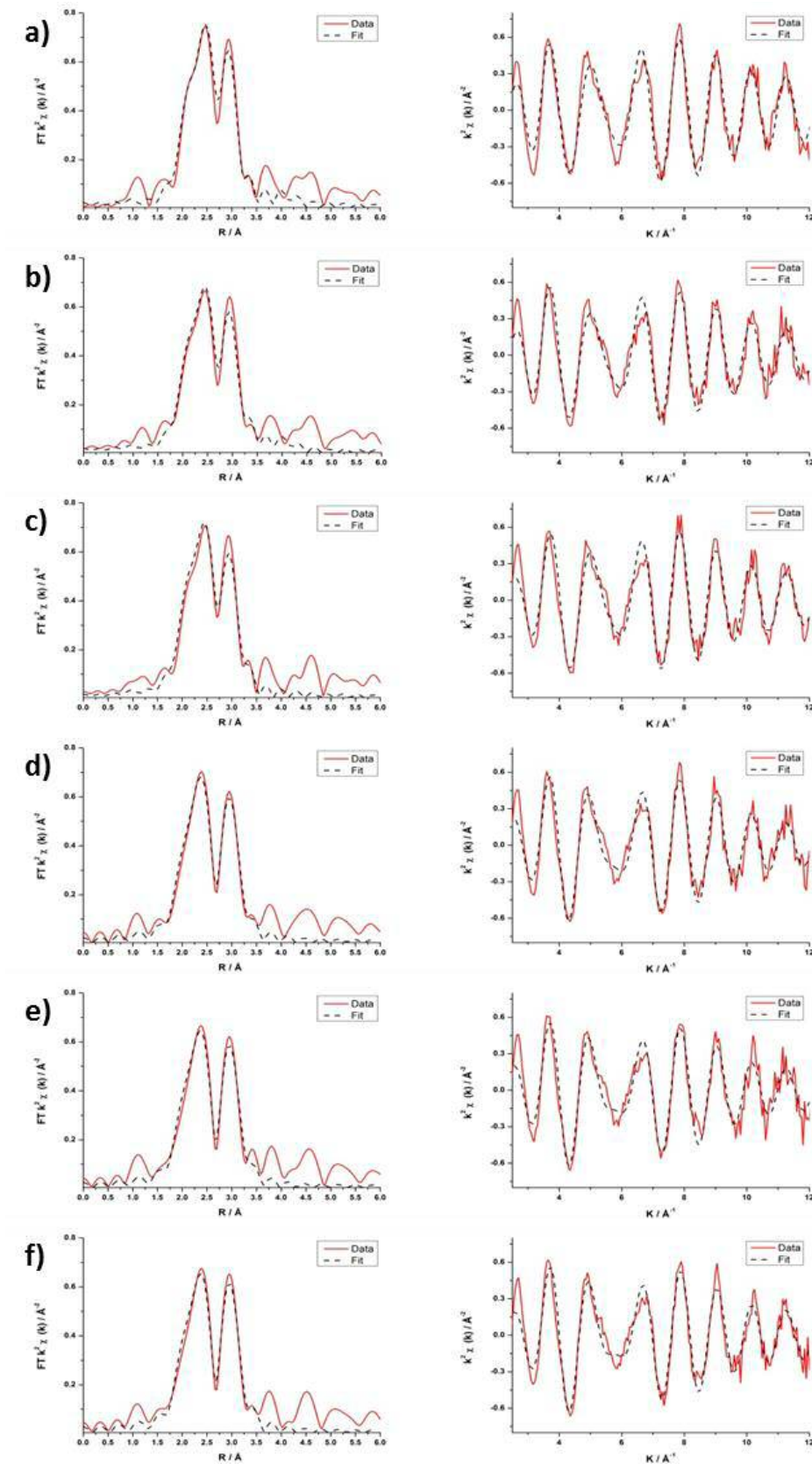


Figure 17 Right Au L₃ edge k^2 weighted experimental data and 1st shell fit, left corresponding furrier transform for a) 1ML PD b) 1ML SR c) 1ML DR d) 2ML PD e) 2ML SR and f) 2ML DR.

Table 8. 1st shell EXAFS fitting parameters derived from the k_2 weighted Fourier transform for both Au L_3 and Ag K data.

Sample	Abs Sc	N	$R / \text{\AA}$	$2\sigma^2 / \text{\AA}^2$	E_f / eV	R_{factor}	
Au-TiO₂	Au L_3	Au – Au	10 (1)	2.84 (2)	0.009 (1)	4 (1)	0.02
1ML PD	Au L_3	Au – Au	10.9 (7)	2.84 (1)	0.009 (1)	3 (1)	0.03
	Ag K	Ag – O	0.9 (2)	2.26 (4)	0.007 (4)	4 (1)	0.03
		Ag – Ag	2.6 (6)	2.91 (2)	0.009 (2)		
		Ag – Au	2.1 (7)	2.96 (3)	0.009 (4)		
1ML DR	Au L_3	Au – Au	11.4 (7)	2.84 (1)	0.010 (1)	3 (1)	0.03
	Ag K	Ag – O	1.1 (2)	2.26 (3)	0.011 (5)	3 (1)	0.05
		Ag – Ag	2.4 (5)	2.93 (2)	0.010 (2)		
		Ag – Au	1.9 (8)	2.95 (7)	0.015 (9)		
1ML SR	Au L_3	Au – Au	10.9 (7)	2.84 (1)	0.010 (1)	3 (1)	0.03
		Ag – O	1.1 (2)	2.24 (2)	0.009 (4)	3 (1)	0.03
	Ag K	Ag – Ag	2.6 (6)	2.91 (2)	0.011 (2)		
		Ag – Au	2.1 (7)	2.91 (4)	0.013 (5)		
2ML PD	Au L_3	Au – Au	10 (2)	2.85 (3)	0.010 (2)	4 (1)	0.02
		Ag – O	1.0 (2)	2.25 (2)	0.009 (4)	1 (1)	0.02
	Ag K	Ag – Ag	3.5 (5)	2.88 (1)	0.011 (1)		
		Ag – Au	2.9 (4)	2.89 (3)	0.013 (4)		
2ML DR	Au L_3	Au – Au	9 (2)	2.85 (3)	0.009 (1)	4 (1)	0.03
		Ag – O	1.0 (2)	2.26 (3)	0.011 (5)	1 (1)	0.02
	Ag K	Ag – Ag	3.2 (4)	2.88 (2)	0.011 (2)		
		Ag – Au	3.5 (6)	2.88 (3)	0.012 (3)		
2ML SR	Au L_3	Au – Au	10 (2)	2.84 (3)	0.009 (2)	4 (1)	0.04
		Ag – O	1.0 (2)	2.28 (3)	0.011 (5)	2 (1)	0.02
	Ag K	Ag – Ag	3.0 (4)	2.90 (1)	0.010 (1)		
		Ag – Au	2.5 (6)	2.90 (3)	0.012 (4)		

4.3.9 Photocatalytic performance evaluations

Samples were sent to Qian Yang at Aarhus University Denmark to perform photocatalytic performance evaluation of the series of AuAg catalysts. Details of the experimental set up and reaction parameters can be found in section (2.4.9). Time-resolved photocatalytic H₂ evolution data and derived H₂ evolution rates can be found in Figure 18. The results determined that Au NPs supported TiO₂ showed the highest catalytic performance and the Ag NPs supported on TiO₂ demonstrated very poor activity relative to the Au catalyst. The performance of Au-TiO₂ was similar to previously reported values using the same reactor system.⁶ It was also observed that when Ag was deposited on to the surface of the Au NPs H₂ generation was decreased in all cases. This is in contrast to reported data for Au_{core}Pd_{shell} or Au_{core}Pt_{shell} NPs as co-catalysts which improved activity compared to Au-TiO₂.^{6, 35, 36} Taking these results into account it was clear that there was not the positive synergistic effect

between the Au and Ag which was hoped for with the 1 and 2 ML catalysts. This was not expected as the results from section 4.2 demonstrated improved activity for a AuAg co-catalyst with the structure Au rich core and Ag rich shell over a Au co-catalyst, with a 1:1 weight ratio. However this does match results from the literature which states that Au is more active than Ag as a co-catalyst for H₂ generation.⁹ Therefore it is clear from the results in this section that Ag alloyed with Au made by the methods detailed here (1 and 2 MLs of Ag) are not a good candidate for a co-catalyst for photocatalytic hydrogen production. This is despite the excellent electron storage capabilities of Ag NPs compared to Au or Pt.⁷ Perhaps as the higher work function of Au facilitates improved electron transfer from the TiO₂ to the Au NP compared to Ag this could be a dominant factor governing relative activity between the two metals. Also it is probable the ethanol being reformed in this study is more easily decomposed on the surface of Au than Ag which would likely improve reaction rates. The synthesis method of the core shell NPs also affected the H₂ evolution performance, where the 1ML PD catalyst exhibited higher activity compared to all other bimetallic co-catalyst NPs. The catalyst demonstrating the least activity for the ML samples was the 1ML DR sample. The characterisation shows little differences of the catalyst made by the three methods therefore it is difficult to attribute variations in activity for the ML sample to structural differences between the NPs. However as the XPS and XAFS characterisation was performed on the catalysts before being exposed to reaction conditions it is possible that some changes to the NP structure may occur during the reaction and that these changes are responsible for the differences observed. An in operando study would be needed to obtain information during the reaction. Before the reaction was begun all the catalysts were subject to 2 hours UV irradiation under reaction condition to help remove the PVA protecting ligand. It is likely (although there is no direct evidence for this here) that the Ag₂O would be reduced to Ag during this step.

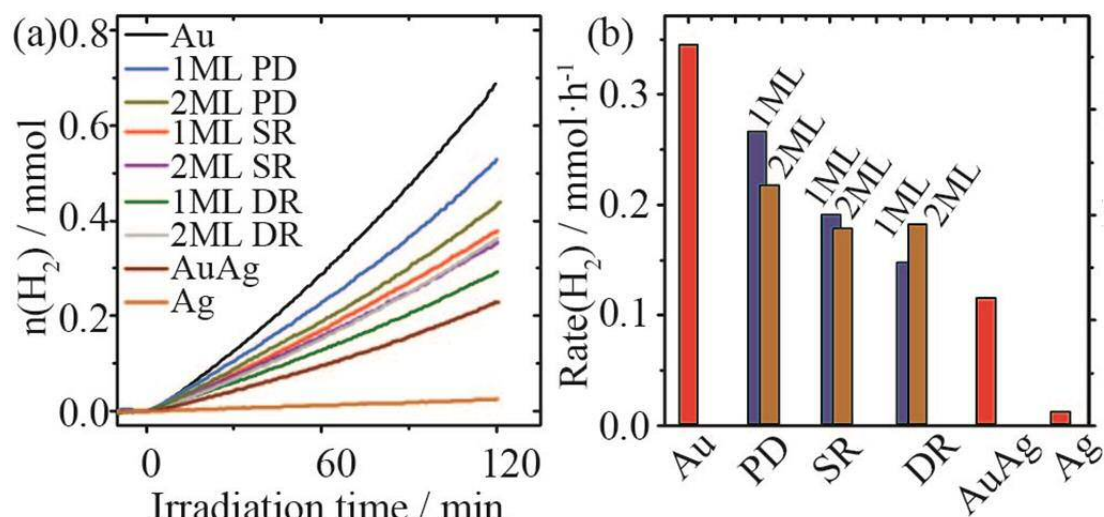


Figure 18. (a) Time-resolved photocatalytic H₂ evolution from 25 vol% ethanol-water solution using metal NPs supported on TiO₂. (b) The derived H₂ evolution rates in mmol h⁻¹.

4.3.10 Conclusions

In this section we have shown the successful synthesis of well-defined AuAg NPs with a core-shell structure, which was confirmed by TEM, XPS and XAFS. The supported model of the average NP structure was an Au_{core} with an over layer of an AuAg alloy and roughly 50% Ag₂O. Three methods were used to produce the bimetallic NPs with characterisation suggesting each method was successful and only little structural differences between the 1ML analogues and 2ML analogues observed by TEM, XPS and XAFS analysis. The results from the combined characterisation suggested that all three synthesis methods are indeed successful methods for producing Au NPs with an over layer of Ag (in the form of Ag₂O and AgAu alloy) on the surface and that these methods could be used to make core shell structures for other uses. Photocatalytic performance evaluation was carried out on the series of synthesised catalysts to explore the effect of the NP co-catalysts on activity for H₂ production. Disappointingly, the addition of Ag onto the Au NPS had a negative effect on the photocatalytic activity of the synthesised catalysts. This is despite the results from section 4.2 showing promising activity with NPs of 1:1 weight ratio of Ag and Au on TiO₂, as well as the excellent electron storage capabilities of Ag NPs compared to Au or Pt.⁷ It is suggested that the higher work function of Au facilitates improved electron transfer from the TiO₂ to the Au NP compared to Ag this could be a dominant factor governing relative activity between the two metals. Therefore from the results presented in this section AuAg core shell NPs (1 and 2 MLs of Ag) are not good candidates for increasing activity of photocatalytic reforming

reactions for H₂ production. However three promising methods of producing core-shell NPs which could potentially be used for other applications were demonstrated.

4.4 References

1. M. Bowker, C. Morton, J. Kennedy, H. Bahruji, J. Greves, W. Jones, P. R. Davies, C. Brookes, P. P. Wells and N. Dimitratos, *Journal of Catalysis*, 2014, 310, 10-15.
2. Z. F. Jiang, J. J. Zhu, D. Liu, W. Wei, J. M. Xie and M. Chen, *Crystengcomm*, 2014, 16, 2384-2394.
3. A. Gallo, M. Marelli, R. Psaro, V. Gombac, T. Montini, P. Fornasiero, R. Pievo and V. Dal Santo, *Green Chem.*, 2012, 14, 330-333.
4. I. Paramasivam, J. M. Macak and P. Schmuki, *Electrochemistry Communications*, 2008, 10, 71-75.
5. R. Su, L. Kesavan, M. M. Jensen, R. Tiruvalam, Q. He, N. Dimitratos, S. Wendt, M. Glasius, C. J. Kiely, G. J. Hutchings and F. Besenbacher, *Chemical Communications*, 2014, 50, 12612-12614.
6. R. Su, R. Tiruvalam, A. J. Logsdail, Q. He, C. A. Downing, M. T. Jensen, N. Dimitratos, L. Kesavan, P. P. Wells, R. Bechstein, H. H. Jensen, S. Wendt, C. R. A. Catlow, C. J. Kiely, G. J. Hutchings and F. Besenbacher, *ACS Nano*, 2014, 8, 3490-3497.
7. A. Takai and P. V. Kamat, *ACS Nano*, 2011, 5, 7369-7376.
8. A. Zielińska-Jurek and A. Zaleska, *Catalysis Today*, 2014, 230, 104-111.
9. V. Jovic, P.-H. Hsieh, W.-T. Chen, D. Sun-Waterhouse, T. Söhnle and G. I. Waterhouse, *International Journal of Nanotechnology*, 2014, 11, 686-694.
10. D. Tsukamoto, A. Shiro, Y. Shiraishi, Y. Sugano, S. Ichikawa, S. Tanaka and T. Hirai, *ACS Catal.*, 2012, 2, 599-603.
11. H. R. Gong, *Mater. Chem. Phys.*, 2010, 123, 326-330.
12. J. Kennedy, W. Jones, D. J. Morgan, M. Bowker, L. Lu, C. J. Kiely, P. P. Wells and N. Dimitratos, *Catalysis, Structure & Reactivity*, 2014, 1, 35-43.
13. J. F. Gomes, A. C. Garcia, C. Pires, E. B. Ferreira, R. Q. Albuquerque, G. Tremiliosi-Filho and L. H. S. Gasparotto, *The Journal of Physical Chemistry C*, 2014, 118, 28868-28875.
14. N. Dimitratos, J. A. Lopez-Sanchez, D. Morgan, A. Carley, L. Prati and G. J. Hutchings, *Catalysis Today*, 2007, 122, 317-324.
15. W. Wang, S. Efrima and O. Regev, *Langmuir*, 1998, 14, 602-610.
16. S. Link, Z. L. Wang and M. A. El-Sayed, *The Journal of Physical Chemistry B*, 1999, 103, 3529-3533.
17. G. Compagnini, E. Messina, O. Puglisi, R. S. Cataliotti and V. Nicolosi, *Chemical Physics Letters*, 2008, 457, 386-390.
18. X. Liu, A. Wang, X. Yang, T. Zhang, C.-Y. Mou, D.-S. Su and J. Li, *Chemistry of Materials*, 2009, 21, 410-418.
19. M. P. Mallin and C. J. Murphy, *Nano Letters*, 2002, 2, 1235-1237.
20. T. Hirakawa and P. V. Kamat, *Journal of the American Chemical Society*, 2005, 127, 3928-3934.
21. H.-L. Jiang, T. Akita, T. Ishida, M. Haruta and Q. Xu, *Journal of the American Chemical Society*, 2011, 133, 1304-1306.
22. Z. Jiang, W. Zhang, L. Jin, X. Yang, F. Xu, J. Zhu and W. Huang, *The Journal of Physical Chemistry C*, 2007, 111, 12434-12439.
23. P. Fu and P. Zhang, *Applied Catalysis B: Environmental*, 2010, 96, 176-184.
24. G. L. Chiarello, M. H. Aguirre and E. Selli, *Journal of Catalysis*, 2010, 273, 182-190.

25. Q. Yang, W. Jones, P. P. Wells, D. Morgan, L. Dong, B. Hu, N. Dimitratos, M. Dong, M. Bowker, F. Besenbacher, R. Su and G. Hutchings, *Applied Catalysis A: General*, 2016, 518, 213-220.
26. K. M. Reddy, S. V. Manorama and A. R. Reddy, *Mater. Chem. Phys.*, 2003, 78, 239-245.
27. Z. Lin, X. Wang, J. Liu, Z. Tian, L. Dai, B. He, C. Han, Y. Wu, Z. Zeng and Z. Hu, *Nanoscale*, 2015, 7, 4114-4123.
28. Z. H. N. Al-Azri, W.-T. Chen, A. Chan, V. Jovic, T. Ina, H. Idriss and G. I. N. Waterhouse, *Journal of Catalysis*, 2015, 329, 355-367.
29. T.-J. Whang, H.-Y. Huang, M.-T. Hsieh and J.-J. Chen, *International Journal of Molecular Sciences*, 2009, 10, 4707-4718.
30. A. N. Mansour, J. W. Cook and D. E. Sayers, *J. Phys. Chem.*, 1984, 88, 2330-2334.
31. N. F. Mott, *Proceedings of the Physical Society of London Section A*, 1949, 62, 416-422.
32. S. Nishimura, T. N. D. Anh, D. Mott, K. Ebitani and S. Maenosono, *J. Phys. Chem. C*, 2012, 116, 4511-4516.
33. J. Ohyama, K. Teramura, T. Shishido, Y. Hitomi, K. Kato, H. Tanida, T. Uruga and T. Tanaka, *Chemical Physics Letters*, 2011, 507, 105-110.
34. L. F. Mattheiss and R. E. Dietz, *Phys. Rev. B*, 1980, 22, 1663-1676.
35. R. Su, M. M. Forde, Q. He, Y. Shen, X. Wang, N. Dimitratos, S. Wendt, Y. Huang, B. B. Iversen, C. J. Kiely, F. Besenbacher and G. J. Hutchings, *Dalton Transactions*, 2014, 43, 14976-14982.
36. W. Jones, R. Su, P. P. Wells, Y. Shen, N. Dimitratos, M. Bowker, D. Morgan, B. B. Iversen, A. Chutia, F. Besenbacher and G. Hutchings, *Physical Chemistry Chemical Physics*, 2014, 16, 26638-26644.

Chapter 5: Supported PdAu nanoparticles for photocatalytic hydrogen production

Table of contents

5.1	Introduction	142
5.2	Photocatalytic H ₂ production from core shell PdAu-TiO ₂ catalysts with controlled shell thickness	143
5.2.1	Introduction	143
5.2.2	Catalysts synthesis	143
5.2.3	UV/Vis analysis.....	144
5.2.4	Bright field TEM Analysis.....	145
5.2.5	XPS analysis	147
5.2.6	XANES analysis	150
5.2.7	EXAFS analysis	151
5.2.8	Model of the AuPd NP structure.....	156
5.2.9	Photocatalytic performance evaluations	156
5.2.10	Conclusion.....	159
5.3	Restructuring AuPd nano particles by heat treatment for photocatalytic hydrogen production reactions.....	160
5.3.1	Introduction	160
5.3.2	Catalyst synthesis.....	160
5.3.3	UV/Vis analysis.....	161
5.3.4	TEM analysis.....	162
5.3.5	XANES analysis	164
5.3.6	EXAFS analysis	168
5.3.7	Photocatalytic activity.....	175
5.3.8	Conclusions	177
5.4	References	177

5.1 Introduction

Bimetallic AuPd supported NP catalysts have shown superior performance compared to their monometallic counterparts for several reactions including CO oxidation,¹ vinyl acetate synthesis,² glycerol oxidation,³ hydrogen peroxide synthesis,^{4, 5} the transformation of biomass to fuels,⁶ and photocatalytic hydrogen production.⁷

In this section AuPd NPs supported on TiO₂ have been used for the production of H₂ photocatalytically. This is an attractive method of converting solar energy into chemical energy,^{7, 8} with H₂ showing great promise as a future fuel. See chapter 1 for more detail on H₂ as a fuel and background of photocatalysis, the key points relating to this chapter are briefly summarised here however.

The addition of precious metal (*i.e.*, Pt, Pd, Au, and Ag) NPs on the surface of TiO₂ greatly enhances the H₂ production efficiency.⁹⁻¹² The promotional effect of the metal NPs can be understood in terms of the energy levels of the semiconductor-metal system, where the photo-excited conduction band electrons on the surface of TiO₂ can be rapidly transferred and trapped at the surface of NPs.¹³ This prolongs the lifetime of the trapped electrons thus improving the photoreactivity.^{14, 15} To further tune the charge separation efficiency, modification of TiO₂ with bimetallic NPs has also been studied (*i.e.* AuPt, AgPt, and AuPd).^{7, 16, 17} Recent work by Su *et al* on AuPd NPs as co-catalysts has shown the structure of the NPs to be important to the activity of the photocatalyst. Their study highlighted Pd_{shell}-Au_{core} structured NPs demonstrated the highest photoreactivity in comparison to other possible structures.^{14, 18} This increase in activity was attributed to the structured NPs increased ability to inhibit the reverse transfer of trapped electrons back to TiO₂, whilst simultaneously providing a fast reduction rate of the surface adsorbed reagents. These investigations also indicate the thickness and composition of the shell layer may influence the electronic properties of the co-catalyst. However, synthesis of metal NPs with controlled shell thickness and composition has been seldom performed due to the challenges in preparation. Moreover, the properties of the shell layer have been normally determined by microscopic methods, which left the overall features of the shell layer remaining uncertain.

5.2 Photocatalytic H₂ production from core shell PdAu-TiO₂ catalysts with controlled shell thickness

5.2.1 Introduction

It was decided that Au core Pd shell catalysts (supported on TiO₂) would be synthesised with the aim being to produce Au NPs with 1 and 2 monolayers (ML) of Pd on the surface. As with the AuAg core shell catalyst (section 4.3) this structure was chosen for two main reasons i) it was hoped that a thin layer of Pd on an Au NP would maximise any effect of Au on the Pd and ii) a thin layer of Pd would allow for surface information from XAFS analysis, whereas a thick layer would not.¹⁹ The majority of work in the section formed the basis for the published paper 'Optimised Photocatalytic Hydrogen Production Using Core-Shell AuPd Promoters with Controlled Shell Thickness' by Wilm Jones.²⁰ All catalysts were synthesised by Wilm Jones. Characterisation by TEM, UV, XRD and XAFS was also performed by Wilm Jones with Peter Wells helping with XAFS analysis, and XPS analysis done at Cardiff University. Catalytic testing was performed by Ren Su at Aarhus University.

5.2.2 Catalysts synthesis

Three methods were used for synthesising the Au NPs with 1 and 2 ML of Pd on the surface based on modifications to the sol immobilisation technique. Detailed experimental procedures for the synthesis are in section (2.2.8). The ML catalysts were given the names PD (photodeposition), SR (sequential reduction) and DR (double reduction) with either 1ML or 2ML denoting the number of MLs of Pd theoretically deposited. For comparison Au-TiO₂, Pd-TiO₂ and AuPd-TiO₂ were also synthesised by the sol immobilisation technique. A list of catalysts made is in Table 1 with theoretical weight loadings based on quantities of metal used, all catalysts were dried and not calcined to preserve the structure of the NPs.

Table 1. List of samples made with theoretical Au and Pd weight loadings based on amounts used in the preparation, all samples dried at 120 °C for 8 hours.

Catalyst	Au weight loading %	Pd weight loading %
Au-TiO₂	1	-
Pd-TiO₂	-	1
AuPd-TiO₂	0.65	0.35
1ML PD	1	0.18
2ML PD	1	0.36
1ML SR	1	0.18
2ML SR	1	0.36
1ML DR	1	0.18
2ML DR	1	0.36

5.2.3 UV/Vis analysis

UV/Vis analysis was performed on the series of samples to gain information on the optical properties of the prepared photocatalysts. Figure 1 shows the Kubelka-Munk transformed diffuse reflectance spectra (DRS) of the series of samples in the range 200 – 800 nm. All samples show the characteristic absorption of TiO₂ in the UV region starting 380 nm and increasing with shorter wavelength, due to the band gap of P25 TiO₂.²¹ The Au-TiO₂ catalyst was the only sample to possess a surface plasmon resonance peak in the region of 450 – 650 nm, which is characteristic of Au NPs on the surface of TiO₂.²² The absence of the Au surface plasmon resonance peak for all the ML samples after the deposition of Pd suggests that the surface of the Au NPs have indeed been modified with Pd.²³ The increase in total absorption for the Pd containing samples in the of 400 – 800 nm region compared to the bare TiO₂ reference can be attributed to d-d transitions in Pd.²⁴

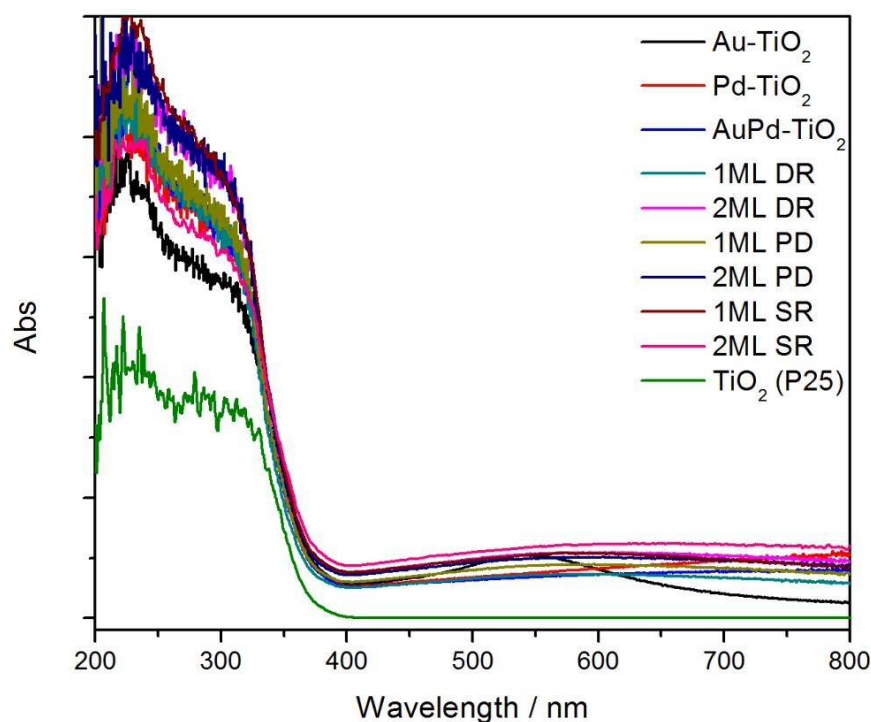


Figure 1. UV/Vis absorption spectra (Kubelka-Munk transformed from diffuse reflectance) for the series of samples and TiO_2 (P25) reference.

5.2.4 Bright field TEM Analysis

Bright field TEM characterisation was performed on all materials to determine the metal particle size distribution. Representative TEM images and the derived histograms are shown in Figure 2 and Figure 3, and the calculated average particle sizes along with standard deviations are summarised in Table 2. It is evident from the TEM images that all metal NPs were deposited on the TiO_2 surface homogeneously with the lack of any aggregation. Particle size for all samples was in a similar range (2.5 – 3.3 nm) with the histograms demonstrating narrow particle size distribution. After deposition of Pd on to preformed Au NPs it could be expected to increase the average size of the newly formed bimetallic NPs. However no significant difference in average particle size was observed for any ML sample. The values of the standard deviation are roughly one third of the average particle size. As such, any particle size increase as a result of the Pd modification is difficult to observe by this method alone. As the particle size has remained roughly constant, it is thought possible to rule out two potential scenarios, (i) Pd was deposited in small particles away from the Au and (ii) Pd was deposited in large particles away from the Au only. In both cases the average particle size would be shifted to either smaller or larger values. This can be seen more clearly from TEM images and the particle size distribution histograms (Figure 3). It is also possible that the Pd has been deposited separately on the surface of TiO_2 with a particle size similar to that of

initial Au NPs, which would mask their detection from this analysis. The TEM analysis has confirmed successful synthesis of metal NP supported catalysts, with further characterisation in this section to focus on the NP microstructure.

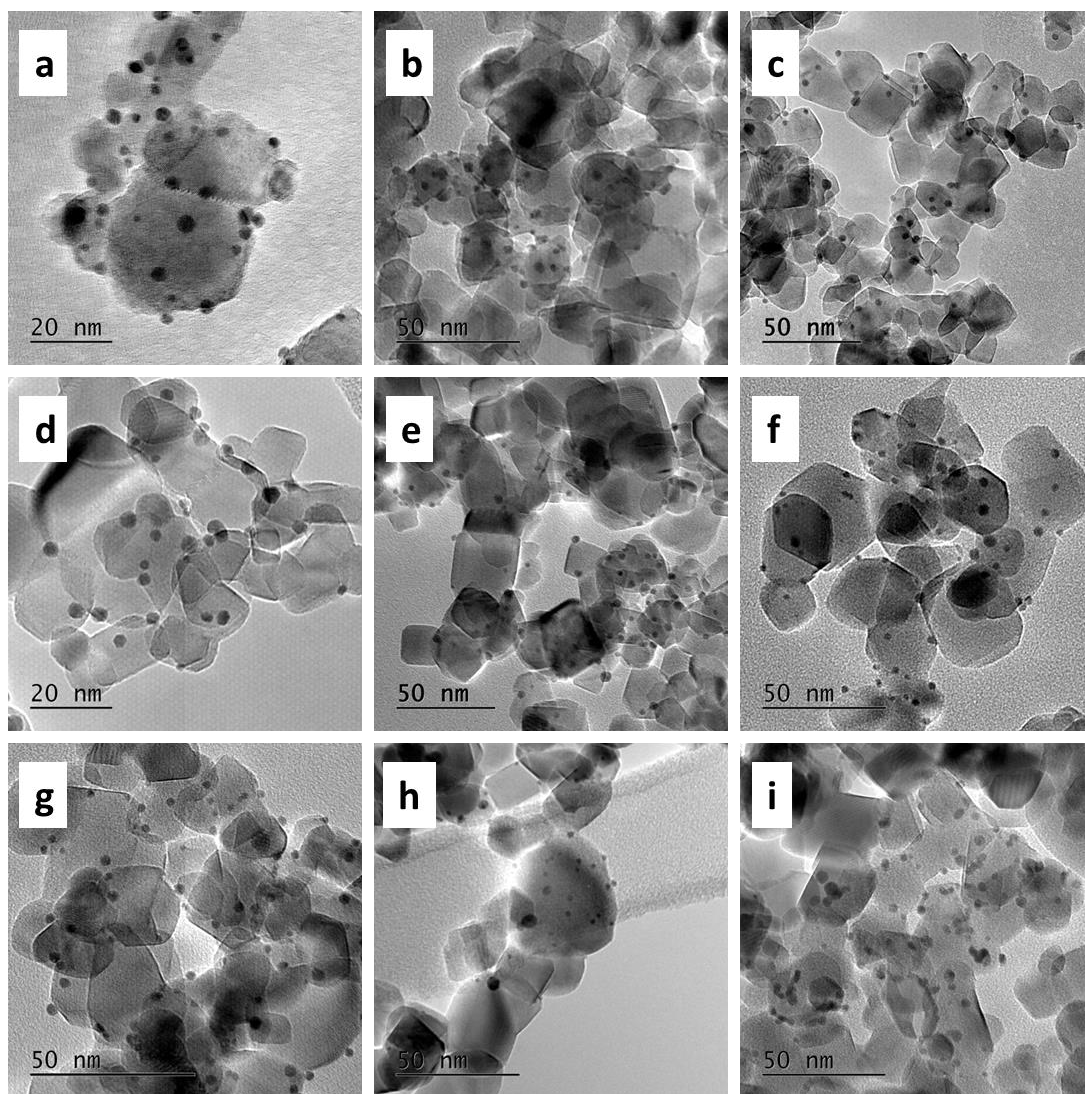


Figure 2. Representative bright field images TEM of a) 1ML SR, b) 2ML SR, c) 1ML PD, d) 2ML PD, e) 1ML DR, f) 2ML DR, g) Au-TiO₂, h) AuPd-TiO₂ and Pd-TiO₂.

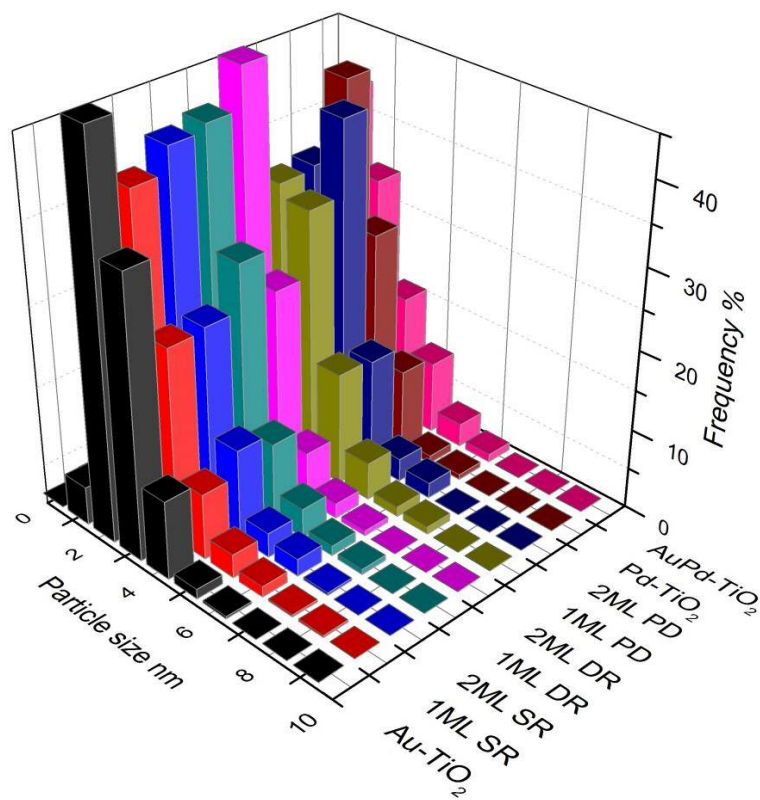


Figure 3. Particle size distributions of as-prepared metal NPs supported on TiO₂

Table 2. Average particle size and standard deviation of the metal NPs calculated from more than 300 particles from multiple sites of all catalysts.

Catalyst	Average Particle size (nm)	Standard deviation (nm)	Number of particles counted
Au-TiO ₂	3.0	1.2	335
AuPd-TiO ₂	2.5	1.2	312
Pd-TiO ₂	2.8	1.0	318
1ML SR	3.1	1.0	314
2ML SR	2.8	1.0	362
1ML PD	3.2	1.1	314
2ML PD	3.3	1.1	378
1ML DR	3.1	1.0	347
2ML DR	2.7	0.9	353

5.2.5 XPS analysis

XPS analysis was performed to gain an understanding of the oxidation states of the elements present in the series of samples as well as the surface Pd/Au atom ratio. Figure 4 depicts the survey scans and high resolution XPS spectra of the Ti 2P, Pd 3d and Au 4f orbitals for the series of as prepared metal NPs supported on TiO₂, while Table 3 summarises the Au 4f (7/2)

and Pd 3f (5/2) binding energies and surface Pd/Au atom ratio. The survey scans suggest all samples are mainly TiO₂ with surface adventitious carbon and minor amount of metals (Au and Pd). Ti 2p spectra clearly show that neither deposition method alters the oxidation state of Ti, which remained to be Ti⁴⁺ in all cases. Meanwhile both the Au 4f and the Pd 3d spectra indicate that the Au and Pd are in their metallic form.^{25, 26} It is worth noting that when Pd in the form of NPs is deposited on the surface of TiO₂ by conventional impregnation methods with the lack of protecting ligands (i.e. PVA or PVP) the dominant species was PdO.²⁷ A similar result was observed in work by Su *et al.* for the chemical vapour impregnated Pd NPs supported on TiO₂, where the molar ratio of Pd⁰:Pd²⁺ was ~1:1.²⁸ This is not the case for the samples of Pd and AuPd NPs on TiO₂ where PVA was still present, thereby preventing Pd oxidation. It is interesting to note that Pd was deposited with the lack of any protecting ligand for catalysts made by the PD and DR methods. However PVA was still present on the surface of NPs for the catalysts made by the SR method as this was a one pot synthesis. Therefore the assumption is that it is association of the Pd with Au which is preventing the formation of PdO for the PD and DR catalysts. This is evidence that the Pd was deposited on the surface of the Au during the synthesis. This is because a significant quantity of uncapped segregated Pd on the surface of TiO₂ would yield a larger Pd²⁺ response. This may still be the case for the SR catalysts, however, isolated PVA-protected Pd NPs cannot be ruled out here. Surface atomic ratios of Pd/Au were also calculated from the XPS spectra to give information on the structure on the NPs (Table 3). As expected increasing the thickness of the shell layer results in an increase of the Pd/Au atomic ratio. Moreover, the surface atom ratio shows that the dominant component is Au in all cases. This suggests that the Pd may not be present at the surface as a segregated overlayer, with the EXAFS analysis providing more detail on this. The position of the Au 4f (7/2) for the Au-TiO₂ reference is 83.4 eV which is in agreement with reports in the literature.²⁹ However all bimetallic samples show a shift to low binding energy 82.6-83.0 eV. This is an indication of some charge transfer from the Pd to the Au, this phenomenon is discussed more in section 5.3.5.

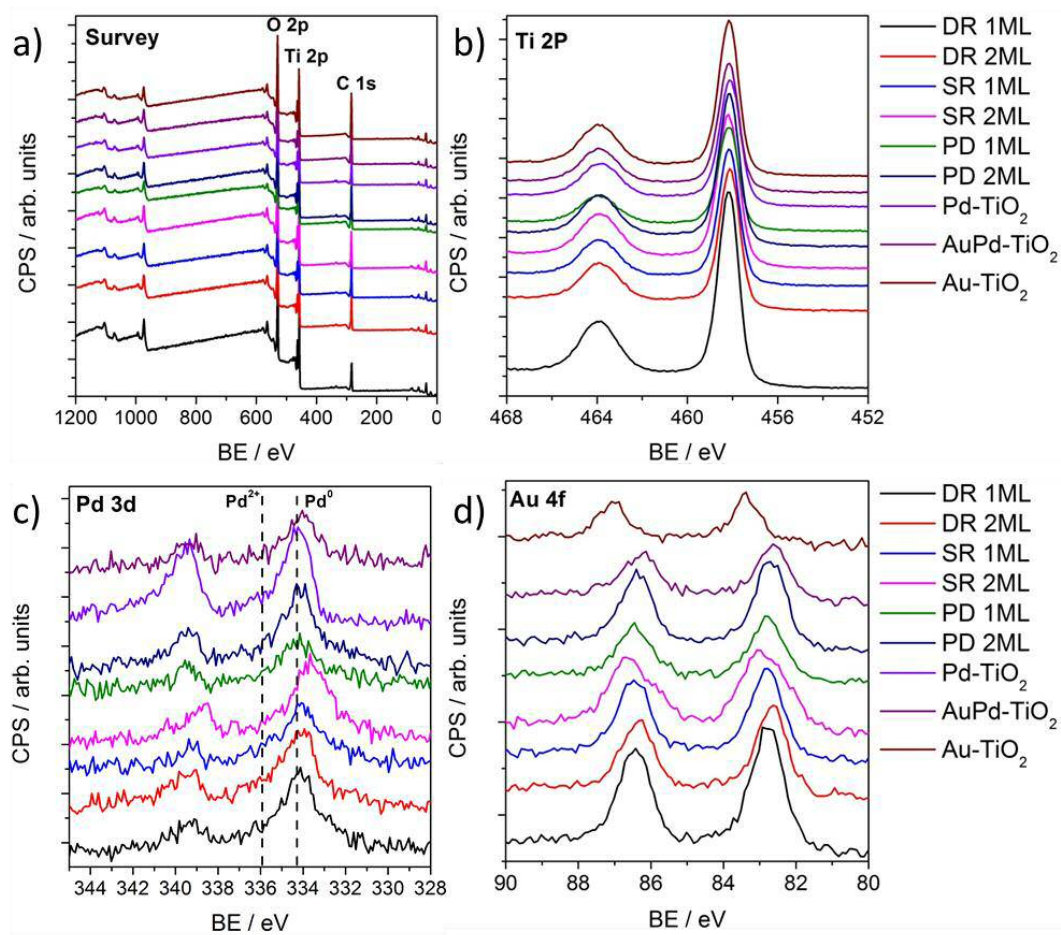


Figure 4. a) XPS survey spectra of the as-prepared metal NPs supported on TiO_2 . b)–d) High resolution XPS spectra of Ti 2p, Pd 3d, and Au 4f, respectively.

Table 3. Summary of Pd 3d and Au 4f binding energies and derived Pd/Au ratios from XPS analysis for the series of prepared catalysts.

Catalyst	Peak name	BE(eV)	Pd/Au ratio
Au-TiO_2	Au 4f (7/2)	83.4	
Pd-TiO_2	Pd 3d (5/2)	334.0	
AuPd-TiO_2	Au 4f (7/2)	82.6	0.83
	Pd 3d (5/2)	334.0	
1ML PD	Au 4f (7/2)	82.8	0.42
	Pd 3d (5/2)	334.2	
1ML SR	Au 4f (7/2)	82.8	0.30
	Pd 3d (5/2)	334.1	
1ML DR	Au 4f (7/2)	82.9	0.38
	Pd 3d (5/2)	334.1	
2ML PD	Au 4f (7/2)	82.7	0.63
	Pd 3d (5/2)	334.3	
2ML SR	Au 4f (7/2)	83.0	0.53
	Pd 3d (5/2)	334.2	
2ML DR	Au 4f (7/2)	82.6	0.92
	Pd 3d (5/2)	334.0	

5.2.6 XANES analysis

X-ray absorption near edge structure (XANES) analysis was also been used to investigate the oxidation states of these materials. Figure 5 a) shows the XANES and EXAFS region of the normalised Pd K edge, with Figure 5 b) and c) showing the XANES and 1st derivative of the XANES region respectively. The position of the main edge in the XANES spectrum is affected by the oxidation state of the element of interest, with the initial maxima in the 1st derivative of the normalised XANES of Pd foil and PdO separated by 4 eV. It was clear that the main edge positions of all core-shell structured AuPd co-catalysts agreed with what would be expected for metallic Pd, with no edge shifted to higher energy. The XANES spectra of a Pd foil exhibits two peaks in the 1st derivative spectrum, due to 1s to 4d and 1s to 5d transitions.³⁰ For the PdAu ML samples reported here the position of these peaks was shifted upon alloying,³¹ however, the centre position of both features was the same for all samples. The differences in the XANES spectra beyond the main edge position between Pd foil and the core-shell structured AuPd spectra can be accounted for by the reduction of metal particle size as well as the alloying with Au.³² Unlike XPS, XANES provides a per atom average, therefore probing all environments – both surface and bulk. By combining both XPS and XANES, it can be inferred that the majority of Pd, in all samples, was presented in its metallic form, suggesting the successful deposition of Pd onto the Au core for the PD and DR catalysts (deposited without protecting ligands).

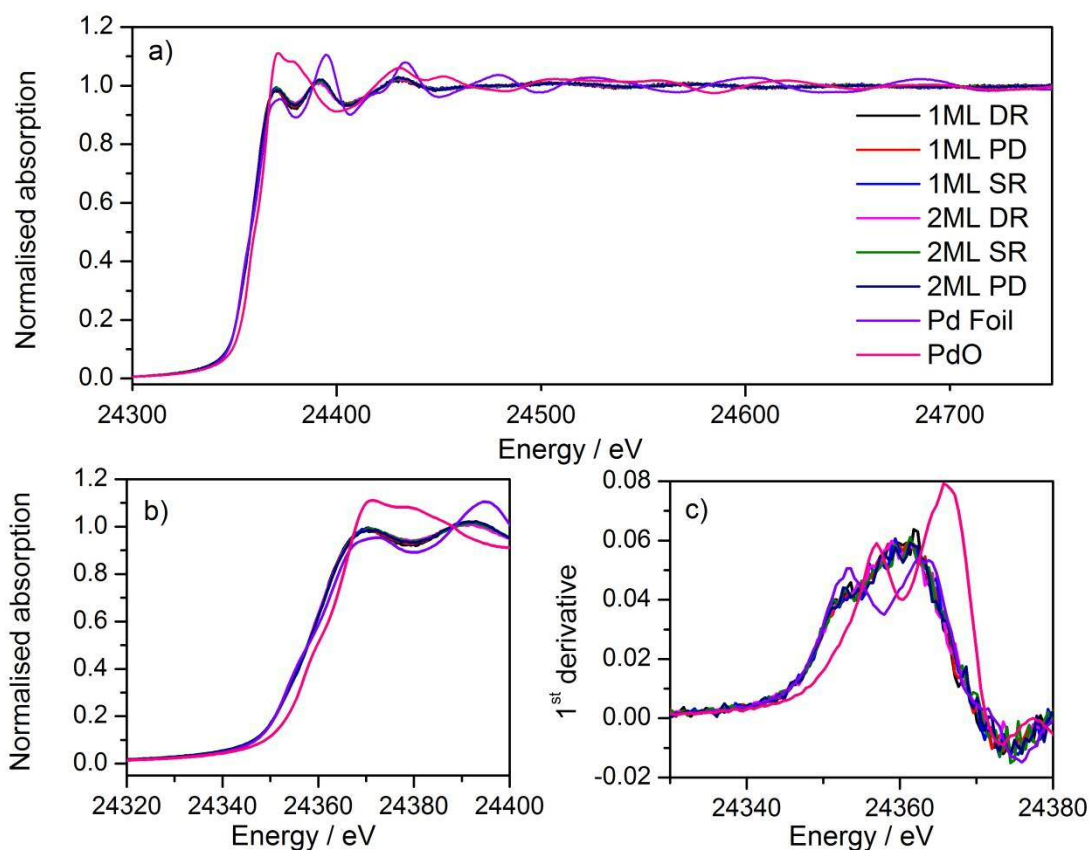


Figure 5. a) Pd K edge normalised absorption b) Normalised absorption in the XANES region and c) first derivative of the normalised absorption for all samples Pd foil and PdO references

5.2.7 EXAFS analysis

The determined 1st shell EXAFS fitting parameters are shown in Table 4, as well as the k^2 weighted magnitude Fourier transform data and corresponding fit shown in Figure 6 (Au L₃) and Figure 7 (Pd K). The EXAFS data show that for all catalysts prepared, both the Au and Pd environments are dominated by a primary Au coordination shell, with similar values observed for all preparation methods. The Au-Au and Pd-Au coordination numbers range between 7.8-8.7 and 6.4-8.9, respectively, and is the most significant coordination shell in both systems. The large Pd-Au contribution confirms that the Pd is present within an Au rich alloy, and not segregated as Pd overlayers. However, the further addition of Pd, from the 1ML to 2ML systems, has little influence on the Au EXAFS (the Au-Au coordination is not significantly altered), confirming that the majority of Au within the core of the NPs remains unchanged. Moreover, although the Au-Pd coordination number increases with Pd loading, a much larger change would be expected if the Pd was evenly distributed throughout the entirety of the particle. Indeed, previous work by Dimitratos *et al.* has demonstrated that the sequential reduction method yields particles where the Pd content remains on the exterior

of the particle.^{33, 34} Crucially, by depositing only small amounts of Pd, in conjunction with EXAFS measurements, it can be demonstrated that the outer Pd is present within an Au rich alloy environment. The presence of significant quantities of Pd not associated with Au can be ruled out by the relatively low Pd-Pd coordination number, which ranges from 0.6 to 3.1. Any significant amount of Pd NPs not associated with Au would result in a much larger Pd-Pd coordination number. Moreover, a larger component of oxidic Pd would be expected for individual Pd NPs, which the XPS and XANES have shown not to be the case. The EXAFS identifies a small component of Pd-O neighbours, which, with the relatively low coordination numbers (0.3 to 0.6), can easily be ascribed to surface oxides as opposed to bulk PdO. An example where discrete Pd over-layers have been deposited has been demonstrated by Russell *et al.*³⁵ They used controlled surface modification routes with organometallic precursors to prepare single monolayer Pd_{shell}Pt_{core} NPs on carbon. Here, cyclic voltammetry (supported by TEM-EDX line scans) was able to show surface characteristics consistent with a Pd surface. EXAFS analysis of these materials showed that the relative Pd-Pd and Pd-Pt coordination neighbours were comparable to each other, as one would expect for Pd exclusively segregated at the surface. Comparison to studies such as these provides further evidence that the Pd in these samples has been incorporated further into the NP to make an Au rich, AuPd alloy, at the surface. Three variations on the sol immobilisation technique was undertaken to synthesise the core-shell NPs, however the XAFS characterisation suggests that each method produced a similar structured NP.

Table 4. 1st shell EXAFS fitting parameters derived from the k^2 weighted Fourier transform for both Au L_3 and Pd K data. The EXAFS data was fitted in R space with a typical fit range of $1 < R < 3.5 \text{ \AA}$

Sample	Abs Sc	N	$R / \text{\AA}$	$2\sigma^2 / \text{\AA}^2$	E_f / eV	R_{factor}	
1ML (PD)	Au L_3	Au – Au	8.7 (5)	2.84 (1)	0.008 (1)	4 (1)	0.02
		Au – Pd	1.5 (4)	2.82 (3)	0.009(3)		
	Pd K	Pd – O	0.3 (1)	1.95 (1)	0.001 (1)	1 (1)	0.003
		Pd – Pd	0.8 (3)	2.78 (2)	0.009 (2)		
		Pd – Au	8.3 (3)	2.78 (1)	0.011 (1)		
1ML (DR)	Au L_3	Au – Au	8.4 (5)	2.84 (1)	0.008 (1)	4 (1)	0.02
		Au – Pd	1.7 (4)	2.84 (2)	0.010(2)		
		Pd – Pd	0.6 (2)	2.75 (4)	0.010(4)	1 (1)	0.006
		Pd – Au	8.9 (3)	2.78 (1)	0.011 (1)		
1ML (SR)	Au L_3	Au – Au	8.0 (6)	2.83 (1)	0.009 (1)	5 (1)	0.02
		Au – Pd	1.5 (4)	2.83 (3)	0.009 (3)		
	Pd K	Pd – O	0.7 (2)	1.96 (1)	0.001 (1)	1 (1)	0.02
		Pd – Pd	8.0 (5)	2.78 (1)	0.011 (1)		
	Pd – Au	1.5 (4)	2.72 (5)	0.013 (4)			
2ML (PD)	Au L_3	Au – Au	8.3 (6)	2.81 (1)	0.008 (1)	4 (1)	0.02
		Au – Pd	2.2 (4)	2.80 (2)	0.009(2)		
	Pd K	Pd – O	0.3 (1)	1.96 (1)	0.001 (1)	1 (1)	0.007
		Pd – Pd	3.1 (5)	2.76 (1)	0.011 (1)		
	Pd – Au	6.9 (8)	2.78 (1)	0.011 (1)			
2ML (DR)	Au L_3	Au – Au	8.5 (6)	2.81 (2)	0.009 (2)	4 (1)	0.02
		Au – Pd	2.1 (4)	2.84 (2)	0.008 (1)		
	Pd K	Pd – O	0.6 (1)	1.97 (2)	0.002 (1)	1 (1)	0.004
		Pd – Pd	1.5 (2)	2.76 (1)	0.011 (2)		
	Pd – Au	7.4 (3)	2.78 (2)	0.011 (1)			
2ML (SR)	Au L_3	Au – Au	7.8 (6)	2.81 (1)	0.008 (1)	5 (1)	0.02
		Au – Pd	2.1 (4)	2.82 (5)	0.008 (2)		
	Pd K	Pd – O	0.5 (1)	1.95 (1)	0.001 (1)	2(1)	0.004
		Pd – Pd	2.4 (4)	2.76 (1)	0.011 (1)		
	Pd – Au	6.4 (5)	2.78 (1)	0.011 (1)			

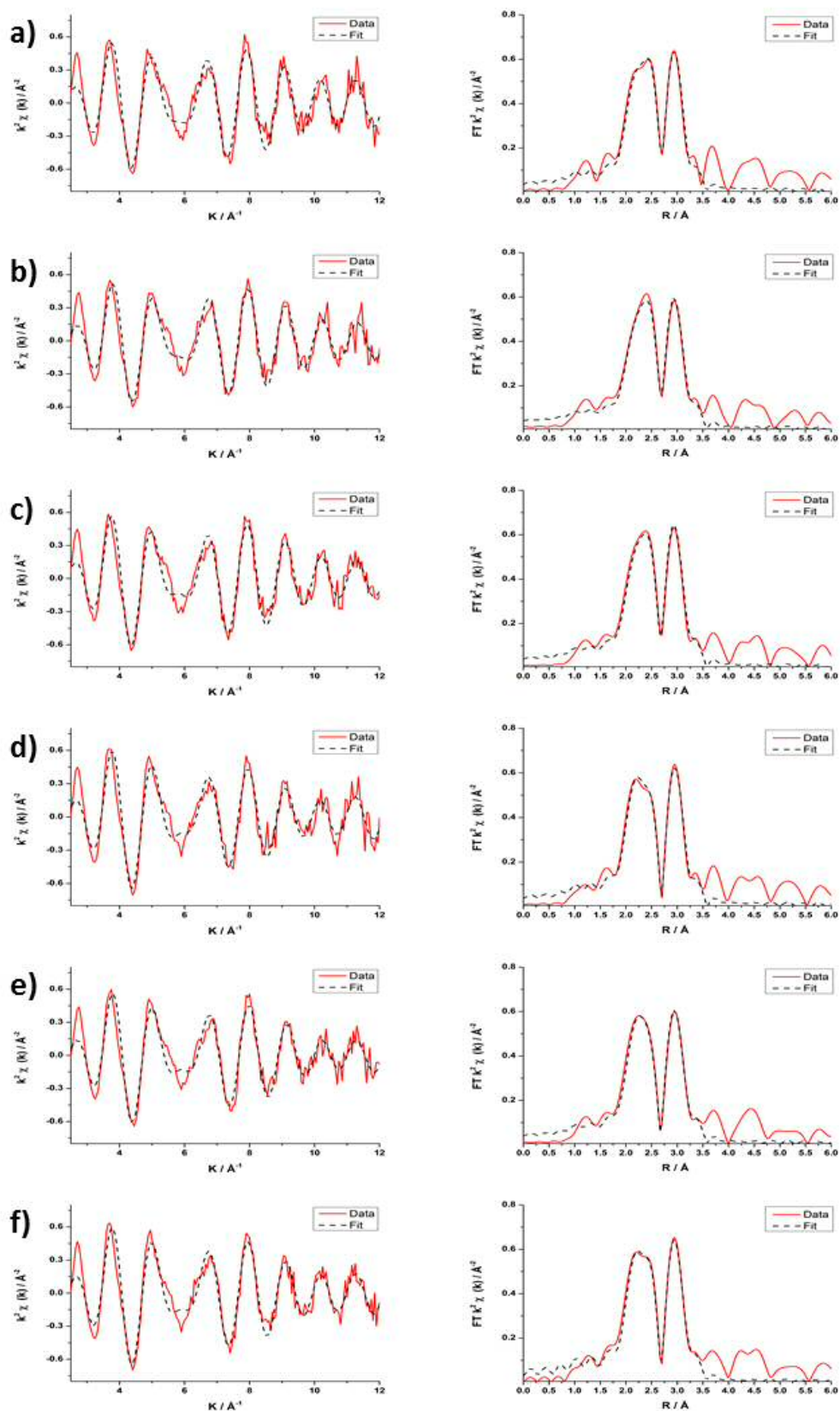


Figure 6. left Au L₃ edge k^2 weighted experimental data and 1st shell fit, right corresponding Fourier Transform for a) 1ML (PD), b) 1ML (SR), c) 1ML (DR), d) 2ML (PD), e) 2ML (SR) and f) 2ML (DR)

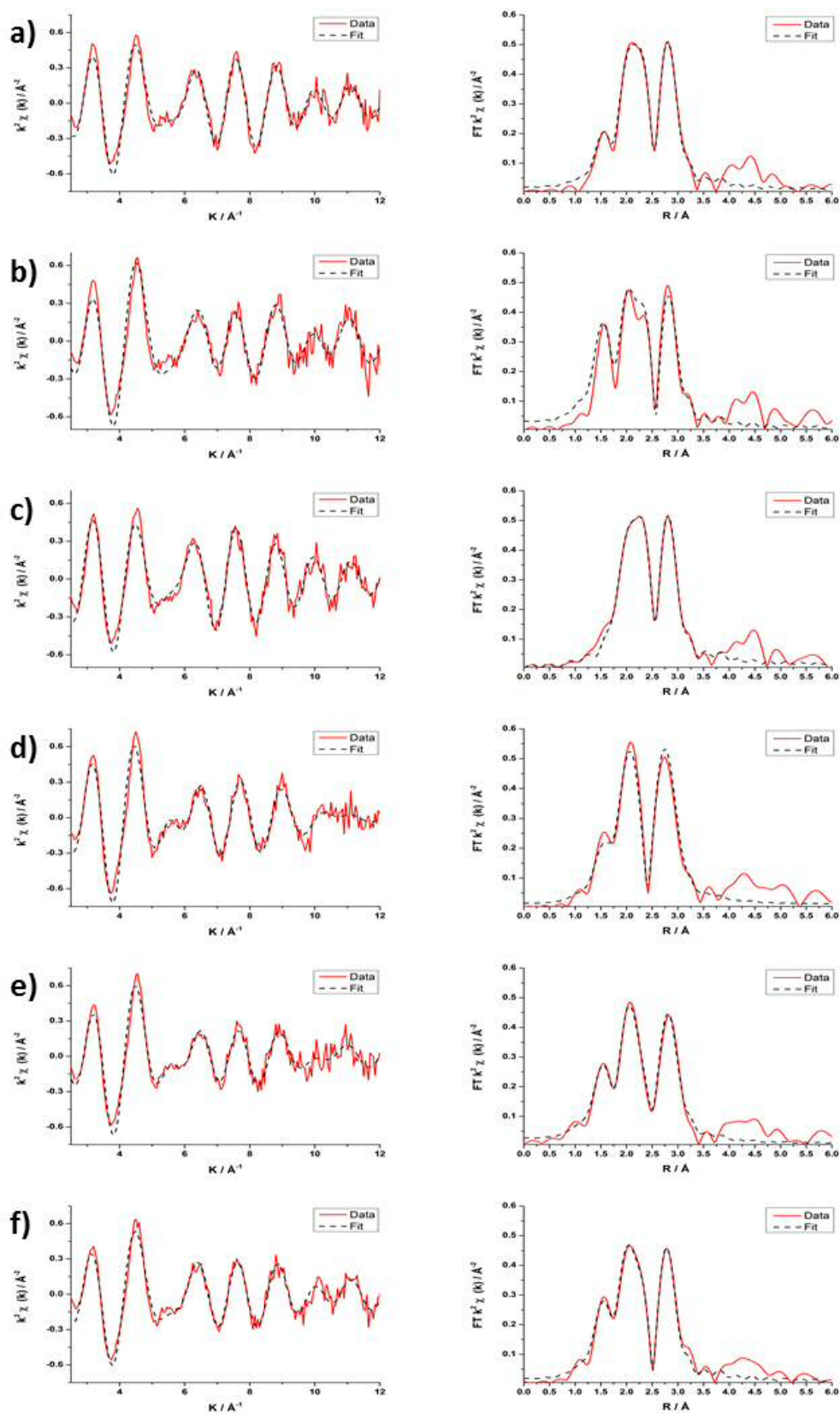


Figure 7. left Pd K edge k^2 weighted experimental data and 1st shell fit, right corresponding Fourier Transform for a) 1ML (PD), b) 1ML (SR), c) 1ML (DR), d) 2ML (PD), e) 2ML (SR) and f) 2ML (DR)

5.2.8 Model of the AuPd NP structure

As a result of the characterisation performed on the 1 ML and 2 ML NPs, the model of an Au core and AuPd shell structure is supported. These NPs are of the order ~ 3 nm with predominant metal oxidation states of Au(0) and Pd(0). Figure 8 represents illustrative diagrams showing the supported model of the AuPd NPs after deposition of Pd, image provided by Arun Chutia.

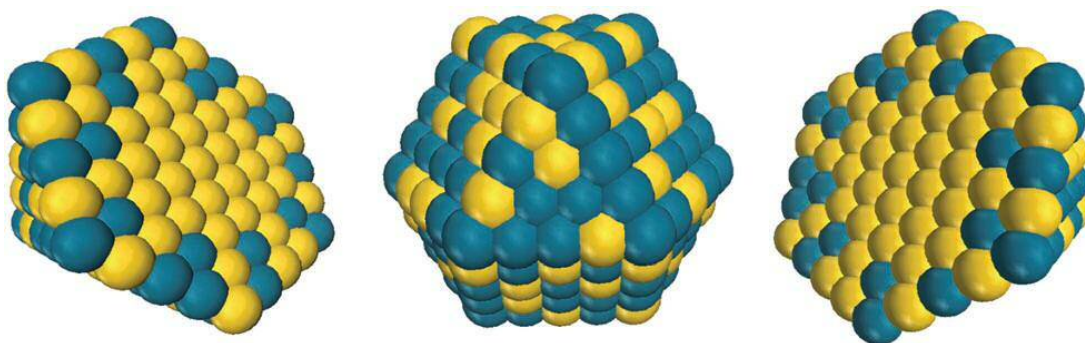


Figure 8. Schematic diagram representing the supported model of the AuPd NPs, containing a gold core and an AuPd alloyed shell, where Au atoms are yellow and Pd atoms are blue. The scheme does not quantitatively present the composition information of the NPs.

5.2.9 Photocatalytic performance evaluations

The photocatalytic H_2 production performance of the synthesised AuPd ML catalysts was determined by Ren Su at Aarhus University in Denmark. Figure 9 depicts the time-resolved photocatalytic H_2 evolution while Figure 10 shows the derived rates from 25 vol% EtOH solution for the series of ML catalysts with reference samples. Details of experimental procedures and reactor set up can be found in section 2.4.9. Metal NPs decorated on TiO_2 photocatalysts have been shown to generate H_2 under UV irradiation; however, their performance varies depending on the identity and microstructure of the co-catalyst. Pure Au as the co-catalyst showed comparable but slightly enhanced H_2 production performance compared to that of pure Pd. It was noticed that the Pd- TiO_2 sample showed a slight drop in photocatalytic performance compared to that of previous observations.^{14, 36} These samples tested here were not calcined to remove the protecting ligand PVA to preserve the structure of the NPs. However the samples were subjected to 2.5 hours of irradiation prior to the reaction to remove the protecting ligand, so blocking of the sites is not thought to be a factor governing activity. Previous studies comparing photocatalytic activity of Au and Pd TiO_2 catalysts made by incipient wetness and sol immobilisation suggested that the preparation

method will have a significant affect. Catalysts made by incipient wetness demonstrated almost double the activity for Pd over Au, whereas when made by the colloidal method reaction rates were comparable.⁷ Therefore it is likely the choice of synthesis method is results in the lower than expected rate for the monometallic Pd catalyst. The AuPd-TiO₂ alloyed catalyst demonstrated improved activity over both the monometallic references, which is consistent with reports in the literature.¹⁸

Interestingly, the core-shell structured PdAu_{shell}Au_{core} NP co-catalysts showed improvement in photocatalytic performance over reference samples. Evidence from XAFS characterisation indicates that the Pd is associated with the Au NPs surface; therefore the increase in activity can be attributed to the presence of a surface AuPd alloy at the Au NPs. Previous studies have reported that core-shell structured AuPd NPs demonstrate a higher activity compared to that of the random AuPd alloys NPs.¹⁴ It is therefore proposed that the improved activity reported here results from the interplay between the Au-core and the AuPd alloy shell of the promoter NPs.

The 1 ML AuPd samples yield the slightly improved performance synthesised by both PD and DR methods over the 2 ML samples, however this trend is reversed for the catalyst made by the SR method. Both the preparation method for the PD and DR methods shared the most similarities in that the Pd was reduced onto a premade 1%Au-TiO₂ in solution with the absence of PVA. Whereas the AuPd NPs made in the SR method were synthesised by sequential reduction of the precursors before deposition onto the TiO₂. This could be a potential reason for the reverse trend in the SR sample. However evidence from the combined characterisation suggests the three 1 ML and three 2 ML AuPd NPs have little difference structurally between themselves.

Furthermore, for the case of the catalysts made by the PD and DR method, as it was observed that the activity decreased slightly for the 2 ML samples compared to the 1 ML samples, this indicates the electronic properties of the co-catalyst can be tuned precisely by engineering the thickness of surface layer.

Although the total metal loading has increased after the deposition of Pd, this is not considered to be the primary reason for the increased activity. The Pd is primarily associated with the Au and not present as isolated Pd NPs, therefore the number of NPs would not have increased significantly. This leads to the conclusion that there has been no significant rise in the number of active sites and the increase in activity can be attributed to the structure of the NPs.

Figure 10 depicts the H₂ evolution rates of all the samples, with all of the AuPd ML samples showing impressive improvement over the reference samples. Specifically the 1ML PD and 2ML SR NPs on TiO₂ presented roughly double enhancement of rate over the metallic Au. Therefore the synthesis approaches demonstrated here represent an interesting way to improve the activity of bimetallic AuPd NPs supported on TiO₂ for photocatalytic reforming reactions. However some caution must be taken when assigning activity to the microstructure of the NPs in this study as the possibility of restructuring during the reaction can't be ruled out here.

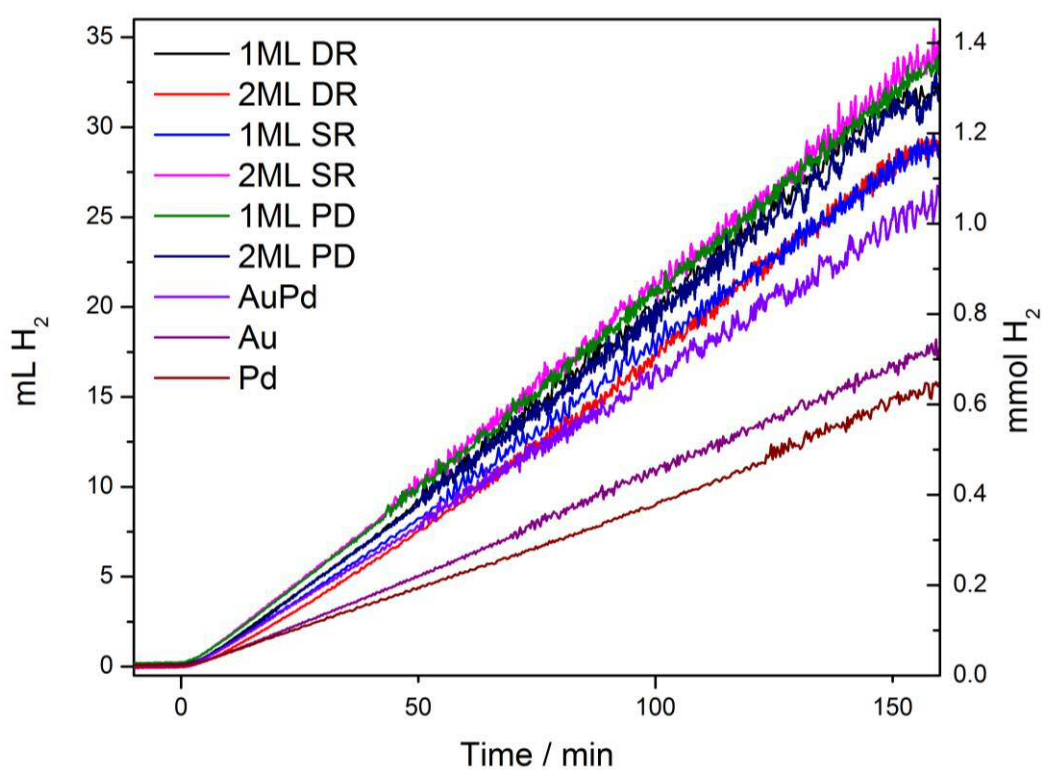


Figure 9. Photocatalytic H₂ evolution from a 25 vol% of ethanol solution using the metal/TiO₂ photocatalyst materials.

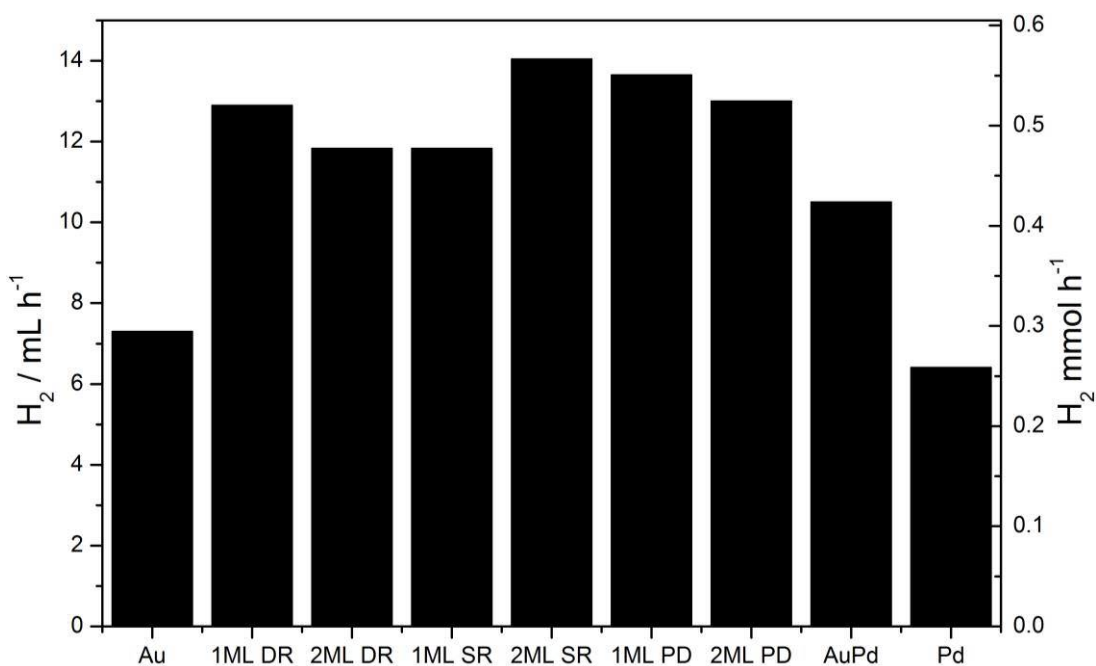


Figure 10. The derived H_2 production rates of the metal/ TiO_2 photocatalyst materials

5.2.10 Conclusion

Three promising approaches were demonstrated for the deposition of thin layers of Pd on to the surface of Au NPs using both a traditional colloidal approach and a novel photodeposition method. XPS and XAFS characterisations confirmed that the microstructures of these co-catalysts are in the form of $PdAu_{shell}-Au_{core}$, with no evidence of significant amounts of isolated Pd or Au NPs. The particle size of all core-shell NPs was determined to be ~ 3 nm regardless of the shell thickness and preparation method. The Au and Pd were found to be predominately in their metallic form. Photocatalytic performance evaluations suggested that the $PdAu_{shell}-Au_{core}$ NPs as co-catalysts exhibited improved H_2 evolution compared to the mono and bimetallic (Au, Pd and AuPd) references. The optimum reactivity was observed when 1 ML equivalent of Pd was deposited on Au for the PD and DR methods with 2 ML optimum for the SR method, suggesting that a thin layer of AuPd covering an Au core can maximise the alteration in electronic properties of surface atoms therefore boost the photocatalytic hydrogen production rate. We expect by fine tuning the surface Pd composition of the Au NPs the hydrogen production performance can be further enhanced.

5.3 Restructuring AuPd nano particles by heat treatment for photocatalytic hydrogen production reactions

5.3.1 Introduction

In this section the sol immobilisation method was again employed to produce a set of catalysts with structured AuPd NPs supported on TiO₂ (P25). Two structures were chosen at the outset, one with a random alloy structure and the other having an Au core Pd shell structure. This was achieved by the order of reduction of the metal precursors during the synthesis of the NPs. Previous reports in the literature have suggested that both a random alloy and Au rich core Pd rich shell NPs can be synthesised and supported on TiO₂ by this method.¹⁴ Also it was reported that the Au rich core Pd rich shell structure NPs on TiO₂ had superior photocatalytic activity for reforming of simple alcohols compared to Pd rich core Au Rich shell NPs on TiO₂. Once our catalyst was synthesised a sample of each was heat treated at 400 °C. Characterisation by UV/Vis and TEM analysis was performed to determine the optical properties and particle size/shape of the synthesised NPs. Further analysis by XAFS was performed to support the synthesised structure of the NPs and follow the restructuring of the NPs during calcination. After determining a structural model of the synthesised catalyst NPs supported on TiO₂ photocatalytic performance was evaluated, which would be related to the structure of the NPs on the TiO₂

5.3.2 Catalyst synthesis

Details of the preparation methods of the core shell AuPd NPs catalysts supported on TiO₂ can be found in section 2.2.5. As described, a bimetallic colloid of AuPd random alloy was prepared by reducing the precursors simultaneously along with an AuPd colloid prepared by reducing the Au precursor first followed by the reduction of the Pd precursor. This method of sequential reduction of the precursors was chosen with the aim to produce an Au rich core and Pd rich shell structure of the colloidal NPs. Once the colloids were formed they were immobilised onto TiO₂ and a sample of each was calcined at 400 °C. The catalysts synthesised by co-precipitation were given the name CP while the 'core-shell' catalysts prepared by sequential reduction were given the name SR with the preceding number relating to the heat treatment. A list of the sample prepared is in Table 5. All the catalysts have a total weight loading of metal of 1wt% on TiO₂ with an Au:Pd ratio of 1:1 by moles.

Table 5. List of catalyst made with code name and heat treatment.

Catalyst	Heat treatment	Code
AuPd-TiO ₂	120 °C dried	CP 120
AuPd-TiO ₂	400 °C calcined	CP 400
Pd[Au]-TiO ₂	120 °C dried	SR 120
Pd[Au]-TiO ₂	400 °C calcined	SR 400

5.3.3 UV/Vis analysis

UV analysis was performed on the series of samples to gain information on the optical properties of the prepared photocatalysts. Figure 11 shows the Kubelka-Munk transformed diffuse reflectance spectra (DRS) of the series of samples in the range 200 – 800 nm. As expected all samples exhibited the characteristic absorption related to the band gap of TiO₂ below ~400 nm.²¹ Interestingly the surface plasmon resonance peak of Au (450 – 650 nm) was not evident in any sample, which would be expected from segregated Au NPs on the surface of TiO₂.²² This would indicate that the surface of the Au NPs has indeed been modified, which may be in the form of Pd, PdO or an alloy.²³

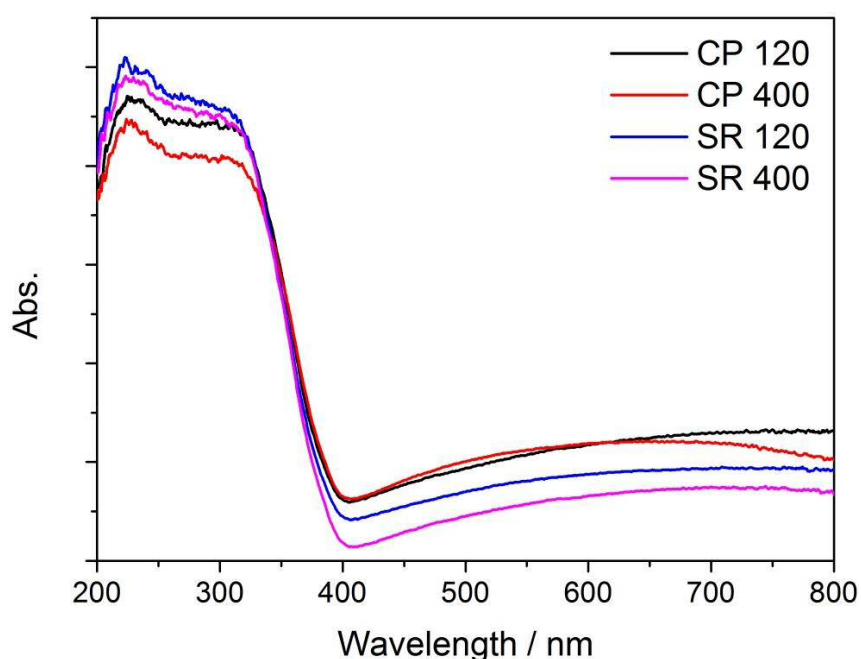


Figure 11. UV/Vis absorption spectra (Kubelka-Munk transformed from diffuse reflectance) for the series of AuPd catalysts.

5.3.4 TEM analysis

Bright field TEM analysis was performed on the series of prepared AuPd catalysts made by the CP and SR methods before and after calcination. Representative TEM images are shown in Figure 12 with associated particle size distribution histograms (produced using imageJ software,³⁷) in Figure 13, and a summary of average particle size with corresponding standard deviation is in Table 6. The TEM analysis confirms NPs were formed and deposited homogeneously on the surface of the TiO₂ support with the lack of aggregation. As can be seen the average particle size of both dried samples is comparable with an average size of 2.5 (\pm 1.2) and 2.8 (\pm 0.9) nm consistent with AuPd NPs made by the sol immobilisation method.^{14, 32} After calcination there is an increase in average particle size by roughly 2 nm compared to the dried catalyst for both preparation methods. This can be seen clearly in the particle size histograms in Figure 13. After heat treatment the histograms are characterised by a broader distribution of particle sizes which is reflected in the increased standard deviation values in Table 6. It is therefore clear that sintering has occurred and hence the structure of the NPs has been affected. As the heat treatment was performed in static air conditions it would be expected that the Pd at the surface of the NPs or potentially segregated Pd on the TiO₂ will be in the oxidic form. However TEM will not be able to confirm this and XAFS analysis will provide more information. It has been previously reported that heat treatment in a CO environment of AuPd NPs made by co-reduction of the precursors by the sol immobilisation method led to Pd migrating to surface of the NP with Au remaining in the core.³⁸ Further characterisation in this chapter will focus on the restructuring of the NPs after heat treatment.

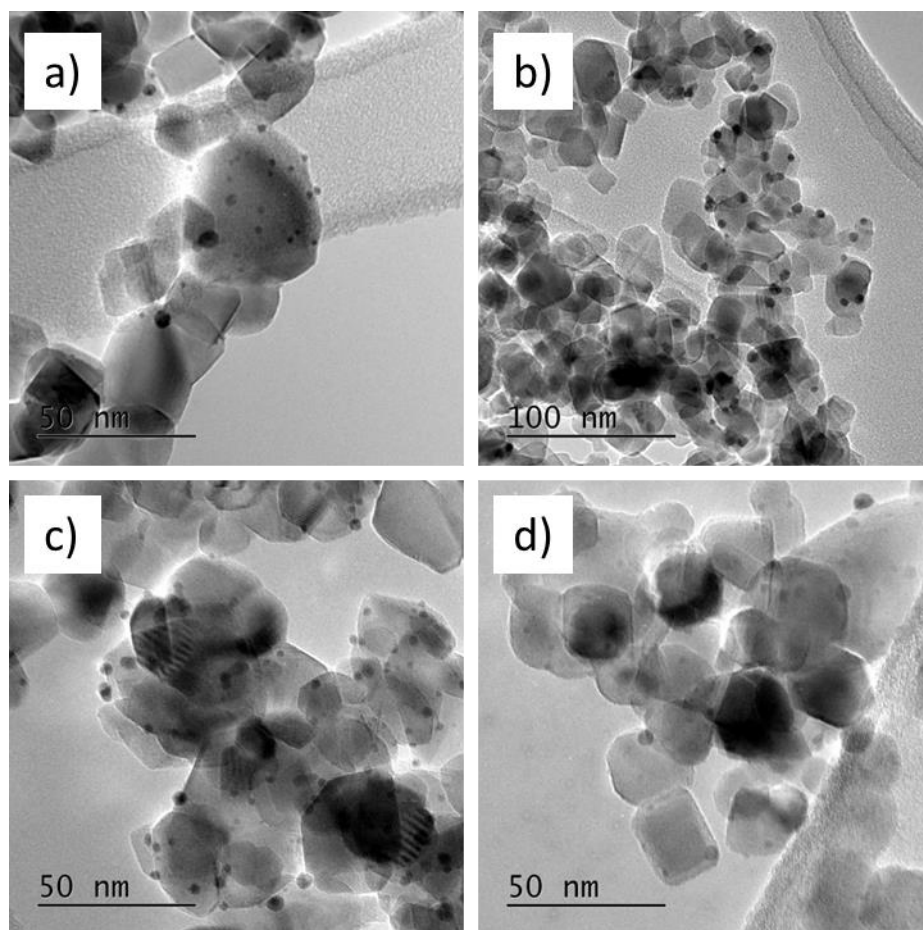


Figure 12. Representative bright field TEM images of a) CP 120, b) CP 400, c) SR 120 and d) SR 400

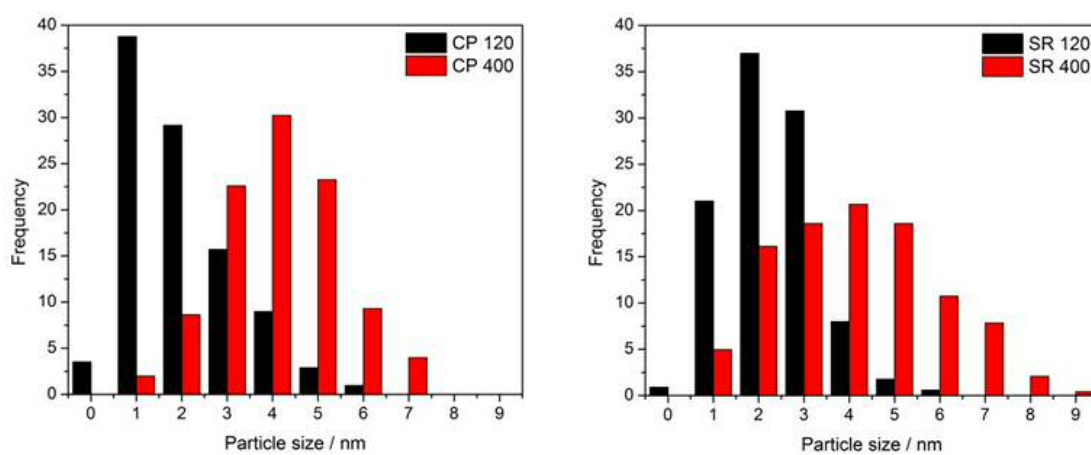


Figure 13. particle size distribution histograms for catalyst made by the CP and SR methods dried at 120 °C and heat treated and 400 °C

Table 6. Summary of average particle size for the series of AuPd catalysts with standard deviation and number of particles measured

Catalyst	Average Particle size (nm)	Standard deviation (nm)	Number of particles counted
AuPd-TiO₂ (CP 120)	2.5	1.2	312
AuPd-TiO₂ (CP 400)	4.6	1.3	301
Pd[Au]-TiO₂ (SR 120)	2.8	0.9	338
Pd[Au]-TiO₂ (SR 400)	4.6	1.7	242

5.3.5 XANES analysis

XAFS analysis of the four AuPd catalysts was performed at the diamond light synchrotron on the Au L₃ and Pd k edge. Analysis of the Pd K edge by XANES was undertaken to gain information regarding Pd oxidation state in the samples. Figure 14 shows the normalised absorption of both the EXAFS and XANES regions for the four bimetallic samples and references (PdO and Pd foil) as well as a close up of the XANES region and the first differential of the XANES region. There are distinct differences between the Pd K edge absorption spectra of the Pd foil and the PdO reference, such as a shift of +4 eV of the PdO absorption edge and phasing of the EXAFS oscillations, which can be seen in Figure 14. The shift to higher binding energy of the Pd²⁺ is a consequence of an increase in energy requirement to remove an electron from a positively charged atom whilst the changes in the EXAFS region between Pd foil and PdO is due to differences in the scattering environment. Therefore the position of the main absorption edge of Pd in the samples will give an indication of what degree the Pd is in its oxidic form. The 1st derivative of the XANES data, Figure 14 c) is an alternative method for observing the shift in the edge position and allows for subtle changes to be seen in more detail. The Pd foil and PdO exhibited two peaks in the 1st derivative spectrum, due to 1s to 4d and 1s to 5d transitions.³⁰ As can be seen in Figure 14 c) the CP 120 sample closely follows the profile of the Pd foil reference indicating a significant proportion of metallic Pd. The SR 120 first derivative peak is shifted slightly from the Pd reference suggesting a mix of Pd oxidation states. Finally the position of the peaks associated with the calcined samples more follows more closely resembles the PdO reference. This supports what would be expected taking into account the synthesis method and heat treatment of the samples, with linear combination fits supporting this.

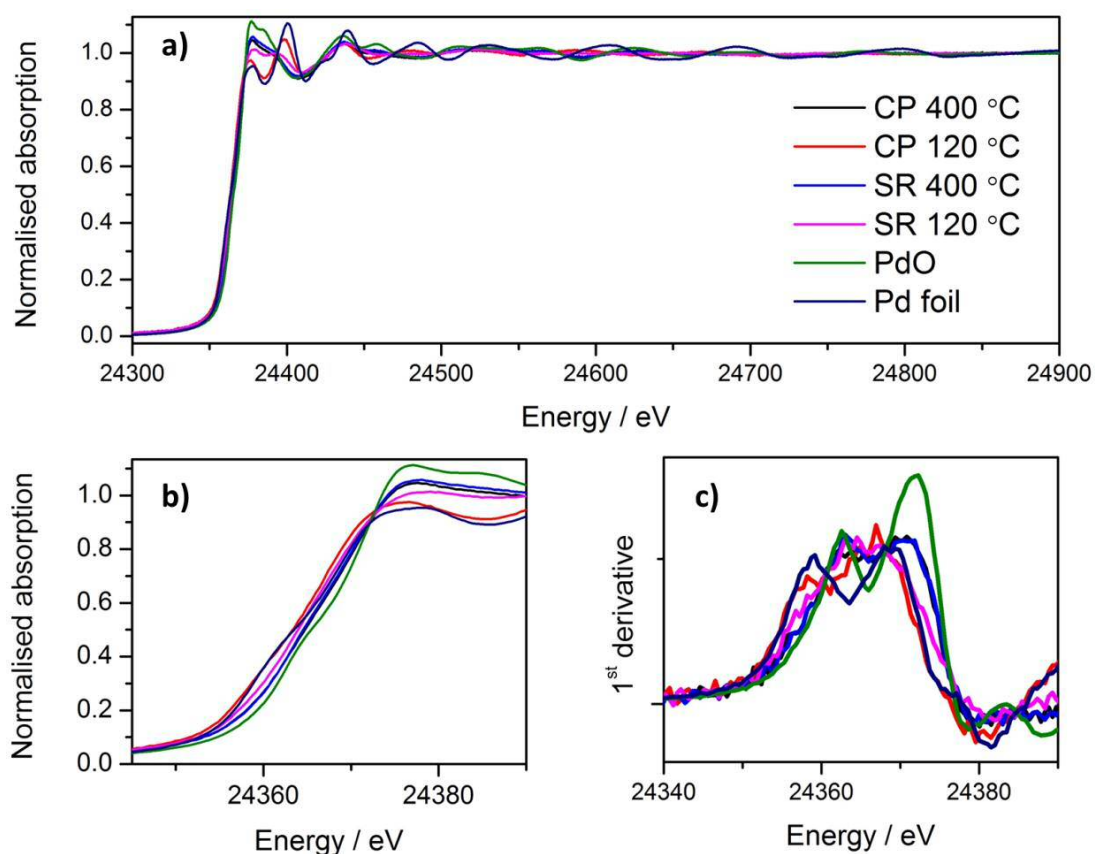


Figure 14. a) normalised absorption of the Pd K edge including the XANES and EXAFS regions b) normalised absorption in the XANES region c) first derivative of the normalised XANES region for all samples and references.

Linear combination fits of the of the four AuPd samples was performed between -20 and 60 eV relative to E_0 , a summary of results are in

Table 7, while the associated plot fits are shown in Figure 15. The fits are generated by multiplying the constituent references to be fit by a constant and adding them together, which is generated in the Athena software.³⁹ This will result in a generated fit which should follow the real spectra closely for the data to be accurate, and is typically performed in the XANES region only. For the case of the AuPd samples the references used was a Pd foil and PdO absorption spectra and the fits shown in Figure 15 represent weighted contributions of each. This is somewhat incomplete as no AuPd or AuPdO reference foils were available and there will be an effect of alloying of the Au and Pd on the shape of the absorption, although this will be seen in the EXAFS region mainly and to a lesser extent in the XANES. However as the spectra were recorded on the Pd edge with only the XANES being used for fitting and the heat treated samples resembling mainly segregated PdO linear combination fits were

performed. However the data especially from the dried samples must be treated with a degree of caution. As can be seen from the R-factors in

Table 7 and the fit data in Figure 15 the calcined samples have a more accurate match, as a consequence of the increased PdO content. The calculated oxide content from the linear combination fits broadly matches with the information from the position of the absorption edge (Figure 14) with the 120 °C dried samples more closely resembling Pd metal and the calcined samples showing a shift with similar profile to PdO.²⁰ The sample CP 120 has the lowest calculated oxide content with which would be expected as this sample designed to be an AuPd alloy, hence the Pd will be able to resist oxidation by association with Au or by being in the centre of the NP. The NP structure of the SR 120 sample should be expected to have the form of an Au rich core and a Pd rich outer layer from the sequential reduction synthesis method. It is therefore likely that the Pd rich shell of the NPs will be more easily oxidised as the catalyst is exposed to the air. This is indeed what is observed in the calculated oxide content.

Table 7. Linear combination fit data for Pd metal and PdO content of the AuPd samples with R factors for the range of 24344.3 to 24424.3 eV

Catalyst	PdO	Pd	R-factor
SR 120	0.51	0.49	0.00486
SR 400	0.74	0.26	0.00204
CP 120	0.14	0.86	0.00611
CP 400	0.71	0.29	0.00265

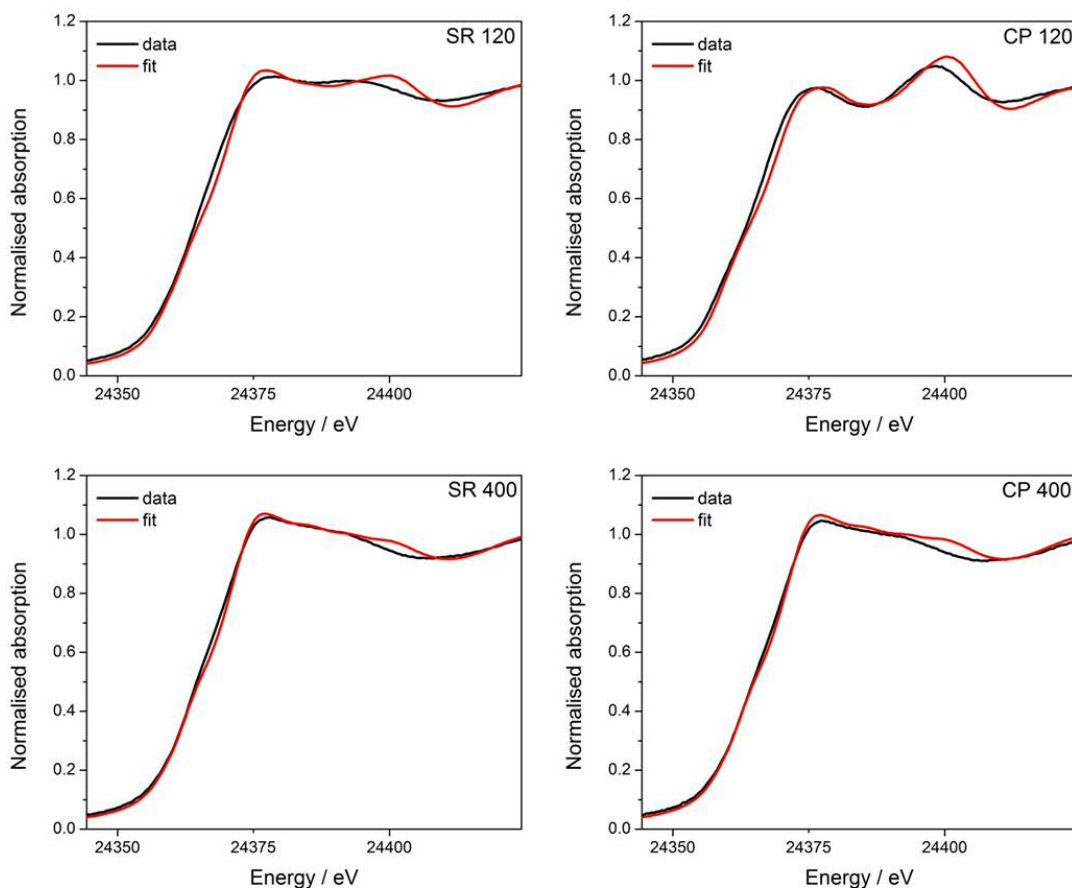


Figure 15. Linear combination fit plots between -20 and 60 eV relative to E_0 for the series of catalyst.

Figure 16 shows plots of the normalised XANES region of the Au L_3 edge for the four AuPd catalysts and Au foil reference. The position of the main absorption edge is in agreement with Au in the zero oxidation state as what would be expected. Some differences in the shape after the absorption edge are observed however, these can be attributed the effect of particle size and alloying with the Pd.³⁸ There is a white line feature in the edge region of 11925 eV which can be seen more clearly in the Au foil than the AuPd samples. The intensity of this white line depends on transitions of 2p electrons to unoccupied 5d states ($2p_{3/2} \rightarrow 5d_{3/2}$ and $5d_{5/2}$ dipole allowed transitions for the Au L_3).⁴⁰ The electronic configuration of bulk Au would be expected to be $[\text{Xe}]5d^{10}6s^1$ with no unoccupied d states. However overlapping bands can lead to hybridisation of the s-p-d orbitals which can result in the transfer of electrons from the d orbitals to the s-p orbitals, thus resulting in an electronic configuration of $[\text{Xe}]5d^{10-x}6s^{1+x}$.²⁴ Therefore the weak white line in the Au foil can be attributed to the depletion of the d band. Nano sized Au particles will have less overlapping bands due to decrease in the lattice size, which leads to less s-p-d hybridisation. This will be observed as a

decrease in white line intensity.^{32, 41, 42} Another factor which will affect the intensity of the white line at 11925 eV is the interaction of the Pd with Au. This can be a result of charge transfer from the Pd s band into the Au d band, weakening the white line.⁴³ It is worth noting that the EXAFS data (explained in detail in the next section) show that the sample with the most Au-Pd interactions is the CP 120 catalyst. This sample also showed the smallest white line feature at 11925 eV which would also support association of the Au and Pd and charge transfer from the Pd to the Au.

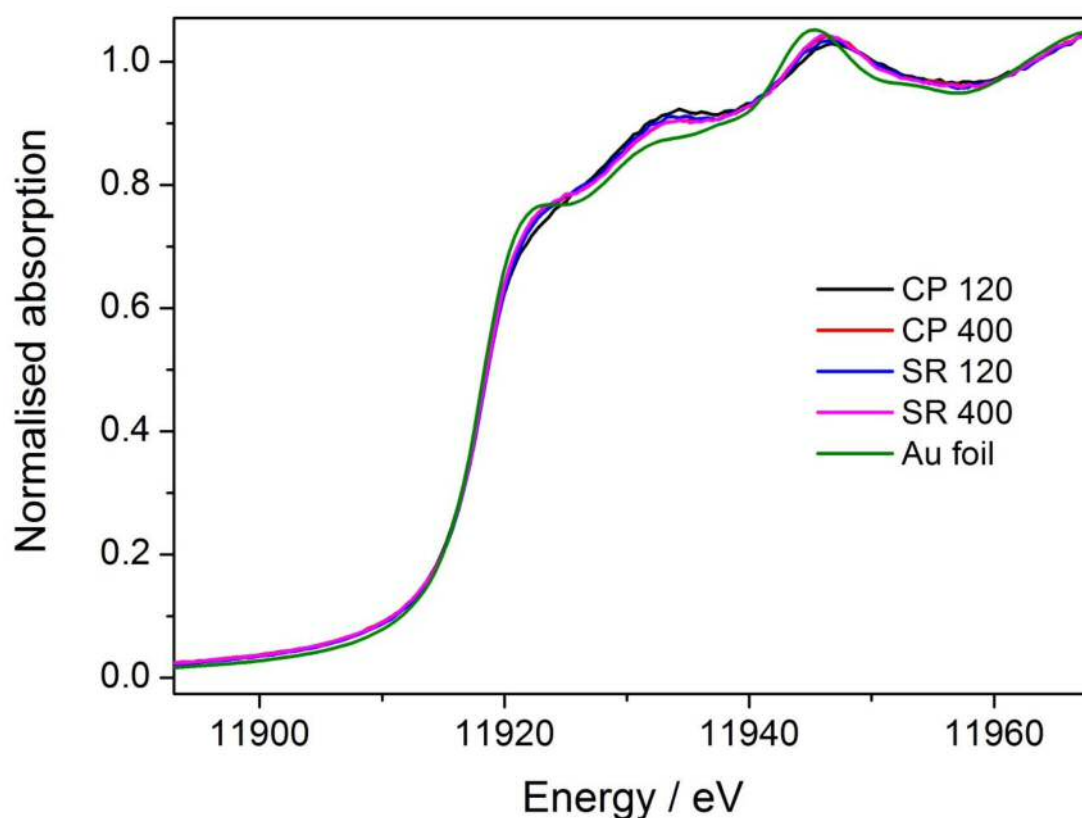


Figure 16. Plot of the normalised Au L₃ XANES region for the four AuPd catalysts and the Au reference foil.

5.3.6 EXAFS analysis

EXAFS data for the series of AuPd catalysts was collected at the Diamond light source synchrotron and processed using the software packages of Athena and Artemis.³⁹ Analysis of the EXAFS data will allow for calculation of the coordination environment of the AuPd samples before and after calcination. As seen in the XANES there was a large increase in the PdO content and a decrease of metallic Pd after heat treatment in air which will have a large effect on the scattering environment of the absorbing Pd atom. Figure 18 shows the k² weighted Fourier transform of the Pd K EXAFS data for the series of AuPd catalyst with Pd

foil and PdO references. By looking at the data in this form it is possible to observe scattering contributions at specific R distances (Å). It is worth noting that the data in this figure is not phase corrected, which will result in the scattering components being at slightly different values (typically -0.5 Å) to the true R distances.^{44, 45} Table 8 shows the phase corrected R values for the series of AuPd NP catalysts.

The Pd foil exhibits a large peak at ~2.3-2.6 (Å) which can be attributed to the Pd-Pd contribution while the PdO plot contains two peaks at 1.3-1.6 (Å) and 2.9-3.2 (Å) which can be assigned to Pd-O and Pd-Pd in PdO scattering respectively. Figure 17 shows the bond lengths in PdO and Pd metal references. The expansion of the Pd-Pd length in PdO is due to oxygen being incorporated into the metal structure, where each Pd atom will be bonded to 4 oxygen and 4 adjacent Pd atoms, opposed to the metallic form which will have a coordination number of 12.

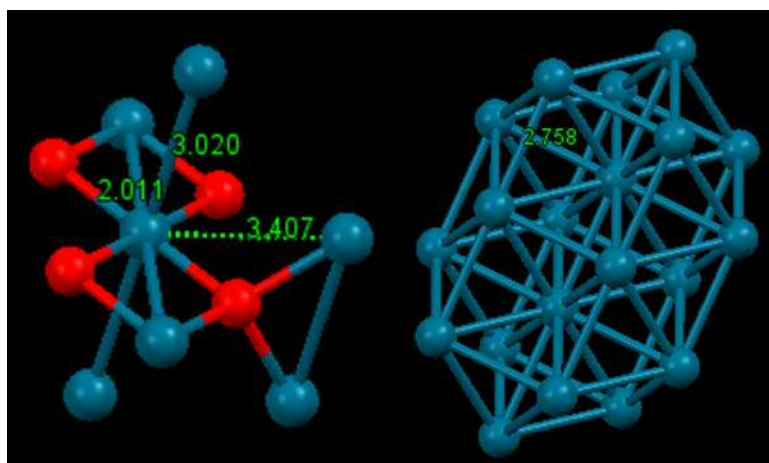


Figure 17. Visual representation of bond lengths for left image PdO, 2.011 Å Pd-O, 3.020 Å Pd-Pd first shell, 3.407 Å Pd-Pd second shell. Right image, Pd metal, 2.758 Å Pd-Pd first shell. Images were created from standard cif files using mercury software.

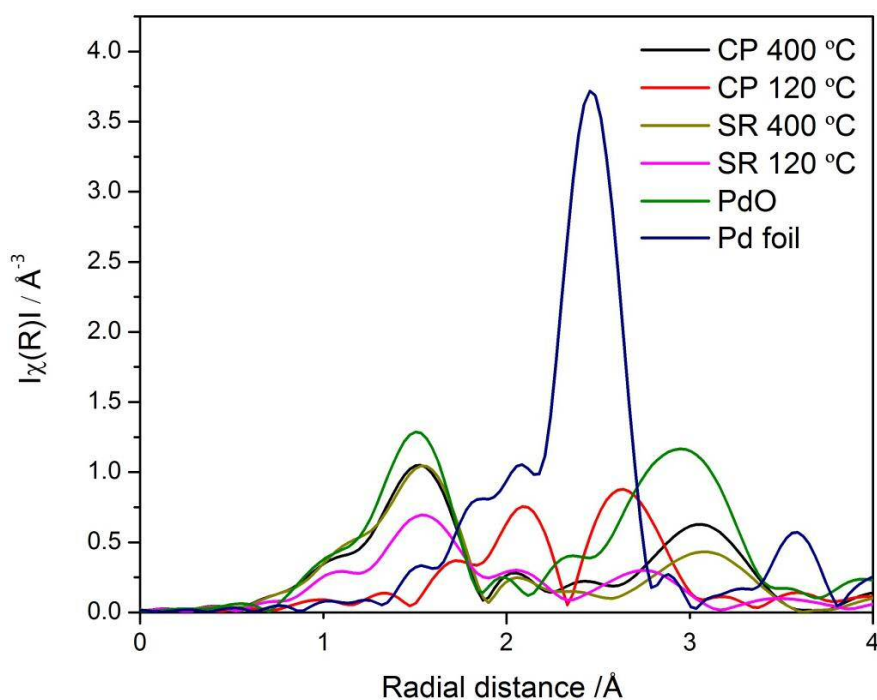


Figure 18. k^2 weighted Fourier transform of the Pd K EXAFS data for the series of AuPd catalyst with Pd foil and PdO references. Not phase corrected.

It is clear from Figure 18 that the samples with the highest oxide content are the two heat treated AuPd catalysts, which is indicated by the peaks at 1.3-1.6 Å (Pd-O) and to a lesser extent 2.9-3.2 Å (Pd-Pd in PdO).⁴⁶ This was expected as the XANES and linear combination fits gave a similar result. The sample with the least oxidic nature based on radial distance scatters was the CP 120 which again was supported by the XANES analysis, Figure 14 and Figure 15.

The coordination numbers of the series of AuPd catalysts was calculated from the EXAFS data in order to gain an insight into the average local environment of the Au and Pd. The determined 1st shell EXAFS fitting parameters derived from the k^2 weighted Fourier transform for both Au L_3 and Pd K data are shown in Table 8, as well as the k^2 weighted magnitude of Fourier transform data and corresponding 1st shell fit is shown in Figure 19 (Au L_3) and Figure 20 (Pd K). The R factors in Table 8 are a measure of how close the generated fit is to the real data, with a lower value being a better fit. The number in brackets after the CNs indicates the error in the last significant figure of the CN value. It is clear that the R factors from the Au L_3 edge are lower than from the Pd K edge in all cases. This is due to the larger Z number of the Au atom ($Z=79$) compared the Pd ($Z=46$) which will result in a higher scattering contribution and therefore data which can be more readily fit.

The calculated coordination numbers derived from the Au L₃ edge for Au-Au scattering of the two dried catalysts have values of 6.1 (0.5) for CP 120 and 8.0 (0.3) for SR 120. This can be understood in terms of the preparation method, in the SR method the Au precursor was reduced first followed by reduction of the Pd, while for the CP method both precursors were reduced simultaneously. Therefore the lower Au-Au coordination number for the CP method are very likely due to the alloying effect of the Au with Pd with the higher values of the SR method likely to be a result of an Au core Pd shell NPs structure, segregated Au NPs or perhaps a combination of the two. When taking into account the Au-Pd scattering environment the Au is coordinated to Pd on average more in the CP 120 sample than the SR 120 sample, with values of 3.4 and 2.3 respectively. This is further evidence of the CP 120 sample being more alloy in nature than the SR 120 sample.

After heat treatment at 400 °C there are clear differences in the EXAFS fitting parameters compared to the dried samples. In both cases the Au environment has become dominated by Au scatters, with increased Au-Au coordination numbers of 8.9 for the CP 400 and 9.2 for the SR 400 samples. It is therefore likely that the Au in the NPs has migrated together by the heat treatment creating a more closely monometallic structure. Some AuPd alloy however is likely to still remain as the Au-Pd scatters has a coordination of 1.5 for CP 400 and 1.5 for the SR 400 sample. From the Au L₃ EXAF alone it is not possible to say whether the Pd is randomly dispersed in the NPs or is more concentrated in any one region. However it is possible to say that much of the Pd has separated from the Au. It is evident from the TEM of the calcined samples (Figure 13) that sintering has occurred between the NPs as the average particle size has increased. Despite this it would seem the two heat-treated catalysts have similar structures. From the Pd K edge the Pd scattering environments of two dried samples varies as would be expected from the different preparation methods. For the CP 120 sample the CNs for Pd-Pd is 4.5 and Pd-Au is 4.7, with almost negligible Pd-O component of 0.2. This combined with analysis from the Au L₃ edge supports alloyed structured NPs. For the case of the SR 120 sample the CNs are Pd-Pd is 2.1 and Pd-Au is 0.7, with Pd-O component of 2.2. The degeneracy of Pd-O in PdO is 4 as can be seen in Figure 17, therefore it can be estimated that roughly half the Pd in the SR 120 sample is in the oxidic form, in agreement with results from the linear combination fits in

Table 7. The coordination number values for the Pd-Pd and Pd-Au are 2.1 and 0.7 respectively, suggesting very little interaction of the Au and Pd, perhaps considering the uncertainty from the error values. This leads to the conclusion that the Pd is present as a discrete layer over the Au NPs, separate from the Au or a combination of the two. No Au

surface plasmon resonance was observed by UV/Vis analysis for any of the AuPd samples (Figure 11). Therefore it can be assumed that the Pd has been deposited on the surface of the Au modifying the NPs optical properties, however to what extent is still unclear.

Data from the Pd K edge for the two calcined samples shows several similarities. In that the Pd-Au scattering contribution is very low, perhaps negligible considering the error values. The same is also true for the Pd-Pd scattering which is very low and perhaps within error. Moreover the data for the calcined samples resemble that of PdO with a large Pd-O coordination, which would be expected from the calcination in air.

Taking into account the combined XAFS characterisation it is clear the NPs have restructured significantly during calcination. The CP 120 sample exhibited an alloyed AuPd NP structure, which upon heat treatment the Au coordination increased and the Pd migrated to the surface and oxidised. Resulting in what is suggested as a core shell structure of Au core PdO shell. The SR 120 sample exhibited some core shell structure due to the preparation method. After heat treatment it is apparent to Au has coalesced and the Pd has segregated and oxidised. Indeed both heat treated catalysts exhibit very similar structure of the AuPd NPs by XAFS analysis.

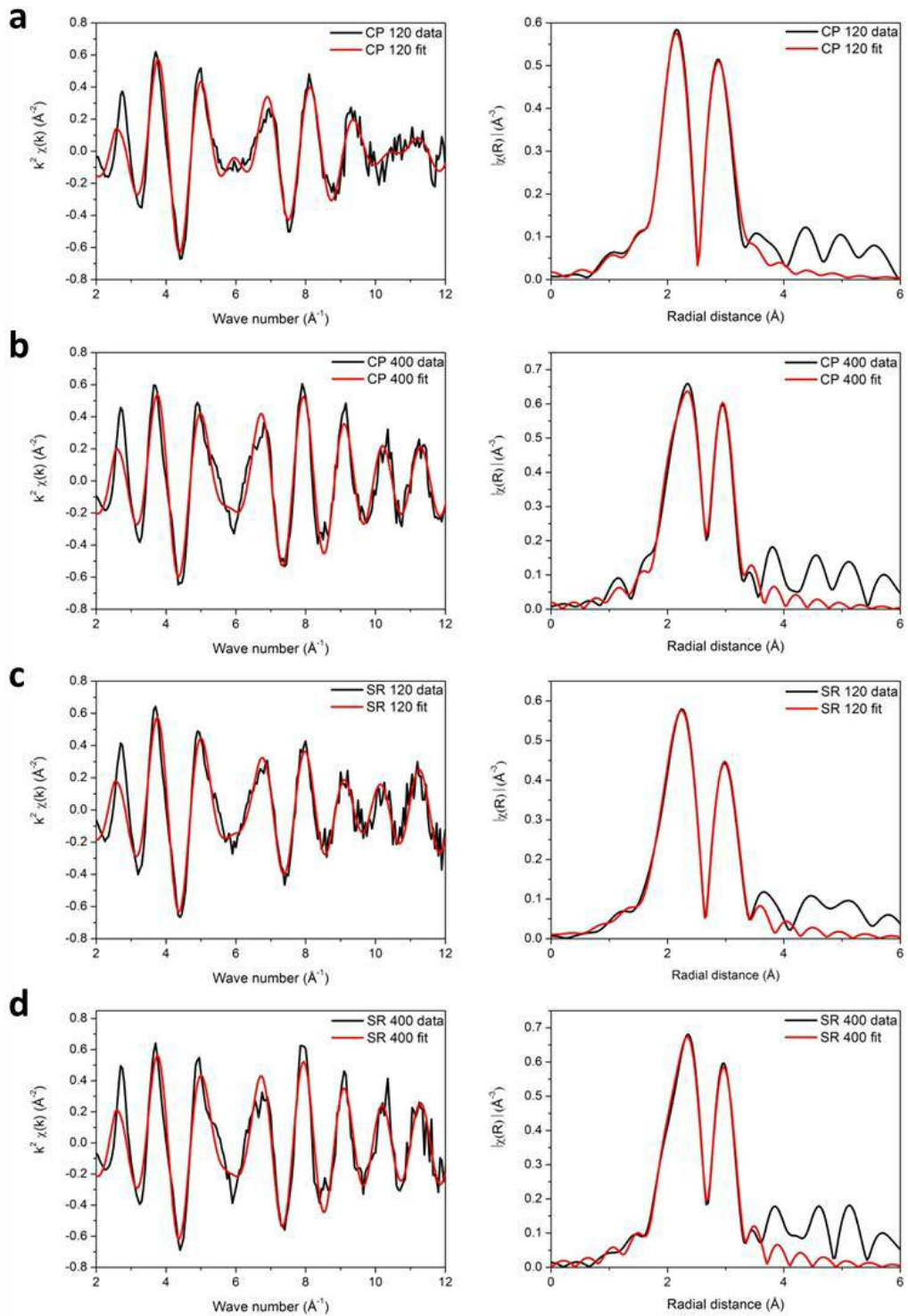


Figure 19. Left Au L_3 edge k^2 weighted experimental data and 1st shell fit, right corresponding Fourier Transform for a) SR 120 b) SR 400 c) CP 120 and d) CP 400

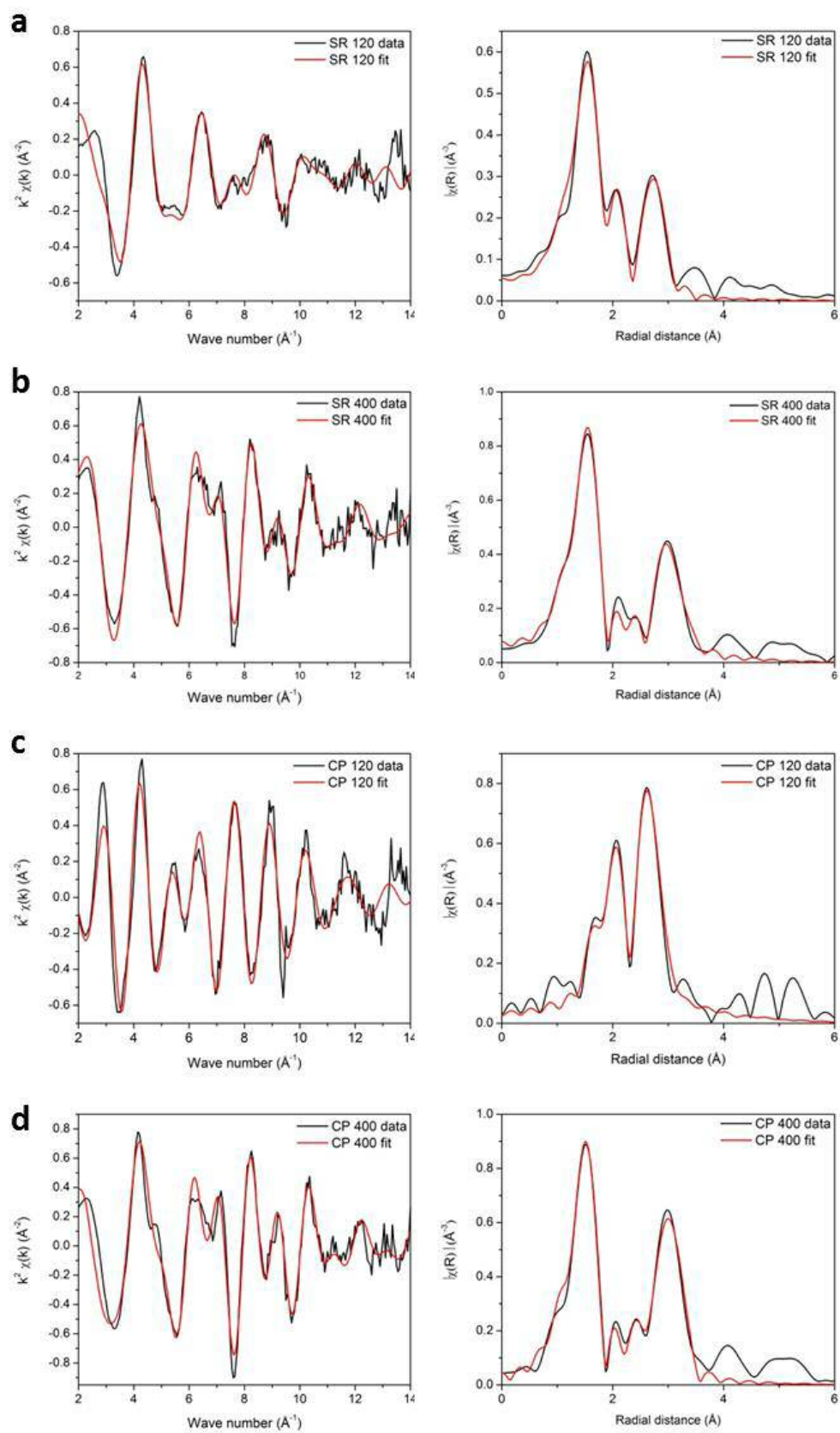


Figure 20. Left Pd K edge k^2 weighted experimental data and 1st shell fit, right corresponding Fourier Transform for a) SR 120 b) SR 400 c) CP 120 and d) CP 400.

Table 8. 1st shell EXAFS fitting parameters derived from the k² weighted Fourier transform for both Au L₃ and Ag K data. PdO-PdO indicates a Pd-Pd distance in PdO, while Pd₂O-Pd₂O indicates a second shell Pd-Pd distance in PdO. The EXAFS data was fitted in R space with a typical fit range of 1 < R < 3.5 Å.

Sample	Abs Sc	N	R / Å	2σ ² / Å ²	E _f / eV	R _{factor}	
120 CP	Au L ₃	Au – Au	6.1(5)	2.82(1)	0.0080	4(1)	0.007
		Au – Pd	3.4(4)	2.78(1)	0.0080	4(1)	
	Pd K	Pd – Pd	4.5(4)	2.79(4)	0.0028	-3(1)	0.016
		Pd – Au	4.7(7)	2.06(5)	0.0031	-3(1)	
		Pd – O	0.2(2)	2.79(1)	0.0073	-3(1)	
400 CP	Au L ₃	Au – Au	8.9(4)	2.83(1)	0.0080	4(1)	0.005
		Au – Pd	1.5(3)	2.80(1)	0.0080	4(1)	
	Pd K	Pd – Pd	0.2(4)	2.82(7)	0.0700	-3(1)	0.015
		Pd – Au	0.9(9)	2.82(2)	0.0700	-3(1)	
		Pd – O	3.1(0.2)	2.010(3)	0.0029	-3(1)	
		PdO – PdO	3.5(1.3)	3.04(2)	0.0093	-3(1)	
	Pd ₂ O – Pd ₂ O	6.2(0.7)	3.41(2)	0.0088	-3(1)		
120 SR	Au L ₃	Au – Au	8.0(3)	2.82(1)	0.0080	4(1)	0.005
		Au – Pd	2.3(2)	2.77(2)	0.0080	4(1)	
	Pd K	Pd – Pd	2.1(5)	2.84(8)	0.0101	1(1)	0.012
		Pd – Au	0.7(8)	2.84(4)	0.0032	1(1)	
	Pd – O	2.2(4)	2.03(2)	0.0053	1(1)		
400 SR	Au L ₃	Au – Au	9.2(3)	2.83(1)	0.0080	4(1)	0.004
		Au – Pd	1.5(2)	2.80(1)	0.0080	4(1)	
	Pd K	Pd – Pd	0.2(4)	2.83(4)	0.0700	2(1)	0.018
		Pd – Au	0.5(8)	2.85(3)	0.0700	2(1)	
		Pd – O	3.0(2)	2.01(3)	0.0033	2(1)	
		PdO – PdO	5.2(1.3)	3.06(4)	0.0140	2(1)	
	Pd ₂ O – Pd ₂ O	4.6(7)	3.44(3)	0.0104	2(1)		

5.3.7 Photocatalytic activity

The series of synthesised AuPd-TiO₂ catalysts were tested for hydrogen production activity by photocatalytic reforming of MeOH. Details of experimental set up and procedures used for testing can be found in sections 2.3.1 → 2.3.4. All reactions were performed with 200 mL of water 150 mg of catalyst using a 150 W Xenon arc lamp. The samples were tested twice with all parameters being identical with the exception of the quantity of MeOH. One test was performed with 1 mL of MeOH and another with 0.1 mL of MeOH. These were performed to see if the catalyst performed differently with different levels of MeOH. Time-resolved photocatalytic H₂ evolution data and derived H₂ evolution rates can be found in Figure 21 for the series of catalysts.

For reaction with 1 mL of MeOH in 200 mL water it is clear that there is only marginal differences between the four catalysts in terms of activity. There is a slight increase in rate of the two calcined catalysts compared to the dried, however this is within experimental error. The XAFS characterisation showed a similar NP structure between the two heat treated catalysts, but with differences from the dried catalysts. This is especially evident in the CP 120 sample. Despite this, all catalysts performed with comparable activity. Also the dried catalyst possessed a smaller average TEM particle size (~2.5-2.8 nm) compared to the

calcined samples (~4.6 nm). Therefore due to the larger particle size there will be less NPs in total on the calcined catalysts. However as there are fewer particles on the calcined samples it can be assumed that each NPs is producing more hydrogen.

As the XAFS characterisation presented a different structure of the NPs, with the calcined samples showing aggregation of Au in the NPs and the migration of Pd to the surface followed by oxidation of the remaining Pd metal. It is likely the PdO will be quickly reduced to Pd metal when under reaction conditions. If indeed the PdO is covering the Au core as the characterisation suggests then this will result in Au core Pd shell structure during photo the reaction. Some caution must be taken however as the structure was only determined pre-reaction and no *in situ* studies were performed. For the catalysts tested under these conditions it is clear that the structure of the NPs on TiO₂ has little effect on the activity. Also the difference in particle size between the dried and calcined catalysts results in negligible changes to the total activity. It is then assumed that the weight loading of metal, which is identical for each catalyst, has the dominant effect on activity.

A set of reactions was also run with less MeOH (0.1 mL) and it was found under these conditions that the amount of hydrogen produced varied significantly between the dried and calcined samples. However both dried and calcined samples demonstrated similar activity compared to each other. It is clear that under these conditions the effect of calcination has a more dominant outcome on the activity and appears to be beneficial to activity, probably because of the dominance of Pd at the surface. Pd has been consistently shown previously to be more active for this photocatalysis.⁴⁷

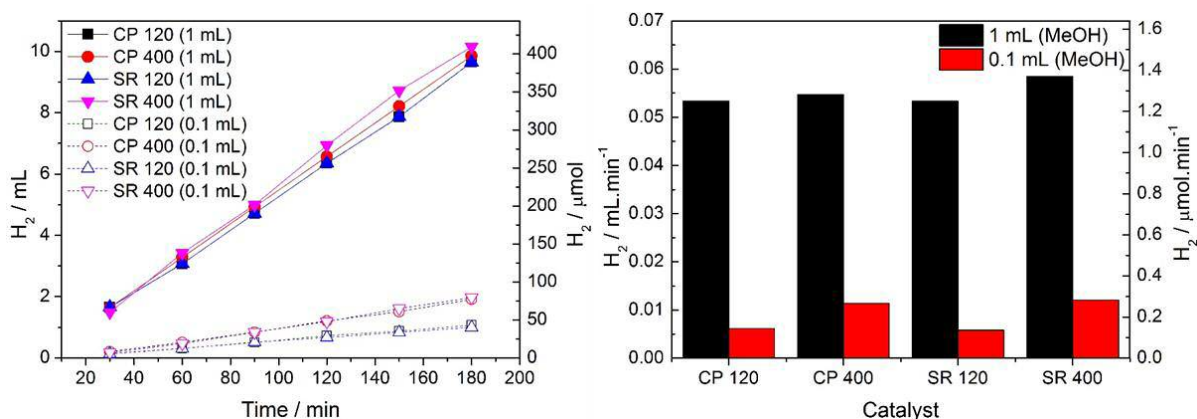


Figure 21. Time-resolved photocatalytic H₂ evolution data and derived H₂ evolution rates for the series of AuPd catalysts

5.3.8 Conclusions

The sol immobilisation method was used to synthesis AuPd NPs (~3 nm) with a microstructure of AuPd random alloy and Au rich core Pd rich shell, which were supported on TiO₂ (P25). The combined characterisation supported successful synthesis of the structured NPs. Heat treatment (400 °C) was performed on a sample of each catalyst and the restructuring of the Au and Pd in the NPs was followed by XAFS analysis. After calcination the Au in the NPs coalesced while the Pd migrated to the surface and oxidised, which was evident from the calculated coordination numbers. This was less pronounced in the SR 400 catalyst as it possessed a core-shell structure from the outset. Both the SR 400 and CP 400 samples demonstrated a similar NP microstructure after the heat treatment despite the differences in the preparation method. Photocatalytic hydrogen production reactions were performed on the series of AuPd catalysts to observe any differences in activity between the catalysts. Two sets of reactions were performed with different amount of the sacrificial agent (MeOH 0.1 mL and 1mL). Under the lower MeOH conditions the calcined catalyst produced roughly double the amount of hydrogen as the uncalcined catalysts. However under the higher MeOH conditions all the catalysts performed with a similar activity. Therefore improvement in activity has been achieved at low MeOH conditions.

5.4 References

1. J. Xu, T. White, P. Li, C. He, J. Yu, W. Yuan and Y.-F. Han, *Journal of the American Chemical Society*, 2010, 132, 10398-10406.
2. Y. F. Han, J. H. Wang, D. Kumar, Z. Yan and D. W. Goodman, *Journal of Catalysis*, 2005, 232, 467-475.
3. W. C. Ketchie, M. Murayama and R. J. Davis, *Journal of Catalysis*, 2007, 250, 264-273.
4. H. C. Ham, G. S. Hwang, J. Han, S. W. Nam and T. H. Lim, *The Journal of Physical Chemistry C*, 2009, 113, 12943-12945.
5. S. E. Davis, M. S. Ide and R. J. Davis, *Green Chem.*, 2013, 15, 17-45.
6. H. Zhang and N. Toshima, *Catalysis Science & Technology*, 2013, 3, 268-278.
7. M. Bowker, C. Morton, J. Kennedy, H. Bahruji, J. Greves, W. Jones, P. R. Davies, C. Brookes, P. P. Wells and N. Dimitratos, *Journal of Catalysis*, 2014, 310, 10-15.
8. C. G. Silva, R. Juarez, T. Marino, R. Molinari and H. Garcia, *Journal of the American Chemical Society*, 2011, 133, 595-602.
9. J. Greaves, L. Al-Mazroai, A. Nuhu, P. Davies and M. Bowker, *Gold Bulletin*, 2006, 39, 216-219.
10. K. Mogyorosi, A. Kmetyko, N. Czirbus, G. Vereb, P. Sipos and A. Dombi, *React. Kinet. Catal. Lett.*, 2009, 98, 215-225.
11. Y. Z. Yang, C. H. Chang and H. Idriss, *Applied Catalysis B-Environmental*, 2006, 67, 217-222.
12. M. S. Park and M. Kang, *Mater. Lett.*, 2008, 62, 183-187.
13. A. Takai and P. V. Kamat, *ACS Nano*, 2011, 5, 7369-7376.

14. R. Su, R. Tiruvalam, A. J. Logsdail, Q. He, C. A. Downing, M. T. Jensen, N. Dimitratos, L. Kesavan, P. P. Wells, R. Bechstein, H. H. Jensen, S. Wendt, C. R. A. Catlow, C. J. Kiely, G. J. Hutchings and F. Besenbacher, *ACS Nano*, 2014, 8, 3490-3497.
15. V. Subramanian, E. E. Wolf and P. V. Kamat, *Journal of the American Chemical Society*, 2004, 126, 4943-4950.
16. Z. F. Jiang, J. J. Zhu, D. Liu, W. Wei, J. M. Xie and M. Chen, *Crystengcomm*, 2014, 16, 2384-2394.
17. A. Gallo, M. Marelli, R. Psaro, V. Gombac, T. Montini, P. Fornasiero, R. Pievo and V. Dal Santo, *Green Chem.*, 2012, 14, 330-333.
18. R. Su, R. Tiruvalam, A. J. Logsdail, Q. He, C. A. Downing, M. T. Jensen, N. Dimitratos, L. Kesavan, P. P. Wells, R. Bechstein, H. H. Jensen, S. Wendt, C. R. A. Catlow, C. J. Kiely, G. J. Hutchings and F. Besenbacher, *ACS Nano*, 2014, 8, 3490-3497.
19. C. Brookes, P. P. Wells, G. Cibin, N. Dimitratos, W. Jones, D. J. Morgan and M. Bowker, *ACS Catal.*, 2014, 4, 243-250.
20. W. Jones, R. Su, P. P. Wells, Y. Shen, N. Dimitratos, M. Bowker, D. Morgan, B. B. Iversen, A. Chutia, F. Besenbacher and G. Hutchings, *Physical Chemistry Chemical Physics*, 2014, 16, 26638-26644.
21. K. M. Reddy, S. V. Manorama and A. R. Reddy, *Mater. Chem. Phys.*, 2003, 78, 239-245.
22. Z. Lin, X. Wang, J. Liu, Z. Tian, L. Dai, B. He, C. Han, Y. Wu, Z. Zeng and Z. Hu, *Nanoscale*, 2015, 7, 4114-4123.
23. A. Tanaka, K. Fuku, T. Nishi, K. Hashimoto and H. Kominami, *The Journal of Physical Chemistry C*, 2013, 117, 16983-16989.
24. J. A. van Bokhoven and J. T. Miller, *The Journal of Physical Chemistry C*, 2007, 111, 9245-9249.
25. G. B. Hoflund, H. A. E. Hagelin, J. F. Weaver and G. N. Salaita, *Applied Surface Science*, 2003, 205, 102-112.
26. A. Zwijnenburg, A. Goossens, W. G. Sloof, M. W. J. Crajé, A. M. van der Kraan, L. Jos de Jongh, M. Makkee and J. A. Moulijn, *The Journal of Physical Chemistry B*, 2002, 106, 9853-9862.
27. Z. B. Wu, Z. Y. Sheng, H. Q. Wang and Y. Liu, *Chemosphere*, 2009, 77, 264-268.
28. R. Su, M. M. Forde, Q. He, Y. Shen, X. Wang, N. Dimitratos, S. Wendt, Y. Huang, B. B. Iversen, C. J. Kiely, F. Besenbacher and G. J. Hutchings, *Dalton Transactions*, 2014, 43, 14976-14982.
29. P. Fu and P. Zhang, *Applied Catalysis B: Environmental*, 2010, 96, 176-184.
30. M. Tromp, J. A. van Bokhoven, G. P. F. van Strijdonck, P. W. N. M. van Leeuwen, D. C. Koningsberger and D. E. Ramaker, *Journal of the American Chemical Society*, 2005, 127, 777-789.
31. A. F. Lee, C. J. Baddeley, C. Hardacre, R. M. Ormerod, R. M. Lambert, G. Schmid and H. West, *The Journal of Physical Chemistry*, 1995, 99, 6096-6102.
32. P. Dash, T. Bond, C. Fowler, W. Hou, N. Coombs and R. W. J. Scott, *The Journal of Physical Chemistry C*, 2009, 113, 12719-12730.
33. N. Dimitratos, J. A. Lopez-Sanchez, J. M. Anthonykutti, G. Brett, A. F. Carley, R. C. Tiruvalam, A. A. Herzing, C. J. Kiely, D. W. Knight and G. J. Hutchings, *Phys. Chem. Chem. Phys.*, 2009, 11, 4952-4961.
34. R. C. Tiruvalam, J. C. Pritchard, N. Dimitratos, J. A. Lopez-Sanchez, J. K. Edwards, A. F. Carley, G. J. Hutchings and C. J. Kiely, *Faraday Discuss.*, 2011, 152, 63-86.
35. P. P. Wells, E. M. Crabb, C. R. King, R. Wiltshire, B. Billsborrow, D. Thompsett and A. E. Russell, *Physical Chemistry Chemical Physics*, 2009, 11, 5773-5781.
36. Z. H. N. Al-Azri, W.-T. Chen, A. Chan, V. Jovic, T. Ina, H. Idriss and G. I. N. Waterhouse, *Journal of Catalysis*, 2015, 329, 355-367.

37. C. A. Schneider, W. S. Rasband and K. W. Eliceiri, *Nat Meth*, 2012, 9, 671-675.
38. E. K. Gibson, A. M. Beale, C. R. A. Catlow, A. Chutia, D. Gianolio, A. Gould, A. Kroner, K. M. H. Mohammed, M. Perdjon, S. M. Rogers and P. P. Wells, *Chemistry of Materials*, 2015, 27, 3714-3720.
39. B. Ravel and M. Newville, *J. Synchrot. Radiat.*, 2005, 12, 537-541.
40. S. Nishimura, T. N. D. Anh, D. Mott, K. Ebitani and S. Maenosono, *J. Phys. Chem. C*, 2012, 116, 4511-4516.
41. F. Liu, D. Wechsler and P. Zhang, *Chemical Physics Letters*, 2008, 461, 254-259.
42. P. Zhang and T. K. Sham, *Physical Review Letters*, 2003, 90, 245502.
43. S. Marx and A. Baiker, *The Journal of Physical Chemistry C*, 2009, 113, 6191-6201.
44. A. I. Frenkel, M. Vairavamurthy and M. Newville, *J. Synchrot. Radiat.*, 2001, 8, 669-671.
45. D. C. Koningsberger, B. L. Mojet, G. E. van Dorssen and D. E. Ramaker, *Top. Catal.*, 2000, 10, 143-155.
46. J. Keating, G. Sankar, T. I. Hyde, S. Kohara and K. Ohara, *Physical Chemistry Chemical Physics*, 2013, 15, 8555-8565.
47. L. S. Al-Mazroai, M. Bowker, P. Davies, A. Dickinson, J. Greaves, D. James and L. Millard, *Catalysis Today*, 2007, 122, 46-50.

Chapter 6: Photocatalytic hydrogen production reactions of carbon nitride

Table of contents

6.1	Introduction	181
6.2	g-C ₃ N ₄ properties and background	183
6.2.1	Carbon nitride history	183
6.2.2	Carbon nitride synthesis	183
6.2.3	XRD analysis	184
6.2.4	XPS analysis	184
6.2.5	UV/Vis analysis	186
6.3	Photoatalytic activity of g-C ₃ N ₄	187
6.3.1	Comparison of Pd-C ₃ N ₄ catalysts made by incipient wetness and in situ photodeposition	187
6.3.2	Comparison of H ₂ production from photoreforming reactions of g-C ₃ N ₄ loaded with Pd and Pt	189
6.3.3	Variation of TEOA concentration	191
6.3.4	Gas phase photocatalytic reactions of Pd-C ₃ N ₄	192
6.4	Comparison of photocatalytic reforming reactions of methanol and triethanolamine on titania and graphitic carbon nitride	194
6.4.1	Incipient wetness impregnation catalysts comparison of photocatalytic hydrogen production on TiO ₂ and C ₃ N ₄	194
6.4.2	UV-Vis analysis	194
6.4.3	Photo-deposition catalysts comparison of photocatalytic hydrogen production on TiO ₂ and C ₃ N ₄	198
6.4.4	Transmission electron microscopy	199
6.4.5	Effect of pH on rate of hydrogen produced from carbon nitride	202
6.5	Visible light photocatalysis with g-C ₃ N ₄	203
6.6	Photocatalytic reforming reactions of Pd-TiO ₂ and Pd-C ₃ N ₄ with various amines and alcohols	204
6.6.1	Amine reforming reactions on Pd-C ₃ N ₄	204
6.6.2	Amine reforming reactions on Pd-TiO ₂	208

6.7	Conclusions	210
6.8	References	211

6.1 Introduction

The production of hydrogen photocatalytically over semiconductor supports has gained interest as an attractive method for converting solar energy into stored chemical energy.^{1,2} To date TiO₂ has been perhaps the most promising and most studied semiconductor photocatalyst for hydrogen production applications by reforming reactions.³⁻⁸ This is due largely to its abundance, non-toxicity and stability, with excellent activity under UV irradiation.⁹

As mentioned in previous chapters when a semiconductor is irradiated with equal or greater energy than the band gap photons can be absorbed to produce electron-hole (e⁻ and h⁺) pairs, which can either recombine or react with surface absorbed species. For the case of TiO₂ the band gap is 3.2 eV (or ~387 nm) which is in the ultra-violet region of the spectrum.¹⁰ This results in TiO₂ being an efficient photocatalyst in the UV regime. However TiO₂ has a poor response to sunlight with only about 4% the solar radiation reaching the earth's surface of sufficient energy to enable bandgap excitation. Graphitic carbon nitride (g-C₃N₄) has recently gained interest as an inorganic semiconductor for photocatalytic water splitting.¹¹⁻¹³ This is predominately due to the band gap of g-C₃N₄ ~2.7-2.9 eV (~420-460 nm) lying partly into the visible region of spectrum, potentially utilising a larger amount of solar radiation compared to TiO₂. Also g-C₃N₄ has proven attractive as it is relatively cheap, with proven stability.¹⁴ Previous studies have shown that pristine TiO₂ and C₃N₄ typically demonstrate poor activity for photocatalytic hydrogen production. However, the addition of precious metal NPs (i.e., Pt, Pd, Au, and Ag) to the surface of the TiO₂ can greatly enhance the efficiency of the photocatalytic reforming reaction.¹⁵ This increase in activity can be understood in terms energy levels of the semiconductor, the photo-excited electron in the conduction band of TiO₂ can be transferred to the metal NPs. This electron can then be trapped in the NPs thus increasing the life-time of the electron-hole pair. This ultimately results in inhibition of electron-hole recombination and an increased likelihood electron transfer to the substrate, thus improving photoreactivity. Further, the metal is also important for activation of the hole scavenger molecules that are used in hydrogen production.¹⁶

Both metal NP loaded TiO₂ and C₃N₄ demonstrate poor efficiency for photocatalytic H₂ production from pure water however. Activity is typically enhanced by the use of a hole

scavenger (sometime called a sacrificial agent), which will react with the photogenerated holes. The hole in the valence band is then removed by this reaction, further increasing the life-time of the electron hole pair and thus activity. As a result of this the hydrogen produced comes partly from water splitting and partly from dehydrogenation of the hole scavenger. Therefore the reaction can also be called photocatalytic reforming of the hole scavenger molecule. Common hole scavengers for a Pd-TiO₂ catalyst are simple alcohols such as methanol, ethanol and glycerol, as discussed in chapter 1.¹⁶ However the hole scavenger commonly found in the literature for use with a metal NP supported C₃N₄ catalyst is triethanolamine (TEOA).^{13, 17, 18}

Often no explanation is given as to the breakdown products of TEOA in the photoreaction; instead the focus is on the H₂ yield. Also the choice of TEOA as a hole scavenger is rarely justified, especially as TEOA is regulated chemical which can be difficult to obtain.

In this chapter synthesis and characterisation of urea derived g-C₃N₄ is investigated by XRD, XPS, UV/Vis and TEM. Photocatalytic reactions of noble metal loaded g-C₃N₄ comparing preparation methods of Pd-C₃N₄ (incipient wetness vs *in situ* photodeposition), choice of metal co-catalyst (Pd vs Pt) and gas phase reactions vs liquid phase reaction were performed. Also in this chapter we compare photoreforming reactions of methanol and TEOA on both Pd-TiO₂ and Pd-C₃N₄ catalysts with the use of a solar simulator. Often it is typical for studies to use different reaction parameters between g-C₃N₄ and TiO₂ for photocatalytic hydrogen production. It is common to see between 5-20 mg of g-C₃N₄ used for a reaction, with a large amount of hole scavenger (~10% volume).¹⁹ Whereas for titania the reverse is often the case, low hole scavenger content and larger amounts of the catalyst. Therefore, to make proper comparison of the two types of photocatalyst, experiments were performed under similar conditions for both, to gain an understanding of the relative activities of both semiconductors under UV and visible light irradiation. Photocatalytic reforming reactions of a variety of amine hole scavengers on both g-C₃N₄ and TiO₂ based catalysts were also investigated. The g-C₃N₄ (urea derived) was provided by David Martin, some help was provided in running the photocatalytic test by Angel Caravaca and Gareth Hartley.

6.2 g-C₃N₄ properties and background

6.2.1 Carbon nitride history

The first reported synthesis of carbon nitride derivatives dates back to work published by Berzelius and Liebig in 1834, in which they reported the synthesis of the polymer ‘melon’ (linear polymer consisting of interconnected heptazine units connected via secondary nitrogen’s).²⁰ However polymeric g-C₃N₄ in a sheet like structure was only synthesised relatively recently in 2006.²¹ This was achieved via thermal condensation of nitrogen and carbon containing precursors (explained in more detail below). Both triazine and heptazine have been discussed as possible tectonic units to constitute stable allotropes of g-C₃N₄, see Figure 1.²² Work by Kronke *et al.* based on density functional theory (DFT) has calculated that the structure based on repeating heptazine unit is 30 kJ. mol⁻¹ more stable than the alternative based on triazine units, this was supported by further ab initio calculations done by Sehnert *et al.*^{23, 24} Indeed this has also been established experimentally.²⁵

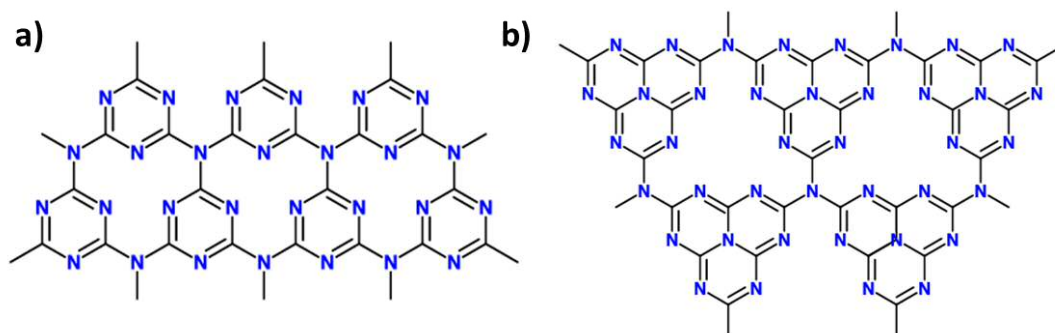


Figure 1. a) Representation of g-C₃N₄ based on triazine units and b) representation of g-C₃N₄ based on heptazine units).

6.2.2 Carbon nitride synthesis

The g-C₃N₄ used in this study was supplied by Dr David Martin and was synthesised at Research complex Harwell. The g-C₃N₄ was prepared by thermal decomposition of urea and was produced with an identical procedure as in previous published work by Martin *et al.*¹⁸ Details of the synthesis procedure can also be found in section 2.3.6. As well as urea, g-C₃N₄ can be synthesised by thermal condensation of a variety of nitrogen rich precursors including dicyandiamine,²⁶ melamine,²⁷ cyanamide,¹⁵ and thiourea.²⁸ However for the results shown in this section only urea derived g-C₃N₄ was used as this has been demonstrated to produce among the most active catalysts.¹⁸

6.2.3 XRD analysis

The XRD pattern of urea synthesised $g\text{-C}_3\text{N}_4$ is displayed in Figure 2. The lack of several peaks is a consequence of relatively simple sheet like structure of $g\text{-C}_3\text{N}_4$.²¹ The distinct peak at $2\theta = 27.4^\circ$ ($d = 0.326$ nm) is indexed by the 200 plane and is a consequence of the inter-planer stacking of the aromatic systems. The smaller peak at $2\theta = 13.0^\circ$ ($d = 0.681$ nm) can be indexed as the 100 peak which corresponds to the in plane distance of repeating structural motifs.^{29, 30}

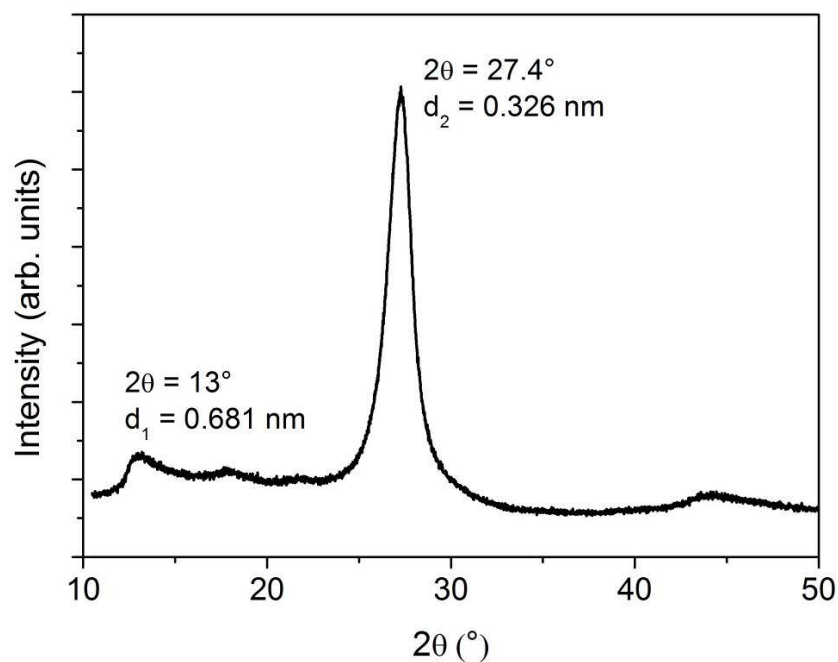


Figure 2. XRD pattern of urea synthesised $g\text{-C}_3\text{N}_4$.

6.2.4 XPS analysis

XPS analysis of the pure $g\text{-C}_3\text{N}_4$ (urea) was performed to investigate the status of the carbon and nitrogen elements present and any oxygen impurities. Figure 3 shows the wide survey scan and high resolution spectra of the peaks C1S, N1S and O1S in $g\text{-C}_3\text{N}_4$. The C1S spectra consist of two deconvoluted peaks at ~ 284.1 eV corresponds to sp^2 bonded carbon (C-C) and the major peak at ~ 288.2 eV is associated with sp^2 bonded carbon from the heptazine rings (N-C=N).²⁸ The N 1s spectrum can be deconvoluted into four peaks at 398.7 eV, 400.1 eV, 401.2 eV and 404.3 eV. The main peak is centred at 398.7 eV and originates from the sp^2 bonded nitrogen in the triazine ring (N-C=N), the weak peak at 400.1 eV is created by the tertiary nitrogen group N-(C)₃. Together these two nitrogen peaks with the addition of the carbon peak (N-C=N) make up the heptazine heterocyclic ring units of C_6N_7 , which is the basic substructure unit of the $g\text{-C}_3\text{N}_4$.¹⁸ Another two weak peaks in the nitrogen spectra are observed at 401.2 eV and 404.3 eV. The latter is a result of the presence of amino functional

groups (C–N–H) which originating from defective condensation, with the former attributed to charging effects or positive charge localization in the heterocycles.¹⁴ The O1S spectra consist of one peak centred at 532.5 eV and can be assigned to N-C-O which is a result of defect sites and contamination from air during calcination. However this peak is weaker and less significant compared to the C1S and N1S peaks as can be seen from the atomic % at the surface in Table 1.

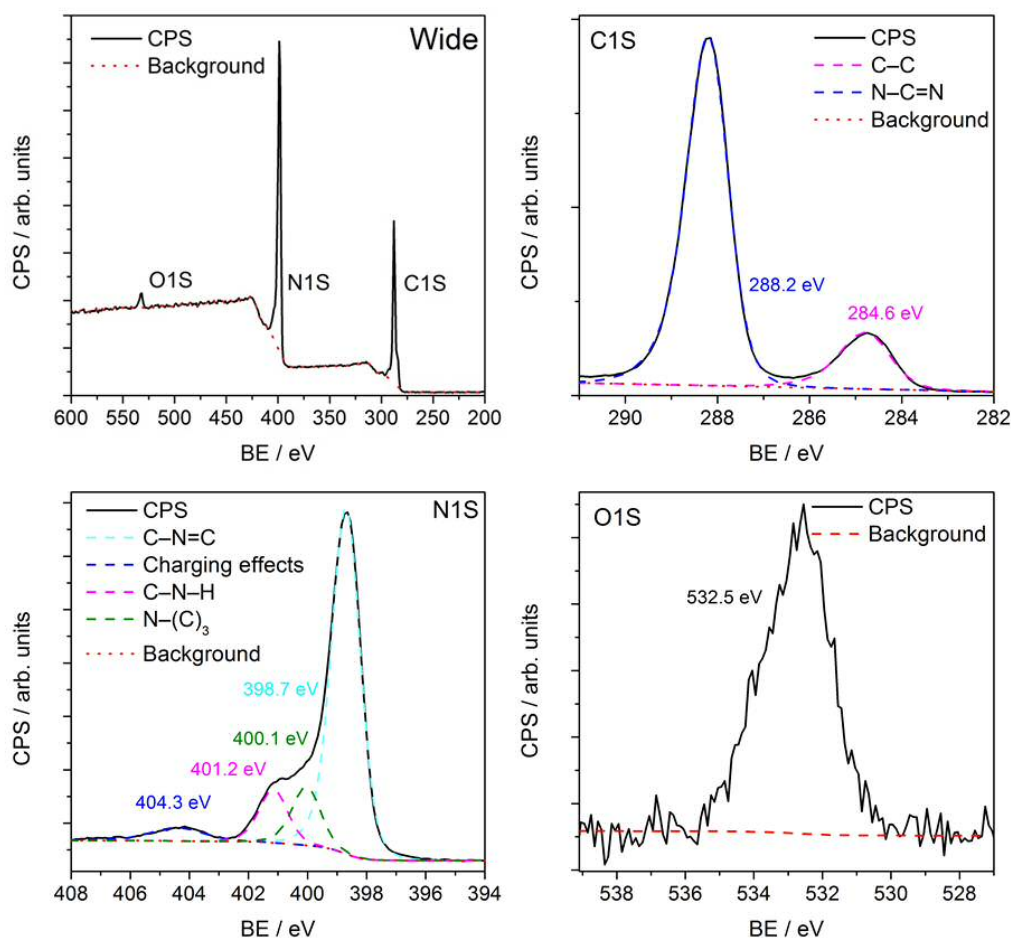


Figure 3. Survey scan and high resolution spectra with deconvolution of the peaks C1S, N1S and O1S in g-C₃N₄ (urea).

Table 1. List of O 1S, C 1S and N 1S peak position and atomic percent at the surface from XPS analysis.

Peak name	Position / eV	Atomic %
O 1S	532.5	1.52
C 1S	288.0	45.64
N 1S	399.0	52.84

6.2.5 UV/Vis analysis

The absorption properties of pristine g-C₃N₄ were analysed by diffuse reflectance UV-Vis spectroscopy and the results are displayed in Figure 4. The main absorption edge in the region of 420-440 nm corresponds to the band gap of the synthesised g-C₃N₄.¹⁸ The absorption edge is sharp at lower wavelength (~400 nm), however there is a tail in the region 440-520 nm, this can be attributed to sub band states from n- π^* transitions.^{31, 32}

Also included in Figure 4 is a Tauc plot, in which the absorption spectrum of g-C₃N₄ is manipulated by Equation 1 to have the x axis in units of eV. Generation of a plot of this type is a method for determining the optical band gap of semiconductors.³⁰

Equation 1

—

Where α is the absorption coefficient, h is planks constant (6.6×10^{-34} J.s), ν is the wavenumber, E_g is the optical band gap and n is a constant related to the transition of the band gap ($n=0.5$ for direct and $n=2$ indirect band gaps). Figure 4 shows the Tauc plot transformed UV/Vis spectra of g-C₃N₄ (urea), where the red line indicates the region where Equation 1 is satisfied. Care must be taken selecting the correct region for g-C₃N₄ semiconductors due to the tail associated with n- π^* transitions.^{31, 32} Since g-C₃N₄ has an indirect band gap,³³ the E_g can be calculated where the red line crosses at $(\alpha\nu)^{(1/n)} = 0$. From the generated Tauc plot in Figure 4 a band gap of 2.77 eV was calculated for the urea synthesised g-C₃N₄ which is in good agreement with reports in the literature.^{18, 30, 34}

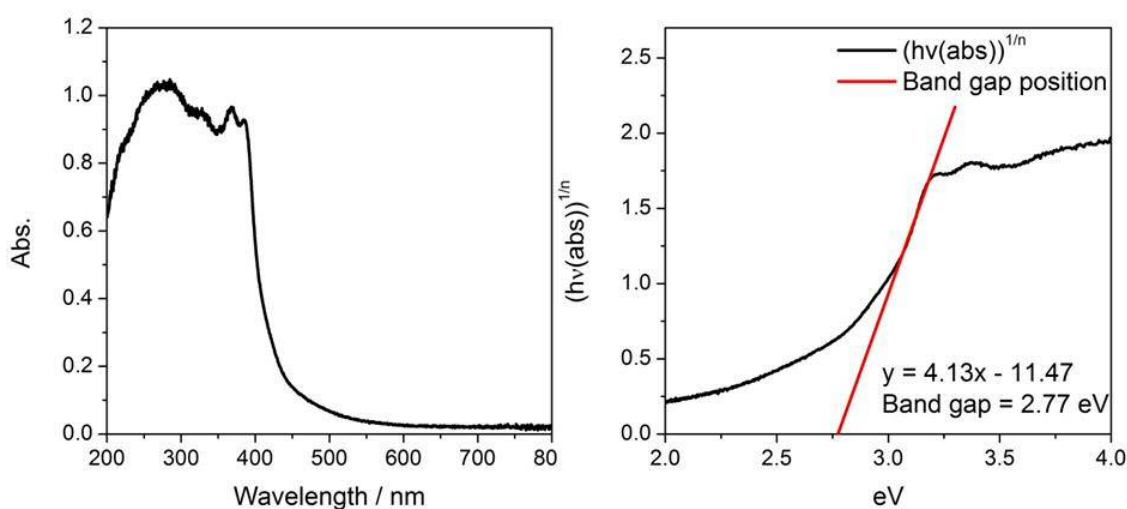


Figure 4. UV-Vis absorption spectra of pure g-C₃N₄ (urea) and associated Tauc plot

6.3 Photoalytic activity of g-C₃N₄

6.3.1 Comparison of Pd-C₃N₄ catalysts made by incipient wetness and in situ photodeposition

To achieve improved rates of hydrogen production g-C₃N₄ is often modified with a noble metal in the form of NPs on the surface as with other semiconductors such as TiO₂.^{11, 35} This is to improve the life time of the electron hole pair and to provide a site for the reaction to occur.¹⁶ A very common method for depositing noble metal on to the surface of g-C₃N₄ is by photodeposition during the reaction, in which the evolved hydrogen is measured simultaneously.^{11, 18, 34} Here a comparison of photocatalytic activity of a 3wt% Pd-C₃N₄ catalyst made by traditional incipient wetness (IW) and 3wt% Pd-C₃N₄ catalysts made by *in situ* photodeposition (isPD) is made. Figure 5 shows the hydrogen production plots for reactions with 3wt% Pd-TiO₂ made by IW and isPD as well as average rates after the initial induction period. When the catalyst was tested with either the absence of light or hole scavenger no hydrogen products were detected.

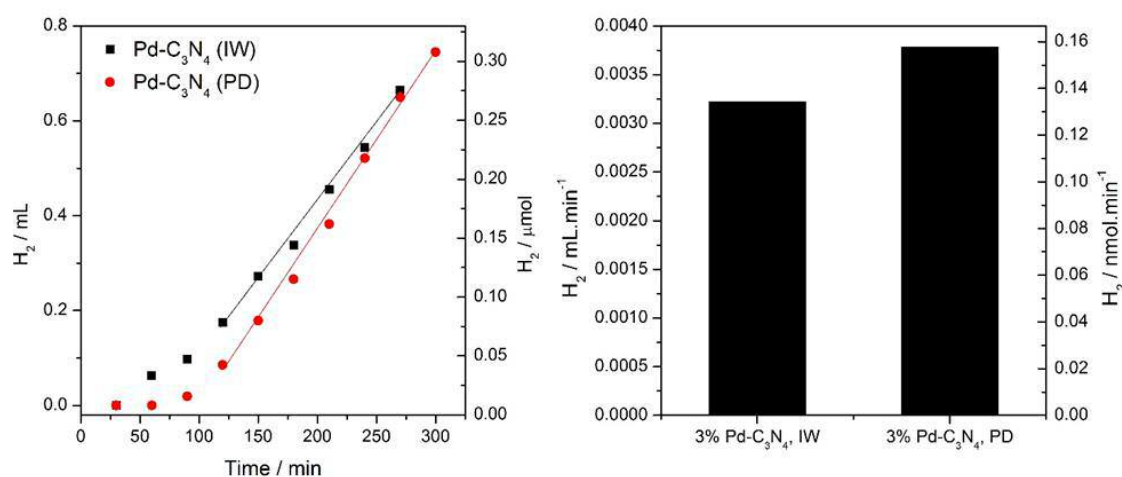


Figure 5. Hydrogen production plots for reactions with 3wt% Pd-TiO₂ (20 mg) made by incipient wetness and *in situ*. photodeposition from 200 mL of 10% methanol solution.

The catalyst made by isPD demonstrates an induction period of ~ 120 minutes after which the reaction proceeds in a first order fashion. For the incipient wetness catalyst the induction period is reduced slightly to around 90 minutes however the rate after this period is less, 0.00322 mL.min⁻¹ opposed to 0.00378 mL.min⁻¹ of H₂. This is somewhat unexpected when taking into account the Pd particle size of both the IW and isPD catalysts. Figure 6 shows representative TEM images of both the IW and isPD catalysts after reaction along with

particle size histogram for the isPD catalyst. As can be seen in Figure 6 a) and b) the IW catalyst produced mainly large Pd particles $\sim 20\text{-}60\text{ nm}$, as such it was not possible to create an accurate histogram. This is in contrast to TiO_2 IW catalysts where a weight loading of up to 5% Pd has been achieved by this method with an average particle size as low as $\sim 2\text{ nm}$.³⁶ The isPD catalyst showed an average particle size of 3.0 nm (with a standard deviation of 0.9 nm) which will result in a higher dispersion (ratio of surface palladium to the bulk) compared to the IW catalyst. Therefore despite the isPD catalyst having an increased number of surface metal sites and palladium $g\text{-C}_3\text{N}_4$ interface sites compared with the IW catalyst, activity is comparable. The majority of the reactions involving $g\text{-C}_3\text{N}_4$ in this chapter were done using the isPD method as the data could be more easily compared to that in the literature and gave a slight improvement in rate compared to the IW catalysts tested here.

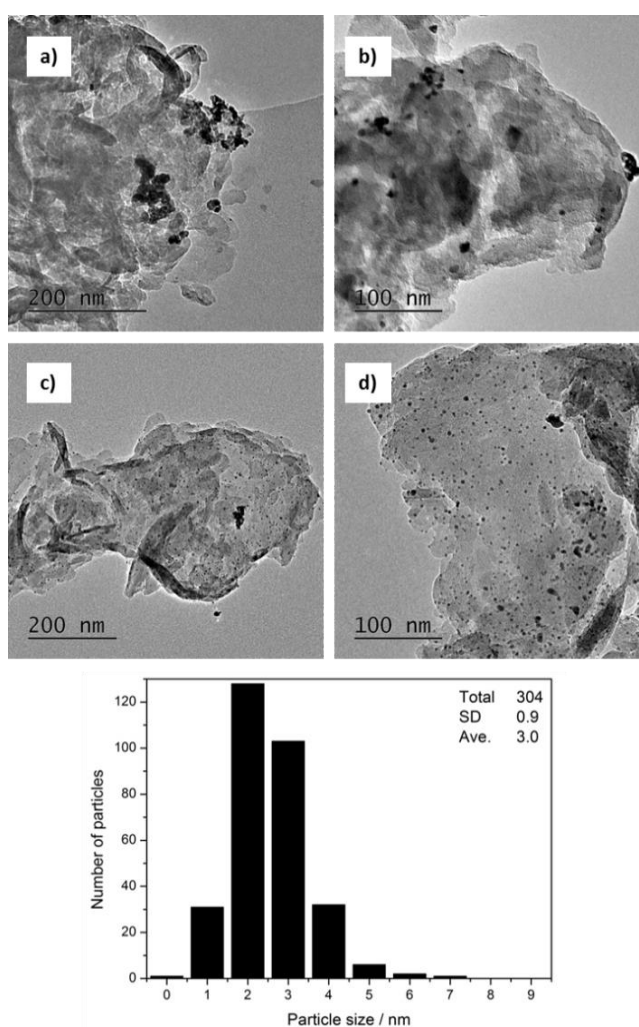


Figure 6. TEM images of a + b) 3wt%- C_3N_4 IW after reaction and c + d) 3wt%- C_3N_4 PD after reaction, with associated particle size histogram for the PD catalyst

6.3.2 Comparison of H₂ production from photoreforming reactions of g-C₃N₄ loaded with Pd and Pt

Several noble metals have been reported in the literature as suitable for *in situ*. photodeposition onto g-C₃N₄ during photocatalytic reforming reactions, such as Pd, Pt, Ru and Au.¹⁸ However, perhaps the most common of these metals is Pt owing to its often cited excellent activity on a both TiO₂ and g-C₃N₄ for photocatalytic reactions.^{18, 35, 37} Here a comparison between Pd and Pt as the metal co-catalyst for hydrogen production by photocatalytic methanol reforming over g-C₃N₄ is made, as these two are among the most active.

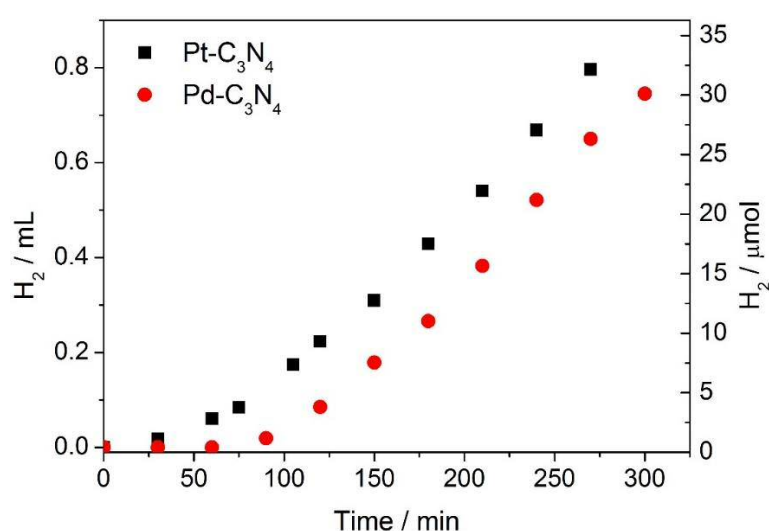


Figure 7. Hydrogen production plots for reactions with 3wt% Pd-TiO₂ and 3wt% Pt-TiO₂ (20 mg) *in situ*. photodeposition from 200 mL of 10% methanol solution.

Figure 7 shows hydrogen production plots for 3wt% Pd and Pt loaded g-C₃N₄. Both metals show an initial induction period where no hydrogen is produced, which corresponds to the time taken for the metal precursor to be reduced on the surface of the semiconductor.³⁸ After this induction period, ~ 60 min for the Pt and ~ 90 min for the Pd catalyst the rate of hydrogen production becomes linear in both cases, with the Pt-C₃N₄ having a rate of 0.00376 mL.min⁻¹ and the Pd-C₃N₄ with a rate of 0.00378 mL.min⁻¹. The difference in induction time between the two metals could stem from the differing of enthalpy of reduction, for the case of PdO and PtO₂ these values are -110 and -304 kJ.mol⁻¹ respectively.³⁵ Therefore it is likely that the Pt will reduce faster than the Pd and this is responsible for the shorter induction period observed. The two measured rates are practically identical indicating that the activity of these two metals very similar under these conditions, despite the difference in particle size of the Pd and Pt after photoreduction. Figure 8 shows representative TEM images of the

used isPD catalysts of Pd and Pt, with corresponding histograms and particle size summary for each. The Pt NPs demonstrated a smaller average size and standard deviation $1.9 \text{ nm} \pm 0.6$ opposed to the Pd NPs $4.6 \text{ nm} \pm 3.1$. Despite this clear difference in NPs size the H_2 production rate for the Pd and Pt on $\text{g-C}_3\text{N}_4$ under these reaction conditions is comparable. This could suggest that both metals have a similar activity and particle size is not a significant governing factor, or that there is a difference in intrinsic activity and a dependence on particle size which happens compensated in a manner to give identical activity here. The main objective for running this comparison was to decide which metal to use for subsequent reactions. As the rate observed for both Pt and Pd was practically identical it was thought that either would be suitable, however it was decided that Pd would be used for following reactions.

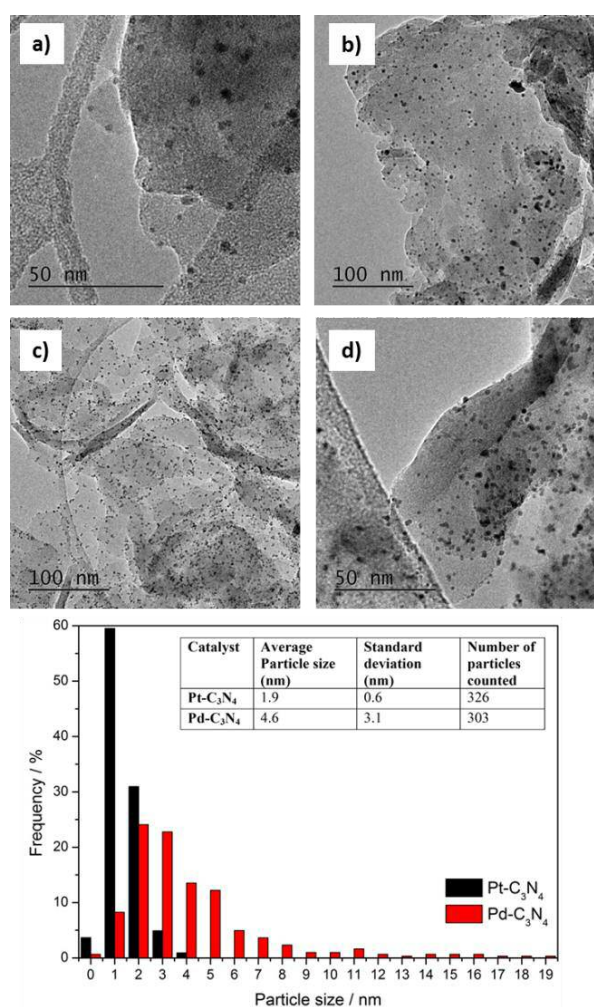


Figure 8. Example TEM images of a + b) 3wt%Pd-C₃N₄ and c +d) 3wt%Pt-C₃N₄ made by isPD, with particle size histograms of the synthesised Pd and Pt NPs and summary of particle size below.

6.3.3 Variation of TEOA concentration

For the preliminary reactions in this chapter methanol was used as the hole scavenger being reformed for photocatalytic hydrogen production. Methanol was chosen as it is the model chemical of choice for many photocatalytic reforming reactions using TiO_2 , used in this thesis and in the literature. However primarily in the literature Triethanolamine (TEOA) is the choice hole scavenger for photo reforming reactions involving noble metal NP decorated $g\text{-C}_3\text{N}_4$ catalysts. Later sections in this chapter will compare in detail the differences between alcohols and amines as hole scavengers for photo reactions on both $g\text{-C}_3\text{N}_4$ and TiO_2 . Here a series of reactions were performed with a 3wt%Pd- C_3N_4 (isPD) catalyst with a variety of different quantities of TEOA made up to 200 mL with H_2O to assess the effect of TEOA concentration on the rate of the reaction. Figure 9 shows the hydrogen production plot and the rate of the reaction at various TEOA concentrations, for a 3wt%Pd- C_3N_4 (isPD) catalyst. The trend observed is similar to that of methanol reforming reaction on a Pd- TiO_2 catalyst, where at low methanol concentrations the rate is greatly affected by the methanol concentration (Pseudo first order) and less affected at higher concentrations (pseudo zeroth order).³⁹ This trend is consistent with Langmuirian catalytic behaviour, as at higher concentrations it is assumed the surface of the catalyst is saturated with TEOA and hence addition of more will not affect the rate significantly. The two highest amounts of TEOA used in these experiments (0.25 and 0.025 moles in 200 mL H_2O) is equivalent to $\sim 16\%$ and 1.6% by volume. In both these cases the rate of hydrogen production achieved was higher than with 10% methanol and the same 3wt%Pd- C_3N_4 (isPD) catalyst.

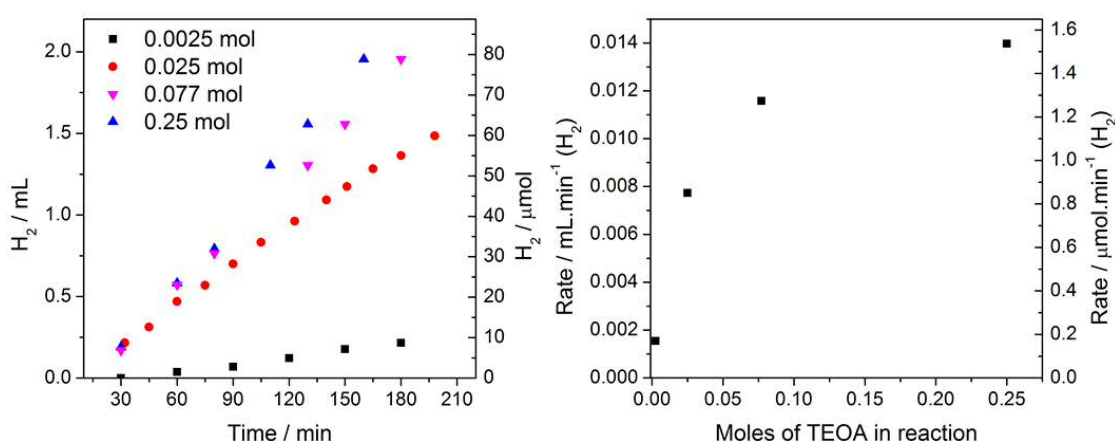


Figure 9. Hydrogen production plots from a 3wt%Pd- C_3N_4 (isPD) catalyst with a variety of different quantities of moles of TEOA in 200 mL H_2O , and plot of rate of reaction versus moles of TEOA in the reaction.

6.3.4 Gas phase photocatalytic reactions of Pd-C₃N₄

As well as running liquid phase reactions where the g-C₃N₄ based catalysts were stirred in a solution of water and respective hole scavenger during irradiation by the solar simulator, gas phase reactions were also undertaken. Previous work by Bahruji *et al.* identified that Pd-TiO₂ based catalysts demonstrated improved activity for photocatalytic methanol reforming when the reaction was performed in the gas phase opposed to liquid phase.³⁶ To investigate whether a similar trend could be observed for g-C₃N₄ based photo catalysts gas and liquid phase reactions were compared. Figure 10 shows a pellet of 13 mm diameter consisting of the 3wt %Pd-C₃N₄ (100 mg made by incipient wetness) catalysts attached to a glass slide. This slide was then placed inside the Pyrex reactor so that the pellet was suspended above the amine hole scavenger at the bottom. With this set up only the vapour of the solution below will be available to interact with the catalyst surface during the photoreaction. The amine hole scavenger chosen was triethylamine (TEA) as it has a higher vapour pressure opposed to TEOA and will produce an improved rate compared to methanol, which will be discussed in sections 6.6. Figure 11 shows hydrogen production plots for gas phase reactions of a 13 mm diameter 3wt%-C₃N₄ pellets (100 mg) suspended above TEA and suspended above TEA water mixture as well as data for a liquid phase reaction of TEA for comparison. Direct comparison between the gas and liquid phase reactions is difficult to do accurately considering the difference in reaction parameters. However it is clear that the gas phase reaction involving TEA and H₂O will have a smaller surface area of catalyst exposed to the arc lamp irradiation and have a lower concentration of reactants at the surface of the catalyst. Despite these factors the gas phase reaction involving TEA and H₂O produces in the order of 8 time more hydrogen than the liquid phase reaction. Also plotted in Figure 11 is the hydrogen production from a gas phase reaction involving pure TEA and no added H₂O, so that the vapour present on the surface of the catalyst is that of the amine. Under these conditions the rate is significantly reduced indicating that both the amine and the H₂O are required for the reaction to proceed efficiently. It is worth noting that although care was taken to avoid H₂O being present in the reaction it is likely that there will be some present, perhaps from the TEA. The exact reason for the improvement in rate in the gas phase is unclear at present, but may relate to more favourable ratio of amine/water and a reduction of completion for surface sites with water. Further work on photocatalytic gas phase reactions involving noble metal loaded g-C₃N₄ could be a promising method for increasing activity of hydrogen production for these systems.



Figure 10. Left, image of an 8 mm diameter 3wt% Pd-C₃N₄ pellet (100 mg made by incipient wetness) attached to a glass slide. Right, image of the glass slide with pellet attached inside the photo reactor with the pellet held above the liquid at the bottom.

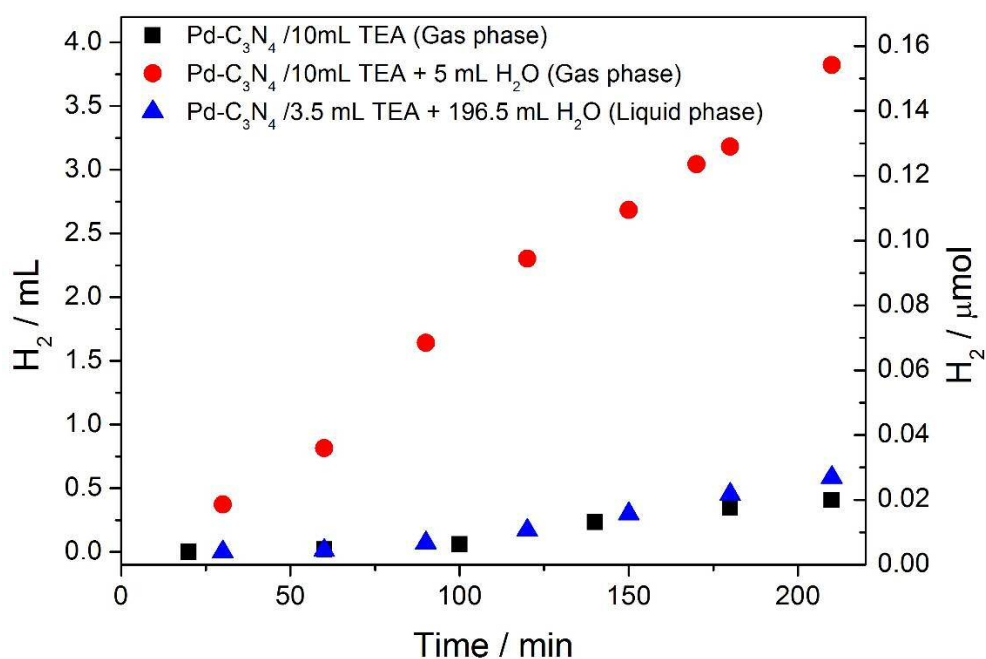


Figure 11. Hydrogen production plots for gas phase reactions of 8 mm diameter 3wt%-C₃N₄ pellets (100 mg) suspended above 10 mL TEA (black dots) and suspended above 10 mL TEA + 5 mL H₂O (red dots). For comparison (blue dots) liquid phase reaction

6.4 Comparison of photocatalytic reforming reactions of methanol and triethanolamine on titania and graphitic carbon nitride

For direct comparison of the activity of Pd loaded g-C₃N₄ and TiO₂, a set photocatalytic reforming reactions of methanol and TEOA were performed under identical conditions. One set of reaction was performed with a Pd loaded incipient wetness catalyst and another with an isPD Pd catalyst. Both catalysts were tested with TEOA and methanol as the sacrificial agent. Techniques such as doping of C₃N₄ (I,S and Fe)⁴⁰⁻⁴⁴ and structural engineering (thin films, porous or hollow structures)^{11, 19, 34, 45} have been applied to the generate improved electronic and physical properties for enhanced activity. This is also true for synthesised TiO₂ materials where the band gap has been tuned by doping with N, C and S etc.⁴⁶⁻⁴⁹ However for the purposes of this study only the pure unmodified g-C₃N₄ (urea) and TiO₂ (P25) were used for a fair comparison of intrinsic activity.

6.4.1 Incipient wetness impregnation catalysts comparison of photocatalytic hydrogen production on TiO₂ and C₃N₄

Loading of 0.5wt% Pd on both semiconductors was achieved by incipient wetness impregnation prior to the reaction. With a mass of catalyst of 150 mg and 0.025 moles of hole scavenger (200mL of 0.125 M solution). The reaction was performed under full arc conditions of a 150 W Xe arc lamp solar simulator.

6.4.2 UV-Vis analysis

The absorption properties of pristine TiO₂ (P-25) and g-C₃N₄ (urea) were analysed by diffuse reflectance UV-Vis spectroscopy (Figure 12). TiO₂ shows negligible absorption in the visible range with a sharp increase below roughly 400 nm corresponding the band gap of TiO₂ (380 nm, 3.2 eV).³⁷ In contrast, the absorption edge of C₃N₄ is shifted by roughly ~30 nm towards the visible compared to TiO₂, which can be attributed to the lower energy band gap of g-C₃N₄. While the absorption edge of C₃N₄ is sharp there is a tail between approximately 440 – 520 nm before flattening out, this tail maybe due to some sub band states from n-π* transitions, as mentioned earlier^{31, 32}.

In the region of 380 nm C₃N₄ shows transitions which can be assigned to π -π* transitions commonly observed in heterocyclic aromatics.³¹ Absorption spectra of both C₃N₄ and TiO₂ prepared with 0.5wt% Pd by incipient wetness were also recorded (Figure 12), with their catalytic activity discussed in the next section. In both cases the shape of the absorption

spectrum is broadly similar, with a slight shift in edge position to longer wavelength. However, the Pd-TiO₂ sample shows increased absorption over a broad range of wavelengths in the visible region. This is likely to be due to the presence of PdO on the surface of the semiconductor remaining after the calcination step in the catalyst preparation. This PdO can absorb visible light in the 400-550 nm range owing to d-d transitions of the PdO particles.⁵⁰ After reduction during the reaction the Pd-TiO₂ catalyst changes colour becoming a darker shade of grey, with the Pd-C₃N₄ catalyst remaining largely the same colour. This is consistent with the post-reaction UV-vis, which shows increased absorption over a wide range of wavelengths for the Pd-TiO₂ with the Pd-C₃N₄ not changing significantly neither after preparation nor use. The differences in optical properties between pristine g-C₃N₄ and TiO₂ can be seen visually in the colour variation Figure 13. This fits with the absorption spectra in Figure 12 where the TiO₂ demonstrates no absorption in the visible range, hence the white colour.

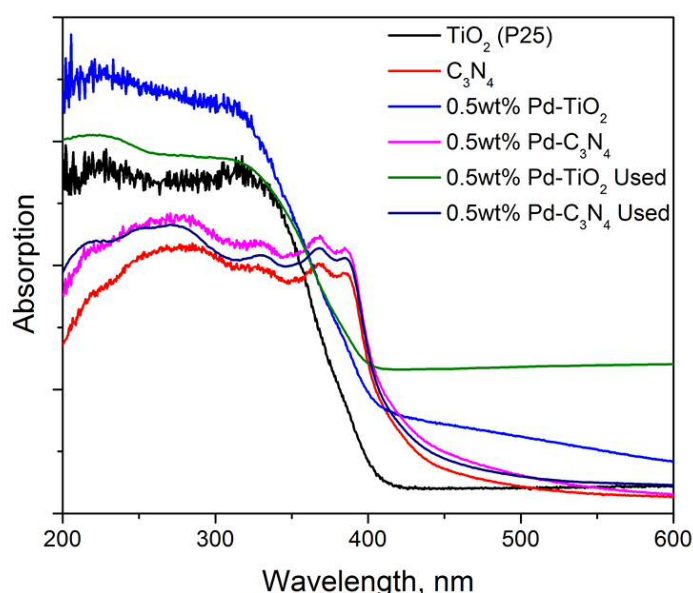


Figure 12. UV-Vis absorption spectra of pure TiO₂ (P-25) and C₃N₄, and with 0.5% Pd loaded, both before and after use



Figure 13. Photograph of g-C₃N₄ (urea derived) and TiO₂ (P25) showing the difference in colour.

Figure 14 shows the hydrogen production plots from both methanol and TEOA using 0.5% Pd-C₃N₄ and 0.5% Pd-TiO₂ incipient wetness catalysts. As can be seen the choice of hole scavenger and semiconductor has a strong influence on the quantities of hydrogen produced. Both reaction systems follow the same trend, with TEOA producing a greater yield of H₂ compared to methanol. The TiO₂ based catalyst was significantly more active with full arc illumination than those of C₃N₄, producing of the order of 8 times more H₂ for the TEOA reactions and 60 times more hydrogen for the methanol reactions after 3 hours.

Although the concentrations of the hole scavengers are identical, methanol contains only four hydrogen atoms while TEOA has 15, therefore this could be one contribution to the improved H₂ yield for TEOA for the Pd-TiO₂ sample. Thus, in Figure 14 the H₂ evolution comparison for TEOA and methanol when the same number of moles of hydrogen present in the sacrificial agent is also shown. The results show that the H₂ evolution is comparable under these conditions. For this to be accurate assumptions are made that the TEOA dehydrogenated completely on the Pd-TiO₂ and both the TEOA and methanol react with a similar rate.

For the case of the Pd-C₃N₄ sample it is of particular note that the yield of hydrogen from aqueous methanol was significantly less than that of TEOA, especially when compared to the Pd-TiO₂ catalyst, while the latter shows far less difference between the two hole scavengers. Also an induction period of about 90 minutes was seen before H₂ was evolved for the methanol reaction, whereas with TEOA H₂ production began immediately. This difference can be explained when considering the necessity for the metal to be in the reduced, metallic state, as a prerequisite for the reaction to produce H₂. The Pd begins in the oxidic state, since it was calcined in air prior to use, and is photoreduced during the reaction. Actual, H₂ evolution begins only once the Pd is fully reduced.³⁵ Indeed, at least 0.08 mL of hydrogen would be needed to reduce the 4 μmol of PdO present. At the rate of hydrogen evolution observed for the methanol reaction on Pd-C₃N₄ (after 90 mins it is $\sim 7 \times 10^{-4}$ mL.min⁻¹) that would take around 100 minutes, as observed. On the other hand, on Pd-TiO₂, the rate is 3×10^{-2} mL.min⁻¹, which corresponds with only around 3 minutes for reduction, which is before the first data point is measured. However, it is usually our contention that it is necessary to have the NPs in the metallic form to be active.¹⁶ This then, appears only to be the case in the sense that before the metal is reduced the H₂ which could be produced is used up in reducing the oxide to metal. As shown by Bahruji *et al.* recently,³⁵ the ability to produce hydrogen depends on the reducibility of the metal, so Ni, for instance, will not produce hydrogen normally, but will if it is carefully pre-reduced before placing in the photoreactor.

The lower reaction rate and the induction time for methanol indicates that it is a poor hole scavenger for C_3N_4 . In contrast, TEOA is obviously a much better scavenger – yet it works even better with TiO_2 . The poor behaviour for methanol on the nitride is explained by the mechanism previously proposed for the reaction on $Pd-TiO_2$,^{2, 16} which is describe as the photo-reforming of methanol. Basically it can be summarised as follows –



Here step 1 proceeds on the Pd NPs, since methanol has been shown to decarbonylate at ambient temperature,^{4, 16, 51} and leaves CO adsorbed on the surface. When the surface is saturated with CO, no further reaction takes place (self-poisoning) until step 2 occurs by bandgap excitation in the TiO_2 to create an electron-hole pair. The CO is then cleaned off the Pd by the highly electrophilic oxygen species (the hole) in step 3. The final step is filling of the vacancy in the TiO_2 by water. Thus, an essential element of this scheme is the active oxygen and this is not available on the nitride, hence the very low reaction rate on that material. This then raises questions regarding the mechanism of reaction of TEOA. Since this does react on the nitride, it is likely that reaction proceeds through the nitrogen group, initially presumably via the lone pair of the nitrogen, section 6.6.1 will investigate this further.

Indeed, results from section 6.6 and elsewhere,^{13, 52} shows that amines react well photocatalytically with both materials. At this stage we know little about the mechanism of this part of this reaction, except that it is a net dehydrogenation.

When comparing the two semiconductors with these identical reaction parameters, using the full spectrum of simulated solar light, it is clear that TiO_2 is significantly more active for photocatalytic hydrogen production with TEOA and methanol.

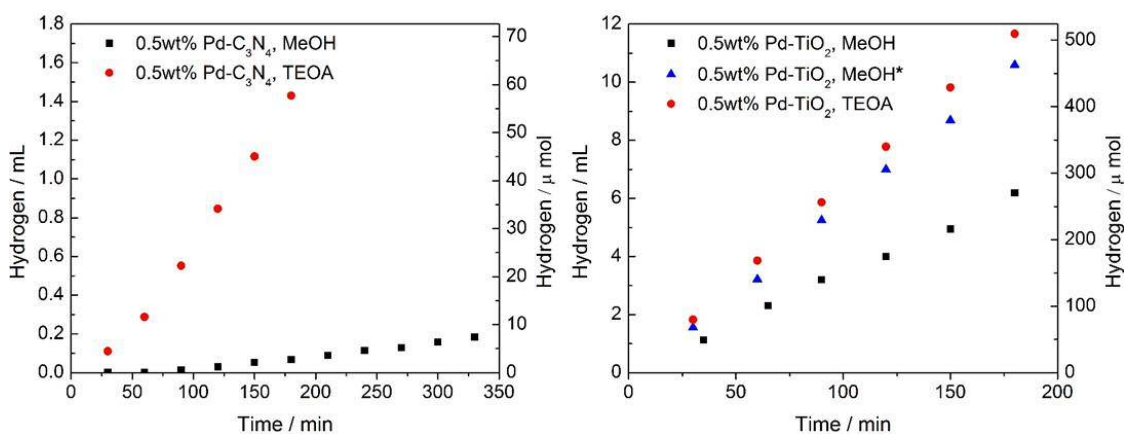


Figure 14. Hydrogen production plots for reactions with 150 mg catalyst and 0.025 moles of hole scavenger. *0.09375 moles of methanol used.

6.4.3 Photo-deposition catalysts comparison of photocatalytic hydrogen production on TiO₂ and C₃N₄

A second set of comparison reactions under different reaction parameters was also performed, using a much lower amount of 20 mg of the semiconductor (20 mg) in 200mL of 0.125 M solution of hole scavenger with 3wt % Pd loading. This was done as reaction parameters for photocatalytic reactions involving g-C₃N₄ can vary in the literature; however it is perhaps most common to use a relatively small amount of the catalyst (5-50 mg) with higher loadings of metal compared to reactions involving TiO₂.^{16, 22}

In-situ photo-deposition by irradiation with UV light is a common method for reducing metal precursors to prepare NPs immobilised onto semiconductor surfaces. It has been reported that the role of the semiconductor such as TiO₂ or C₃N₄, during photo-excitation is to transfer electrons from the valence band to the metal precursor, whilst the hole reacts with a scavenger species.^{53, 54} This results in the formation of Pd NPs in a dispersed manner across the surface of the C₃N₄, as can be seen in the TEM images in Figure 16, (discussed in more detail below).

Figure 15 shows the hydrogen production plots for reactions with 20 mg catalyst and a 3wt% loading of Pd on both C₃N₄ and TiO₂ by in situ photodeposition with TEOA and methanol. Similar to the results for the incipient wetness method, TEOA was again found to be the most active hole scavenger for such materials with the TiO₂ based catalysts being the most active. One suggestion for the higher yield of hydrogen from TEOA is explained by the increased hydrogen content and extra functional groups of the molecule compared to methanol. However, a rate of hydrogen production from TEOA that is much higher than that of

methanol cannot be explained solely by the extra OH groups of TEOA. Therefore, it may be that the nitrogen functional group on TEOA is responsible for the majority of the activity observed, and is primarily responsible for the rapid deposition of the Pd.

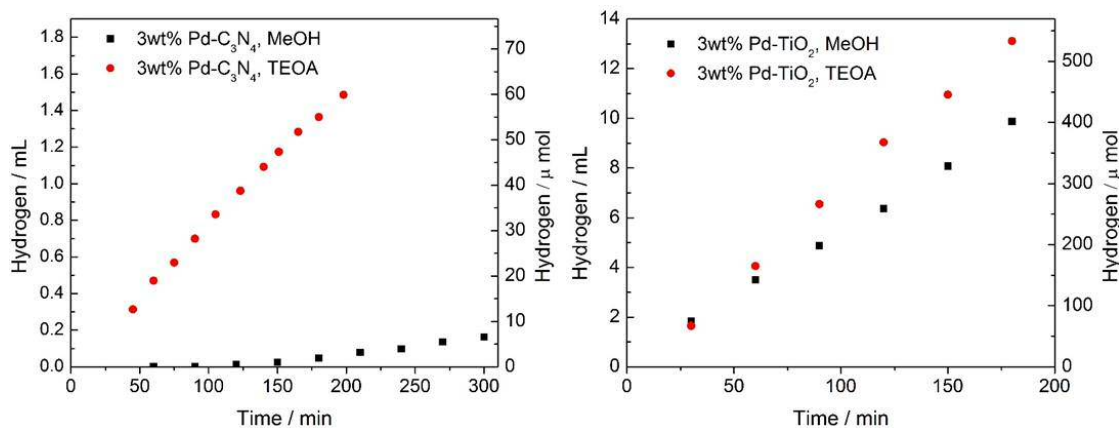


Figure 15. Time dependent hydrogen production plots for reactions with 20 mg catalyst and 0.025 moles of hole scavenger in 200 mL water, left, 3%Pd-C₃N₄ and right, 3%Pd -TiO₂

6.4.4 Transmission electron microscopy

TEM analysis of both the used and unused 0.5%Pd weight loading IW catalysts was performed. However no Pd NPs were observed for all cases, it was assumed that the Pd NPs formed by this method were too small and well dispersed to be observed. However for the higher Pd loading isPD catalysts observation of the NPs by TEM was successful. Therefore analysis of the used 3wt% Pd-C₃N₄ and 3%Pd-TiO₂ catalysts from both the methanol and TEOA reactions was performed by TEM to gain information on the particle size and morphology of the Pd NPs produced during *in situ* photodeposition. Representative images of each along with particle size histograms are shown in Figure 16. As can be seen, in all cases the Pd NPs are well dispersed over the surface of the support. The Pd particles photo deposited on g-C₃N₄ have some heterogeneity containing some agglomerates of particles present whereas the Pd particles on TiO₂ shows primarily spherical particles homogeneously dispersed with a narrow particle size distribution.

Table 2 summarises the average particle size of the Pd NPs along with the standard deviation made during the 3wt% Pd-C₃N₄ and 3wt% Pd-TiO₂ reactions from both the methanol and TEOA. Particle sizes for the Pd on C₃N₄ made from both hole scavengers differ by around 1 nm with an average size of 4.6 nm for the methanol reaction and 5.4 for the TEOA reaction. Whereas the particle size after the photo deposition reaction on TiO₂ demonstrate a greater difference with 3.0 nm for the methanol reaction and 5.5 for the TEOA reaction. It is

interesting to note that the average particle size for Pd is smaller for reactions with methanol for both C_3N_4 and TiO_2 even though the rate is less for this reaction compared to the TEOA equivalent. For both catalysts TEOA produces a higher rate and larger particles of Pd relative to methanol. It is therefore unlikely that the higher activity of the TEOA reactions is due to a particle size effect as smaller NPs are typically more active and exhibit a higher metal surface area. Results from section 6.3.1 which compared reactions of an 3wt%Pd- C_3N_4 IW catalyst with large particles (too large and aggregated to generate an accurate particle size) to a 3wt%Pd- C_3N_4 isPD catalysts with an average particle size of 3 nm, found little difference in H_2 production rate when using methanol as the hole scavenger. This leads to the conclusion that perhaps the differences in particle size here do not have a significant effect on the H_2 production rate, while the choice of hole scavenger is the major factor governing activity. For the Pd^{2+} in solution to be reduced photo excited electrons in the conduction band need to be transferred to the Pd precursor in solution, whilst the hole in the valence band will need to be reduced by the hole scavenger. As the role of TEOA and methanol in these reactions is to remove the hole then the efficiency of this process could affect the particle size during the photo-deposition.

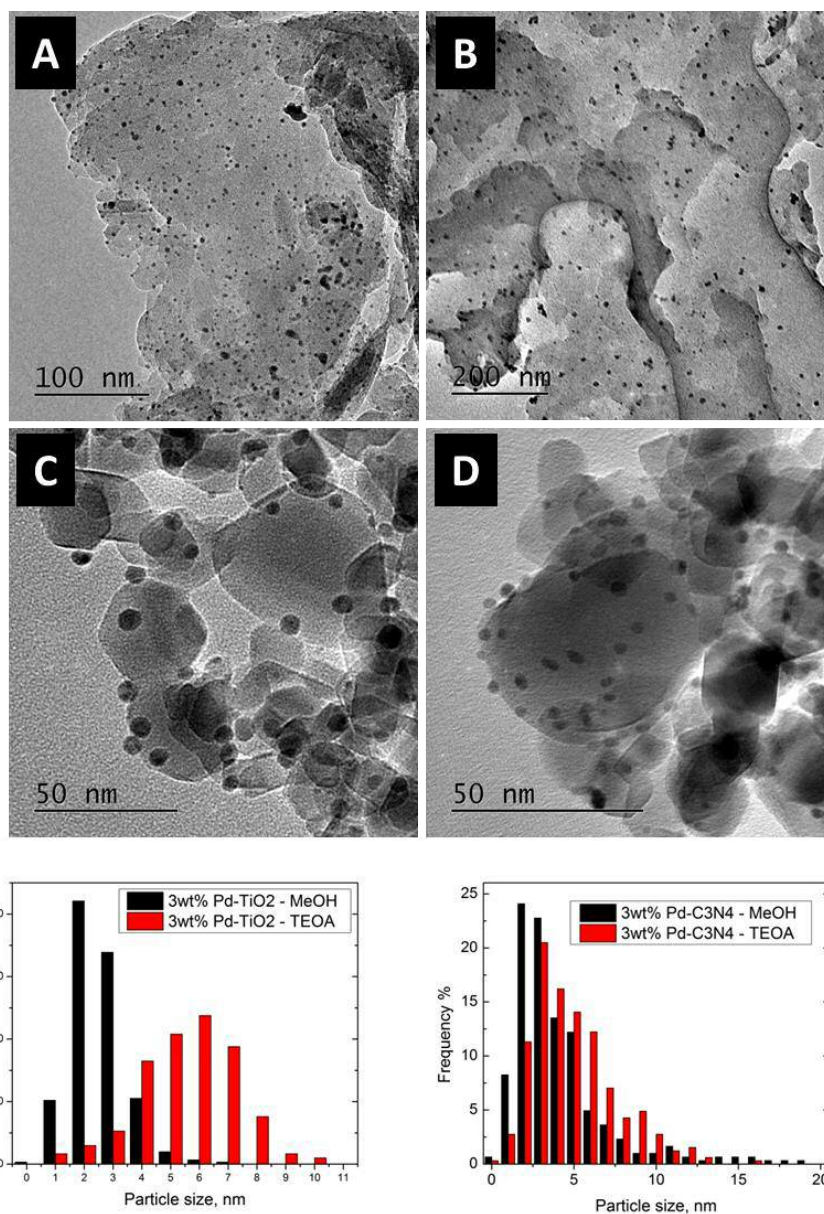


Figure 16. TEM images of 3%Pd-C₃N₄ after reaction with A) MeOH B) TEAO and 3%Pd-TiO₂ after reaction with C) TEAO and D) MeOH. The particle size histograms are also shown, obtained from counts of more than 300 NPs.

Table 2. Average particle size with standard deviation of Pd NPs made by isPD for reaction of TiO₂ and C₃N₄ with MeOH and TEAO

Catalyst system	Average Particle size (nm)	Standard deviation (nm)	Particles counted
3%Pd-C ₃ N ₄ MeOH	4.6	3.1	303
3%Pd-C ₃ N ₄ TEAO	5.4	2.6	327
3%Pd-TiO ₂ MeOH	3.0	0.9	304
3%Pd-TiO ₂ TEAO	5.5	2.6	303

6.4.5 Effect of pH on rate of hydrogen produced from carbon nitride

It is worth noting that the pH of the initial reaction mixture containing TEOA, g-C₃N₄ and water (from section 6.4.3) is very basic (pH 11.5 for 0.025 moles in 200 mL miliQ water) while the reaction mixture containing methanol, g-C₃N₄ and water was slightly acidic (pH 5.5 for 0.025 moles in 200 mL miliQ water). To investigate this further a reaction was performed where NaOH was added to g-C₃N₄ methanol mixture before the reaction to adjust the pH to 11.5. Figure 17 shows the hydrogen production plots for the 3wt% Pd isPD reactions of g-C₃N₄ with methanol at pH 5.5 and 11.5. The rate measured with the pH 5.5 and 11.5 reactions was 9.28×10^{-4} and 11.3×10^{-4} mL.min⁻¹ of H₂ respectively. This corresponds to an improvement in rate of about 22% for the reaction at higher pH, once the rate becomes stable. This is likely to be another factor as to why the methanol reaction on Pd-C₃N₄ produced less H₂ than the TEOA reaction in sections 6.4.1 and 6.4.3. However it is thought that the arguments made in those sections are still valid as the changed observed in the rate is small compared to the large increase in rate of TEOA over methanol measured.

Wu et al found a positive effect of high pH on visible light driven hydrogen evolution reactions of Pt loaded g-C₃N₄ from a 20% vol methanol solution. Although it wasn't until pH >> 10 that a significant change in H₂ production rate was observed.⁵⁵ The reaction parameters used by Wu et al varied to what was used by us, i.e. 20 % vol methanol solution, 1wt%Pt as the metal co-catalyst and a 400 nm long band pass filter. This could be factor as to why we did not see as much of an improvement in rate at higher pH for the methanol reaction.

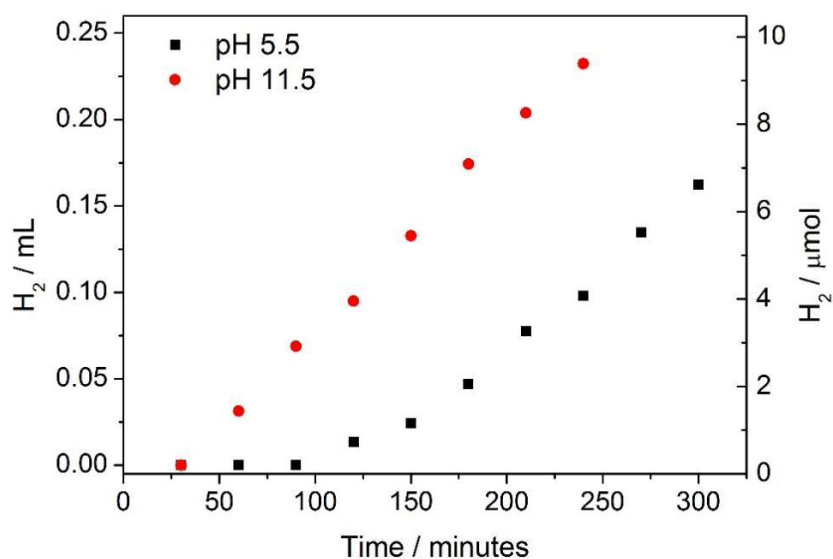


Figure 17. Hydrogen production plots for reactions with 20 mg catalyst 3% Pd-C₃N₄ 0.025 moles of methanol at pH 5.5 and 11.5 adjusted with NaOH.

6.5 Visible light photocatalysis with g-C₃N₄

As shown in the UV-Vis spectra in Figure 12, the C₃N₄ support displays an absorption shift into the visible compared to the TiO₂. The band gap of the urea synthesised C₃N₄ is estimated to be in the region of ~420 nm (~2.8 eV) while that of TiO₂ (P-25) is 387 nm (3.2 eV). It is worth noting that the band gap of C₃N₄ synthesised from thiourea and dicyandiamide (DCDA) have been reported to possess a smaller band gaps (2.75 eV) when compared to urea derived C₃N₄. However despite absorbing further into the visible, urea synthesised g-C₃N₄ exhibited greater activity in photo reforming reactions under full arc illumination.¹⁸ However this band gap shift of the thiourea and DCDA g-C₃N₄ can be attributed to morphology changes as well as defects/sub-stoichiometries within the sample.³⁴

Long band pass filters (350, 375, 400 and 420 nm, see section 2.4.6) were used to block the UV region of the incident irradiation during the photocatalytic reactions of C₃N₄ and TiO₂. Figure 18 shows the average rate of hydrogen production from IW 0.5% Pd-TiO₂ and 0.5% Pd-C₃N₄ catalysts using TEOA as the hole scavenger. As can be seen for the 0.5% Pd-TiO₂ catalyst the rate of hydrogen production decreases as the UV region is blocked until no hydrogen is produced with the 400nm filter in place, which is consistent with the TiO₂ band gap. Note that the UV-Vis spectra of 0.5% Pd-TiO₂ (Figure 12) show significant absorption in the visible region, but this does not contribute at all to any photocatalytic activity. For the 0.5%Pd-C₃N₄ catalyst system, again the rate of hydrogen production decreases with successive addition of the long band pass filters of 350, 375 and 400 nm, but does have some activity for the 400nm filter, that is, in the visible. This is consistent with the UV-Vis spectrum of the g-C₃N₄ support. However, when a 420 nm filter was employed neither the C₃N₄ or TiO₂ catalyst produced any hydrogen after 3 hours of illumination. It is often reported that g-C₃N₄ will be active for this reaction with a 420 nm filter in place; however none was measured for this reaction here perhaps due to the comparatively larger band gap of urea derived C₃N₄. So some visible light activity is observed for the g-C₃N₄ catalysts, but it is very low and much lower than when full spectrum light is used.

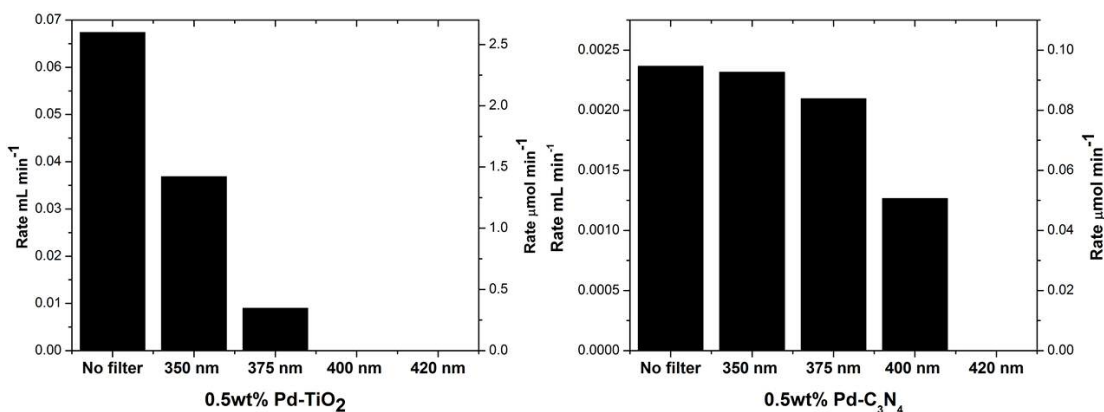


Figure 18. Average rates in mL.min⁻¹ and μmol.min⁻¹ of hydrogen production with a set long band pass filters (350, 375, 400 and 420 nm) for left, 0.5%Pd-TiO₂ and right, 0.5%Pd-C₃N₄ with TEOA reaction.

6.6 Photocatalytic reforming reactions of Pd-TiO₂ and Pd-C₃N₄ with various amines and alcohols

6.6.1 Amine reforming reactions on Pd-C₃N₄

For majority of results in this chapter the primary hole scavengers used for photocatalytic reactions involving g-C₃N₄ has been methanol and TEOA, with the exception of TEA for the gas phase reaction. To investigate alternative hole scavengers a variety of different amines was tested for photocatalytic hydrogen production. Figure 19 shows hydrogen production plots for the various amines and methanol (all 0.025 moles in 200 mL H₂O) from a 3wt%Pd-C₃N₄ isPD catalyst, while Figure 20 shows the associated hydrogen production rate results. When the catalyst was tested with either the absence of light or hole scavenger no H₂ was detected. The figures demonstrate that all the amines tested produced an improved rate of hydrogen production over methanol, which is in agreement with the results from section 6.4. It is worth noting that the physical characteristics of the amine used here vary significantly, Table 3 lists some properties. Both methylamine and ethylamine are gas at room temperature and so were bought as gasses dissolved in water, while N,N-diisopropylethylamine was immiscible with water, floating on the top of the reaction mixture when not stirred. Despite these characteristics all the amine produced significantly more hydrogen than methanol. It is interesting to note that under these reaction conditions more hydrogen was produced from TEA than from TEOA, despite TEA having a similar structure with the OH groups replaced with H. This again supports the assumption made in section 6.4 that it is the amine group on TEOA which is ultimately responsible for the improvement in H₂

production over methanol. The amine with the most structural similarities to methanol is methylamine, which has the –OH group replaced with an –NH₂, and produced in the order of 10 times the rate of hydrogen production as methanol. This indicates that the reaction will proceed with an alcohol albeit with a significantly lower rate. Currently the mechanism and intermediates of photocatalytic amine reforming is unclear. On Pd-TiO₂/methanol systems it is thought that the first step is methanol decomposition on the surface of the Pd to form a tightly bound CO species and release of two moles of H₂. This is followed by band gap excitation in the TiO₂ to generate a reactive O[•] species which will attack and remove the bound CO as a CO₂. The oxygen vacancy on the TiO₂ left from the leaving O[•] can then be filled by a water molecule (releasing a further mole of H₂), while the free site on the Pd can accommodate another methanol molecule completing the cycle, as discussed in section 6.4.1.^{16, 39, 56} As the O[•] species is generated from TiO₂ lattice oxygen this reaction pathway is clearly not available on Pd-C₃N₄ systems. Also this route is not possible for amines reacting with either Pd-TiO₂ or Pd-C₃N₄ photocatalysts as CO cannot be formed on the surface of the Pd.

J.J. Chen *et al.* investigated the adsorption and decomposition of methylamine on a Pd(111) surface by a combination of thermal desorption spectrometry (TDS), SIMS (secondary ion mass spectrometry) and XPS.⁵⁷ Their suggestion is that methylamine will dehydrogenate forming intermediates of the type CH_xN_{ads} (x = 0, 1, 2) species, with CN being the final state bound to Pd. This is supported by density functional theory (DFT) calculations by Liu *et al.* of the adsorption and dissociation mechanism for methylamine on Pd(111).⁵⁸ Based on their calculations they suggest the most likely decomposition path is H₃CNH₂ → H₂CNH₂ → HCNH → HNC + HCN → CN + H₂. In both the experimental and computational work referenced above it was found that no C-N bond cleavage occurred. Taking this into account an overall equation of the form H₃CNH₂ → CN + 5/2H₂ is suggested as the first step, this results in the release of hydrogen purely from the decomposition of methylamine on the Pd surface. Also it was calculated by Liu *et al.* that the methylamine was initially activated by the C-H bond cleavage and not N-H bond.⁵⁸ This would fit with the amine reforming data in Figure 19 as tertiary amines containing no N-H bonds produce comparable rates of hydrogen production as primary amines, assuming that this step is important for photocatalytic hydrogen production. For secondary or tertiary amines and primary amines containing a carbon chain longer than one carbon some C-N bond cleavage must occur if the final decomposition product on the surface of Pd is to be a CN group. Ammonium hydroxide which has no N-C or C-H bonds did produce some hydrogen in our experiments, albeit with a much reduced rate

compared to the primary, secondary and tertiary amines tested. Kominami *et al.* found that for photocatalytic reforming reactions of NH_3 on a Pt-TiO₂ catalyst the products were N_2 and H_2 , while no N_2 was formed from methylamine. This suggested different mechanisms of decomposition of ammonia and methylamine on a Pt surface, which could also hold true for a Pd surface.⁵⁹

If the results from the methylamine decomposition onto a Pd(111) surface from the references,^{57, 58} can be applied to the other amines tested here and holds true for Pd NPs surface on a g-C₃N₄ support then some hydrogen can be produced decomposition and dehydrogenation of the amine hole scavengers. However this this step alone is not a photocatalytic process. Therefore the surface species on the surface of the Pd NPs must be removed by the photoexcitation of the g-C₃N₄, if we assume a similar mechanism to photocatalytic methanol reforming on Pd-TiO₂.^{16, 38, 56} The chemical nature of the e^-/h^+ pair generated by photoexcitation of C₃N₄ is that the h^+ will be on a carbon P_z orbital and the e^- will be on a nitrogen P_z orbital.¹³ It is therefore proposed that these species are responsible for completing the cycle of removing the partially decomposed amine with the use of the e^-/h^+ pair generated by photoexcitation of C₃N₄. Results from section 6.3.4 indicate that water plays an important role, as the reaction with only TEA produced significantly less H_2 than the reaction with TEA and water. However a detailed understanding of the mechanism involved here is currently not known by us.

Often in the literature another mechanism is proposed where the role of the amine hole scavenger in photocatalytic hydrogen production reactions involving C₃N₄, most commonly TEOA, is reported to remove the photogenerated h^+ . After providing an electron the TEOA becomes TEOA⁺ leaving the photogenerated electrons to reduce 2H^+ (or H_2O) to H_2 .^{17, 60, 61} This may happen to some extent however this neglects the decomposition of the amine on the surface of the metal, be it Pt or Pd.

The main goal of the photocatalytic reforming reactions in this chapter has been for the production of hydrogen. However it is clear that there will be other by products will also be produced during this process from the various amines tested. Analysis of the gas phase products for the photocatalytic reaction involving N,N-diisopropylethylamine was carried out by GC-MS. As conversion of the amines in these reaction is low to increase the likelihood of seeing the by-products the reaction was performed with extra catalyst (0.5 g) and N,N-diisopropylethylamine (10 mL). By this method it was possible to identify the presence of methane, ethane, propane and ethylene in the gas phase at the end of a reaction. Currently it is not known if these are major products or side products, however their presence does

indicate some N-C and C-C bond cleavage has occurred. This supports the experimental and computational data above that the amines are decomposing on the surface of the Pd.^{57, 58} These results also suggest that the role of the amine in this reaction is more than simply as an electron donor. However no direct observation of any nitrogen containing breakdown products was observed in these experiments here.

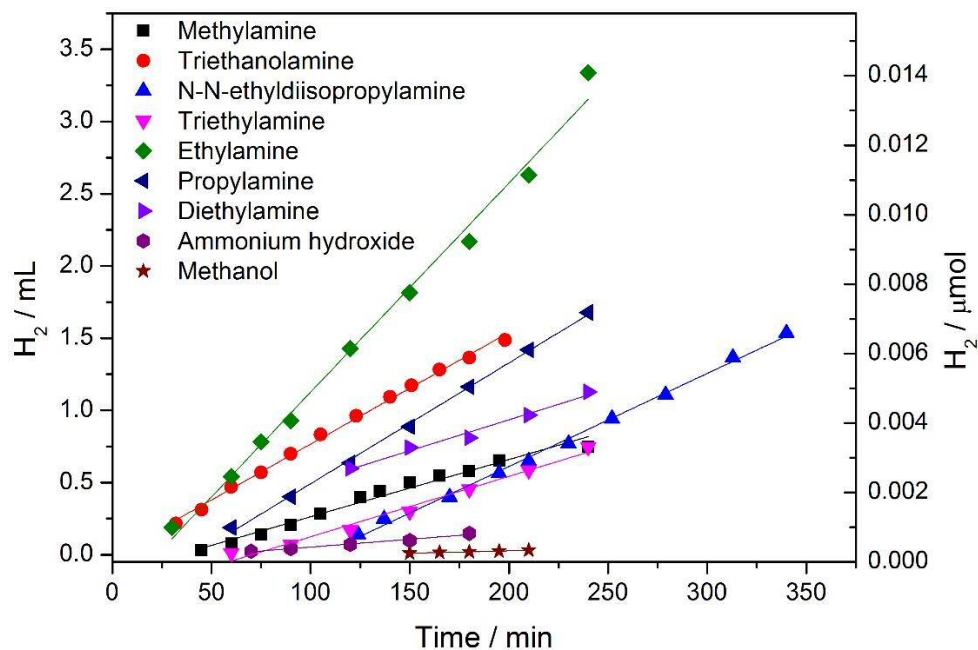


Figure 19. Hydrogen production plots for 3wt%Pd-C₃N₄ (isPD) catalyst with a variety of amine hole scavengers and methanol (0.025 moles in 200 mL H₂O)) under full arc irradiation. Points are plotted when the reaction hydrogen production becomes stable.

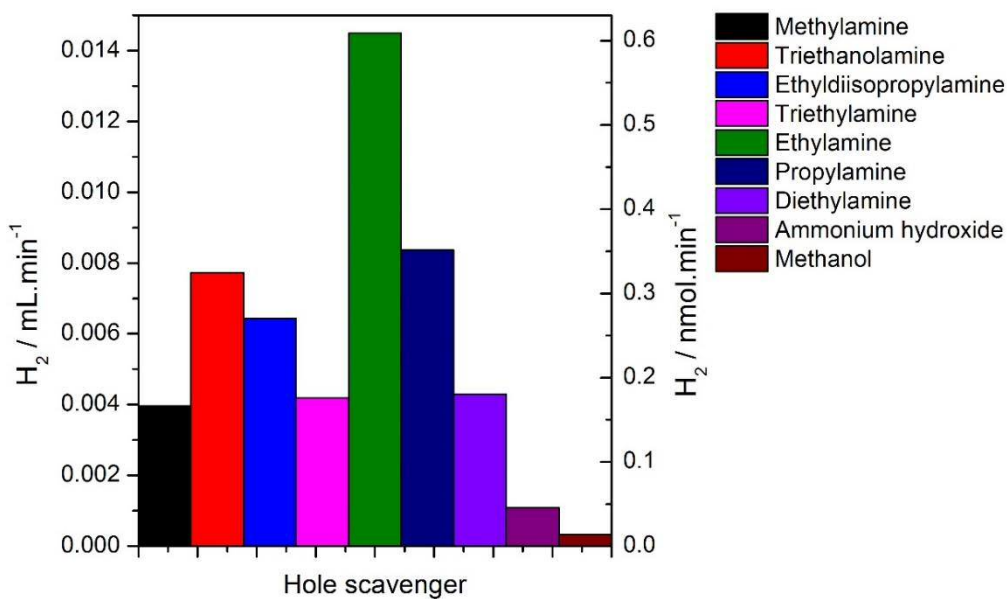


Figure 20. Average rates of hydrogen production after initial induction period for a variety of holes scavengers (0.025 moles in 200 mL H₂O) with a 3wt%Pd-C₃N₄ (isPD) catalyst under full arc irradiation.

Table 3. List of basic properties, boiling point, molar mass and density of sacrificial agents used for reaction in Figure 19. ^a Methylamine 40% solution in water, ^b Ethylamine 70% solution in water, N,N-Diisopropylethylamine immiscible with water (floated on top of water without stirring) and, ^d Ammonium hydroxide 25% in water. All amines were bought from Sigma Aldrich.

Scarificial agent	Boiling point (°C)	Molar mass (g.mol ⁻¹)	Density (g.cm ⁻³)
Methylamine, ^a	-6.6	31.06	0.90
Ethylamine, ^b	16	45.08	0.80
Triethylamine	88.6	101.19	0.72
Triethanolamine	200	149.19	1.14
Methanol	46	32.04	0.79
N,N-Diisopropylethylamine, ^c	126.6	129.24	0.74
Diethylamine	56.4	73.14	0.71
propylamine	47	59.11	0.72
Ammonium hydroxide, ^d	27	35.04	0.91

6.6.2 Amine reforming reactions on Pd-TiO₂

To compare with the results of amine reforming on a 3wt%Pd-C₃N₄ (isPD) catalyst from Figure 19 a set of photocatalytic hydrogen production reactions was also performed using a Pd-TiO₂ catalyst. Figure 21 shows hydrogen production plots for the various amines and methanol (0.0025 moles in 200 mL H₂O) from a 0.5wt%Pd-C₃N₄ (IW) catalyst and Figure 22 show the associated hydrogen production rate data.

Although the data shows that there is a variation in the amount of H₂ produced from each amine under these conditions it is evident that the Pd-TiO₂ catalyst is more active than the 3wt%Pd-C₃N₄ (isPD) catalyst despite there being 10 times less of the respective hole scavenger for this set of reactions. Also that the rate of H₂ production from methanol is more comparable to the rates achieved with the amines tested here. This combined with results from section 6.4 would suggest that Pd-TiO₂ catalysts react almost equally well with both amines and alcohols to produce H₂, unlike the g-C₃N₄ catalysts tested in this chapter.

Analysis of the gas phase products for the photocatalytic reaction involving N,N-diisopropylethylamine was carried out by GC-MS. Again this reaction was done with an increase of reactants (0.5 g of catalyst and 10 mL of N,N-diisopropylethylamine) to increase

the likelihood of detection of the gas phase products. By this method it was possible to verify the presence in the gas phase after a photocatalytic reaction of methane, ethane, ethylene, propane and carbon monoxide. This analysis was run as a purely qualitative so it is not possible to know without further work whether gases detected are major or side products. However their presence does indicate some N-C and C-C bond cleavage has occurred as for the N,N-diisopropylethylamine, as with the photo reaction 3wt%Pd-C₃N₄ isPD catalyst. Again as with the 3wt%Pd-C₃N₄ isPD catalyst the final state of the nitrogen from the amines was not found in these experiments as so is currently unclear.

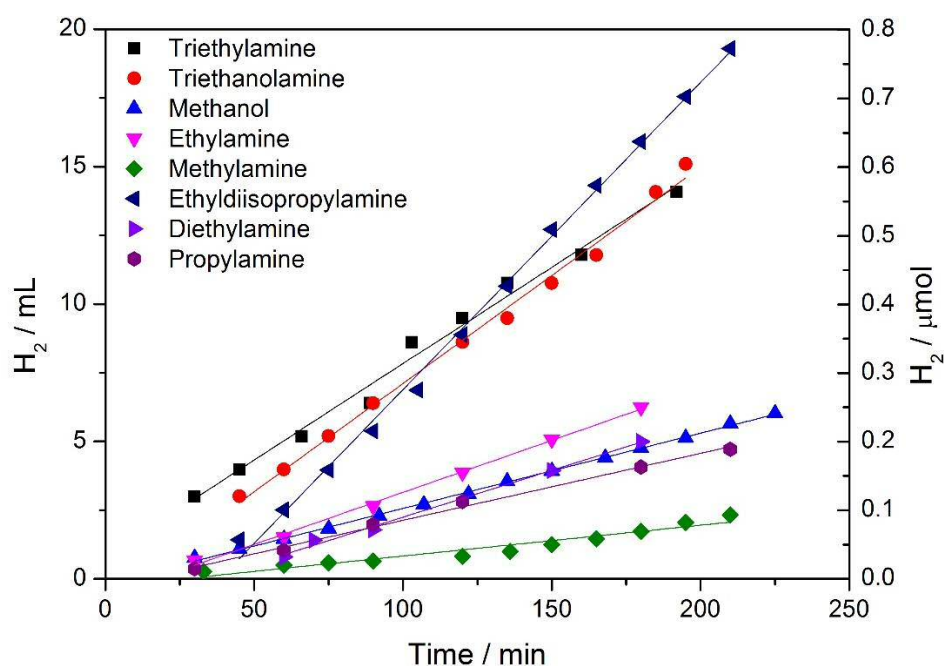


Figure 21. Hydrogen production plots for 0.5wt%Pd-TiO₂ catalyst with a variety of amine hole scavengers and methanol (0.0025 moles of each) under full arc irradiation. Points are plotted when the reaction hydrogen production becomes stable.

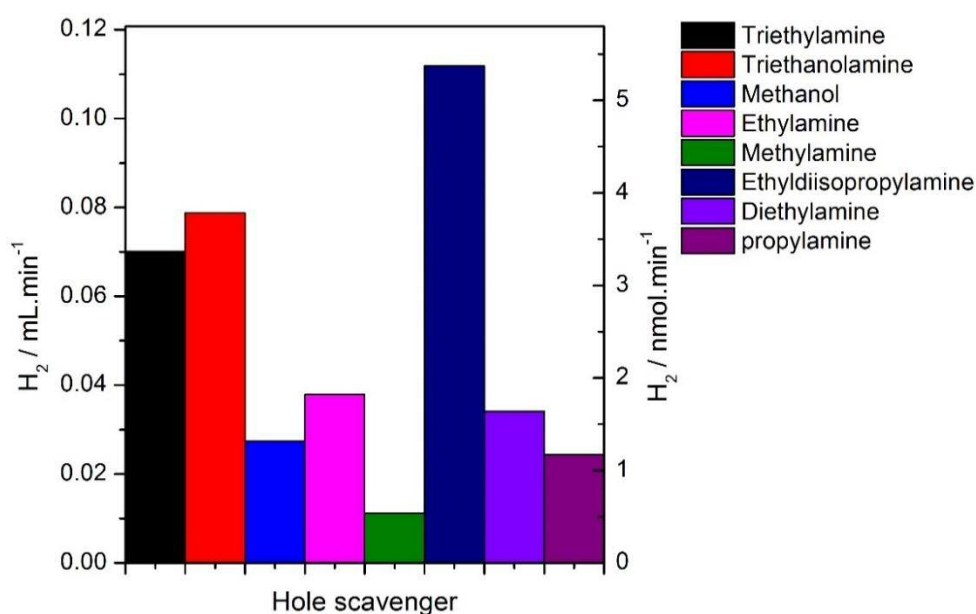


Figure 22. Average rates of hydrogen production after initial induction period for a variety of holes scavengers (0.0025 moles in 200 mL H_2O) with a 0.5wt%Pd-TiO₂ (IW) catalyst under full arc irradiation.

6.7 Conclusions

The $g\text{-C}_3\text{N}_4$ was synthesised by the thermal decomposition of urea for use as a semiconductor for photocatalytic reforming reactions. Characterisation by XRD, XPS, UV/vis and TEM was performed to gain an understanding of the properties of the urea derived $g\text{-C}_3\text{N}_4$ and was found to be in good agreement with $g\text{-C}_3\text{N}_4$ in the literature. Photocatalytic reactions comparing preparation methods of Pd- C_3N_4 (IW vs isPD), choice of metal co-catalyst (Pd vs Pt) and gas phase reactions vs liquid phase reaction were performed. Reactions using isPD was found to produce the highest rates of H_2 production for 3wt%Pd on $g\text{-C}_3\text{N}_4$ opposed to the same metal loading achieved by IW, with Pt and Pd found to give almost identical rates after the initial induction period by isPD. Gas phase reactions with an IW 3wt%Pd catalyst were found to be significantly more active than liquid phase reactions. This was a promising result which given more time could have been explored in more detail.

Comparison of $g\text{-C}_3\text{N}_4$ and TiO₂ (P-25), both loaded with Pd has been made for photocatalytic hydrogen production from TEOA and methanol. When irradiated with a solar simulator, Pd-TiO₂ was found to be the most active for these reactions. Of the hole scavengers used TEOA was demonstrated to be more active for this reaction compared to methanol and Pd- C_3N_4 showed almost no activity for methanol photo-reforming. Photocatalytic hydrogen

production using g-C₃N₄ is shown to be strongly correlating with the hole scavenger used; TEOA is over 14 times more effective than methanol. However under the same conditions but using TiO₂, it was demonstrated that TEOA is only twice as effective at scavenging holes in comparison to methanol. By performing tests under identical pH conditions, we experimentally verified that the pH difference between TEOA and methanol in aqueous solutions is not the primary reason for enhanced activity, with the presence of a nitrogen group thought to be more significant.

Photocatalytic tests were performed with long band pass filters in place to block out the UV radiation, allowing only visible light to interact with the TiO₂ and g-C₃N₄ based catalysts. Under these conditions g-C₃N₄ based catalysts were found to be active partially into the visible, with wavelengths up to 400 nm, but not up to 420 nm. The equivalent reaction using TiO₂ based catalyst was found to be inactive for visible light, but significantly more active with UV irradiation than the g-C₃N₄ based catalysts. This leads to the conclusion that g-C₃N₄ based catalysts have the advantage over TiO₂ based catalyst in that activity is observed with longer wavelength of light. However the rates of hydrogen production are poor, especially when under to full arc conditions for both semiconductors. Therefore currently pure undoped g-C₃N₄ based photocatalysts are inferior to TiO₂ based catalysts.

6.8 References

1. C. G. Silva, R. Juarez, T. Marino, R. Molinari and H. Garcia, *Journal of the American Chemical Society*, 2011, 133, 595-602.
2. M. Bowker, C. Morton, J. Kennedy, H. Bahruji, J. Greves, W. Jones, P. R. Davies, C. Brookes, P. P. Wells and N. Dimitratos, *Journal of Catalysis*, 2014, 310, 10-15.
3. H. Bahruji, M. Bowker, P. R. Davies, L. S. Al-Mazroai, A. Dickinson, J. Greaves, D. James, L. Millard and F. Pedrono, *Journal of Photochemistry and Photobiology a-Chemistry*, 2010, 216, 115-118.
4. L. S. Al-Mazroai, M. Bowker, P. Davies, A. Dickinson, J. Greaves, D. James and L. Millard, *Catalysis Today*, 2007, 122, 46-50.
5. A. Fujishima, X. T. Zhang and D. A. Tryk, *Surf. Sci. Rep.*, 2008, 63, 515-582.
6. K. Hashimoto, H. Irie and A. Fujishima, *Japanese Journal of Applied Physics Part 1- Regular Papers Brief Communications & Review Papers*, 2005, 44, 8269-8285.
7. A. Mattsson and L. Osterlund, *J. Phys. Chem. C*, 2010, 114, 14121-14132.
8. M. A. Henderson, *Surf. Sci. Rep.*, 2011, 66, 185-297.
9. M. D. Hernandez-Alonso, F. Fresno, S. Suarez and J. M. Coronado, *Energy Environ. Sci.*, 2009, 2, 1231-1257.
10. K. M. Reddy, S. V. Manorama and A. R. Reddy, *Mater. Chem. Phys.*, 2003, 78, 239-245.
11. X. C. Wang, K. Maeda, X. F. Chen, K. Takanabe, K. Domen, Y. D. Hou, X. Z. Fu and M. Antonietti, *Journal of the American Chemical Society*, 2009, 131, 1680-+.
12. G. Liu, P. Niu, C. H. Sun, S. C. Smith, Z. G. Chen, G. Q. Lu and H. M. Cheng, *Journal of the American Chemical Society*, 2010, 132, 11642-11648.

13. X. Wang, K. Maeda, A. Thomas, K. Takanahe, G. Xin, J. M. Carlsson, K. Domen and M. Antonietti, *Nat Mater*, 2009, 8, 76-80.
14. A. Thomas, A. Fischer, F. Goettmann, M. Antonietti, J. O. Muller, R. Schlogl and J. M. Carlsson, *J. Mater. Chem.*, 2008, 18, 4893-4908.
15. K. Maeda, X. C. Wang, Y. Nishihara, D. L. Lu, M. Antonietti and K. Domen, *J. Phys. Chem. C*, 2009, 113, 4940-4947.
16. H. Bahruji, M. Bowker, P. R. Davies and F. Pedrono, *Appl. Catal. B-Environ.*, 2011, 107, 205-209.
17. Z. Xing, Z. Chen, X. Zong and L. Wang, *Chemical Communications*, 2014, 50, 6762-6764.
18. D. J. Martin, K. P. Qiu, S. A. Shevlin, A. D. Handoko, X. W. Chen, Z. X. Guo and J. W. Tang, *Angewandte Chemie-International Edition*, 2014, 53, 9240-9245.
19. K. Schwinghammer, M. B. Mesch, V. Duppel, C. Ziegler, J. Senker and B. V. Lotsch, *Journal of the American Chemical Society*, 2014, 136, 1730-1733.
20. J. Liebig, *Annalen*, 1834, 10.
21. F. Goettmann, A. Fischer, M. Antonietti and A. Thomas, *Angewandte Chemie-International Edition*, 2006, 45, 4467-4471.
22. D. M. Teter and R. J. Hemley, *Science*, 1996, 271, 53-55.
23. E. Kroke, M. Schwarz, E. Horath-Bordon, P. Kroll, B. Noll and A. D. Norman, *New Journal of Chemistry*, 2002, 26, 508-512.
24. J. Sehnert, K. Baerwinkel and J. Senker, *The Journal of Physical Chemistry B*, 2007, 111, 10671-10680.
25. B. V. Lotsch and W. Schnick, *Chem.-Eur. J.*, 2007, 13, 4956-4968.
26. H. Ji, F. Chang, X. Hu, W. Qin and J. Shen, *Chemical Engineering Journal*, 2013, 218, 183-190.
27. S. C. Yan, Z. S. Li and Z. G. Zou, *Langmuir*, 2009, 25, 10397-10401.
28. G. Zhang, J. Zhang, M. Zhang and X. Wang, *J. Mater. Chem.*, 2012, 22, 8083-8091.
29. P. Apopei, C. Catrinescu, C. Teodosiu and S. Royer, *Applied Catalysis B: Environmental*, 2014, 160-161, 374-382.
30. Y. Zhang, J. Liu, G. Wu and W. Chen, *Nanoscale*, 2012, 4, 5300-5303.
31. A. B. Jorge, D. J. Martin, M. T. S. Dhanoa, A. S. Rahman, N. Makwana, J. W. Tang, A. Sella, F. Cora, S. Firth, J. A. Darr and P. F. McMillan, *J. Phys. Chem. C*, 2013, 117, 7178-7185.
32. M. Deifallah, P. F. McMillan and F. Cora, *J. Phys. Chem. C*, 2008, 112, 5447-5453.
33. H. J. Zhang, X. Q. Zuo, H. B. Tang, G. Li and Z. Zhou, *Physical Chemistry Chemical Physics*, 2015, 17, 6280-6288.
34. X. Li, G. Hartley, A. J. Ward, P. A. Young, A. F. Masters and T. Maschmeyer, *The Journal of Physical Chemistry C*, 2015, 119, 14938-14946.
35. H. Bahruji, M. Bowker, P. R. Davies, J. Kennedy and D. J. Morgan, *International Journal of Hydrogen Energy*, 2015, 40, 1465-1471.
36. H. Bahruji, M. Bowker, P. R. Davies, D. J. Morgan, C. A. Morton, T. A. Egerton, J. Kennedy and W. Jones, *Top. Catal.*, 2015, 58, 70-76.
37. Z. H. N. Al-Azri, W.-T. Chen, A. Chan, V. Jovic, T. Ina, H. Idriss and G. I. N. Waterhouse, *Journal of Catalysis*, 2015, 329, 355-367.
38. Z. Jiang, Z. Zhang, W. Shangguan, M. A. Isaacs, L. J. Durndell, C. M. A. Parlett and A. F. Lee, *Catalysis Science & Technology*, 2016, 6, 81-88.
39. L. Saeed Al-Mazroai, M. Bowker, P. Davies, A. Dickinson, J. Greaves, D. James and L. Millard, *Catalysis Today*, 2007, 122, 46-50.
40. G. Zhang, M. Zhang, X. Ye, X. Qiu, S. Lin and X. Wang, *Advanced Materials*, 2014, 26, 805-809.

41. J. Zhang, J. Sun, K. Maeda, K. Domen, P. Liu, M. Antonietti, X. Fu and X. Wang, *Energy Environ. Sci.*, 2011, 4, 675-678.
42. G. Liu, P. Niu, C. Sun, S. C. Smith, Z. Chen, G. Q. Lu and H.-M. Cheng, *Journal of the American Chemical Society*, 2010, 132, 11642-11648.
43. J. Zhang, M. Zhang, S. Lin, X. Fu and X. Wang, *Journal of Catalysis*, 2014, 310, 24-30.
44. X. Wang, X. Chen, A. Thomas, X. Fu and M. Antonietti, *Advanced Materials*, 2009, 21, 1609-1612.
45. J. Sun, J. Zhang, M. Zhang, M. Antonietti, X. Fu and X. Wang, *Nat Commun*, 2012, 1139.
46. Z. Zhang, Z. Luo, Z. Yang, S. Zhang, Y. Zhang, Y. Zhou, X. Wang and X. Fu, *RSC Advances*, 2013, 3, 7215-7218.
47. J. S. Im, S.-M. Yun and Y.-S. Lee, *Journal of Colloid and Interface Science*, 2009, 336, 183-188.
48. N. Serpone, *The Journal of Physical Chemistry B*, 2006, 110, 24287-24293.
49. P. Periyat, S. C. Pillai, D. E. McCormack, J. Colreavy and S. J. Hinder, *The Journal of Physical Chemistry C*, 2008, 112, 7644-7652.
50. Z. Zhang, G. Mestl, H. Knozinger and W. M. H. Sachtler, *Appl. Catal. A-Gen.*, 1992, 89, 155-168.
51. A. Dickinson, D. James, N. Perkins, T. Cassidy and M. Bowker, *J. Mol. Catal. A-Chem.*, 1999, 146, 211-221.
52. M. Yasuda, T. Tomo, S. Hirata, T. Shiragami and T. Matsumoto, *Catalysts*, 2014, 4, 162.
53. J. Ohyama, K. Teramura, S. Okuoka, S. Yamazoe, K. Kato, T. Shishido and T. Tanaka, *Langmuir*, 2010, 26, 13907-13912.
54. F. X. Zhang, J. X. Chen, X. Zhang, W. L. Gao, R. C. Jin and N. J. Guan, *Catalysis Today*, 2004, 93-5, 645-650.
55. P. Wu, J. Wang, J. Zhao, L. Guo and F. E. Osterloh, *Chemical Communications*, 2014, 50, 15521-15524.
56. M. Bowker, D. James, P. Stone, R. Bennett, N. Perkins, L. Millard, J. Greaves and A. Dickinson, *Journal of Catalysis*, 2003, 217, 427-433.
57. J. J. Chen and N. Winograd, *Surface Science*, 1995, 326, 285-300.
58. J.-H. Liu, C.-Q. Lv, Y. Guo and G.-C. Wang, *Applied Surface Science*, 2013, 271, 291-298.
59. H. Kominami, H. Nishimune, Y. Ohta, Y. Arakawa and T. Inaba, *Applied Catalysis B: Environmental*, 2012, 111-112, 297-302.
60. X. Yue, S. Yi, R. Wang, Z. Zhang and S. Qiu, *Scientific Reports*, 2016, 6, 22268.
61. J. Chen, S. Shen, P. Wu and L. Guo, *Green Chem.*, 2015, 17, 509-517.

Chapter 7: Conclusions and future work

Table of contents

7.1.1	Conclusions	214
7.1.2	Future work.....	217
7.1.3	References	218

7.1.1 Conclusions

The early experimental work in this thesis (chapter 3) focused on preparation of mono metallic Au NPs supported on TiO₂. Of the synthesis methods performed, sol immobilisation proved to be the most reliable for producing small NPs of ~3 nm which were deposited onto the TiO₂ surface. After investigating changing parameters during the sol immobilisation synthesis, such as the concentrations of precursors and solution temperature, a standard procedure was decided upon. A photoreactor was set up in the Research Complex at Harwell along with a GC, and the necessary methods developed to measure H₂ evolution. Initial photocatalytic hydrogen production reactions were performed with a 1 wt% Au-TiO₂ catalyst to choose the appropriate concentration of MeOH and mass of catalyst to use for standard reactions in the new reactor system. This was performed to maximise the amount of H₂ which could be produced from the lowest quantities of catalyst and MeOH, whilst not exceeding the capabilities of the reactor. Further initial testing was performed where the effect of catalyst calcination temperature and Au weight loading on H₂ production was investigated, in order to optimise activity. Calcination of the Au-TiO₂ catalyst at 400 °C was found to significantly improve activity. This is thought to be a consequence of the removal of the protecting ligand PVA from the surface of the Au NPs.¹ By varying the percentage weight loading of Au on TiO₂ a double maximum in rate of H₂ production was observed, at 0.5 and 1% for the dried and 0.7 and 2.0 % for the calcined catalyst. Other than Au NPs on TiO₂, catalysts containing Pd and Ag NPs were also synthesised, with the sol immobilisation method producing small NPs for Pd (~3 nm on average) but not with Ag (~8/9 nm on average). The colloidal synthesis methods from chapter 3 were built upon and developed in the following two chapters to produce bimetallic and core-shell NPs on TiO₂ for photocatalytic reactions.

Chapter 4 focused on bimetallic AuAg-TiO₂ catalysts with the aim of alloying the two metals to produce a less expensive catalyst while keeping or improving activity over mono metallic Au-TiO₂ catalyst. Two sets of AuAg-TiO₂ catalysts were produced by the sol immobilisation method. The first involved reducing the precursors (1:1 metal ratio by moles total loading 1%) simultaneously and sequentially in different orders. The goal of this was to see if NPs with a gold rich core, silver rich core or random alloy NP could be produced, to see the effect on photocatalytic activity. It was discovered that the order of reduction does indeed influence the amount of H₂ evolved photocatalytically, with catalysts made by producing a Au sol first, then reducing Ag being found to be the most active. Furthermore, this catalyst was also found to have superior activity when compared to monometallic reference catalysts of Au-TiO₂ and Ag-TiO₂. This improvement in activity was thought to be due to the bimetallic co-catalyst having an average structure of a Au rich core and a Ag rich shell.²

Since the Au core Ag shell NPs on TiO₂ was the most active catalyst it was decided to produce a second set of catalysts consisting of Au NPs (~3 nm) with thin layers of Ag on the surface. This was achieved by three variations of the sol immobilisation method refined in chapter 3, and Au NPs were produced with a theoretical covering of 1 and 2 mono layers Ag. The amount of Ag needed for the 1 and 2 monolayer coverage of the Au NPs was calculated based on a TEM particle size histogram which could be used to estimate the dispersion and hence number of surface sites of Au. Deposition was achieved by (i) first making a standard 1%Au-TiO₂ putting the catalyst in water with appropriate Ag precursor then reducing with NaBH₄ with the aim of the Ag being selectively reduced on the surface of the Au (sample name DR). The second method (ii) was done by repeating the steps of (i) with reduction performed by photodeposition (sample name PD). Finally (iii) in this method the Ag precursor was deposited onto the Au NPs in its sol form before deposition onto the support (sample name SR). As far as we are aware the preparation of core shell noble metal (AgAu or PdAu) NPs by a photodeposition route is novel and has not been reported in the literature, before this work was published.³ Characterisation by a combination of TEM, XPS and XAFS supported the deposition of Ag onto the preformed Au NPs by all three methods. The XAFS determined that the NPs consisted of an Au core with a mixture of Ag₂O, Ag and AgAu alloy at the surface. The set of six AgAu-TiO₂ core-shell samples with references of Au-TiO₂, AgAu-TiO₂ (1:1 by weight ratio total loading 1% random alloy) and Ag-TiO₂ were sent to Qian Yang at Aarhus University for photocatalytic H₂ production testing. Disappointingly and unexpectedly, based on the previous set of results, the mono layer catalysts were all less active than the mono

metallic Au-TiO₂ reference. Amongst the mono layer catalysts the PD method proved to produce the most H₂, with all outperforming the AgAu-TiO₂ and Ag-TiO₂ references.⁴

As well as the six AgAu-TiO₂ monolayer catalysts that were synthesised in chapter 4, a set of bimetallic AuPd catalyst were synthesised by the sol immobilisation method, again with the aim of producing structured NPs to investigate the effect on photocatalytic H₂ production, which would form the basis for chapter 5. The three preparation methods for depositing 1 and 2 monolayers of Pd onto the preformed Au NPs were identical to the deposition of Ag. Combined characterisation of TEM, XPS and XAFS supported the deposition of Pd onto the preformed Au NPs by all three methods, also labelled PD, SR and DR. This time XAFS determined that the NPs consisted of an Au core with an AuPd alloy at the surface with the absence of segregated Pd at the surface of the TiO₂. This set of catalysts was tested for photocatalytic H₂ production (by Ren Su at Aarhus University) with references of Au-TiO₂, PdAu-TiO₂ (1:1 by moles total loading 1% random alloy) and Pd-TiO₂. For this set of samples all of the core shell materials were found to be more active than all of the references, with the catalyst made by the PD method with 1 monolayer equivalent of Pd being the most active. This indicates that the presence of an AuPd alloy covering an Au NP supported on TiO₂ is responsible for the improved activity.³

Another set of bimetallic AuPd-TiO₂ was produced, this time with a 1:1 molar ratio and total loading 1%, similar to the AgAu-TiO₂ catalysts from chapter 4. Initially two catalysts were produced by the sol immobilisation method one with the precursors reduced together to produce a random alloy NPs and another with the Au precursor reduced first followed by the Pd precursor, to produce core shell NPs. Once this was done a sample of each was calcined at 400 °C to restructure the AuPd NPs on TiO₂, with this followed by EXAFS coordination numbers. After heat treatment the structure of the AuPd random alloy NPs was changed as the Au migrated to the centre of the NP while the Pd moved to the surface and oxidised. The sample which was made to have Au core Pd shell NPs on TiO₂ from the outset has less change after heat treatment as the Au was primarily in the core of the NP already, with the PdO at the surface. Testing of these catalysts for photocatalytic MeOH reforming was performed at two different MeOH concentrations. For the reaction with the higher level of methanol (1mL in 200 mL water) all catalysts display nearly identical activities despite the differences in AuPd NP structure from the EXAFS. However when testing was performed under low methanol conditions (0.1 mL in 200 mL water) the two calcined catalysts produced about twice as much H₂ as the dried. This could be a reflection of MeOH being able to penetrate the PVA layer on the dried catalysts more effectively at higher concentrations. In any case, for these catalysts

it was clear that the structure of the NPs on TiO₂ did not have a significant effect on the activity.

The vast majority of work done in this thesis performed with TiO₂ (P25) as the semiconductor support as a standard, with attempts to improve the photocatalytic H₂ production focusing on tuning the noble metal co-catalyst. The final experimental work performed (chapter 6) investigated using g-C₃N₄ as semiconductor support for photocatalytic H₂ production reactions. This was done as g-C₃N₄ has a narrower band gap compared to TiO₂ and therefore can utilise UV and some visible light (up to ~420 nm) for photoexcitation. The g-C₃N₄ used in these studies was synthesised by a colleague David Martin and was urea derived.⁵ Comparative reactions were performed to ascertain whether TiO₂ or g-C₃N₄ was the most active photocatalyst under full arc conditions, as well as looking at the effect of the hole scavenger used. Despite possessing a larger band gap TiO₂ produced more H₂ than g-C₃N₄ using both MeOH and TEOA as a hole scavenger. However g-C₃N₄ was found to have some visible light activity (400 nm long band pass filter) whereas TiO₂ did not. Therefore TiO₂ is the most active semiconductor support of the two under full arc irradiation, although g-C₃N₄ did have the advantage of some visible light activity. Further reactions were performed with a variety of simple amines and methanol with a Pd-g-C₃N₄ and Pd-TiO₂ catalyst under full arc irradiation. From these experiments it was again clear the TiO₂ was the most active semiconductor support, and that Pd-g-C₃N₄ produced significantly more H₂ with amines, as opposed to MeOH reactivity. This was opposite to Pd-TiO₂ which produced H₂ with comparable rates from both amine and MeOH.

7.1.2 Future work

- Several parameters were investigated which could affect the photocatalytic activity of Au-TiO₂ catalysts for H₂ production from MeOH reforming. These include effect of calcination temperature and total weight loading of Au, however one parameter not looked at was the effect of particle size at a constant weight loading. Determination of a particle size effect on activity could lead to a deeper understanding of photocatalytic reforming reactions on Au-TiO₂.
- Small NPs (~3 nm) were achieved by using the sol immobilisation method for Au and Pd, however this was not the case for Ag NPs (8/9 nm). Variation for the preparation method by changing the Ag/NaBH₄ or Ag/PVA ratios may lead to smaller particles which could lead to better photocatalytic activity for Ag-TiO₂ catalysts.
- Variation of the percentage weight loading of Au on TiO₂ yielded a double maximum in rate for both the dried and calcined catalyst. The exact reason for this is still

somewhat unclear, investigating this further could yield useful mechanistic information for photocatalytic reforming reactions on Au-TiO₂.

- One reaction of g-C₃N₄ was performed where the catalyst was pressed into a pellet and placed inside the photoreactor with some triethanolamine and water. Under these conditions only the gaseous vapour could come in contact with the catalyst under Xe arc lamp irradiation. Although a direct comparison with a liquid phase photo reaction is difficult it is clear that the gas phase reaction produced significantly more H₂. This was a promising result and the exact reason could be explored further as a method for maximising activity from g-C₃N₄ catalysts. This gas phase reaction could also be investigated with long band pass filters as a way of increasing activity of g-C₃N₄ as activity was disappointing compared to TiO₂.
- For reforming reactions of a Pd-g-C₃N₄ catalysts involving amines a complete understanding of the break down products and the final state of the nitrogen is not complete. Investigating this further could lead to an understanding of why amines outperform alcohols as hole scavengers for H₂ production. This could also lead to a more complete understanding of the mechanism of amine reforming on Pd-g-C₃N₄ catalysts

7.1.3 References

1. M. Bowker, C. Morton, J. Kennedy, H. Bahruji, J. Greves, W. Jones, P. R. Davies, C. Brookes, P. P. Wells and N. Dimitratos, *Journal of Catalysis*, 2014, 310, 10-15.
2. J. Kennedy, W. Jones, D. J. Morgan, M. Bowker, L. Lu, C. J. Kiely, P. P. Wells and N. Dimitratos, *Catalysis, Structure & Reactivity*, 2014, 1, 35-43.
3. W. Jones, R. Su, P. P. Wells, Y. Shen, N. Dimitratos, M. Bowker, D. Morgan, B. B. Iversen, A. Chutia, F. Besenbacher and G. Hutchings, *Physical Chemistry Chemical Physics*, 2014, 16, 26638-26644.
4. Q. Yang, W. Jones, P. P. Wells, D. Morgan, L. Dong, B. Hu, N. Dimitratos, M. Dong, M. Bowker, F. Besenbacher, R. Su and G. Hutchings, *Applied Catalysis A: General*, 2016, 518, 213-220.
5. D. J. Martin, K. Qiu, S. A. Shevlin, A. D. Handoko, X. Chen, Z. Guo and J. Tang, *Angewandte Chemie International Edition*, 2014, 53, 9240-9245.